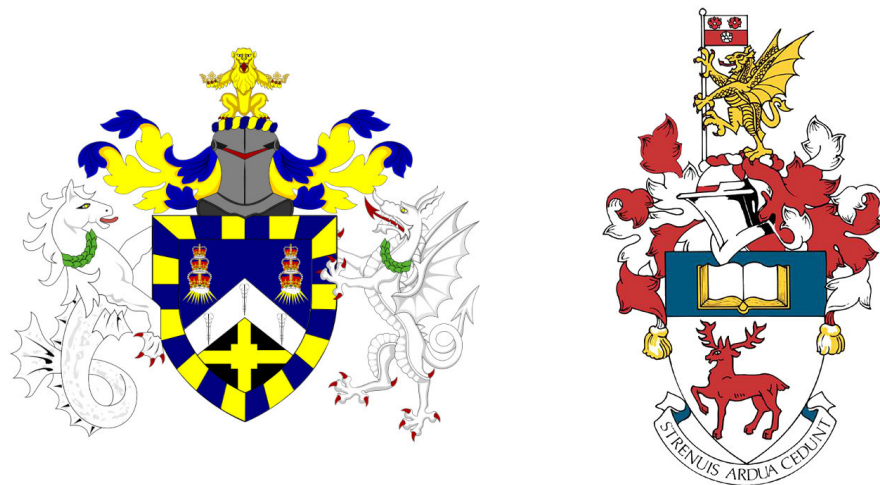


¹ ADVANCING NEUTRINO
² DETECTION AND TRIGGERING IN
³ DUNE



⁵ Francisco Martínez López

⁶ Submitted in partial fulfillment of the requirements
⁷ of the Degree of Doctor of Philosophy

⁸ School of Physical and Chemical Sciences
⁹ Queen Mary University of London

¹⁰ School of Physics and Astronomy
¹¹ University of Southampton

¹² December 2024

¹³ Statement of originality

- ¹⁴ I, Francisco Martínez López, confirm that the research included within this thesis is my
¹⁵ own work or that where it has been carried out in collaboration with, or supported by
¹⁶ others, that this is duly acknowledged below and my contribution indicated. Previously
¹⁷ published material is also acknowledged below.
- ¹⁸ I attest that I have exercised reasonable care to ensure that the work is original, and
¹⁹ does not to the best of my knowledge break any UK law, infringe any third party's
²⁰ copyright or other Intellectual Property Right, or contain any confidential material.
- ²¹ I accept that the University has the right to use plagiarism detection software to check
²² the electronic version of the thesis.
- ²³ I confirm that this thesis has not been previously submitted for the award of a degree
²⁴ by this or any other university.
- ²⁵ The copyright of this thesis rests with the author and no quotation from it or information
²⁶ derived from it may be published without the prior written consent of the author.
- ²⁷ Signature: [can be digital signature]
- ²⁸ Date:
- ²⁹ Details of collaboration and publications:
³⁰ [insert details here if applicable]

³¹ Abstract

³² Work in progress . . .

¡Oh memoria, enemiga mortal de mi descanso!

El ingenioso hidalgo don Quijote de la Mancha

MIGUEL DE CERVANTES SAAVEDRA

³³ Acknowledgements

³⁴ Work in progress . . .

³⁵ Contents

³⁶	Statement of originality	3
³⁷	Abstract	5
³⁸	Acknowledgements	9
³⁹	List of Figures	15
⁴⁰	List of Tables	31
⁴¹	List of Abbreviations	33
⁴²	1 Introduction	35
⁴³	2 Neutrino physics	37
⁴⁴	2.1 Neutrinos in the SM	37
⁴⁵	2.2 Trouble in the neutrino sector	41
⁴⁶	2.2.1 The solar neutrino problem	41
⁴⁷	2.2.2 The atmospheric neutrino problem	43
⁴⁸	2.3 Massive neutrinos	45
⁴⁹	2.4 Neutrino oscillation formalism	48
⁵⁰	2.4.1 Oscillations in vacuum	50
⁵¹	2.4.2 Oscillations in matter	52
⁵²	2.4.3 Current status of neutrino oscillations	54
⁵³	2.5 Open questions in the neutrino sector	55
⁵⁴	2.6 Neutrino interactions	57

CONTENTS

55	3 The Deep Underground Neutrino Experiment	59
56	3.1 Overview	59
57	3.2 Physics goals of DUNE	61
58	3.3 Far Detector	63
59	3.3.1 Horizontal Drift	64
60	3.3.2 Vertical Drift	67
61	3.3.3 FD Data Acquisition System	69
62	3.4 Near Detector	70
63	3.4.1 ND-LAr	72
64	3.4.2 TMS/ND-GAr	73
65	3.4.3 PRISM	74
66	3.4.4 SAND	76
67	3.5 LBNF beamline	76
68	4 ND-GAr	79
69	4.1 Requirements	79
70	4.2 Reference design	80
71	4.2.1 HPgTPC	80
72	4.2.2 ECal	81
73	4.2.3 Magnet	82
74	4.2.4 Muon system	83
75	4.3 GArSoft	83
76	4.3.1 Event generation	83
77	4.3.2 Detector simulation	84
78	4.3.3 Reconstruction	85
79	5 FWTPG offline software	89
80	6 Matched Filter approach to induction wire Trigger Primitives	91
81	6.1 Motivation	91

CONTENTS

82	6.2 Signal-to-noise ratio definition	93
83	6.3 Low-pass FIR filter design	95
84	6.4 Matched filters	98
85	6.5 Using simulated samples	104
86	6.5.1 Angular dependence	110
87	6.5.2 Distortion and peak asymmetry	112
88	6.5.3 Hit sensitivity	115
89	7 DM searches with neutrinos from the Sun	125
90	7.1 Motivation	125
91	7.2 Gravitational capture of DM by the Sun	125
92	7.3 Neutrino flux from DM annihilations	132
93	7.4 Computing limits from solar neutrino fluxes	133
94	7.5 Example: Kaluza-Klein Dark Matter	137
95	7.6 High energy DM neutrino signals	141
96	7.6.1 DIS events	143
97	7.6.2 Single proton QEL events	148
98	7.6.3 Results	151
99	7.7 Example: Leptophilic Dark Matter	153
100	8 Particle ID in GArSoft	159
101	8.1 dE/dx measurement in the TPC	160
102	8.1.1 Energy calibration	162
103	8.1.2 Truncated dE/dx mean	172
104	8.1.3 Mean dE/dx parametrisation	175
105	8.1.4 Particle identification	179
106	8.2 Muon and pion separation in the ECal and MuID	179
107	8.2.1 Track-ECal matching	182
108	8.2.2 Classification strategy	186
109	8.2.3 Feature selection and importance	190

CONTENTS

110	8.2.4	Hyperparameter optimisation	201
111	8.2.5	Probability calibration	205
112	8.2.6	Performance	207
113	8.3	ECal time-of-flight	207
114	8.3.1	Arrival time estimations	209
115	8.3.2	Proton and pion separation	210
116	8.4	Charged pion decay in flight	213
117	8.4.1	Track breakpoints	214
118	8.5	Neutral particle identification	221
119	8.5.1	ECal clustering	221
120	8.5.2	π^0 reconstruction	224
121	9	Event selection in ND-GAr	227
122	9.1	CAFs and CAFAna	227
123	9.2	Event selection	227
124	9.2.1	ν_μ CC selection	227
125	9.2.2	Charged pion multiplicity	227
126	10	Conclusions	229
127	A	An appendix	231
128	Bibliography		233

¹²⁹ List of Figures

130	2.1	Solar neutrino fluxes for the solar model BS05(OP).	42
131	2.2	Zenith angle distributions for the selected ν_e and ν_μ events in the SK detector.	44
132	2.3	$K^0 \rightleftharpoons \bar{K}^0$ mixing through W^\pm exchange.	48
134	2.4	57
135	2.5	Schematic representation of a ν_μ CCQE interaction with a neutron inside a nucleus.	58
137	3.1	Schematic diagram of the DUNE experiment and the LBNF beamline [1].	60
138	3.2	Schematic diagram showing the operating principle of a LArTPC with wire readout	64
140	3.3	Proposed design for the FD-1 and FD-2 modules following the HD principle.	65
141	3.4	Schematic representation of an APA frames showing the U, V, X and G wires.	66
143	3.5	A PDS module containing 24 X-ARAPUCAs and the location of the modules on the APAs.	66
144	3.6	Proposed design for the FD-3 module following the VD principle.	67
146	3.7	Schematic representation of the electrode strip configuration for a top and bottom CRU.	68
148	3.8	Detailed diagram of the DUNE FD DAQ system. Figure taken from Ref. [2].	69
150	3.9	Representation of the ND hall in Phase II, showing the different subcomponents.	71

LIST OF FIGURES

151	3.10 Schematic representation of the external components of ND-LAr, including the cryostat and the PRISM movable system and detailed drawing of one ArgonCube module.	72
152		
153		
154	3.11 Schematic view of the TMS detector, highlighting its main parts.	73
155		
156	3.12 Cross section of the ND-GAr geometry, showing the HPgTPC, ECal and magnet.	74
157		
158	3.13 Predicted beam muon neutrino flux at the ND location for different off-axis positions.	75
159		
160	3.14 Schematic longitudinal section of the LBNF beamline at Fermilab.	76
161		
162	3.15 Predicted neutrino fluxes at the FD in FHC mode and RHC mode.	77
163		
164		
165	4.1 Diagram of the ALICE TPC, showing the two drift chambers, inner and outer field cages and readout chambers.	81
166		
167		
168	4.2 Diagram of the ALICE TPC, showing the two drift chambers, inner and outer field cages and readout chambers.	82
169		
170		
171	6.1 <i>Schematic representation of an APA. The black lines represent the APA steel frame. The green and magenta lines correspond to the direction of the U and V induction wires respectively. The blue lines indicate the direction of the X collection wires and the wire shielding G.</i>	92
172		
173		
174		
175	6.2 <i>Left panel: Zoomed unfiltered waveform corresponding to channel 7840 from the ProtoDUNE-SP raw data capture felix-2020-07-17-21:31:44 (blue line). The green dashed lines mark the region $\pm 3\sigma_{raw}$. The resulting noise waveform is also shown (red line). Top right panel: ADC distribution for channel 7840, where the green shaded region represents $\pm \sigma_{raw}$. Bottom right panel: noise ADC distribution for channel 7840, where the green shaded region represents $\pm \sigma_{noise}$.</i>	93
176		

LIST OF FIGURES

176	6.3 <i>Left panel:</i> Zoomed filtered waveform corresponding to channel 7840 from the ProtoDUNE-SP raw data capture <i>felix-2020-07-17-21:31:44</i> (blue line). The filter used was the current implementation of the low-pass FIR filter in <i>dtp-firmware</i> . The green dashed lines mark the region $\pm 3\sigma_{\text{raw}}$. The resulting noise waveform is also shown (red line). <i>Top right panel:</i> ADC distribution for channel 7840 after filtering, where the green shaded region represents $\pm \sigma_{\text{raw}}$. <i>Bottom right panel:</i> noise ADC distribution for channel 7840 after filtering, where the green shaded region represents $\pm \sigma_{\text{noise}}$	95
184	6.4 Power spectrum in decibels for the current implementation of the low-pass FIR filter in <i>dtp-firmware</i> (blue line), compared to the response of an optimal filter obtained using the Parks-McClellan algorithm for the same pass-band (red line). Also for comparison I include the spectrum of the optimal filter when taking only the integer part of the coefficients (red dashed line).	96
190	6.5 Relative change in the S/N for the ProtoDUNE-SP raw data capture <i>felix-2020-07-17-21:31:44</i> , using different values of the cutoff frequency f_c and the transition width δf . The optimal Chebyshev filters were applied using just the integer part of the coefficients given by the Parks-McClellan algorithm.	97
195	6.6 Distribution of the relative change of the S/N on the different wire planes from the ProtoDUNE-SP raw data capture <i>felix-2020-07-17-21:31:44</i> after the optimal Chebyshev filter was applied. The filter was computed with the Parks-McClellan algorithm using a cutoff of $f_c = 0.068 \text{ ticks}^{-1}$ and a transition width $\delta f = 0.010 \text{ ticks}^{-1}$.	98

LIST OF FIGURES

200	6.7 Left panel: Zoomed match filtered waveform corresponding to channel 7840 201 from the ProtoDUNE-SP raw data capture <i>felix-2020-07-17-21:31:44</i> 202 (blue line). The filter used was directly extracted from the data, being 203 the 32 values around the first peak in the original waveform. The green 204 dashed lines mark the region $\pm 3\sigma_{\text{raw}}$. The resulting noise waveform is 205 also shown (red line). Top right panel: ADC distribution for channel 7840 206 after match filtering, where the green shaded region represents $\pm \sigma_{\text{raw}}$. 207 Bottom right panel: noise ADC distribution for channel 7840 after match 208 filtering, where the green shaded region represents $\pm \sigma_{\text{noise}}$	99
209	6.8 Relative improvement in the S/N for the raw data capture <i>felix-2020-07-17-21:31:44</i> , 210 using the matched filter following the parametrisation in Eq. (6.17). The 211 black crosses in both panels denote the location of the maximum ratio value.	102
212	6.9 Left panel: Optimal matched filter coefficients for the U (blue line) and V 213 (red line) planes. The filters were computed with our parametrisation in 214 Eq. (6.17) for the parameter values $\delta = 0.035$, $\sigma = 0.191$ and $\delta = 0.018$, 215 $\sigma = 0.191$ respectively. Right panel: Distribution of the relative change of 216 the S/N on the two induction wire planes from the ProtoDUNE-SP raw 217 data capture <i>felix-2020-07-17-21:31:44</i> after their respective optimal 218 matched filters were applied.	105
219	6.10 Left panel: distributions of the particles track length in the liquid argon 220 for the generated $E_k = 100$ MeV monoenergetic samples, electrons (blue), 221 muons (red), protons (green) and neutral pions (purple). Right panel: 222 distribution of the length of the longest photon in the neutral pion sample 223 after the decay process $\pi^0 \rightarrow \gamma\gamma$	106

LIST OF FIGURES

LIST OF FIGURES

249	6.15 Selected consecutive waveforms corresponding to two monoenergetic $E_k =$	
250	100 MeV muon events, one is parallel to the APA and to the wires in	
251	the U plane (left panel) and the other is normal to the APA plane and	
252	perpendicular to the U plane wires (right panel). The solid lines represent	
253	the raw waveforms whereas the dashed lines correspond to the waveforms	
254	after the matched filter was applied. The waveforms on the left panel have	
255	been scaled by a factor of 0.15 to have similar amplitude to the ones on	
256	the right panel.	113
257	6.16 Left panel: peak asymmetry distribution for the case of the monoenergetic	
258	$E_k = 100$ MeV muon sample. Each value corresponds to a single bipolar	
259	signal peak from a channel in any event. The blue distribution represents	
260	the peaks on U plane channels, whereas the red corresponds to signal peaks	
261	in V wires. Right panel: relation between the mean peak asymmetry per	
262	event with the S/N for U channel waveforms from the $E_k = 100$ MeV	
263	muon sample. The top subplot shows the decimal logarithm of the mean	
264	S/N for the raw (red) and the matched filtered (blue) waveforms. The	
265	bottom subplot contains the mean S/N improvement ratio after the matched	
266	filter was applied.	114
267	6.17 Raw data display in the plane time (in firmware ticks) vs. offline channel	
268	number for an $E_k = 100$ MeV electron event. The produced true hits are	
269	superimposed (black boxes) as well as the hits comming from the standard	
270	hit finder chain (blue circles) and the hit finder using the matched filter	
271	(green triangles).	116

LIST OF FIGURES

- 272 6.18 *Dependence of the precision (blue), sensitivity (red) and F_1 (green) scores*
273 *on the threshold values used in the hit finder, for the FIR (left panel)*
274 *and matched filter (right panel) cases. The results were obtained after*
275 *matching the hits to the true hits in the case of the isotropic muon sample*
276 *with kinetic energy in the range 5 to 100 MeV, taking only into account*
277 *the induction plane channels. The points represent the mean value while*
278 *the error bars indicate one standard deviation around that mean value.* . . 118
- 279 6.19 *Dependence of the averaged hit sensitivity on the kinetic energy of the*
280 *events for the matched filter (blue) and standard (red) hits, for the case of*
281 *the muon (left panel) and electron (right panel) samples, separated between*
282 *U (top plots) and V (bottom plots) induction wire planes. The top subplots*
283 *contain the hit sensitivities for the two hit finder alternatives, while the*
284 *bottom subplots show the ratio between the two. The horizontal lines sit at*
285 *the mean value and represent the size of the energy bins, while the vertical*
286 *error bars indicate one standard deviation around that mean value.* . . . 120
- 287 6.20 *Distributions of the hit sensitivity in the U (top panels) and V (bottom*
288 *panels) planes versus the hit sensitivity in the X plane, both for the*
289 *standard hits (left panels) and the matched filter hits (right panels), in the*
290 *case of the electron sample and a threshold of 30 ADC.* 121
- 291 6.21 *Top panels: standard residual plots of the hit sensitivities between the X*
292 *and U planes. Bottom panels: quantile-quantile plots of the hit sensitivity*
293 *standard residuals between the X and U planes. In all cases, the left*
294 *panel corresponds to the standard hits while the right panel represents the*
295 *matched filter case, all from the electron sample with a 30 ADC threshold.* 122

LIST OF FIGURES

296	7.1	<i>Input solar parameters used in our capture rate computation as functions of the Sun's radius, from left to right: temperature (with respect to the temperature at the core), mass (in solar masses) and electron number density (with respect to the electron density at the core). All quantities shown correspond to the standard solar model BS2005-OP [3].</i>	129
301	7.2	<i>Capture rates as a function of the DM mass for the DM-electron interactions (red lines), SD DM-nucleons interactions (green lines) and SI DM-nucleons interactions (blue lines). Solid lines represent the values computed in this work while the dashed lines are the one given in Ref. [4]. All the rates are shown for a choice of scattering cross section of $\sigma_i = 10^{-40} \text{ cm}^2$. . .</i>	130
306	7.3	<i>NuWro computed $\nu_\mu - {}^{40}\text{Ar}$ charged-current scattering cross section as a function of the neutrino energy E_μ. The black line shows to the total cross section, whereas the others correspond to the different contributions (in red quasi-elastic scattering, in green resonant pion exchange, in blue deep inelastic scattering and in purple meson exchange current).</i>	134
311	7.4	<i>Expected atmospheric neutrino flux as a function of the neutrino energy E_ν at Homestake at solar minimum, taken from Ref. [5]. The blue solid (dashed) line correspond to muon neutrinos (antineutrinos) and the red solid (dashed) line correspond to electron neutrinos (antineutrinos). . . .</i>	136
315	7.5	Feynman diagrams for B^1B^1 annihilation into SM fermions.	138
316	7.6	Feynman diagrams for B^1B^1 annihilation into a Higgs boson pair. . . .	138
317	7.7	<i>Computed spectra of muon neutrinos at the DUNE FD site from B^1 annihilations in the Sun for three different values of M_{LKP}, plotted in relative energy units for legibility.</i>	139

LIST OF FIGURES

<p>320 7.8 <i>Projected 90% confidence level upper limit for DUNE (400 kT yr) on the spin-dependent B^1-proton scattering cross section as a function of M_{LKP} (green dots). I also show the previous limits from IceCube [6] (blue line) and Antares [7] (red line) on the LKP cross section. The shaded area represents the disfavoured region (at 95% confidence level) on the mass of the LKP from LHC data [8].</i></p> <p>321</p> <p>322</p> <p>323</p> <p>324</p> <p>325</p>	140
<p>326 7.9 <i>Computed spectra of muon neutrinos at the DUNE FD site from $\tau^+\tau^-$ (left panel) and $b\bar{b}$ (right panel) annihilations in the Sun for the DM masses $m_{\text{DM}} = 10$ GeV (red line), 50 GeV (green line) and 100 GeV (blue line), plotted in relative energy units.</i></p> <p>327</p> <p>328</p> <p>329</p>	141
<p>330 7.10 <i>Distribution of the muon neutrino energies from the $\tau^+\tau^-$ (left panel) and $b\bar{b}$ (right panel) annihilation channels, for $m_{\text{DM}} = 10$ GeV, separated by CC interaction type: QEL (blue), MEC (orange), RES (green) and DIS (red).</i></p> <p>331</p> <p>332</p> <p>333</p>	143
<p>334 7.11 <i>Distributions of θ_μ (left panel), θ_j (central panel) and θ_{plane} (right panel) for the $b\bar{b}$ sample with $m_{\text{DM}} = 10$ GeV (blue) and the atmospheric background (red).</i></p> <p>335</p> <p>336</p>	144
<p>337 7.12 <i>Left panel: signal efficiencies (blue lines) and background rejections (red lines) for events passing the cuts $\theta < \theta_{\text{cut}}$ for the jet (solid lines) and muon (dashed lines) angles. Right panel: signal efficiency (blue line) and background rejection (red line) for events passing the cut $\theta_{\text{plane}} < \theta_{\text{cut}}$ for the momentum conservation plane deviation.</i></p> <p>338</p> <p>339</p> <p>340</p> <p>341</p>	145
<p>342 7.13 <i>Signal efficiencies for the $\tau^+\tau^-$ (blue line) and $b\bar{b}$ (red line) DIS samples as functions of the DM mass, m_{DM}, obtained by applying the optimal angular cuts $\theta_\mu < 27^\circ$, $4^\circ < \theta_j < 26^\circ$ and $\theta_{\text{plane}} < 3.5^\circ$.</i></p> <p>343</p> <p>344</p>	147
<p>345 7.14 <i>Distributions of $\cos \theta_\mu$ (left panel), $\cos \theta_p$ (central panel) and $\cos \theta_N$ (right panel) for the $\tau^+\tau^-$ QEL sample with $m_{\text{DM}} = 5$ GeV (blue) and the atmospheric background (red).</i></p> <p>346</p> <p>347</p>	148

LIST OF FIGURES

348	7.15 Left panel: value of the loss function for the training sample (blue line) and accuracy for the validation sample (red line) versus the number of iterations for the MLP classifier training. Right panel: distributions of the predicted probabilities assigned by the MLP classifier to the test sample for the $\tau^+\tau^-$ QEL signal with $m_{\text{DM}} = 5$ GeV (blue) and the atmospheric background (red).	149
354	7.16 Signal efficiencies for the $\tau^+\tau^-$ (blue line) and $b\bar{b}$ (red line) single proton QEL samples as functions of the DM mass, m_{DM} , obtained by requiring a minimum predicted probability from the MLP classifier of 0.97 in order to achieve a background rejection greater than 99.8%.	150
358	7.17 Projected 90% confidence level upper limit for DUNE (400 kT yr) on the spin-dependent DM-nucleon scattering cross section as a function of m_{DM} , for the annihilation channels $\tau^+\tau^-$ (blue) and $b\bar{b}$ (red) separated by interaction type (up triangles denote DIS interactions whereas down triangles represent QEL interactions). I also show the previous limits from IceCube [9] (solid lines) and the projected sensitivities for Pingu [10] (dashed lines) and Hyper-Kamiokande [11] (dash-dotted lines), as well as the direct detection limits from PICASSO [12] (solid green line) and PICO-60 C ₃ F ₈ [13] (dashed green line).	152
367	7.18 Left panel: Projected 90% confidence level sensitivity of DUNE (400 kT yr) to the scale Λ of an EFT containing only leptophilic DM axial-axial interactions (blue line). Right panel: . In both cases the corresponding limits from DarkSide-50 [14] (dotted green line) and XENON1T [15] (dashed red line) are also shown, together with the configurations for which the correct relic density is achieved (black line), all for the coupling values $c_A^e = 10^3$ and $c_A^\nu = 10^{-2}$	156

LIST OF FIGURES

374	8.1 Distribution of the fraction of energy deposits with residual range less than 20% of the total track length, and distribution of the ionisation per unit length after removing the tracks with less than 30% of their energy deposits in the last 20% of the track.	163
378	8.2 Distribution of the reconstructed ionisation charge per unit length for different reclustering values, and distribution of the median change in dQ/dx per track for the $N_{group} = 4$ reclustering.	164
381	8.3 Distribution of the Geant4-simulated energy losses per unit length versus residual range for the stopping proton sample.	166
383	8.4 Fitted most probable dQ/dx values for each dE/dx bin, together with best fit to the logarithmic calibration function.	167
385	8.5 Fitted most probable dQ/dx values for each dE/dx bin for three different ADC bit limits.	169
387	8.6 Area normalised dE/dx distributions for the true and the reconstructed energy deposits in the stopping proton sample, both after applying the calibration and the calibration and the normalisation correction.	170
390	8.7 Fractional residuals between the true and the corrected dE/dx means and the 60% truncated means, and fractional residuals between the true and the uncorrected, corrected and uncalibrated dE/dx 60% truncated means.	172
394	8.8 Estimated values of the mean dE/dx bias and resolution for the stopping proton sample at different values of the truncation factor.	173
396	8.9 Examples of the truncated mean dE/dx LanGauss fits for various $\beta\gamma$ bins, from a simulated FHC neutrino sample.	175
398	8.10 Resulting one and two dimensional projections of the posterior probability distributions of the ALEPH $\langle dE/dx \rangle$ parameters obtained by fitting the 60% truncated mean dE/dx values from a FHC neutrino sample.	176

LIST OF FIGURES

401	8.11 Truncated mean dE/dx obtained for the FHC neutrino sample as a function of the $\beta\gamma$ product, together with the fitted most probable values for each $\beta\gamma$ bin and the best fit obtained using the ALEPH parametrisation.	177
404	8.12 Distribution of the 60% truncated mean dE/dx versus reconstructed momentum for the FHC neutrino sample.	178
406	8.13 Estimated values of the mean dE/dx bias and resolution obtained for the true protons in a FHC neutrino sample.	179
408	8.14 True momentum distribution for the primary muon in ν_μ CC $N\pi^\pm$ interactions inside the fiducial volume of ND-GAr, compared to the post FSI charged pion spectrum.	180
411	8.15 Distributions of energy deposits in the ECal for a muon and a charged pion with similar momenta.	181
413	8.16 Left panel: comparison between the precision (blue), sensitivity (yellow) and F_1 score (red) obtained for the default (horizontal lines) and new algorithms, both with the χ^2 -based direction estimator (squares) and cheating the directions (circles), for different values of the χ^2 cut. Right panel: comparison of the performance of the new algorithm when applying the cluster t_0 correction (squares) and when (circles).	183
419	8.17 Schematics of a possible option to deal with track-ECal associations in non-zero t_0 neutrino interaction events, trying to correct for the drift direction uncertainty in a cluster-by-cluster basis using the cluster time, $t_{cluster}$	185
423	8.18 Momentum distribution for the reconstructed muons (top panel) and charged pions (bottom panel) in a FHC neutrino sample, together with the fraction of them reaching the ECal (red) and MuID (blue). Each entry corresponds to a reconstructed track, backtracked to a true muon or pion which has not produced any other reconstructed track.	187

LIST OF FIGURES

428	8.19 Predicted truncated mean dE/dx versus momentum, for electrons, muons, 429 charged pions and protons, obtained using the ALEPH parametrisation. 430 The vertical dashed lines represent the boundaries of the six regions used 431 for the muon and pion classification training.	188
432	8.20 Example ECal feature distributions for muons and charged pions in the 433 five different momentum ranges considered.	192
434	8.21 Example MuID feature distributions for muons and charged pions in the 435 three different momentum ranges considered.	193
436	8.22 Left panel: cumulative explained variance for the first three principal 437 components (top panel) and contribution of the different features to the 438 principal axes in feature space (bottom panel). Right panel: Shapley 439 (blue) and Gini (red) feature importances for the different input features. 440 Both figures correspond to the samples in the momentum range $0.3 \leq$ 441 $p < 0.8 \text{ GeV}/c$	195
442	8.23 Left panel: cumulative explained variance for the first three principal 443 components (top panel) and contribution of the different features to the 444 principal axes in feature space (bottom panel). Right panel: Shapley 445 (blue) and Gini (red) feature importances for the different input features. 446 Both figures correspond to the samples in the momentum range $0.8 \leq$ 447 $p < 1.5 \text{ GeV}/c$	196
448	8.24 Evolution of the SHAP importance for the top six most important features 449 across all five momentum ranges.	198
450	8.25 Permutation importances for the ten most important features in the 451 different momentum ranges (from left to right, top to bottom, in increasing 452 momentum order). The bars indicate the effect that permutations of 453 each feature have on the purity (blue) and the sensitivity (yellow), the 454 translucent regions representing one standard deviation around the central 455 value.	200

LIST OF FIGURES

456	8.26 Values of the precision and sensitivity obtained for 10000 BDT hyperparameter	
457	configurations, for the momentum regions I, III and V.	203
458	8.27 Reliability diagrams for the BDT classifier used in the momentum range	
459	$0.3 \leq p < 0.8 \text{ GeV}/c$, both for the original (blue circles) and calibrated	
460	(yellow squares) responses. For reference, the response of a perfectly	
461	calibrated classifier is also shown (black dashed line).	205
462	8.28 Uncalibrated (left panel) and calibrated (right panel) predicted probabilities	
463	assigned by the BDT classifiers for true muons (blue) and charged pions	
464	(red) in the momentum range $0.3 \leq p < 0.8 \text{ GeV}/c$	206
465	8.29 Schematic of the hit selection used for the ToF measurement. The grid	
466	represents the layers of the inner ECal, with coloured squares indicating	
467	the tiles with hits. Green squares indicate the selected hits.	208
468	8.30 Particle velocity versus momentum measured with different ECal arrival	
469	time estimations. From left to right: earliest hit time, average hit time,	
470	and fitted hit time. In all cases the time resolution is $\Delta\tau = 0.1 \text{ ns}$	210
471	8.31 Mass spectra for p (blue) and π^\pm (yellow) particles, using different ECal	
472	time resolution values (from top to bottom, in ascending order), and	
473	arrival time estimates. From left to right: earliest hit time, average hit	
474	time, and fitted hit time. The dashed lines indicate the true masses of	
475	the particles.	211
476	8.32 Efficiency (top panel) and purity (bottom panel) for the proton selection	
477	as a function of the momentum, for $\Delta\tau = 0.10 \text{ ns}$	212
478	8.33 Distributions of the velocities measured by ToF with the inner ECal, for	
479	different momentum bins, in a FHC neutrino interaction sample. The	
480	Gaussian fits are performed around the maxima for each particle species.	213

LIST OF FIGURES

481	8.34 Left panel: number of non-decaying, decaying and decaying in the fiducial volume pions for a MC sample of 100000, $p = 500$ MeV/ c isotropic positively charged pions inside the TPC. Right panel: event display for a positive pion decaying inside the fiducial volume, with a single reconstructed track for the pion and muon system.	214
486	8.35 Values of $\chi_k^2(FB)$ (top left panel), F_k (top right panel), $D_k^{1/R}$ (bottom left panel) and D_k^ϕ (bottom right panel) versus position along the drift direction for a reconstructed track in a positive pion decay event. The vertical red dashed line indicates the true location of the decay point. . .	216
490	8.36 Fractional residual distributions of the true and reconstructed decay position along the drift coordinate, using the position of the maximum of $\chi_k^2(FB)$ (left panel) and F_k (right panel) as estimates of the decay position. Also shown are double Gaussian fits to these points (red lines). . .	217
494	8.37 Distributions of the extreme values of $\chi_k^2(FB)$ (top left panel), F_k (top right panel), $D_k^{1/R}$ (bottom left panel) and D_k^ϕ (bottom right panel) for non-decaying reconstructed pion tracks (blue) and tracks which include the decay inside the fiducial volume (red).	219
498	8.38 Left panel: distributions of the predicted probabilities assigned by the BDT classifier to a test sample of decaying pion+muon tracks (blue) and non-decaying pion tracks (red). Left: signal efficiency versus background acceptance (ROC curve) obtained from the BDT for the test sample. . .	220
502	8.39 Left panel: dependence of the decay position finding resolution on the true value of the decay angle for the $\chi_k^2(FB)$ (red) and F_k (blue) methods. Right panel: signal efficiency (blue line) and background rejection (red line) from the BDT classifier versus true decay angle.	220

LIST OF FIGURES

506	8.40 Mean values of the F_1 -score marginal distributions for the different	
507	free parameters of the new clustering algorithm, with the error bars	
508	representing one standard deviation around the mean. The F_1 -score	
509	values were computed for the 6561 possible parameter configurations	
510	using 1000 ν_μ CC interaction events.	223
511	8.41 Left panel: distributions of the number of ECal clusters per photon from	
512	π^0 decays for the standard (red) and new (blue) clustering algorithms.	
513	Right panel: reconstructed invariant mass distributions for photon pairs	
514	from single π^0 events using the standard (red) and new (blue) ECal	
515	clustering algorithms.	225

516 List of Tables

517	2.1	Values of T_3 and $Y/2$ assigned to the first generation of fermions.	39
518	2.2	Neutral current couplings.	40
519	2.3	Summary of neutrino oscillation parameters determined in the Neutrino	
520		Global Fit of 2020 [16].	56
521	3.1	Summary of the two-phased plan for DUNE	61
522	3.2	Exposure and time required to achieve the different physics milestones of	
523		the two phases	62
524	6.1	<i>Characteristic parameters of the two monoenergetic muon events selected, relative to the U plane: projected angles in the xz' and y'z' planes, S/N values for the raw and filtered waveforms, mean improvement of the S/N and peak asymmetry.</i>	113
528	8.1	Calibration parameters obtained from the fit of the ND-GAr simulated stopping proton sample to the calibration function, for different ADC limits.	169
530	8.2	Momentum ranges and description of the PID approach assumed for the	
531		muon and pion classification task.	189
532	8.3	Optimal values of the hyperparameters used by the BDT, for each	
533		momentum range.	204
534	8.4	Performance metrics of the BDTs with optimal hyperparameters, for the	
535		different momentum ranges.	204

LIST OF TABLES

536	8.5 Summary of parameters and sampled values used in the optimisation of	
537	the clustering algorithm.	223

538

⁵³⁹ List of Abbreviations

ADC	Analog to Digital Converter.
ALEPH	Apparatus for LEP PHysics.
ALICE	A Large Ion Collider Experiment.
BDT	Boosted Decision Tree.
CC	Charged Current.
DM	Dark Matter.
DUNE	Deep Underground Neutrino Experiment.
ECal	Electromagnetic Calorimeter.
FD	Far Detector.
FHC	Forward Horn Current.
HPgTPC	High Pressure gaseous Time Projection Chamber.
LBL	Long BaseLine.
MuID	Muon IDentification system.
NC	Neutral Current.
ND	Near Detector.
ND-GAr	Near Detector Gaseous Argon.
ND-LAr	Near Detector Liquid Argon.
PDG	Particle Data Group.
RHC	Reverse Horn Current.

540 Chapter 1

541 Introduction

542 Chapter 2

543 Neutrino physics

544 *Little particles of inspiration sleet through the universe all the time traveling
545 through the densest matter in the same way that a neutrino passes through a
546 candyfloss haystack, and most of them miss.*

547 – Terry Pratchett, *Sourcery*

548 Ever since they were postulated in 1930 by Wolfgang Pauli to explain the continuous
549 β decay spectrum [17] and later found by F. Reines and C. Cowan at the Savannah
550 River reactor in 1953 [18], neutrinos have had a special place among all other elementary
551 particles. They provide a unique way to probe a wide range of quite different physics,
552 from nuclear physics to cosmology, from astrophysics to colliders. Moreover, there is
553 compelling evidence to believe that the study of neutrinos may be key to unveil different
554 aspects of physics beyond the SM, difficult to test elsewhere.

555 In this Chapter, I will review the basics of neutrino physics, from its role within the
556 SM to the main open questions related to the neutrino sector, paying special attention
557 to the phenomenology of neutrino oscillations.

558 2.1 Neutrinos in the SM

559 The SM of fundamental interactions was initially proposed in 1967 by S. Glashow, S.
560 Weinberg and A. Salam[19–21]. This theoretical framework describes the dynamics

Chapter 2. Neutrino physics

of leptons and quarks, by introducing a collection of mediating gauge vector bosons and one scalar particle, known as the Higgs boson. It assumes that the local $SU(3) \times SU(2)_L \times U(1)_Y$ gauge symmetry is an internal symmetry of the system, with $SU(3)$ describing quantum chromodynamics, and $SU(2)_L \times U(1)_Y$ being the gauge groups of the electroweak sector. For a detailed overview of the SM of electroweak interactions, see Ref. [22].

In the SM, neutrinos appear in three flavours, namely ν_e , ν_μ , and ν_τ . These are associated with the corresponding charged leptons, e , μ , and τ . Neutrinos exist only as left-handed particles, grouped in doublets with the charged leptons, while the later come in both chirality states:

$$\begin{pmatrix} \nu_e \\ e_L^- \end{pmatrix}, \quad \begin{pmatrix} \nu_\mu \\ \mu_L^- \end{pmatrix}, \quad \begin{pmatrix} \nu_\tau \\ \tau_L^- \end{pmatrix}, \quad e_R^-, \quad \mu_R^-, \quad \tau_R^-. \quad (2.1)$$

Similarly, quarks also exist in both chirality states, and are grouped as:

$$\begin{pmatrix} u_L \\ d_L \end{pmatrix}, \quad \begin{pmatrix} s_L \\ c_L \end{pmatrix}, \quad \begin{pmatrix} t_L \\ b_L \end{pmatrix}, \quad u_R, \quad d_R, \quad s_R, \quad c_R, \quad t_R, \quad b_R. \quad (2.2)$$

The fact that there are no right-handed neutrino fields implies that neutrinos are strictly massless within the SM. This restriction follows from the experimental observation that all neutrinos produced via weak interactions are pure left-handed helicity states (and similarly antineutrinos are pure right-handed states). The hypothetical existence of right-handed neutrinos could be indirectly inferred from the observation of non-zero neutrino masses, nevertheless the existence of neutrino masses is not a sufficient condition for the existence of such fields.

Left and right-handed fermions transform differently under $SU(2)_L \times U(1)_Y$ rotations, as the right-handed particles are singlets under $SU(2)_L$. Applying a local transformation, they change as:

$$\begin{aligned} \psi_L &\longrightarrow e^{-iY\beta(x)/2} e^{-iT_a\alpha_a(x)} \psi_L, \\ \psi_R &\longrightarrow e^{-iY\beta(x)/2} \psi_R, \end{aligned} \quad (2.3)$$

2.1. Neutrinos in the SM

Table 2.1: Values of T_3 and $Y/2$ assigned to the first generation of fermions.

	e_L	ν_e	e_R	u_L	d_L	u_R	d_R
T_3	-1/2	1/2	0	1/2	-1/2	0	0
$Y/2$	-1/2	-1/2	-1	1/6	1/6	2/3	-1/3

582 where $Y/2$ and T_a are the generators of $SU(2)_L$ and $U(1)_Y$, respectively, and $\beta(x)$ and
 583 $\alpha_a(x)$ are the parameters of the rotation.

584 The values of the quantum numbers $Y/2$ and T_3 , the third component of the weak
 585 isospin, have to be assigned to the different particles. The values of T_3 follow from the
 586 commutation relations of the generators of $SU(2)$. After the spontaneous symmetry
 587 breaking $SU(2)_L \times U(1)_Y \rightarrow U(1)_{EM}$, one finds the relation which determines the electric
 588 charge:

$$Q = T_3 + \frac{Y}{2}, \quad (2.4)$$

589 Setting the electric charge to -1 for electrons, we can find the values of the hypercharge
 590 for the rest of the fermions. The resulting values for the first generation of leptons and
 591 quarks are shown in Tab. 2.1.

592 It is clear that the free Lagrangian of the theory is not be invariant under the gauge
 593 transformations, as the kinetic terms contain derivatives. Therefore, to make it invariant,
 594 one needs to introduce a set of gauge bosons. They appear in the so-called covariant
 595 derivative, which replaces the common derivative and transforms in the same way as the
 596 fermion fields under local rotations. This constrain fixes completely the transformations
 597 of the spin-1 fields. For left and right-handed particles, the covariant derivatives are
 598 given by:

$$\begin{aligned} D_\mu \psi_L &= \left(\partial_\mu + ig' \frac{Y}{2} B_\mu + ig T_a W_\mu^a \right) \psi_L, \\ D_\mu \psi_R &= \left(\partial_\mu + ig' \frac{Y}{2} B_\mu \right) \psi_R, \end{aligned} \quad (2.5)$$

599 where W_μ^i , $i = 1, 2, 3$ and B_μ are the gauge bosons for the $SU(2)_L$ and $U(1)_Y$ factors,
 600 respectively, and g and g' are the corresponding gauge couplings. It can be shown that

Chapter 2. Neutrino physics

Table 2.2: Neutral current couplings.

	u	d	ν_e	e
$2v_f$	$1 - \frac{8}{3}\sin^2\theta_W$	$-1 + \frac{4}{3}\sin^2\theta_W$	1	$-1 + 4\sin^2\theta_W$
$2a_f$	1	-1	1	-1

601 these fields transform in the adjoint representation of the gauge group.

602 So far, the theory only contains massless particles, as adding bare mass terms to
 603 the Lagrangian would spoil the gauge symmetry. Therefore, the mass terms need to
 604 be induced by a spontaneous violation of the symmetries. In the SM, the responsible
 605 for this is the Higgs mechanism. The Higgs doublet is coupled to the gauge bosons
 606 through the covariant derivative, and to the fermions through the Yukawa couplings.
 607 Upon spontaneous symmetry breaking, the vacuum expectation value of the Higgs field
 608 generate the mass terms of the particles.

609 In order to obtain the physical intermediate vector boson states, we need to perform
 610 the following redefinitions:

$$\begin{aligned} A_\mu &= \sin \theta_W W_\mu^3 + \cos \theta_W B_\mu, \\ Z_\mu &= \cos \theta_W W_\mu^3 - \sin \theta_W B_\mu, \\ W_\mu^\pm &= \frac{1}{\sqrt{2}} (W_\mu^1 \mp i W_\mu^2), \end{aligned} \tag{2.6}$$

611 where A_μ is the photon field, and Z_μ and W_μ^\pm are the neutral and the charged weak
 612 boson fields, respectively. The Weinberg angle, θ_W , relates the weak coupling constants
 613 and the electric charge:

$$e = g' \cos \theta_W = g \sin \theta_W. \tag{2.7}$$

614 At this point, the interacting part of the electroweak Lagrangian can be re-written
 615 as the sum of three contributions: the electromagnetic (EM), charged-current (CC) and

2.2. Trouble in the neutrino sector

616 neutral-current (NC) components:

$$\begin{aligned}\mathcal{L}_{\text{EW}}^{\text{int}} &= \mathcal{L}_{\text{EM}} + \mathcal{L}_{\text{CC}} + \mathcal{L}_{\text{NC}} \\ &= -eA_\mu J_{\text{EM}}^\mu - \frac{g}{2\sqrt{2}}(W_\mu^+ J_{\text{CC}}^\mu + \text{h.c.}) - \frac{g}{2\cos\theta_W}Z_\mu J_{\text{NC}}^\mu,\end{aligned}\tag{2.8}$$

617 with the currents defined as:

$$\begin{aligned}J_{\text{EM}}^\mu &= \sum_f Q_f \bar{f} \gamma^\mu f, \\ J_{\text{CC}}^\mu &= \sum_\ell \bar{\nu}_\ell \gamma^\mu (1 - \gamma_5) \ell + \sum_f \bar{u}_f \gamma^\mu (1 - \gamma_5) d_f, \\ J_{\text{NC}}^\mu &= \sum_f \bar{f} \gamma^\mu (v_f - a_f \gamma_5) f,\end{aligned}\tag{2.9}$$

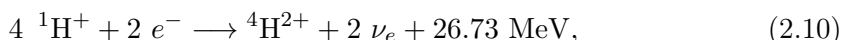
618 where f denotes any SM fermion, ℓ and ν_ℓ a charged lepton and a neutrino of any flavour,
619 and u_f and d_f an up-like and a down-like quarks of any flavour. For the NC case, the
620 values of the v_f and a_f couplings are given in Tab. 2.2.

621 As seen in Eq. (7.8), in the electroweak theory neutrinos are coupled to the Z boson
622 in a universal way. Therefore, by measuring the so-called invisible decay width of the Z
623 boson we have an estimate of the number of light (i.e. lighter than the Z boson) neutrino
624 flavours. This number was measured by LEP in a combined analysis of $e^+e^- \rightarrow \mu^+\mu^-$
625 and $e^+e^- \rightarrow \text{hadrons}$ to be $N_\nu = 2.9840 \pm 0.0082$ [23].

626 2.2 Trouble in the neutrino sector

627 2.2.1 The solar neutrino problem

628 Neutrinos are produced everywhere in vast amounts. One of the most prominent sources
629 of neutrinos in our vicinity is our Sun. The Sun is powered mainly by two nuclear fusion
630 reactions, the p – p chain and the CNO cycle. In both cases, the overall reaction is:



Chapter 2. Neutrino physics

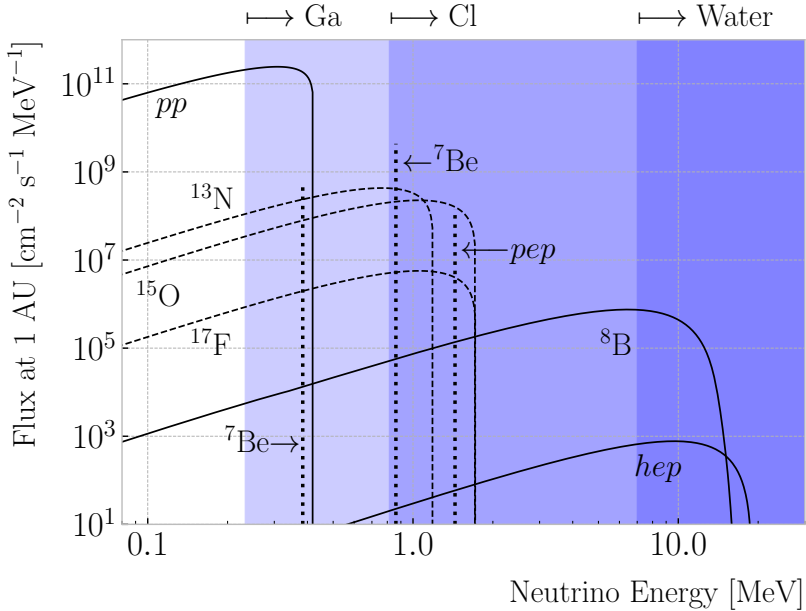


Figure 2.1: Solar neutrino fluxes for the solar model BS05(OP). The detection thresholds for Gallium, Chlorine and water-based experiments are also shown. Figure adapted from Ref. [3].

where part of the released energy is lost to the neutrinos. The electron neutrinos produced are often labelled after the processes that generate them. Figure 2.1 shows the solar neutrino flux as a function of the neutrino energy, broken down by the production process.

In the late 1960s, the Brookhaven Solar Neutrino Experiment, led by R. Davis, started data taking with the goal of measuring the solar neutrino flux [24]. The experiment used a tank containing 380 m^3 of tetrachloroethene (C_2Cl_4), a liquid commonly used in dry-cleaning, located 1.5 km underground in the Homestake mine, in Lead, South Dakota. The incoming neutrinos would get captured following the reaction:



therefore allowing to measure the neutrino flux by counting the ${}^{37}\text{Ar}$ isotopes. The threshold for this reaction is 0.814 MeV, just below the 0.862 MeV line from the ${}^7\text{Be}$ ground state transition.

2.2. Trouble in the neutrino sector

643 The results of the experiment were compared to the theoretical predictions made by
644 J. Bahcall [25]. During its operation from 1968 to 2002, the experiment observed a solar
645 ν_e flux that was approximately a third of the total prediction [26].

646 In the early 1990s, the SAGE [27] and GALLEX [28] experiments started operations.
647 The detection principle used for both experiments was similar to that of the Homestake
648 experiment, but using ^{71}Ga instead of C_2Cl_4 . With a detection threshold of 0.233 MeV,
649 the Gallium-based experiments were able to observe the pp neutrino flux. Both
650 experiments measured a solar electron neutrino flux that was a factor of two lower
651 than the predictions, demonstrating that this deficit was energy-dependent.

652 In the early 2000s, the SNO experiment put an end to the solar neutrino puzzle
653 [29, 30]. Thanks to its directionality capabilities, being a Cherenkov light detector, as
654 well as to its heavy water target, SNO measured the total solar neutrino flux through
655 the NC process:

$$\nu_\alpha + d \longrightarrow n + p + \nu_\alpha, \quad (2.12)$$

656 where $\alpha = e, \mu, \tau$. This measurement agreed with the solar model predictions. Then,
657 measuring the CC reaction:

$$\nu_e + d \longrightarrow p + p + e^-, \quad (2.13)$$

658 they were able to establish that the ν_μ and ν_τ solar fluxes are in fact non-zero, revealing
659 that electron neutrinos were transitioning into different flavours.

660 2.2.2 The atmospheric neutrino problem

661 When cosmic-rays interact with the atoms in the upper atmosphere, a plethora of
662 hadrons, mainly π and K mesons, are produced. In particular, for the charged pions,
663 we have the following decay chain dominates:

$$\begin{aligned} \pi^+ &\longrightarrow \mu^+ + \nu_\mu, \\ \mu^+ &\longrightarrow e^+ + \bar{\nu}_\mu + \nu_e, \end{aligned} \quad (2.14)$$

Chapter 2. Neutrino physics

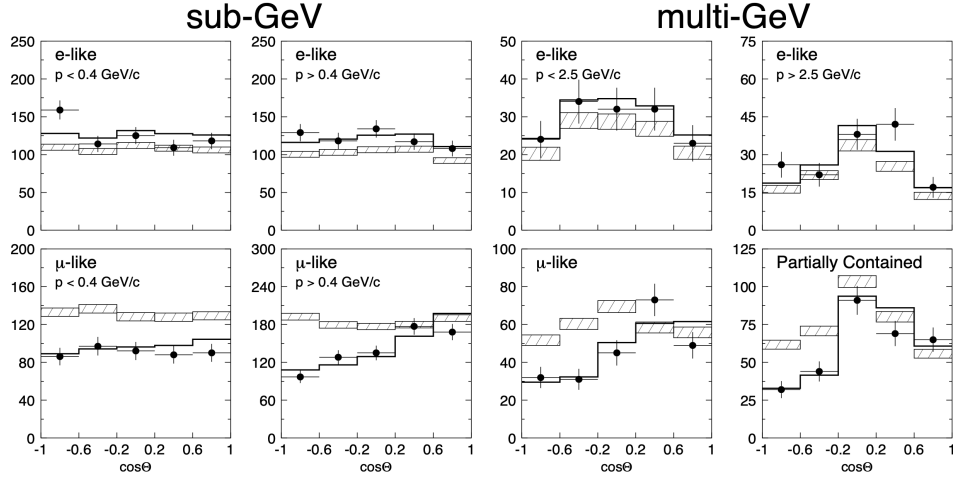


Figure 2.2: Zenith angle distributions for the selected ν_e (top row) and ν_μ (bottom row) events in the SK detector. The hatched region corresponds to the expectation in the case of no oscillations, whereas the solid line indicates the best-fit in the case of $\nu_\mu \rightarrow \nu_\tau$ oscillations. Figure taken from Ref. [36].

and similar for the antiparticles. For neutrino energies < 1 GeV, the ratio:

$$\frac{N(\nu_\mu + \bar{\nu}_\mu)}{N(\nu_e + \bar{\nu}_e)}, \quad (2.15)$$

of produced neutrinos and antineutrinos is, in good approximation, equal to two [31].

During the 1980s, several proton decay experiments, like Kamiokande [32], IMB [33], MACRO [34], and Soudan-2 [35], measured the flux of atmospheric neutrinos. This was an important part of their research programme, as the atmospheric neutrinos constitute their main background. All these experiments reported an atmospheric neutrino ratio lower than the predictions.

A few years before the SNO discovery, in 1998, Super-Kamiokande (SK) collaboration measured the atmospheric ν_e and ν_μ spectra as a function of the zenith angle [36]. Upward-going particles have negative zenith angle, $\cos \Theta < 0$, indicating that they entered from the bottom of the detector. These upward-going neutrinos had to travel through the Earth in order to reach the detector, allowing SK to probe a broad range of baselines. Figure 2.2 shows the reported distributions (black dots), compared to the no oscillations prediction (hatched region). This measurement confirmed that muon

2.3. Massive neutrinos

neutrinos transition to other flavours, and that this phenomenon depends both on the energy and the path length of the neutrino.

The SK and SNO findings provided definitive evidence for the existence of neutrino oscillations, and therefore non-zero neutrino masses. This constitutes one of the groundbreaking discoveries of modern physics and has acted as driving force for beyond the Standard Model (BSM) physics. The minimal extension of the SM we can do to address these phenomena is introducing different masses for at least two of the neutrinos. This way, we are left with three neutrino mass eigenstates ν_1 , ν_2 , and ν_3 , with masses m_1 , m_2 , and m_3 respectively, which in general will not coincide with the flavour eigenstates, ν_e , ν_μ , and ν_τ .

2.3 Massive neutrinos

The existence of neutrino oscillations imply that neutrinos are massive particles. However, as we have seen before, within the SM neutrinos are massless, as they do not have a mass term in the Lagrangian. If one wants to give neutrinos a mass, the particle content of the SM needs to be expanded.

A way of generating massive neutrinos while maintaining gauge invariance is by introducing an arbitrary number of sterile neutrinos N_i , $i = 1, \dots, m$. These allow for two different types of neutrino mass terms:

$$-\mathcal{L}_{M_\nu} = \sum_{i=1}^m \sum_{j=1}^3 M_D^{ij} \bar{N}_i \nu_{Lj} + \frac{1}{2} \sum_{i=1}^m \sum_{j=1}^m M_N^{ij} \bar{N}_i N_j^c + \text{h.c.}, \quad (2.16)$$

where M_D is a complex $m \times 3$ matrix and M_N a complex and symmetric $m \times m$ matrix. The first term, often referred to as the Dirac mass term, arises from the corresponding Yukawa interaction after the spontaneous electroweak symmetry breaking, similar to the other fermions. The second term, called the Majorana mass term, is allowed in the Lagrangian, as it is a singlet of the gauge group. However, it violates lepton number conservation by two units.

Chapter 2. Neutrino physics

If one imposes lepton number symmetry conservation, the Majorana term must banish, $M_N = 0$. In this case, if $m = 3$ we can identify the sterile neutrinos as the right-handed component of the neutrino field. The Dirac mass matrix can be diagonalised using two unitary matrices, V_R^ν and V_L^ν , as:

$$M_D = V_R^\nu \text{ diag}(m_1, m_2, m_3) V_L^{\nu\dagger}, \quad (2.17)$$

where m_i , $i = 1, 2, 3$ are the masses of the three neutrino mass eigenstates.

The neutrino mass term can be written in term of the resulting eigenstates as:

$$-\mathcal{L}_{M_\nu} = \sum_{i=1}^3 m_i \bar{\nu}_{Di} \nu_{Di}, \quad (2.18)$$

with:

$$\nu_{Di} = \left(V_L^{\nu\dagger} \nu_L \right)_i + \left(V_R^{\nu\dagger} N \right)_i. \quad (2.19)$$

In this scenario, both the low energy particle budget and the symmetries of the SM have to be modified. Moreover, the masses of the neutrinos are generated exclusively through the Higgs mechanism, which does not explain why they are much smaller than those of the charged leptons.

Going back to the general case, we can re-write Eq. (2.16) in matrix form as:

$$-\mathcal{L}_{M_\nu} = \frac{1}{2} (\bar{\nu}_L^c, \bar{N}) \begin{pmatrix} 0 & M_D^T \\ M_D & M_N \end{pmatrix} \begin{pmatrix} \nu_L \\ N^c \end{pmatrix} + \text{h.c.} = \bar{\nu}^c M_\nu \nu + \text{h.c.}, \quad (2.20)$$

with $\nu = (\nu_L, N^c)^T$ being a $(3+m)$ -dimensional vector grouping the active and the sterile neutrinos. The matrix M_ν , which is a complex $(3+m) \times (3+m)$ symmetric matrix, can be diagonalised by means of a unitary matrix V^ν , yielding:

$$M_\nu = V^\nu \text{ diag}(m_1, m_2, \dots, m_{3+m}) V^{\nu T}. \quad (2.21)$$

2.3. Massive neutrinos

717 Using this eigendecomposition, the neutrino mass term can be expressed as:

$$-\mathcal{L}_{M_\nu} = \frac{1}{2} \sum_{i=1}^{3+m} m_i \bar{\nu}_{Mi} \nu_{Mi}, \quad (2.22)$$

718 where the states ν_{Mi} , commonly referred to as Majorana neutrinos, are defined as:

$$\nu_{Mi} = \left(V^{\nu\dagger} \nu \right)_i + \left(V^{\nu\dagger} \nu \right)_i^c, \quad (2.23)$$

719 in such a way that the Majorana condition, $\nu_M^c = \nu_M$, holds true.

720 As a consequence of the Majorana condition, the neutrino and the antineutrino states
721 can be described in terms of a single field. As opposed to the charged leptons, which
722 need to be represented by a four-component or Dirac spinor, the Majorana neutrino is
723 described by a two-component or Weyl spinor.

724 If the eigenvalues of the Majorana mass matrix, M_N , are much larger than the
725 electroweak symmetry breaking scale, the diagonalisation of M_ν leads to 3 light and m
726 heavy neutrino states:

$$-\mathcal{L}_{M_\nu} = \frac{1}{2} \bar{\nu}_l M_l \nu_l + \frac{1}{2} \bar{\nu}_h M_h \nu_h, \quad (2.24)$$

727 where the two mass matrices are given by:

$$\begin{aligned} M_l &\simeq -V_l^T M_D^T M_N^{-1} M_D V_l, \\ M_h &\simeq V_h^T M_N V_h, \end{aligned} \quad (2.25)$$

728 with V_l and V_h two unitary matrices.

729 This scenario represents the so-called see-saw mechanism [37–41]. The name comes
730 from the fact that the masses of the heavy states are proportional to M_N , whereas for
731 the light states they are proportional to M_N^{-1} . While both the heavy and the light
732 neutrinos are Majorana particles, it can be shown that the heavy states are mainly
733 right-handed, whereas the light ones are mostly left-handed.

Chapter 2. Neutrino physics

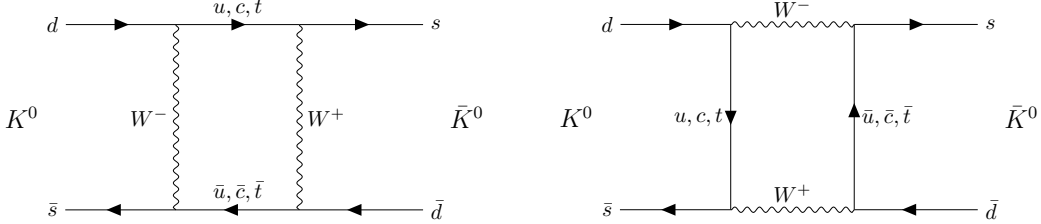


Figure 2.3: $K^0 \rightleftharpoons \bar{K}^0$ mixing through W^\pm exchange.

2.4 Neutrino oscillation formalism

734 Neutrino oscillations were first proposed in 1958 by B. Pontecorvo [42], inspired by the
 735 neutral kaon oscillation phenomenon [43]. Neutral kaons, K^0 and \bar{K}^0 , have opposite
 736 strangeness (± 1) and are produced in strong processes. It was observed that, when
 737 having a beam initially pure of neutral kaons of one type, these would transition into
 738 their antiparticles while propagating. Because the weak interaction does not conserve
 739 strangeness, neutral kaons can change their identity via the processes shown in Fig. 2.3.
 740

741 The mixing considered initially by Pontecorvo was between the neutrino and the
 742 antineutrino states, as only one neutrino flavour was known at the time. After the
 743 discovery of the muon neutrino, the mixing between flavours was also explored [44].

744 In the general case, we have 3 active and m sterile neutrinos, resulting in $3 + m$
 745 neutrino mass eigenstates. Working in the mass basis, the leptonic charged-current
 746 Lagrangian can be written as:

$$-\mathcal{L}_{CC}^{lep} = \frac{g}{\sqrt{2}} (\bar{e}_L, \bar{\mu}_L, \bar{\tau}_L) \gamma^\mu U \begin{pmatrix} \nu_1 \\ \nu_2 \\ \vdots \\ \nu_{3+m} \end{pmatrix} W_\mu^+ + \text{h.c.}, \quad (2.26)$$

747 where U is a $3 \times (3 + m)$ matrix which obeys $UU^\dagger = I_{3 \times 3}$, but in general will not be
 748 unitary, $U^\dagger U \neq I_{(3+m) \times (3+m)}$.

749 The leptonic mixing matrix, U , establishes how the neutrino mass states couple to
 750 the charged leptons. In general, a complex $n \times n$ matrix can be fully specified by $2n^2$ real
 751 parameters. If the matrix is unitary, then the number of independent parameters reduces

2.4. Neutrino oscillation formalism

752 to n^2 , as one has to impose n normalisation and $n(n - 1)$ orthogonality constraints.
 753 In our case, we can further reduce the number of parameters by performing a phase
 754 redefinition of the charged lepton fields, without affecting the physics. This is not true
 755 for the neutrinos. As they may be their own antiparticles, one is not allowed to remove
 756 any physically relevant phases. If we consider n generations of leptons, the total number
 757 of parameters in the mixing matrix is $n^2 - n$. Out of these, half of them are mixing
 758 angles, while the other half are complex phase factors.

759 Considering the extended SM without any additional sterile neutrino states, the
 760 resulting 3×3 mixing matrix is unitary. This matrix, often called the Pontecorvo-Maki-
 761 Nakagawa-Sakata (PMNS) matrix [45, 46], relates the set of active neutrinos and the
 762 three mass eigenstates as:

$$|\nu_\alpha\rangle = \sum_{i=1}^3 U_{\alpha i}^* |\nu_i\rangle, \quad (2.27)$$

763 where the Greek index α denotes the flavour $\{e, \mu, \tau\}$ and the Latin index i the mass state
 764 $\{1, 2, 3\}$. This leptonic mixing matrix may be parametrized in terms of 6 parameters, 3
 765 of which are mixing angles θ_{12} , θ_{13} and θ_{23} , one CP-violating phase δ_{CP} and 2 Majorana
 766 phases α and β :

$$U = \begin{pmatrix} 1 & 0 & 0 \\ 0 & c_{23} & s_{23} \\ 0 & -s_{23} & c_{23} \end{pmatrix} \begin{pmatrix} c_{13} & 0 & s_{13} e^{-i\delta_{CP}} \\ 0 & 1 & 0 \\ -s_{13} e^{i\delta_{CP}} & 0 & c_{13} \end{pmatrix} \begin{pmatrix} c_{12} & s_{12} & 0 \\ -s_{12} & c_{12} & 0 \\ 0 & 0 & 1 \end{pmatrix} \begin{pmatrix} 1 & 0 & 0 \\ 0 & e^{i\alpha} & 0 \\ 0 & 0 & e^{i\beta} \end{pmatrix}, \quad (2.28)$$

767 where $c_{ij} \equiv \cos \theta_{ij}$ and $s_{ij} \equiv \sin \theta_{ij}$. This matrix is analogous to the Cabibbo-Kobayashi-
 768 Maskawa (CKM) matrix in the quark sector. If neutrinos are Dirac fermions, we can
 769 drop the Majorana phases in the PMNS matrix, as in this case we can perform the
 770 phase redefinitions. However, these phases play no role on the neutrino oscillation
 771 phenomenology.

772 In the case that additional sterile neutrino states are present, the full leptonic mixing
 773 matrix would not be unitary in general. For instance, in the see-saw scenario, the 3×3
 774 submatrix for the three light Majorana neutrinos is not unitary. However, the deviations
 775 from unitarity are of the order $\mathcal{O}(M_D/M_N)$, and therefore expected to be negligible.

Chapter 2. Neutrino physics

2.4.1 Oscillations in vacuum

Consider the case where a neutrino of flavour α is produced at $t = 0$, and then it propagates through vacuum. Such a state will evolve in time according to the relation:

$$|\nu_\alpha(\vec{x}, t)\rangle = \sum_{i=1}^3 U_{\alpha i}^* e^{-i(E_i t - \vec{p}_i \cdot \vec{x})} |\nu_i(\vec{x} = \vec{0}, t = 0)\rangle, \quad (2.29)$$

in the plane wave approximation, as the mass eigenstates are also eigenstates of the free Hamiltonian.

This way, the probability for the neutrino to transition from flavour α to flavour β will be given by:

$$\begin{aligned} P(\nu_\alpha \rightarrow \nu_\beta) &= |\langle \nu_\beta | \nu_\alpha(\vec{x}, t) \rangle|^2 = \left| \sum_{i=1}^3 \sum_{j=1}^3 U_{\alpha i}^* U_{\beta j} e^{-i(E_i t - \vec{p}_i \cdot \vec{x})} \langle \nu_j | \nu_i \rangle \right|^2 \\ &= \left| \sum_{i=1}^3 U_{\alpha i}^* U_{\beta i} e^{-i(E_i t - \vec{p}_i \cdot \vec{x})} \right|^2, \end{aligned} \quad (2.30)$$

where we have used the orthogonality relation $\langle \nu_i | \nu_j \rangle = \delta_{ij}$. A usual approximation to take at this point is to consider ultra-relativistic neutrinos, i.e. $p_i \simeq E$, so we can write the dispersion relations as:

$$E_i = \sqrt{p_i^2 + m_i^2} \approx E + \frac{m_i^2}{2E}. \quad (2.31)$$

In the end, assuming $t \approx L$ where L is the distance between the production and the detection points, the probability for the $\nu_\alpha \rightarrow \nu_\beta$ transition becomes:

$$\begin{aligned} P(\nu_\alpha \rightarrow \nu_\beta) &= \sum_{i,j} U_{\alpha i}^* U_{\beta i} U_{\alpha j} U_{\beta j}^* e^{-i \frac{\Delta m_{ij}^2}{2E} L} \\ &= \delta_{\alpha\beta} - 4 \sum_{i < j} \Re [U_{\alpha i}^* U_{\beta i} U_{\alpha j} U_{\beta j}^*] \sin^2 \left(\frac{\Delta m_{ij}^2}{4E} L \right) \\ &\quad + 2 \sum_{i < j} \Im [U_{\alpha i}^* U_{\beta i} U_{\alpha j} U_{\beta j}^*] \sin \left(\frac{\Delta m_{ij}^2}{2E} L \right), \end{aligned} \quad (2.32)$$

2.4. Neutrino oscillation formalism

788 where Δm_{ij}^2 is the difference of the squared masses of the j th and i th neutrino mass
 789 eigenvalues. At this point, it is usual to write the phase responsible for the oscillations
 790 as:

$$\Delta_{ij} \equiv \frac{\Delta m_{ij}^2}{4E} L \simeq 1.27 \frac{\Delta m_{ij}^2}{(\text{eV}^2)} \frac{L}{(\text{km})} \frac{(\text{GeV})}{E}. \quad (2.33)$$

791 Notice that, in the case of antineutrinos, the only difference would be the sign of the
 792 last term in the oscillation probability. As the process $\bar{\nu}_\alpha \rightarrow \bar{\nu}_\beta$ is the CP-mirror image
 793 of $\nu_\alpha \rightarrow \nu_\beta$, the differences between their oscillation probabilities would be a measure of
 794 CP symmetry violation:

$$\begin{aligned} A_{CP}^{\alpha\beta} &= P(\nu_\alpha \rightarrow \nu_\beta) - P(\bar{\nu}_\alpha \rightarrow \bar{\nu}_\beta) \\ &= 4 \sum_{i < j} \Im \left[U_{\alpha i}^* U_{\beta i} U_{\alpha j} U_{\beta j}^* \right] \sin 2\Delta_{ij}. \end{aligned} \quad (2.34)$$

795 Assuming that CPT invariance holds, then the following relation must be true:

$$P(\nu_\alpha \rightarrow \nu_\beta) = P(\bar{\nu}_\beta \rightarrow \bar{\nu}_\alpha), \quad (2.35)$$

796 as these two processes are related by the CPT symmetry. From the definition of probability,
 797 we also must have:

$$\sum_\beta P(\nu_\alpha \rightarrow \nu_\beta) = \sum_\beta P(\bar{\nu}_\alpha \rightarrow \bar{\nu}_\beta) = 1, \quad (2.36)$$

798 where the sum includes all flavours, including α . From these two constraints, one can
 799 probe that:

$$A_{CP}^{\alpha\beta} = -A_{CP}^{\beta\alpha}, \quad (2.37)$$

800 and in particular:

$$A_{CP}^{\alpha\alpha} = 0. \quad (2.38)$$

801 A direct consequence of this last relation is that there are no observable CP-violating
 802 effects in the so-called disappearance experiments. One needs to perform appearance
 803 experiments, where the flavour detected is different from the original flavour, in order

Chapter 2. Neutrino physics

804 to measure the CP asymmetry. Neutrino experiments often report the amount of CP-
805 violation through the Jarlskog invariant. In terms of the parametrisation typically used
806 to write the PMNS matrix, it is given by:

$$J = \frac{1}{8} \cos \theta_{13} \sin 2\theta_{12} \sin 2\theta_{13} \sin 2\theta_{23} \sin \delta_{CP}. \quad (2.39)$$

807 The Jarlskog invariant can be used to compare the amount of CP-violation in the lepton
808 and the quark sectors, where $J = 3.12^{+0.13}_{-0.12} \times 10^{-5}$ in the latter [47].

809 2.4.2 Oscillations in matter

810 When neutrinos propagate through matter, their oscillation can be affected in mainly
811 two ways. First, neutrinos can inelastically scatter with nuclei, thus destroying the
812 coherent propagation of their quantum state. Nevertheless, in most cases this effect is
813 negligible (even in very dense mediums like the core of the Sun). Second, neutrinos can
814 also experience coherent or forward scatterings, that can affect their oscillation but not
815 lose the coherent propagation of the state.

816 The first proposed model to account for neutrino oscillations in matter was proposed
817 by Mikhaev, Smirnov and Wolfenstein (MSW) [48]. It relies on the fact that, as the
818 only charged lepton present in ordinary matter is the electron, electron neutrinos can
819 undergo both charged and neutral-current interactions with matter whereas for muon
820 and tau neutrinos just neutral currents are possible.

821 An illustrative way to introduce the MSW mechanism is by considering the two
822 flavours case. It can be shown that the evolution of the two flavour eigenstates in vacuum
823 is given by the following time-dependent Schrödinger equation:

$$i \frac{d}{dt} \begin{pmatrix} \nu_e \\ \nu_\mu \end{pmatrix} = H_V \begin{pmatrix} \nu_e \\ \nu_\mu \end{pmatrix}, \quad (2.40)$$

2.4. Neutrino oscillation formalism

824 with a vacuum Hamiltonian given by:

$$H_V = \frac{\Delta m^2}{4E} \begin{pmatrix} -\cos 2\theta & \sin 2\theta \\ \sin 2\theta & \cos 2\theta \end{pmatrix}, \quad (2.41)$$

825 where Δm^2 is the mass splitting between the two neutrino states and θ the only mixing
826 angle. For simplicity, I omit the terms of the Hamiltonian that are proportional to the
827 identity, as they do not affect the oscillation phenomenology.

828 The NC contribution to the matter potential is identical for all the flavours, and has
829 the form:

$$V_{\text{NC}} = -\frac{G_F}{\sqrt{2}} N_n(x), \quad (2.42)$$

830 where G_F is the Fermi constant and $N_n(x)$ the local neutron density. Because it is
831 common to all flavours, I do not take it into account in the effective Hamiltonian, as it
832 would appear as a term proportional to the identity. The CC component only affects
833 the electron neutrino (and antineutrino). It can be written as:

$$V_{\text{CC}} = \pm \sqrt{2} G_F N_e(x), \quad (2.43)$$

834 with $N_e(x)$ being the local electron density in the material. In the end, the effective
835 Hamiltonian which describes the propagation of the flavour eigenstates in matter only
836 contains an extra $\nu_e - \nu_e$ element:

$$H_M = H_V + \begin{pmatrix} V_{\text{CC}} & 0 \\ 0 & 0 \end{pmatrix}. \quad (2.44)$$

837 The solution to the Schrödinger equation greatly simplifies if one considers the case
838 of a constant matter density. In that case, the effective Hamiltonian can be diagonalised,
839 obtaining the effective neutrino mass eigenstates in matter. It can be re-written in the
840 same form as the vacuum Hamiltonian:

$$H_M = \frac{\Delta m_m^2}{4E} \begin{pmatrix} -\cos 2\theta_m & \sin 2\theta_m \\ \sin 2\theta_m & \cos 2\theta_m \end{pmatrix}, \quad (2.45)$$

Chapter 2. Neutrino physics

841 where the effective mass splitting and the effective mixing angle are given by:

$$\begin{aligned}\Delta m_m^2 &= \lambda \Delta m_m^2, \\ \sin 2\theta_m &= \frac{\sin 2\theta_m}{\lambda}\end{aligned}\tag{2.46}$$

842 with:

$$\begin{aligned}\lambda &= \sqrt{(\cos 2\theta - A)^2 + \sin^2 2\theta}, \\ A &= \pm \frac{2\sqrt{2}G_F N_e E}{\Delta m^2}.\end{aligned}\tag{2.47}$$

843 In terms of the effective matter oscillation parameters, the transition probability

844 $\nu_e \rightarrow \nu_\mu$ (in the two flavour approximation) reads:

$$P(\nu_e \rightarrow \nu_\mu) = \sin^2 2\theta_m \sin^2 \left(\frac{\Delta m_m^2}{2E} L \right)\tag{2.48}$$

845 From this last equation one can see that, when $\cos 2\theta = A > 0$ the oscillations are

846 greatly enhanced. This effect is known as the MSW resonance. For the neutrinos, this

847 resonant condition is only satisfied if $\Delta m^2 > 0$ (the opposite is true for antineutrinos).

848 This is can be exploited by long baseline experiments, which can gain sensitivity to the

849 neutrino mass hierarchy through matter effects.

850 2.4.3 Current status of neutrino oscillations

851 A wide range of neutrino experiments provide experimental input to the neutrino

852 oscillation framework, both using natural or synthetic neutrino sources. The results

853 from one of the neutrino global fit analyses, shown in Tab. 2.3¹, summarise well our

854 current understanding of the different oscillation parameters.

855 **Solar neutrino experiments** detect neutrinos produced in thermonuclear reactions

856 inside the Sun, mainly from the so-called *pp* chain and the CNO cycle. These neutrinos

857 have a typical energy in the range from 0.1 to 20 MeV. These experiments (Homestake

¹These are the results reported during M. Tórtola's talk at Neutrino 2024 (see this link). I need to keep an eye and see if they publish these or other updated results in the near future.

2.5. Open questions in the neutrino sector

[49], GALLEX [28], SAGE [27], Borexino [50], Super-Kamiokande [51] and SNO [52]) provide the best sensitivities to θ_{12} and Δm_{21}^2 .

Atmospheric neutrino experiments detect the neutrino flux produced when cosmic rays scatter with particles in Earth's atmosphere. These collisions generate particle showers that eventually produce electron and muon neutrinos (and antineutrinos). Their energies range from few MeV to about 10^9 GeV. Experiments, like Super-Kamiokande [53] and IceCube [54] use atmospheric neutrinos to measure oscillations and are specially sensitive to θ_{23} and Δm_{32}^2 .

Reactor neutrino experiments look for the $\bar{\nu}_e$ spectrum produced by nuclear reactors, with energies in the MeV scale. Depending on the distance to the source, long-baseline experiments like KamLAND [55] are sensitive to the solar mass splitting Δm_{21}^2 whereas much shorter baseline experiment such as RENO [56] or DayaBay [57] measure θ_{13} and Δm_{31}^2 .

Accelerator experiments measure neutrino fluxes generated in particle accelerators. Usually mesons are produced in the accelerator to be focused into a beam, then some decay to muon neutrinos and the rest are absorbed by a target. Depending on the configuration one can obtain a beam made of mostly neutrinos or antineutrinos. The typical energies of these neutrinos are in the GeV range. Experiments such as NOvA [58], T2K [59], MINOS [60], OPERA [61] and K2K [62] (and in the future DUNE [63]) are primarily sensitive to θ_{13} , θ_{23} and Δm_{32}^2 . Also, in the coming years DUNE [63] and Hyper-Kamiokande [64] will be sensitive to δ_{CP} .

2.5 Open questions in the neutrino sector

A crucial question that remains open these days, and is of vital importance for oscillation phenomena, is whether the mass eigenvalue ν_3 is the heaviest (what we call normal ordering) or the lightest (referred to as inverted ordering) of the mass eigenstates. In other words, this means that we do not know the sign of Δm_{32}^2 , so we can either have $m_1 < m_2 < m_3$ (NO) or $m_3 < m_1 < m_2$ (IO).

Chapter 2. Neutrino physics

Table 2.3: Summary of neutrino oscillation parameters determined in the Neutrino Global Fit of 2020 [16].

Parameter	Best fit $\pm 1\sigma$	3σ range
Δm_{21}^2 [eV $^2 \times 10^{-5}$]	$7.55^{+0.22}_{-0.20}$	6.98 – 8.19
$ \Delta m_{31}^2 $ [eV $^2 \times 10^{-3}$] (NO)	$2.51^{+0.02}_{-0.03}$	2.43 – 2.58
$ \Delta m_{31}^2 $ [eV $^2 \times 10^{-3}$] (IO)	$2.41^{+0.03}_{-0.02}$	2.34 – 2.49
$\sin^2 \theta_{12}/10^{-1}$	3.04 ± 0.16	2.57 – 3.55
$\sin^2 \theta_{23}/10^{-1}$ (NO)	$5.64^{+0.15}_{-0.21}$	4.23 – 6.04
$\sin^2 \theta_{23}/10^{-1}$ (IO)	$5.64^{+0.15}_{-0.18}$	4.27 – 6.03
$\sin^2 \theta_{13}/10^{-2}$ (NO)	$2.20^{+0.05}_{-0.06}$	2.03 – 2.38
$\sin^2 \theta_{13}/10^{-2}$ (IO)	$2.20^{+0.07}_{-0.04}$	2.04 – 2.38
δ_{CP}/π (NO)	$1.12^{+0.16}_{-0.12}$	0.76 – 2.00
δ_{CP}/π (IO)	$1.50^{+0.13}_{-0.14}$	1.11 – 1.87

885 Another big puzzle is related to the value of δ_{CP} . Nowadays it is poorly constrained,
 886 with all values between π and 2π being consistent with data. A prospective measurement
 887 different from $\delta_{CP} = 0, \pi$ will predict CP-violation in the leptonic sector, and thus
 888 contribute along with the one measured in the quark sector to the total amount of
 889 CP-violation. Although it is true that these two contributions by themselves are not
 890 enough to explain the matter anti-matter asymmetry in our universe, the amount of
 891 CP-violation in the leptonic sector can be key to explain such imbalance.

892 Both of these questions, because of their nature, could be understood thanks to
 893 future oscillation experiments.

894 Notwithstanding, there are other mysteries that can not be unveiled just by conducting
 895 oscillation experiments, as certain quantities do not influence these phenomena. Among
 896 these there is the question of the absolute values of the neutrino masses. Depending
 897 on the value of the lightest of the neutrino masses we can have different mass spectra,
 898 from hierarchical $m_1 \ll m_2 < m_3$ (NO) or $m_3 \ll m_1 < m_2$ (IO) to quasi-degenerate
 899 $m_1 \simeq m_2 \simeq m_3$.

900 Other open question concerns the nature itself of the neutrinos. If neutrinos are Dirac
 901 particles then their mass term can be generated through the usual Higgs mechanism

2.6. Neutrino interactions

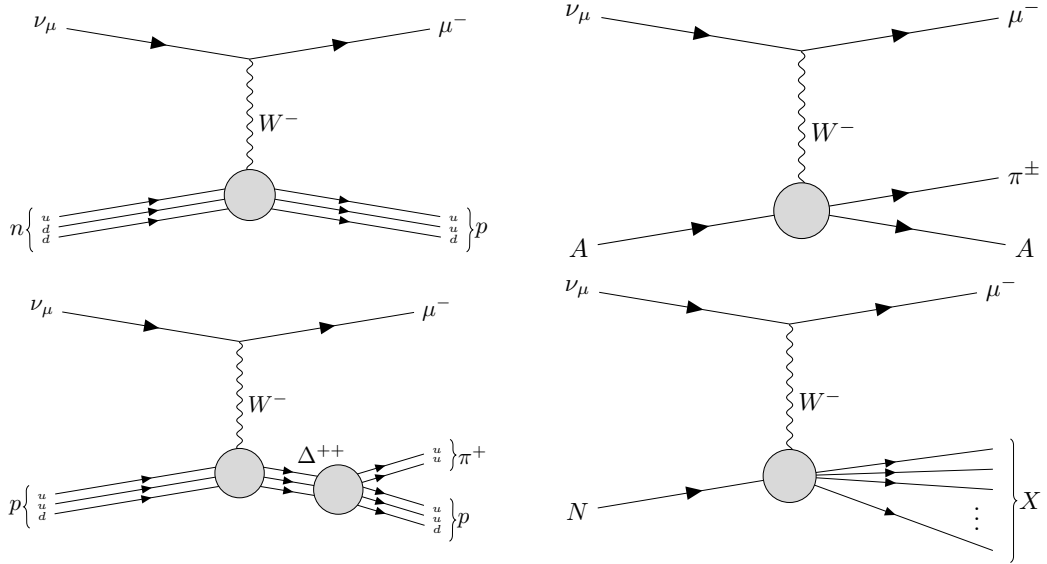


Figure 2.4

902 by adding right-handed neutrino fields. However, if they are Majorana particles and
 903 therefore their own antiparticles, there is no need to add extra fields to have the mass
 904 term in the Lagrangian. Experiments like SuperNEMO [65], SNO+ [66] and NEXT
 905 [67], which search for neutrino-less double beta decay, will be able to determine whether
 906 neutrinos are Dirac or Majorana.

907 2.6 Neutrino interactions

Chapter 2. Neutrino physics

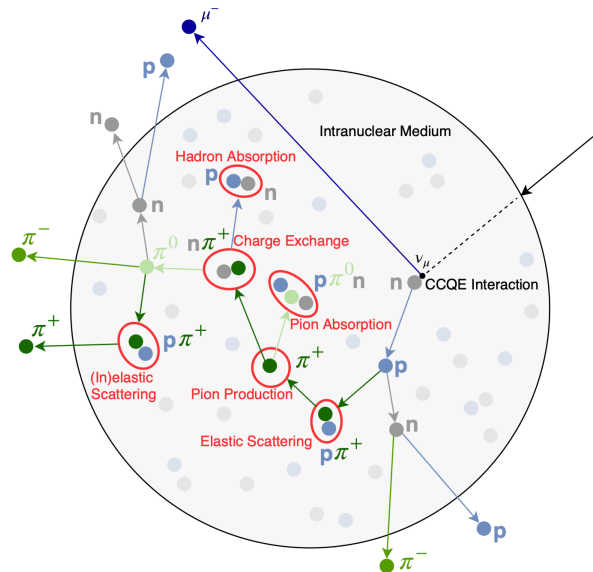


Figure 2.5: Schematic representation of a ν_μ CCQE interaction with a neutron inside a nucleus. The reaction produces a muon and a proton, which travel through the nuclear medium. The outgoing proton undergoes various kinds of hadronic FSIs on its way out. Figure taken from Ref. [68].

908 **Chapter 3**

909 **The Deep Underground Neutrino
910 Experiment**

911 The Deep Underground Neutrino Experiment (DUNE) is a next generation long-baseline
912 neutrino experiment [1]. It will aim to address several questions in neutrino physics,
913 study neutrinos from astrophysical sources and search for beyond the standard model
914 physics.

915 This chapter reviews the main goals of the DUNE experiment, the design of the far
916 detector modules and their data acquisition (DAQ) system, and the role that the near
917 detector plays in the physics program of DUNE.

918 **3.1 Overview**

919 The main physics goals of DUNE are:

- 920 • measure the neutrino mass hierarchy, the amount of CP violation in the leptonic
921 sector and the θ_{23} octant,
- 922 • detect rare low energy neutrino events, like neutrinos from supernova bursts, and
- 923 • search for proton decay and other beyond the standard model phenomena.

Chapter 3. The Deep Underground Neutrino Experiment

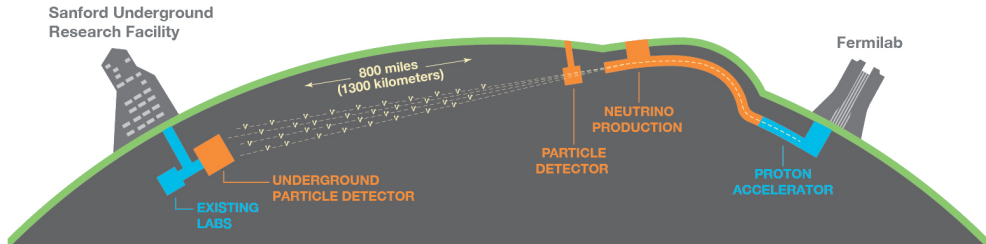


Figure 3.1: Schematic diagram of the DUNE experiment and the LBNF beamline [1].

The design of DUNE has been tailored with these goals in mind. It will consist of two neutrino detectors. A near detector (ND) complex will be placed in Fermilab, 574 m downstream of the neutrino production point, whereas a larger far detector (FD) will be built in the Sandford Underground Research Facility (SURF), South Dakota, approximately 1300 km away. Fig. 3.1 shows a simplified view of the various components of DUNE (not to scale).

The beam neutrinos to be used in DUNE will be provided by the LBNF beamline, the multi-megawatt wide-band neutrino beam planned for Fermilab. First, an intense proton beam is extracted from the Fermilab Main Injector. Then, these protons with energies between 60 GeV and 120 GeV collide with a high-power production target and produce charged mesons. Two magnetic horns allow to focus the mesons and perform a sign selection (thus having the capability to switch between neutrino and antineutrino mode). Soon after that, the mesons decay and produce neutrinos (or antineutrinos) which are then aimed to SURF.

Before arriving to the FD, the neutrino beam meets the ND complex, which serves as the experiment's control. Its role is to measure the unoscillated neutrino energy spectra. From these we can predict the unoscillated spectra at the FD, which can be compared to the spectra measured at the FD in order to extract the oscillation parameters. Therefore, the design of the DUNE ND is mainly driven by the needs of the oscillation physics program.

The liquid Argon time projection chamber (LArTPC) technology has been chosen for

3.2. Physics goals of DUNE

Table 3.1: Summary of the two-phased plan for DUNE. Adapted from Ref. [69].

Parameter	Phase I	Phase II	Benefit
FD mass	20 kt fiducial	40 kt fiducial	FD statistics
Beam power	up to 1.2 MW	2.4 MW	FD statistics
ND config.	ND-LAr, TMS, SAND	ND-LAr, ND-GAr, SAND	Systematic constraints

the FD modules of DUNE. Its four modules will record neutrino interactions from the accelerator-produced beam arriving at predictable times. As it also aims at recording rare events, the FD requires trigger schemes which can deal with both kinds of physics, and also maximum uptime.

DUNE is planned to be built using a staged approach consisting on two phases, which are summarised in Tab. 3.1. Phase I consists of a FD with 50% of the total fiducial mass, a reduced version of the ND complex and a 1.2 MW proton beam. It will be sufficient to achieve some early physics goals, like the determination of the neutrino mass ordering. For its Phase II, DUNE will feature the full four FD modules, a more capable ND and a 2.4 MW proton beam. The physics milestones for the two phases are given in Tab. 3.2, in a staging scenario which assumes that Phase II is completed after 6 years of operation.

A summary of the DUNE science program can be found in the DUNE FD Technical Design Report (TDR) Volume I [1]. For a detailed discussion on the two-phased approach the reader is referred to the DUNE Snowmass 2021 report [69].

3.2 Physics goals of DUNE

As noted in the literature (see for instance Ref. [16] for a review), the parameter space of the neutrino oscillation phenomena within the three-flavour picture is quite constrained by current experimental data. However, there are still crucial open questions, like the mass ordering, the value of δ_{CP} or the θ_{13} octant. One of the main goals of DUNE is to shed some light on the values of these parameters [70].

To address these questions DUNE can look to the subdominant oscillation channel $\nu_\mu \rightarrow \nu_e$ ($\bar{\nu}_\mu \rightarrow \bar{\nu}_e$) and study the energy dependence of the ν_e ($\bar{\nu}_e$) appearance probability.

Chapter 3. The Deep Underground Neutrino Experiment

Table 3.2: Exposure and time required to achieve the different physics milestones of the two phases. The predictions assume a Phase II staging scenario where FD modules 3 and 4 are deployed in years 4 and 6 and both the beam and ND are upgraded after 6 years. Adapted from Ref. [69].

Stage	Physics milestone	Exposure (kt-MW-years)	Years (staged)
Phase I	5σ MO ($\delta_{CP} = -\pi/2$)	16	1-2
	5σ MO (100% of the δ_{CP} values)	66	3-5
	3σ CPV ($\delta_{CP} = -\pi/2$)	100	4-6
Phase II	5σ CPV ($\delta_{CP} = -\pi/2$)	334	7-8
	δ_{CP} resolution of 10 degrees ($\delta_{CP} = 0$)	400	8-9
	5σ CPV (50% of the δ_{CP} values)	646	11
	3σ CPV (75% of the δ_{CP} values)	936	14
	$\sin^2(2\theta_{13})$ resolution of 0.004	1079	16

When we focus on the antineutrino channel $\bar{\nu}_\mu \rightarrow \bar{\nu}_e$ there is a change in the sign of δ_{CP} , thus introducing CP-violation. Moreover, due to the fact that there are no positrons in the composition of Earth, there is a sign difference for the matter effect contribution when looking to the antineutrino channel. This asymmetry is proportional to the baseline length L and is sensitive to the sign of Δ_{31} , and thus to the neutrino mass ordering.

Another of the main physics goals of DUNE is the search for baryon-number violating processes. Specifically, it will try to answer the question of whether protons are stable or not. There is no symmetry argument that forbids protons from decaying, but its apparent stability seems to suggest that baryon number is conserved [71]. However, proton decay is a usual feature of grand-unified theories, where electromagnetic, weak and strong interactions are unified above a certain energy scale [72].

As the energy deposition scale for this kind of searches is nearly the same as the one for long-baseline neutrino oscillations, DUNE will be able to look for them. It has several advantages over other experiments, such as excellent imaging and particle identification, which can be translated to lower backgrounds.

The last of the main objectives of DUNE is the detection of neutrinos originated in supernovae explosions, what is called a supernova neutrino burst (SNB). These neutrinos carry with them information about the core-collapse process, from the progenitor to the explosion and the remnant; but also may have information about new exotic physics. So far, the only neutrino events ever recorded from such a process were a few dozens of $\bar{\nu}_e$

3.3. Far Detector

988 events from the 1987A supernova located in the Magellanic Cloud, 50 kpc away from
989 Earth [73, 74].

990 DUNE aims to collect also some SNB events. Although these are quite rare, as the
991 expected supernovae explosion events are about one every few decades for our galaxy
992 and Andromeda, the long lifetime of the experiment (around a few decades as well)
993 makes it reasonable to expect some. Nowadays the main sensitivity to SNB of most
994 experiments is to the $\bar{\nu}_e$ through inverse beta decay. One of the advantages of DUNE is
995 its expected sensitivity to ν_e , since the dominant channel will be ν_e CC scattering.

996 Moreover, due to the stringent requirements that the main physics goals set for
997 DUNE, it will allow also to perform searches for all kind of BSM physics. Among
998 others, DUNE will be able to look for: active-sterile neutrino mixing, non-unitarity of
999 the PMNS matrix, non-standard interactions, Lorentz and CPT violations, neutrino
1000 trident production, light-mass DM, boosted DM and heavy neutral leptons. The reader
1001 is referred to the DUNE FD TDR Volume II [70] for a full discussion of the physics
1002 scope of DUNE.

1003 3.3 Far Detector

1004 The so-called DUNE FD complex will sit 1.5 km underground at SURF, South Dakota.
1005 Two caverns will host the four FD modules, two of them per cavern, each embedded in
1006 cryostats of dimensions 18.9 m (w) \times 17.8 m (h) \times 65.8 m (l). A central, smaller cavern
1007 will host the cryogenic system.

1008 Three out of the four modules will be liquid argon (LAr) time projection chamber
1009 detectors, often refer to as LArTPCs, with a LAr fiducial mass of at least 10 kt each.
1010 The first and second FD modules, FD-1 and FD-2, will use a Horizontal Drift (HD)
1011 technology, whereas the third module, FD-3, will have a Vertical Drift (VD) direction.
1012 The technology for the fourth module is still to be decided,

1013 For each event, with energies ranging from a few MeV to several GeV, these detectors
1014 collect both the scintillation light and the ionisation electrons created when the charged

Chapter 3. The Deep Underground Neutrino Experiment

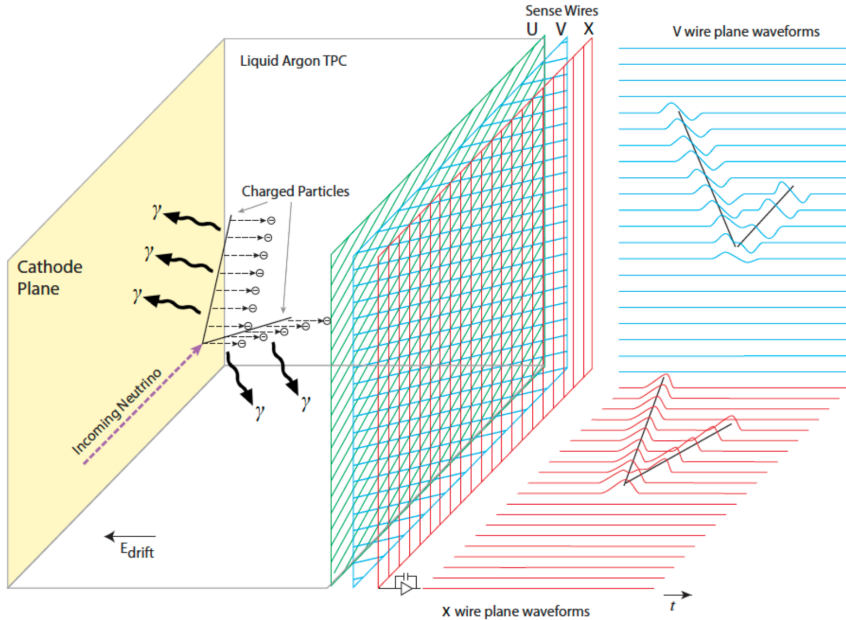


Figure 3.2: Schematic diagram showing the operating principle of a LArTPC with wire readout. Figure taken from Ref. [1].

1015 particles produced in neutrino-nucleus interactions ionise the argon nuclei. In both HD
 1016 and VD designs the characteristic 128 nm scintillation light of argon is collected by a
 1017 photon detection system (PDS). This light will indicate the time at which electrons
 1018 start to drift, thus enabling reconstruction over the drift coordinate when compared
 1019 to the time when the first ionisation electron arrives to the anode. Reconstruction of
 1020 the topology in the transverse direction is achieved using the charge readout. Fig. 3.2
 1021 illustrates the detection principle described, for the case of a HD detector with a wire
 1022 readout.

1023 3.3.1 Horizontal Drift

1024 Within the HD design the ionisation electrons produced as charged particles traverse the
 1025 LAr drift horizontally towards the anode planes, made out of three layers of wire readout,
 1026 due to the effect of an electric field. This design, previously known as single-phase (SP),
 1027 was tested by the ProtoDUNE-SP detector at CERN. The prototype collected data from
 1028 a hadron beam and cosmic rays, providing high-quality data sets for calibration studies
 1029 and proving the excellent performance of this design.

3.3. Far Detector

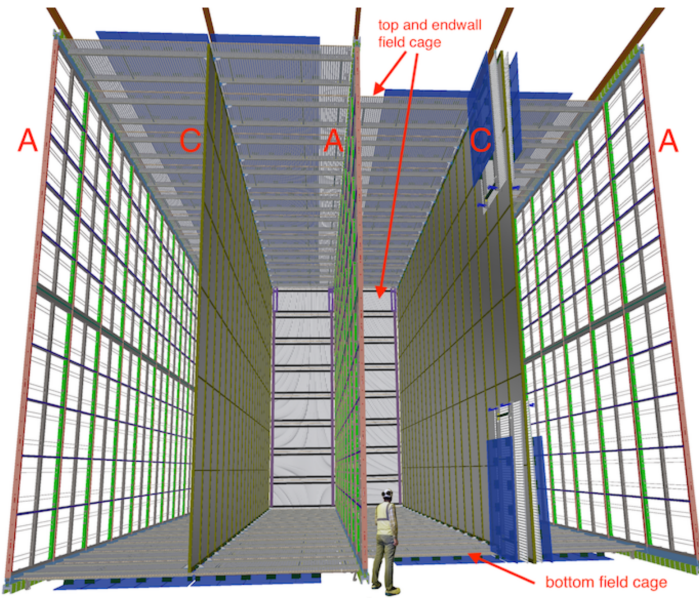


Figure 3.3: Proposed design for the FD-1 and FD-2 modules following the HD principle. Figure taken from Ref. [1].

1030 Each FD HD detector module is divided in four drift regions, with a maximum drift
 1031 length of 3.5 m, by alternating anode and cathode walls. The surrounding field cage
 1032 ensures the uniformity of the 500 V/cm horizontal electric field across the drift volumes.
 1033 The three anode walls, which constitute the charge readout of the detector, are built by
 1034 stacking anode plane assemblies (APAs), 2 high times 25 wide. The design of the HD
 1035 modules is shown in Fig. 3.3.

1036 Each APA is made of 2560 active wires arranged in three layers, plus an extra grid
 1037 layer, wrapped around a metal frame. The two induction wire planes, U and V, sit at
 1038 $\pm 35.7^\circ$ to the vertical on each side of the APA. The collection and shielding plane wires,
 1039 X and G, run parallel to the vertical direction. The ionisation electrons drift past the
 1040 induction planes, generating bipolar signals on those wires, and are collected by the
 1041 collection plane, producing a monopolar positive signal. The spacing between the wires
 1042 is ~ 5 mm, and it defines the spatial resolution of the APA.

1043 The front-end readout electronics, or cold electronics as they are immerse in the LAr,
 1044 are attached to the top of the up APAs and the bottom of the down APAs. Mounted on
 1045 the front-end mother boards we have a series of ASICs that digitize the signals from the

Chapter 3. The Deep Underground Neutrino Experiment

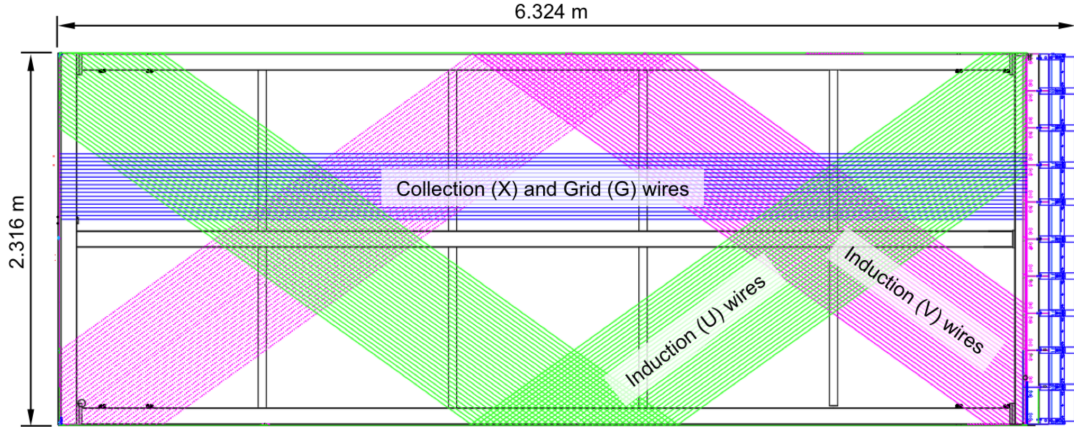


Figure 3.4: Schematic representation of an APA. The black lines represent the APA steel frame. The green and magenta lines correspond to the direction of the U and V induction wires respectively. The blue lines indicate the direction of the X collection wires and the wire shielding G. Figure taken from Ref. [1].

1046 collection and induction planes. Each wire signal goes to a charge-sensitive amplifier,
 1047 then there is a pulse-shaping circuit and this is followed by the analogue-to-digital
 1048 converter. This part of the process happens inside the LAr to minimise the number of
 1049 cables penetrating the cryostat. The digitised signals come out finally via a series of
 1050 high-speed serial links to the warm interface boards (WIBs), from where the data is sent
 1051 to the back-end DAQ through optical fibers.

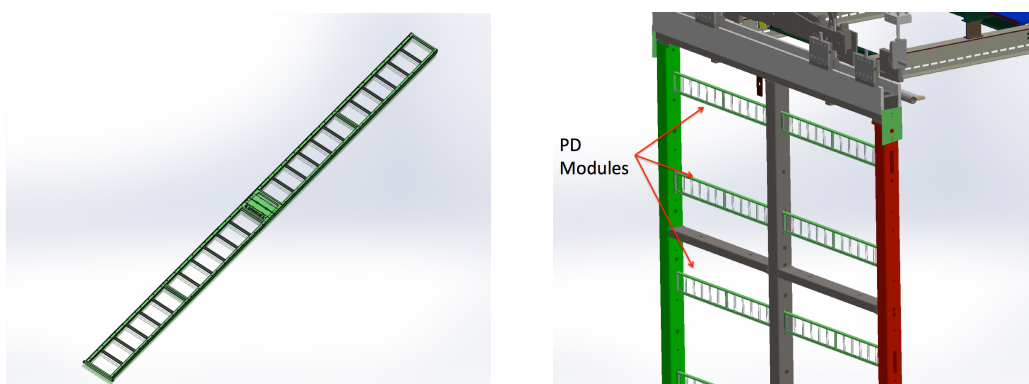


Figure 3.5: A PDS module containing 24 X-ARAPUCAs (left) and the location of the modules on the APAs (right). Figure taken from Ref. [1].

1052 The PDS uses modules of X-ARAPUCA devices, mounted on the APA frames
 1053 between the wire planes. Each X-ARAPUCA consists of layers of dichroic filter and

3.3. Far Detector

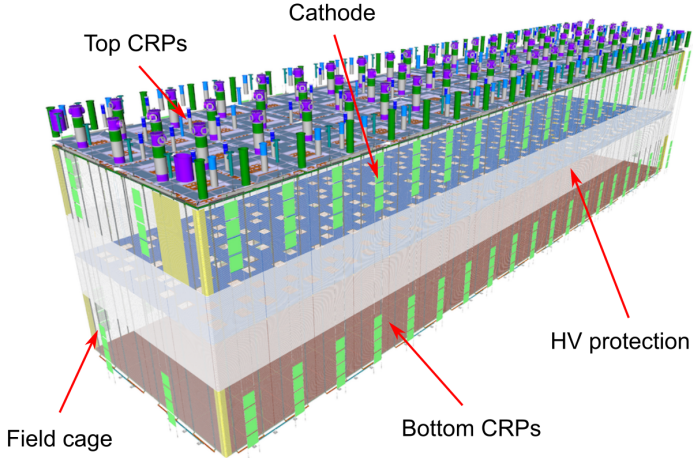


Figure 3.6: Proposed design for the FD-3 module following the VD principle. Figure adapted from Ref. [75].

wavelength-shifter. They shift the VUV scintillation light into the visible spectrum, sending then the visible photons to silicon photomultiplier (SiPM) devices. The PDS modules are $209\text{ cm} \times 12\text{ cm} \times 2\text{ cm}$ bars, containing 24 X-ARAPUCAs. There are 10 of these PDS modules per APA. Fig. 3.5 shows a PDS module (left) and the placement of the modules on the APAs (right).

3.3.2 Vertical Drift

In the VD case the ionisation electrons will drift vertically until they meet a printed circuit board-based (PCB) readout plane. It is based on the original dual-phase (DP) design deployed at CERN, known as ProtoDUNE-DP, used a vertical drift design with an additional amplification of the ionization electrons using a gaseous argon (GAr) layer above the liquid phase. The VD module incorporates the positive features of the DP design without the complications of having the LAr-GAr interface.

The current design of the FD VD module counts with two drift chambers with a maximum drift distance of 6.5 cm. A cathode plane splits the detector volume along the drift direction while the two anode planes are connected to the bottom and top walls of the detector. The layout of the VD module is shown in Fig. 3.6. Compared with

Chapter 3. The Deep Underground Neutrino Experiment

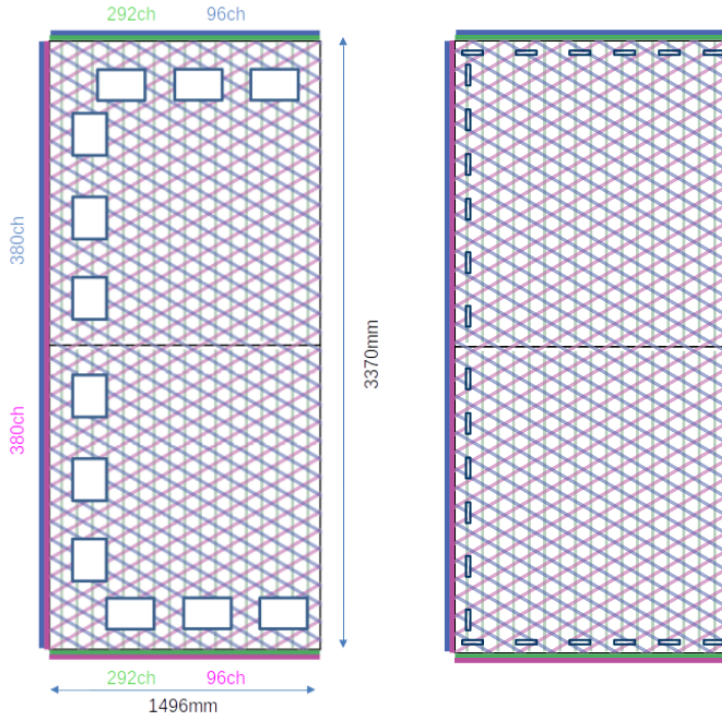


Figure 3.7: Schematic representation of the electrode strip configuration for a top (left) and bottom (right) CRU. Figure taken from Ref. [75].

1070 the HD design, the VD option offers a slightly larger instrumented volume and a more
1071 cost-effective solution for the charge readout.

1072 As in the HD design, each drift volume features a 500 V/cm electric field and a
1073 field cage that ensures its uniformity. The anode planes are arrays of $3.4\text{ m} \times 3\text{ m}$
1074 charge-readout planes (CRPs). These are formed by a pair of charge-readout units
1075 (CRUs), which are built from two double-sided perforated PCBs, with their perforations
1076 aligned. The perforations allow the drift electrons to pass between the layers.

1077 The PCB face opposite to the cathode has a copper guard plane which acts as
1078 shielding, while its reverse face is etched with electrode strips forming the first induction
1079 plane. The outer PCB has electrode strips on both faces, the ones facing the inner PCB
1080 form the second induction plane while the outermost ones form the collection plane. Fig.
1081 3.7 shows the layout of the electrode strips for the top (left) and bottom (right) CRUs.
1082 The magenta and blue lines represent the first and second induction planes respectively,
1083 and the green lines correspond to the collection plane.

3.3. Far Detector

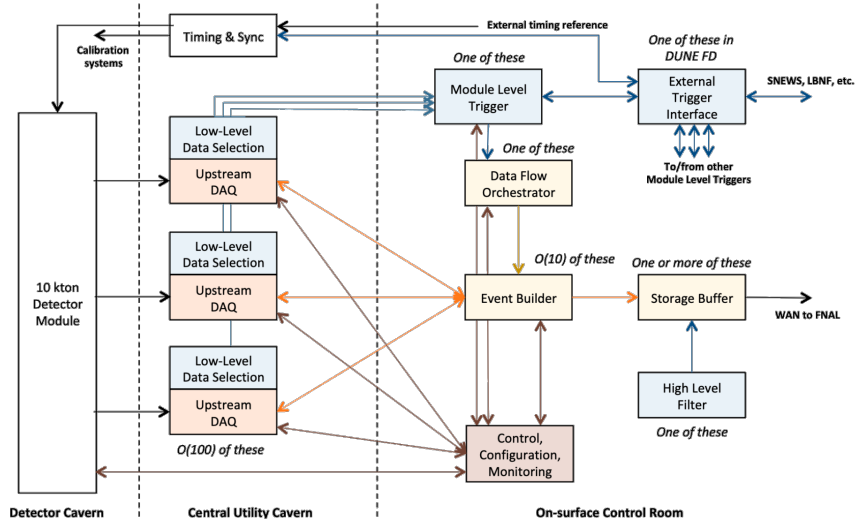


Figure 3.8: Detailed diagram of the DUNE FD DAQ system. Figure taken from Ref. [2].

1084 The PDS in the VD module will use the same X-ARAPUCA technology developed
 1085 for the HD design. The plan is to place the PDS modules on the cryostat walls and on
 1086 the cathode, in order to maximise the photon yield.

1087 3.3.3 FD Data Acquisition System

1088 The task of the data acquisition (DAQ) system is to receive, process and store data from
 1089 the detector modules. In the case of DUNE the DAQ architecture is designed to work
 1090 for all FD modules interchangeably, except some aspects of the upstream part which
 1091 may depend on the specific module technology.

1092 The enormous sample rate and the number of channels in TPC and PD readouts
 1093 will produce a very large volume of data. These pose really strong requirements and
 1094 challenges to the DUNE FD DAQ architecture. It will be required to read out data of
 1095 the order of ten thousand or more channels at rates of a few MHz. In order to cope
 1096 with the huge data volume, segmented readouts and compression algorithms are used to
 1097 reduce the data rate to manageable levels.

1098 The DAQ system of the DUNE FD is composed of five different subsystems. The
 1099 first one is the upstream DAQ, which receives the raw data from the detector, buffers it

Chapter 3. The Deep Underground Neutrino Experiment

and perform some low-level pre-processing. The minimally processed data is then fed into a hierarchical data selection system, which then performs a module level trigger decision. In case of a positive decision a trigger command is produced and executed by the data flow orchestrator, located in the back-end (BE) DAQ subsystem. Subsequently the DAQ BE retrieves the relevant data from the buffers located in the upstream DAQ, adds all the data into a cohesive record and saves it to permanent storage. Watching over all the other subsystems we also have the control, configuration and monitoring subsystem and the time and synchronization subsystem. Fig. 3.8 shows a schematic diagram of the DAQ system, showing the different subsystems and their relations.

A notorious challenge for the DUNE DAQ system comes from its broad physics goals. We must be prepared to process events spanning a wide range of time windows (from 5 ms in the case of beam and cosmic neutrinos and nucleon decay to 100 s in the case of SNBs) and therefore this requires a continuous readout of the detector modules. Moreover, because of the off-beam measurements we need to ensure the capabilities of online data processing and self-triggering. Having this into account, together with the technical constraints, the DUNE FD DAQ faces a series of challenges: it needs to be fault tolerant and redundant to reduce downtime, accommodate new components while it keeps serving the operational modules, have large upstream buffers to handle SNB physics, be able to support a wide range of readout windows and last reduce the throughput of data to permanent storage to be at most 30 PB/year.

3.4 Near Detector

In order to estimate the oscillation parameters we measure the neutrino energy spectra at the FD. This reconstructed energy arises from a convolution of the neutrino flux, cross section, detector response and the oscillation probability. Using theoretical and empirical models to account for the other effects, one can extract the oscillation probability using the measurement. However, these models have associated a number of uncertainties that are then propagated to the oscillation parameters.

3.4. Near Detector

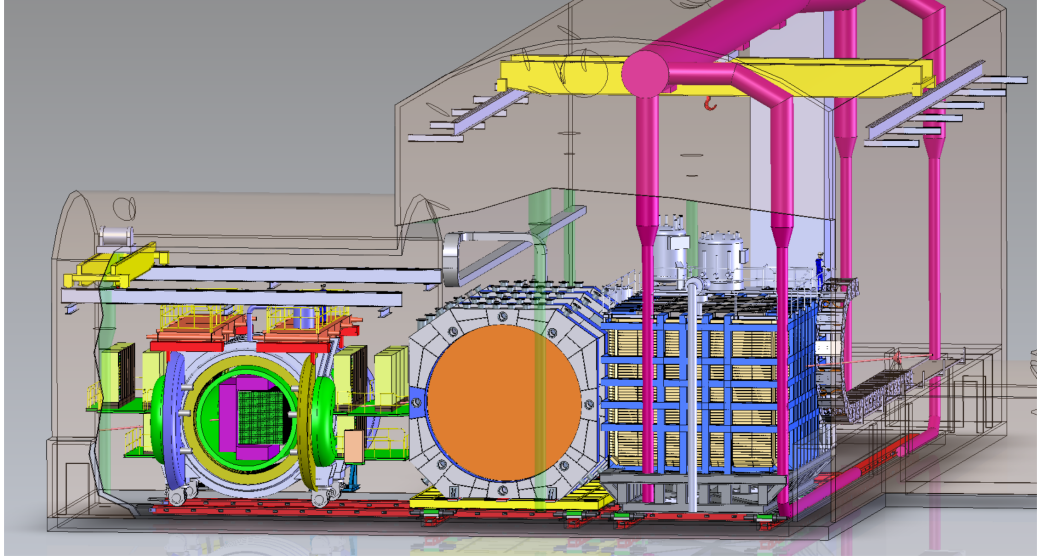


Figure 3.9: Representation of the ND hall in Phase II, showing the different subcomponents. From right to left, in the direction of the beam, we have ND-LAr, ND-GAr and SAND. Figure taken from Ref. [76].

One of the main roles of the ND is to measure the neutrino interaction rates before the oscillation effects become relevant, i.e. close to the production point. By measuring the ν_μ and ν_e energy spectra, and that of their corresponding antineutrinos, at the ND we can constrain the model uncertainties. A complete cancellation of the uncertainties when taking the ratio between the FD and ND measurements is not possible, as that would require both detectors to have identical designs and the neutrino fluxes to be the same. Because of the distance, the flux probed by the FD will have a different energy and flavour composition than that at the ND, as neutrinos oscillate and the beam spreads. The differences in the flux also determine the design of the detectors, therefore the ND is limited in its capability to match the FD design.

Nevertheless, having a highly capable ND DUNE can minimise the systematic uncertainties affecting the observed neutrino energy. The ND data can be used to tune the model parameters by comparison with the prediction. Then, one uses the tuned model to predict the unoscillated FD spectra. Comparing the prediction with the measured spectra it is possible to extract the oscillation parameters.

Additionally, the ND will have a physics program of its own. In particular, it will

Chapter 3. The Deep Underground Neutrino Experiment

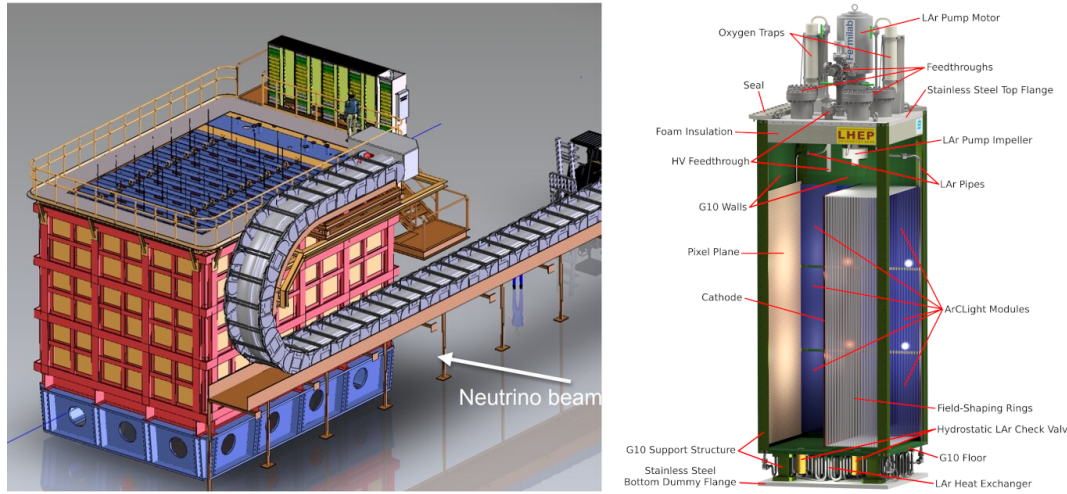


Figure 3.10: Schematic representation of the external components of ND-LAr, including the cryostat and the PRISM movable system (left) and detailed drawing of one ArgonCube module (right). Figure adapted from Ref. [1].

measure neutrino cross sections that will then be used to constrain the model used in the long-baseline oscillation analysis. It will also be used to search for BSM phenomena such as heavy neutral leptons, dark photons, millicharged particles, etc.

The DUNE ND can be divided in three main components, a LArTPC known as ND-LAr, a magnetised muon spectrometer, which will be the Temporary Muon Spectrometer (TMS) in Phase I and ND-GAr in Phase II, and the System for on-Axis Neutrino Detection (SAND). The layout of the Phase II DUNE ND can be seen in Fig. 3.9. The first two components of the ND will be able to move off-axis, in what is called the Precision Reaction-Independent Spectrum Measurement (PRISM) concept. More details on the purpose and design of the ND can be found in the DUNE ND Conceptual Design Report (CDR) [76].

3.4.1 ND-LAr

ND-LAr is a LArTPC, as the ND needs a LAr component in order to reduce cross section and detector systematic uncertainties in the oscillation analysis. However, its design differs significantly from those proposed for the FD modules. Because of the high event rates at the ND, approximately 55 neutrino interaction events per 10 μs spill,

3.4. Near Detector

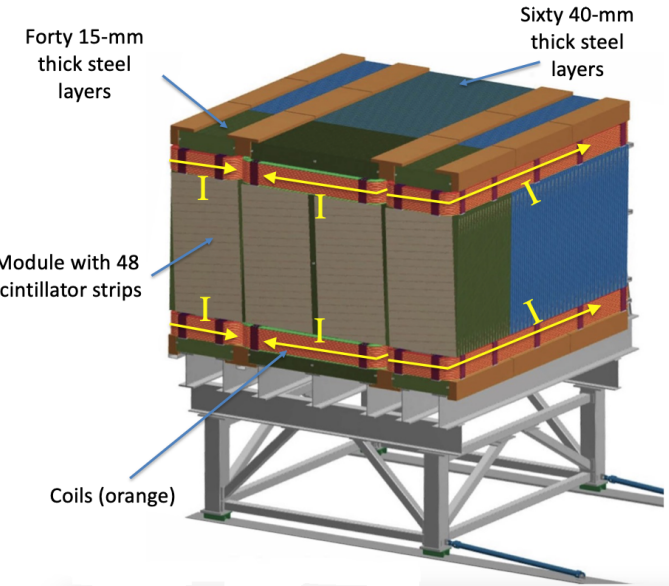


Figure 3.11: Schematic view of the TMS detector, highlighting its main parts. Figure adapted from Ref. [1].

ND-LAr will be built in a modular way. Each of the modules, based on the ArgonCube technology, is a fully instrumented, optically isolated TPC with a pixelated readout. The pixelisation allows for a fully 3D reconstruction and the optical isolation reduces the problems due to overlapping interactions. Fig. 3.10 shows a representation of the external parts of ND-LAr (left) and a detailed diagram of an ArgonCube module (right).

With a fiducial mass of 67 t and dimensions 7 m (w) \times 3 m (h) \times 5 m (l), ND-LAr will be able to provide high statistics and contain the hadronic systems from the beam neutrino interactions, but muons with a momentum higher than 0.7 GeV will exit the detector.

3.4.2 TMS/ND-GAr

In order to accurately estimate the neutrino energy, the momentum of the outgoing muons needs to be determined. That is the reason why a muon spectrometer is needed downstream of ND-LAr.

In Phase I that role will be fulfilled by TMS. It is a magnetised sampling calorimeter, with alternating steel and plastic scintillator layers. Fig. 3.11 shows a schematic view of

Chapter 3. The Deep Underground Neutrino Experiment

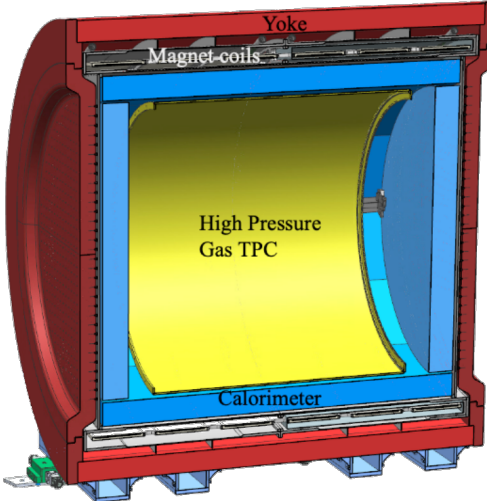


Figure 3.12: Cross section of the ND-GAr geometry, showing the HPgTPC, ECal and magnet. Figure adapted from Ref. [1].

the TMS detector. The magnetic field allows a precise measurement of the sign of the muon, so one can distinguish between neutrino and antineutrino interactions.

After the Phase II upgrade, TMS will be replaced with ND-GAr. This detector is a magnetised, high-pressure GAr TPC (often denoted as HPgTPC) surrounded by an electromagnetic calorimeter (ECal) and a muon tagger. A cross section of its geometry can be seen in Fig. 3.12. ND-GAr will be able to measure the momenta of the outgoing muons while also detect neutrino interactions inside the GAr volume. This allows ND-GAr to constrain the systematic uncertainties even further, as it will be able to accurately measure neutrino interactions at low energies thanks to the lower tracking thresholds of GAr.

3.4.3 PRISM

In general, the observed peak neutrino energy of a neutrino beam decreases as the observation angle with respect to the beam direction increases. This feature has been used in other long-baseline neutrino experiments, like T2K (2.5° off-axis) and NOvA (0.8° off-axis), in order to achieve narrower energy distributions. The DUNE PRISM concept exploits this effect using a movable ND. Within PRISM both ND-LAr and the

3.4. Near Detector

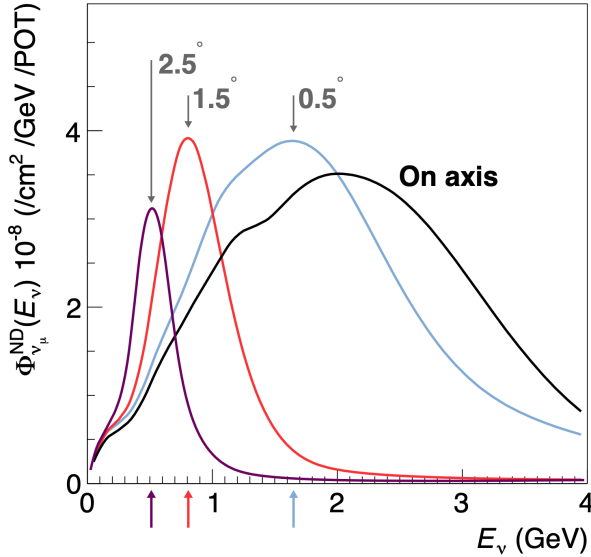


Figure 3.13: Predicted beam muon neutrino flux at the ND location for different off-axis positions. Figure taken from Ref. [76].

1190 muon spectrometer (TMS in Phase I and ND-GAr in Phase II) can be moved up to 3.2°
 1191 off-axis, equivalent to move the detectors 30.5 m laterally through the ND hall.

1192 This allows to record additional data samples with different energy compositions.
 1193 Fig. 3.13 compares the on-axis muon neutrino flux at the ND with the fluxes at different
 1194 off-axis positions. As the off-axis position increases the neutrino flux becomes closer to
 1195 a monoenergetic beam with a lower peak energy. These samples can be used to perform
 1196 a data-driven determination of the relation between true and reconstructed neutrino
 1197 energy, in order to reduce the dependence on the interaction model. The off-axis samples
 1198 are linearly combined to produce a narrow Gaussian energy distribution centered on
 1199 a target true energy. From the combination coefficients one can build a sample of
 1200 reconstructed neutrino events that will determine the energy mapping.

1201 The PRISM samples can also be used to form a flux at the ND location similar in
 1202 shape to the oscillated flux measured by the FD. This method can be used to extract
 1203 the oscillation parameters with minimal input from the neutrino interaction model.

Chapter 3. The Deep Underground Neutrino Experiment

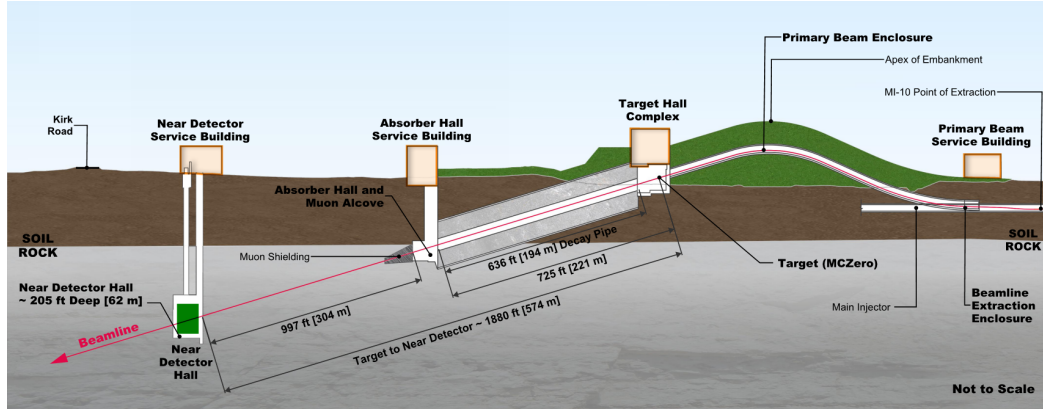


Figure 3.14: Schematic longitudinal section of the LBNF beamline at Fermilab (not to scale). Figure taken from Ref. [77].

1204 3.4.4 SAND

1205 The role of SAND is to monitor the beam stability by measuring the on-axis neutrino
 1206 energy spectra. As the PRISM program requires that ND-LAr and its downstream
 1207 muon spectrometer spend about half of the time in off-axis positions, it is not possible
 1208 to monitor the stability with the movable detectors. Moreover, for the success of PRISM
 1209 it is essential to have a stable beam configuration, or, at least, a quick assessment and
 1210 modeling of the distortions.

1211 The SAND detector is magnetised, and it counts with an inner low density tracker,
 1212 a LAr target with optical readout and surrounding sampling calorimeter.

1213 3.5 LBNF beamline

1214 The Long-Baseline Neutrino Facility (LBNF) project is responsible for producing the
 1215 neutrino beam for the DUNE detectors. A detailed discussion of the LBNF program
 1216 can be found in the DUNE/LBNF CDR Volume III [77].

1217 The LBNF beamline will provide a high-intensity neutrino beam within the adequate
 1218 energy range in order to meet the long-baseline oscillation physics goals of DUNE. A
 1219 schematic diagram of the longitudinal section of the LBNF beamline is shown in Fig.
 1220 3.14. First, a beam of $60 - 120$ GeV protons is extracted from the Fermilab Main

3.5. LBNF beamline

1221 Injector. This beam is aimed towards the target area, where it collides with a cylindrical
 1222 graphite target to produce pions and kaons.

1223 The diffuse, secondary beam of particles is focused by a pair of magnetic horns.
 1224 These select the positively charged particles when operated in Forward Horn Current
 1225 (FHC) mode, or the negatively charged ones when the current is reversed, also known as
 1226 Reverse Horn Current (RHC) mode. The focused secondary beam then enters a 194 m
 1227 decay pipe where the pions and kaons will predominantly produce $\mu^+\nu_\mu$ pairs when in
 1228 FHC mode (or $\mu^-\bar{\nu}_\mu$ in RHC mode).

1229 At the end of the decay pipe a hadron absorber removes the undecayed hadrons and
 1230 muons from the beam, which reduces the ν_e ($\bar{\nu}_e$) and $\bar{\nu}_\mu$ (ν_μ) contamination coming
 1231 from the μ^+ (μ^-) decays. The resulting neutrino flux at the FD is shown in Fig. 3.15,
 1232 both for FHC (left) and RHC (right) modes. These predictions show the intrinsic $(\bar{\nu}_e)$
 1233 contamination and wrong sign component from wrong sign and neutral meson decays,
 1234 as well as muons decaying before reaching the absorber.

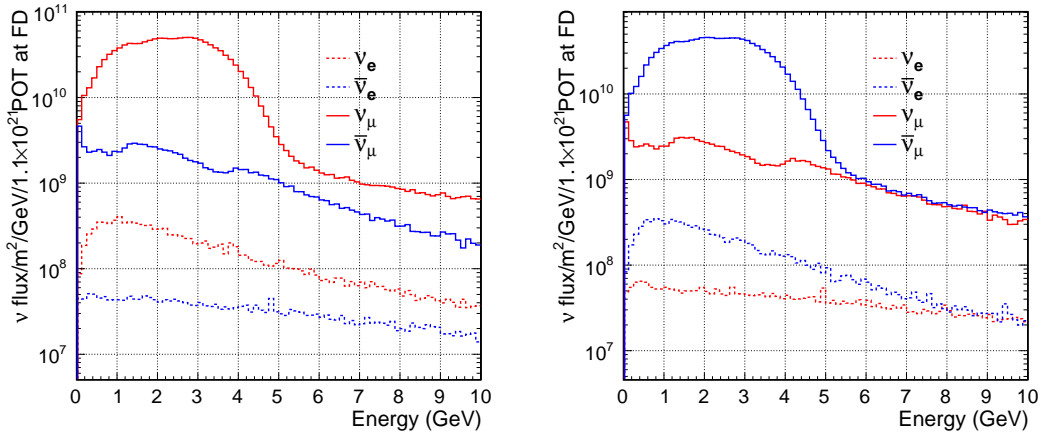


Figure 3.15: Predicted neutrino fluxes at the FD in FHC mode (left panel) and RHC mode (right panel). Figures taken from Ref. [70].

1235 **Chapter 4**

1236 **ND-GAr**

1237 ND-GAr is a magnetised, high-pressure gaseous argon TPC (HPgTPC), surrounded by
1238 an electromagnetic calorimeter (ECal) and a muon detector (commonly refer to as μ ID).
1239 A detailed discussion on the requirements, design, performance and physics of ND-GAr
1240 can be found in the DUNE ND CDR [76] and the ND-GAr whitepaper (cite).

1241 In DUNE Phase II ND-GAr will fulfill the role of TMS, measuring the momentum
1242 and sign of the charged particles exiting ND-LAr. Additionally, it will be able to measure
1243 neutrino interactions inside the HPgTPC, achieving lower energy thresholds than those
1244 of the ND and FD LArTPCs. By doing so ND-GAr will allow to constrain the relevant
1245 systematic uncertainties for the LBL analysis even further.

1246 The goal of the present chapter is to review the requirements that the physics program
1247 of DUNE impose on ND-GAr, present the current status of its design and describe the
1248 GArSoft package, its simulation and reconstruction software.

1249 **4.1 Requirements**

1250 The primary requirement for ND-GAr is to the measure the momentum and charge of
1251 muons from ν_μ and $\bar{\nu}_\mu$ CC interactions in ND-LAr, in order to measure their energy
1252 spectrum. To achieve the sensitivity to the neutrino oscillation parameters described
1253 in the DUNE FD TDR Volume II [70] ND-GAr should be able to constrain the muon

Chapter 4. ND-GAr

1254 energy within a 1% uncertainty or better. The main constraint will come from the
1255 calibration of the magnetic field, performed using neutral kaon decays in the HPgTPC.

1256 Another requirement for ND-GAr is the precise measurement of neutrino interactions
1257 on argon for the energies relevant to the neutrino oscillation program. The goal is to
1258 constrain the cross section systematic uncertainties in the regions of phase space that
1259 are not accessible to ND-LAr. This requires the kinematic acceptance for muons in
1260 ND-GAr to exceed that of ND-LAr, being comparable to the one observed in the FD.

1261 ND-GAr should also be able to the relationship between true and reconstructed energy
1262 from neutrino interactions on argon with low thresholds, being sensitive to particles that
1263 are not observed or may be misidentified in ND-LAr. In particular, ND-GAr needs to
1264 have low tracking thresholds in order to measure the spectrum of pions and protons
1265 produced in final-state interactions (FSI). It also must be able to accurately measure
1266 the pion multiplicity in 1, 2 and 3 pions final states, to inform the pion mass correction
1267 in the LArTPCs.

1268 4.2 Reference design

1269 The final design of ND-GAr is still under preparation. However, a preliminary baseline
1270 design was in place at the time of the ND CDR. This section summarises the main
1271 features of that design, as it is also the one used for the default geometry in our simulation.
1272 A DUNE Phase II whitepaper, discussing the different options under consideration for
1273 the ND-GAr design, is in progress.

1274 4.2.1 HPgTPC

1275 The reference design for the ND-GAr HPgTPC follow closely that of the ALICE TPC.
1276 It is a cylinder with a central high-voltage cathode, generating the electric field for
1277 the two drift volumes, with a maximum drift distance of 2.5 m each. The anodes will
1278 be instrumented with charge readout chambers. The original design repurposed the
1279 multi-wire proportional readout chambers of ALICE, however the current R&D efforts

4.2. Reference design

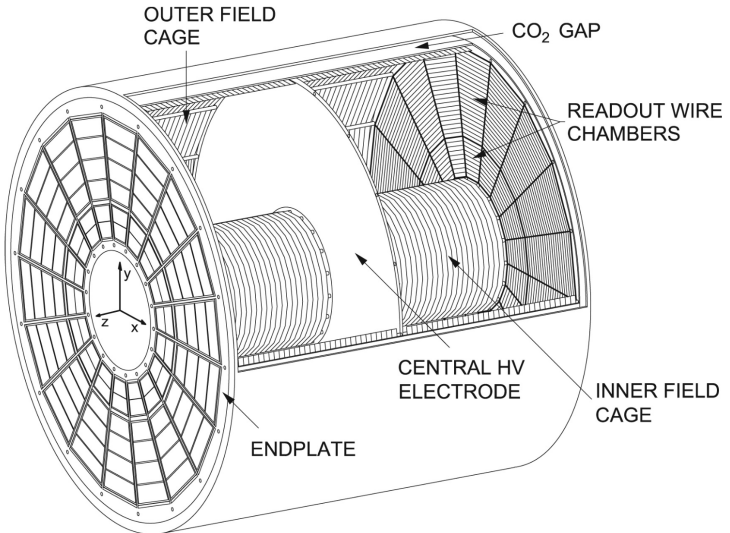


Figure 4.1: Diagram of the ALICE TPC, showing the two drift chambers, inner and outer field cages and readout chambers. Figure taken from Ref. [1].

1280 focus on a gas electron multiplier option instead. Fig. 4.1 shows a schematic diagram of
 1281 the ALICE TPC design. The basic ND-GAr geometry will resemble this, except for the
 1282 inner field cage.

1283 It will use a 90-10 molar fraction argon-CH₄ mixture at 10 bar. With this baseline
 1284 gas mixture light collection is not possible, as the quenching gas absorbs most of the
 1285 VUV photons. Additional R&D efforts are underway, to understand if different mixtures
 1286 allow for the light signal to be used to provide a t_0 while maintaining stable charge gain.

1287 **4.2.2 ECal**

1288 The main role of the ND-GAr ECal is the calorimetric measurement of the electron
 1289 energies and the reconstruction of photons, in particular those from neutral pion decays.
 1290 Also, the ECal is able to provide a t_0 timestamp for neutrino interactions, by associating
 1291 its activity to the tracks in the HPgTPC. The ECal will also be able to perform
 1292 neutron reconstruction using time of flight and reject external backgrounds, thanks to
 1293 its sub-nanosecond time resolution.

1294 The ECal design features three independent subdetectors, two end caps at each side
 1295 and a barrel surrounding the HPgTPC. Each of the detectors is divided in modules,

Chapter 4. ND-GAr

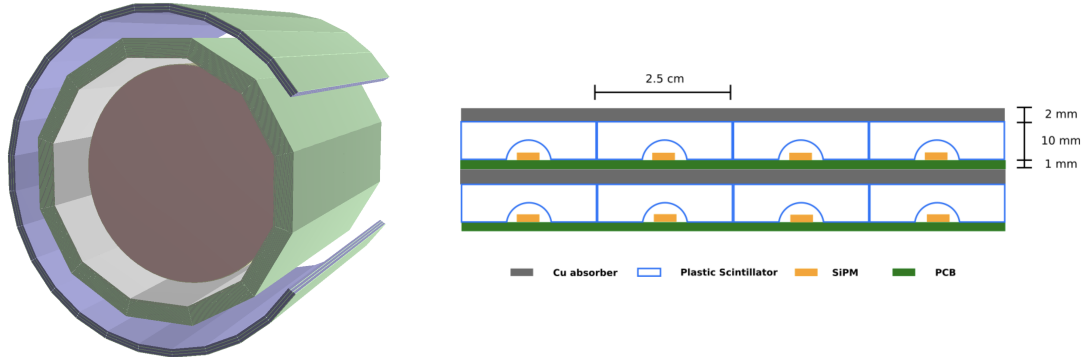


Figure 4.2: View of the 12-sided ECal barrel and outer muon tagger geometries (left) and layout of the ECal tile layers for the 2 mm Cu, 10 mm scintillator option (right). Figure adapted from Ref. [1].

which combine alternating layers of plastic scintillator and absorber material readout by SiPMs. The inner scintillator layers consist of $2.5 \times 2.5 \text{ cm}^2$ high-granularity tiles, whereas the outer ones are made out of 4 cm wide cross-strips spanning the whole module length. The current barrel geometry consists of 8 tile layers and 34 strip layers, while the end caps feature 6 and 36 respectively. The thickness of the scintillator layers is 7 mm and 5 mm for the Pb absorber layers. The 12-sided geometry of the ECal barrel (left) and the layout of the tile layers (left)¹ can be seen in Fig. 4.2.

4.2.3 Magnet

The ND-GAr magnet design, known as the Solenoid with Partial Yoke (SPY), consists of two coupled solenoids with an iron return yoke. The idea behind the design is to have a solenoid as thin as possible, as well as a return yoke mass distribution that minimises the material budget between ND-LAr and ND-GAr. The magnet needs to provide a 0.5 T field in the direction perpendicular to the beam, parallel to the drift electric field. It needs to host the pressure vessel and the surrounding ECal, which points to an inner diameter of $\sim 6.4 \text{ m}$.

The solenoid is a single layer coil, based on niobium titanium superconducting

¹The figure shows the layout of the tile layers for a previous design with 2 mm Cu absorber and 10 mm plastic scintillator, as mentioned in the text the current choice is 5 mm Pb absorber and 7 mm scintillator.

4.3. GArSoft

1312 Rutherford cable. The total length of the coil is 7.5 m. The bobbin will be split in four
1313 segments grouped in pairs with two identical cryostats, connected in series. The iron
1314 yoke features an aperture in the upstream side to allow the muons coming from ND-LAr.
1315 Still, its material will be enough to reduce the magnetic field reaching SAND, and also
1316 stop the charged pions produced inside the HPgTPC.

1317 4.2.4 Muon system

1318 The design of the ND-GAr muon system is still in a preliminary stage. Its role is to
1319 distinguish between muons and pions punching through the ECal. This is especially
1320 important for wrong-sign determination, to separate these from neutral current events.

1321 In its current form, the muon system consists of three layers of longitudinal sampling
1322 structures. It alternates 10 cm Fe absorber slabs with 2 cm plastic scintillator strips.
1323 The transverse granularity required is still under study.

1324 4.3 GArSoft

1325 GArSoft is a software package developed for the simulation and reconstruction of events
1326 in ND-GAr. It is inspired by the LArSoft toolkit used for the simulation of LArTPC
1327 experiments, like the DUNE FD modules. It is based on `art`, the framework for event
1328 processing in particle physics experiments [78]. Other of its main dependencies are `ROOT`,
1329 `NuTools`, `GENIE` and `Geant4`. It allows the user to run all the steps of a generation-
1330 simulation-reconstruction workflow using FHiCL configuration files.

1331 4.3.1 Event generation

1332 The standard generator FHiCLs in GArSoft run the event generation and particle
1333 propagation simulation (i.e. Geant4) in the same job by default. However, it is possible
1334 to split them up if needed. The current version of GArSoft provides five different event
1335 generators, each of them producing `simb::MCTruth` products defined in `NuTools`. The
1336 available modules are:

Chapter 4. ND-GAr

- 1337 • **SingleGen**: particle gun generator. It produces the specified particles with a given
1338 distribution of momenta, initial positions and angles.
- 1339 • **TextGen**: text file generator. The input file must follow the `hepevt` format², the
1340 module simply copies this to `simb::MCTruth` data products.
- 1341 • **GENIEGen**: GENIE neutrino event generator. The module runs the neutrino-nucleus
1342 interaction generator using the options specified in the driver FHiCL file (flux file,
1343 flavour composition, number of interactions per event, t_0 distribution, ...). Current
1344 default version is `v3_04_00`.
- 1345 • **RadioGen**: radiological generator. It produces a set list of particles to model
1346 radiological decays. Not tested.
- 1347 • **CRYGen**: cosmic ray generator. The module runs the CRY event generator with a
1348 configuration specified in the FHiCL file (latitude and altitude of detector, energy
1349 threshold, ...). Not tested.

1350 The module `GArG4` searches for all the generated `simb::MCTruth` data products, using
1351 them as inputs to the Geant4 simulation with the specified detector geometry. A constant
1352 0.5 T magnetic field along the drift coordinate is assumed. The main outputs of this step
1353 are `simb::MCParticle` objects for the generated Geant4 particles, `gar::EnergyDeposit`
1354 data products for the energy deposits in the HPgTPC and `gar::CaloDeposit` data
1355 products for the energy deposits in the ECal and muon system.

1356 4.3.2 Detector simulation

1357 The standard detector simulation step in GArSoft is all run with a single FHiCL, but
1358 the different modules can be run independently as well. First the `IonizationReadout`

²In brief, each event contains at least two lines. The first line contains two entries, the event number and the number of particles in the event. Each following line contains 15 entries to describe each particle. The entries are: status code, pdg code for the particle, entry of the first mother for this particle, entry of the second mother for this particle, entry of the first daughter for this particle, entry of the second daughter for this particle, x component of the particle momentum, y component of the particle momentum, z component of the particle momentum, energy of the particle, mass of the particle, x component of the particle initial position, y component of the particle initial position, z component of the particle initial position and time of the particle production.

4.3. GArSoft

1359 module simulates the charge readout of the HPgTPC, and later the `SiPMReadout` module
1360 runs twice, once for the ECal and then for the muon system, with different configurations.

1361 The `IonizationAndScintillation` module collects all the `gar::EnergyDeposit`
1362 data products, to compute the equivalent number of ionization electrons for each energy
1363 deposit. The `ElectronDriftAlg` module simulates the electron diffusion numerically
1364 both in the longitudinal and transverse directions and applies an electron lifetime
1365 correction factor. The induced charge on the nearest and neighbouring readout pads
1366 is modeled using the provided pad response functions. The digitisation of the data is
1367 then simulated with the `TPCReadoutSimAlg` module. By default, the ADC sampling
1368 rate used is 50.505 MHz. The resulting raw waveforms for each channel are stored with
1369 zero-suppression, in order to save memory and CPU time. The algorithms keep blocks
1370 of ADC values above a certain threshold, plus some adjustable additional early and late
1371 tick counts. The results of these three steps are `gar::raw::RawDigit` data products.

1372 For the ECal and the muon system the `SiPMReadout` module calls either the
1373 `ECALReadoutSimStandardAlg` or `MuIDReadoutSimStandardAlg` modules. These take
1374 all the `gar::CaloDeposit` data products in the corresponding detector and do the
1375 digitisation depending on whether the hit was in a tile or strip layer. They include single
1376 photon statistics, electronic noise, SiPM saturation and time smearing. The resulting
1377 objects are `gar::raw::CaloRawDigit` data products.

1378 4.3.3 Reconstruction

1379 The reconstruction in GArSoft is also run as a single job by default. It first runs the hit
1380 finding, clustering, track fitting and vertex identification in the HPgTPC, followed by
1381 the hit finding and clustering in the ECal and muon system. After those it produces the
1382 associations between the associations between the tracks and the ECal clusters.

1383 Focusing first on the HPgTPC reconstruction, the `CompressedHitFinder` module
1384 takes the zero-suppressed ADCs from the `gar::raw::RawDigit` data products. The
1385 reconstructed hits largely correspond to the above threshold blocks, however the hit
1386 finder identifies waveforms with more than one maximum, diving them in multiple hits

Chapter 4. ND-GAr

1387 if they dip below a certain threshold. The data products produced are of the form
1388 `gar::rec::Hit`. These are the inputs to the clustering of hits in the `TPCHitCluster`
1389 module. Hits close in space and time are merged, and the resulting centroids are found.
1390 This module outputs `gar::rec::TPCClusters` objects and associations to the input
1391 hits.

1392 The following step prior to the track fitting is pattern recognition. The module
1393 called `tpcvecchitfinder2` uses the `gar::rec::TPCClusters` data products to find track
1394 segments, typically called vector hits. They are identified by performing linear 2D fits
1395 to the positions of the clusters in a 10 cm radius, one fit for each coordinate pair. A
1396 3D fit defines the line segment of the vector hit, using as independent variable the one
1397 whose sum of (absolute value) slopes in the 2D fits is the smallest. The clusters are
1398 merged to a given vector hit if they are less than 2 cm away from the line segment. The
1399 outputs are `gar::rec::VecHit` data products, as well as associations to the clusters. The
1400 `tpcpatrec2` module takes the `gar::rec::VecHit` objects to form the track candidates.
1401 The vector hits are merged together if their direction matches, their centers are within
1402 60 cm and their direction vectors point roughly to their respective centers. Once
1403 the clusters of vector hits are formed they are used to make a first estimation of the
1404 track parameters, simply taking three clusters along the track. The module produces
1405 `gar::rec::Track` data products and associations between these tracks and the clusters
1406 and vector hits.

1407 The track is fitted by means of a Kalman filter in the `tpctrackfit2` module, using
1408 the position along the drift direction as the independent variable. Two different fits are
1409 performed per track, a forward and a backwards fit, each starting from one of the track
1410 ends. The Kalman filter state vector ($y, z, R, \phi, \tan\lambda$) is estimated at each point along
1411 the track using a Bayesian update. The track parameters reported in the forward and
1412 backwards fits are the ones computed at the opposite end where the fit started. The
1413 main outputs of the track fit are the `gar::rec::Track` objects. Additionally, the module
1414 stores the fitted 3D positions along the track in the `gar::rec::TrackTrajectory` data
1415 products and the total charge and step sizes for each point also get stored in the form of

4.3. GArSoft

1416 `gar::rec::TrackIonization` objects.

1417 After the tracking step, the `vertexfinder1` module looks at the reconstructed
1418 `gar::rec::Track` products, creating vertex candidates with the track ends that are
1419 within 12 cm of each other. The vertices are then fitted using linear extrapolations from
1420 the different track ends associated. The results are `gar::rec::Vertex` data products,
1421 and associations to the tracks and corresponding track ends.

1422 For the ECal and muon tagger, the `SiPMHitFinder` module runs twice with different
1423 configurations, adapted to the particular capabilities of both. The module simply takes
1424 the `gar::raw::CaloRawDigit` products, applies a calibration factor to convert the ADC
1425 counts to MeV and for the strip layer hits it calculates the position along the strip using
1426 the times recorded of both SiPMs. This module produces `gar::rec::CaloHit` data
1427 products. Next, these objects are used as inputs to the `CaloClustering` module. It
1428 merges the hits based on a simple nearest neighbours (NN) algorithm. For the resulting
1429 clusters it also computes the total energy and position of the centroid. The results are
1430 stored as `gar::rec::Cluster` data products, with associations to the hits.

1431 The last step in the reconstruction is associating the reconstructed tracks in the
1432 HPgTPC to the clusters formed in the ECal and muon system. The `TPCECALAssociation`
1433 module checks first the position of the track end points, considering only the points
1434 that are at least 215 cm away from the cathode or have a radial distance to the center
1435 greater than 230 cm. The candidates are propagated up to the radial position, in the
1436 case of clusters in the barrel, or the drift coordinate position, for the end cap cluster, of
1437 the different clusters in the collection using the track parameters computed at the end
1438 point. The end point is associated to the cluster if certain proximity criteria are met.
1439 This module creates associations between the tracks, the end points and the clusters.
1440 The criteria for the associations are slightly different for the ECal and the muon tagger.

₁₄₄₁ Chapter 5

₁₄₄₂ FWTPG offline software

1443 Chapter 6

1444 Matched Filter approach to
1445 induction wire Trigger Primitives

1446 6.1 Motivation

1447 The filter implemented in the firmware of the upstream DUNE FD DAQ is a 32nd-order
1448 low-pass finite impulse-response (FIR) filter. The output of such filter for a discrete
1449 system can be written as:

$$y[i] = \sum_{j=0}^N h[j]x[i-j], \quad (6.1)$$

1450 where N is the order of the filter, y is the output sequence, x is the input sequence and h
1451 is the set of coefficients of the filter. The current implementation within `dtp-firmware`
1452 [79] uses a set of 16 non-zero integer coefficients.

1453 Filtering is a vital step in the hit finder chain. It helps to suppress the noise and
1454 enhance the signal peaks with respect to the noiseless baseline. A good filtering strategy
1455 allows us to use lower thresholds when forming the trigger primitives (TPs) and thus
1456 increasing the sensitivity of our detector to low energy physics events. In such events,
1457 the hits produced by the ionisation electrons tend to have lower amplitudes than those
1458 of interest to the baseline physics programme of the DUNE experiment.

1459 This is particularly important for the induction planes. In general, signal peaks in

Chapter 6. Matched Filter approach to induction wire Trigger Primitives

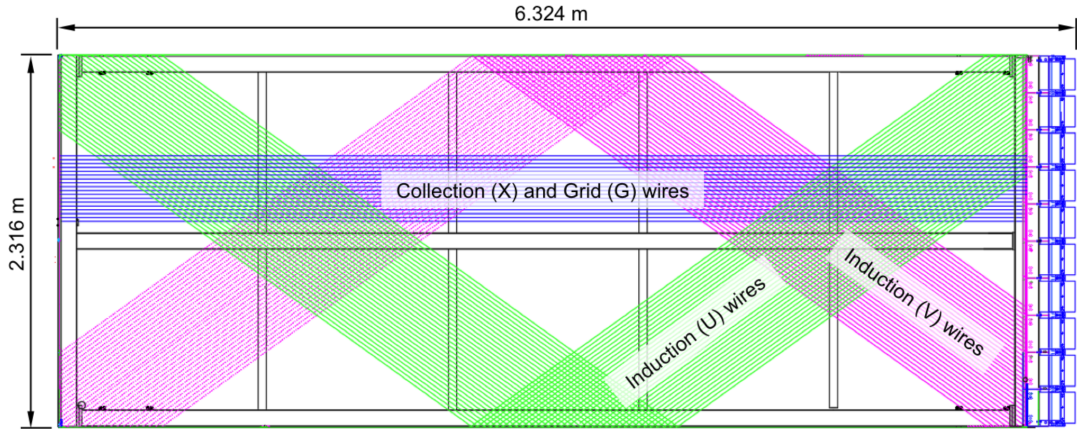


Figure 6.1: Schematic representation of an APA. The black lines represent the APA steel frame. The green and magenta lines correspond to the direction of the U and V induction wires respectively. The blue lines indicate the direction of the X collection wires and the wire shielding G.

1460 the induction wires have smaller amplitude than the ones in the induction plane. This,
 1461 together with the fact that the pulse shapes are bipolar, reduces our capacity to detect
 1462 the hits on these channels. The inefficiency of detecting TPs in the induction planes
 1463 (denoted as U and V planes) lead trigger algorithms to focus mainly on the TPs from
 1464 the collection plane (so-called X plane). As a result, the possibility of making trigger
 1465 decisions based on the coincidence of TPs across the three wire planes remains nowadays
 1466 unexploited in DUNE. Fig. 6.1 shows a schematic view of an anode plane assembly
 1467 (APA), with the different wire plane orientations highlighted.

1468 A possible improvement of the current hit finder chain could require optimising
 1469 the existing or choosing a new filter implementation. A filter strategy which improves
 1470 the induction signals may be able to enhance the detection efficiency of TPs from the
 1471 induction planes and ideally make it comparable to that of the collection plane.

1472 The goal is to implement a better finite-impulse response filter design and to evaluate
 1473 its performance relative to the current filter. To do so, we need to take into account the
 1474 limitations of the firmware: the FIR filter shall have maximum 32 coefficients (so-called
 1475 taps) whose values are 12-bit unsigned integers. Although it is technically possible to
 1476 include non-integer coefficients, it would be a technical challenge as we have 40 FIR

6.2. Signal-to-noise ratio definition

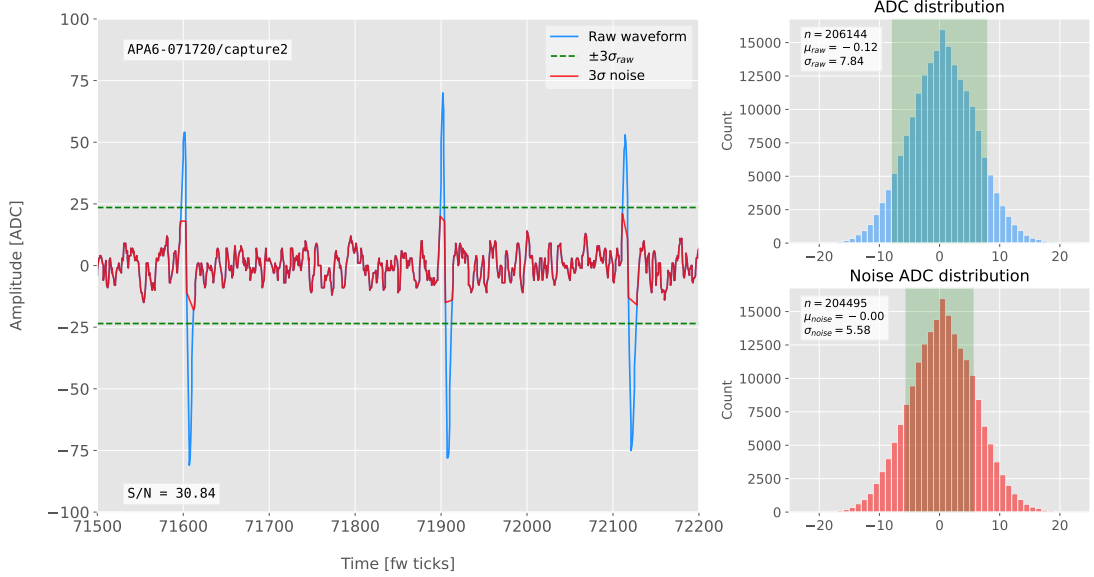


Figure 6.2: Left panel: Zoomed unfiltered waveform corresponding to channel 7840 from the ProtoDUNE-SP raw data capture `felix-2020-07-17-21:31:44` (blue line). The green dashed lines mark the region $\pm 3\sigma_{\text{raw}}$. The resulting noise waveform is also shown (red line). Top right panel: ADC distribution for channel 7840, where the green shaded region represents $\pm \sigma_{\text{raw}}$. Bottom right panel: noise ADC distribution for channel 7840, where the green shaded region represents $\pm \sigma_{\text{noise}}$.

1477 instances per APA, as there are 4 FIR per optical link and 10 optical links per APA.
 1478 With these restrictions, the task is to provide a set of 32 coefficients which yield an
 1479 optimal filter performance for the induction wires.

1480 6.2 Signal-to-noise ratio definition

1481 I introduce the signal to noise ratio (S/N) as a measure of the FIR filter performance
 1482 and demonstrate how to extract its value for a set of ProtoDUNE-SP data. The S/N
 1483 metrics allow us to compare different filter implementations and serve as a basis for more
 1484 detailed studies presented later in this document. Specifically, I use the ADC capture
 1485 `felix-2020-07-17-21:31:44` (data capture taken for firmware validation purposes). I
 1486 defined S/N as the height of the signal peaks relative to the size of the noise peaks.
 1487 To quantify this quantity channel by channel one first need to estimate the standard
 1488 deviation of the ADC data for each channel, σ_{ADC} . Then, I define the corresponding

Chapter 6. Matched Filter approach to induction wire Trigger Primitives

1489 noise waveform to be the ADC values in the range $\pm 3\sigma_{ADC}$. From this new noise data
1490 one can estimate again the mean and standard deviation, μ_{noise} and σ_{noise} , so I can
1491 write the S/N for any given channel as:

$$S/N = \frac{\max [ADC] - \mu_{noise}}{\sigma_{noise}}, \quad (6.2)$$

1492 where $\max [ADC]$ is simply the maximum ADC value found in the corresponding channel.

1493 One can apply this definition of the S/N with a waveform from one of the channels
1494 of the data capture¹. Fig. 6.2 shows a zoomed region of the waveform corresponding to
1495 channel 7840 (blue line), where one can clearly see three signal peaks and continuous
1496 additive noise (we actually see 6 peaks, 3 positive and 3 negative, but, because by design
1497 for induction channels the expected signal pulse shapes are bipolar, I treat them as a
1498 collection of 3 individual signal peaks). I estimated the standard deviation of this raw
1499 waveform to be $\sigma_{raw} = 7.84$ ADC, so I am able to define the noise waveform (red line)
1500 as the ADC values in the range ± 23.52 ADC. This way one obtains $\mu_{noise} = 0$ and
1501 $\sigma_{noise} = 5.58$ ADC, which gives $S/N = 30.84$.

1502 We can repeat this calculation now for the corresponding filtered waveform (using the
1503 current firmware FIR filter). In Fig. 6.3 I plotted the same time window for the filtered
1504 waveform from channel 7840 (blue line). In this case, the standard deviation of the
1505 waveform is larger than before, giving $\sigma_{raw} = 10.99$ ADC. The resulting noise waveform
1506 (red line) results from selection the ADC values in the range ± 32.91 ADC, giving now
1507 $\mu_{noise} = -0.47$ ADC and $\sigma_{noise} = 7.03$ ADC. Finally, one obtains $S/N = 24.68$. Notice
1508 that the value of S/N decreases after the filtering. Clearly, one can see that the noise
1509 baseline has increased by a factor of 1.35 when we applied the FIR filter and at the same
1510 time the amplitude of the signal peaks has remained almost unchanged, leading to this
1511 poorer S/N value.

¹All the original work was done within the `dtp-simulation` package [80], which offers a variety of tools to read raw data and emulate the TPG block (pedestal subtraction, filtering and hit finder). However, the results shown in this report were re-worked later using the C++ based `dtpemulator` package [81]. Its main purpose is the emulation of the TPG block and, in the same way as its predecessor, it has been cross-checked against the current firmware implementation.

6.3. Low-pass FIR filter design

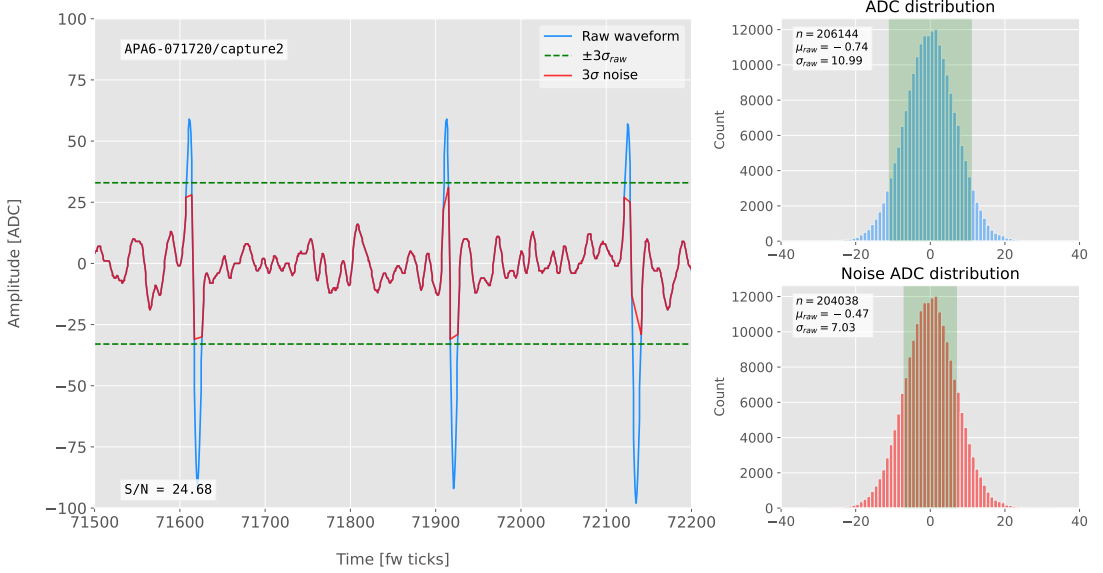


Figure 6.3: Left panel: Zoomed filtered waveform corresponding to channel 7840 from the ProtoDUNE-SP raw data capture `felix-2020-07-17-21:31:44` (blue line). The filter used was the current implementation of the low-pass FIR filter in `dtp-firmware`. The green dashed lines mark the region $\pm 3\sigma_{\text{raw}}$. The resulting noise waveform is also shown (red line). Top right panel: ADC distribution for channel 7840 after filtering, where the green shaded region represents $\pm \sigma_{\text{raw}}$. Bottom right panel: noise ADC distribution for channel 7840 after filtering, where the green shaded region represents $\pm \sigma_{\text{noise}}$

1512 6.3 Low-pass FIR filter design

1513 In general, when one uses a method to optimize the frequency response of a digital filter,
 1514 such as the Parks-McClellan algorithm, one finds a set of N real coefficients that give
 1515 the best response for the specified pass-band and order of the filter [82].

1516 In our case, as the sampling frequency is defined as 1 ticks^{-1} , the Nyquist frequency
 1517 will simply be $1/2 \text{ ticks}^{-1}$. The current implementation of the filter seems to have as
 1518 pass-band the range $[0, 0.1] \text{ ticks}^{-1}$. This can be seen in Fig. 6.4, where I show the
 1519 power spectrum, in decibels, of such filter implementation (blue solid line). For instance,
 1520 the Park-McClellan algorithm finds the optimal Chebyshev FIR filter taking as input
 1521 the boundaries of the target pass-band and stop-band, which can be written in the form:

$$\left\{ \begin{array}{l} [0, f_c] \\ [f_c + \delta f, f_N] \end{array} \right. , \quad (6.3)$$

Chapter 6. Matched Filter approach to induction wire Trigger Primitives

where f_c is the cut-off frequency, δf is the transition width and f_N is the aforementioned Nyquist frequency. A similar behaviour to the one in the current filter can be obtained by setting $f_c = 0$ and $\delta f = 0.1 \text{ ticks}^{-1}$. The response of the resulting filter is also shown in Fig. 6.4 (blue solid line). Notice that the suppression of the stop-band is enhanced for this optimal filter. For comparison I included the power response of the filter obtained by taking the integer part of the coefficients resulting from the Parks-McClellan method (red dashed line). One can see that it does not suppress that much the stop-band, in a similar way to the current implementation of the filter.

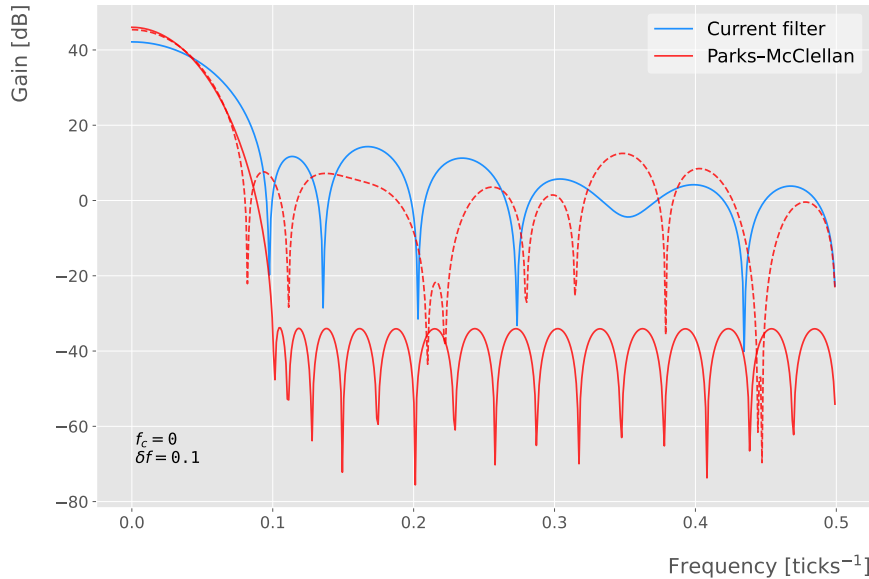


Figure 6.4: Power spectrum in decibels for the current implementation of the low-pass FIR filter in `dtp-firmware` (blue line), compared to the response of an optimal filter obtained using the Parks-McClellan algorithm for the same pass-band (red line). Also for comparison I include the spectrum of the optimal filter when taking only the integer part of the coefficients (red dashed line).

At this point, I tried to improve the performance of the FIR filter using the Parks-McClellan method, i.e. maximize the overall S/N, using the available data captures. I did so by varying the values of the two quantities that parametrize the pass-band and stop-band, the cut-off frequency f_c and the transition width δf .

Fig. 6.5 shows the average relative change in the S/N (i.e. the ratio between the value of the S/N after and before the filtering) for capture `felix-2020-07-17-21:31:44`,

6.3. Low-pass FIR filter design

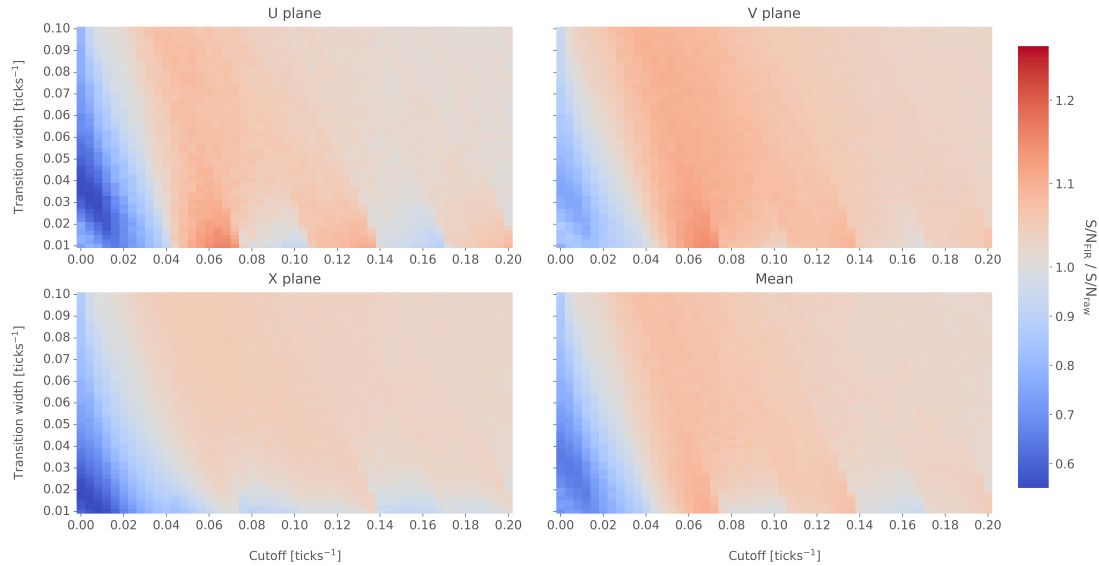


Figure 6.5: Relative change in the S/N for the ProtoDUNE-SP raw data capture `felix-2020-07-17-21:31:44`, using different values of the cutoff frequency f_c and the transition width δf . The optimal Chebyshev filters were applied using just the integer part of the coefficients given by the Parks-McClellan algorithm.

when using filters designed with the Parks-McClellan algorithm for the specified values of the cut-off frequency f_c and the transition width δf , restricted to integer values for the filter coefficients. One can clearly distinguish different regions where we get an improvement of up to a factor of 1.35 for the U plane. For large values of $f_c + \delta f$ the ratio tends to 1, as expected (in that limit the width of the stop-band goes to 0, meaning that no frequencies are filtered out and thus the waveform remains the same).

Using the configuration which gives the best mean performance for the three planes (see bottom right panel of Fig. 6.5), i.e. $f_c = 0.068 \text{ ticks}^{-1}$ and $\delta f = 0.010 \text{ ticks}^{-1}$, we can see how such filter affects the different channels. Fig. 6.6 shows the distribution of the S/N improvement values for all the channels in the raw ADC capture `felix-2020-07-17-21:31:44`, separated by wire plane, after the optimal Chebyshev filter was applied. One can see that there is a clear improvement for both U and V induction wire planes, obtaining a mean change of 1.25 and 1.30 for them respectively. However, in the case of the collection plane X the mean of this distribution is roughly 1, meaning that a good fraction of channels in that plane get a slightly worse S/N after the

Chapter 6. Matched Filter approach to induction wire Trigger Primitives

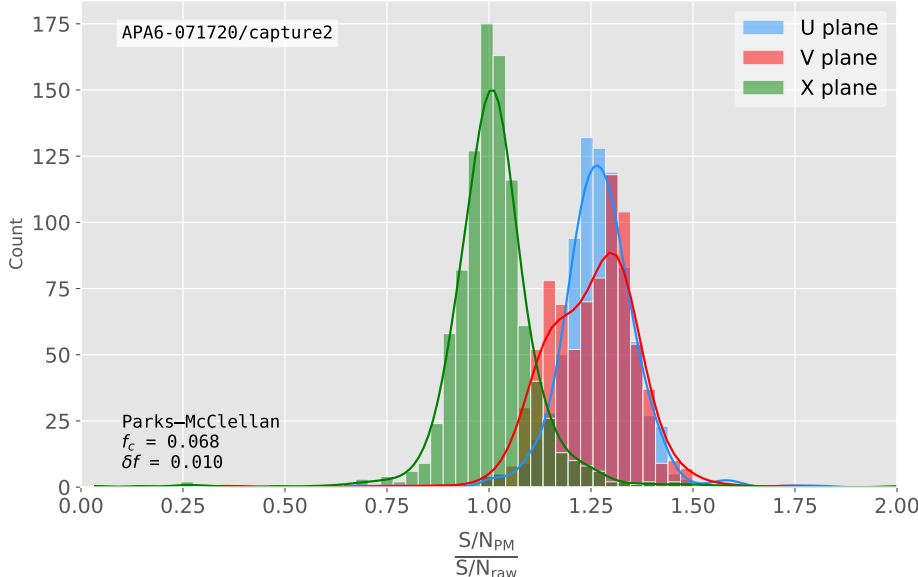


Figure 6.6: Distribution of the relative change of the S/N on the different wire planes from the ProtoDUNE-SP raw data capture *felix-2020-07-17-21:31:44* after the optimal Chebyshev filter was applied. The filter was computed with the Parks-McClellan algorithm using a cutoff of $f_c = 0.068 \text{ ticks}^{-1}$ and a transition width $\delta f = 0.010 \text{ ticks}^{-1}$.

filter is applied. In any case, this is not a big issue as the S/N for collection channels is usually much higher than the one for induction channels.

The results I obtained optimising the low pass filter with the Parks-McClellan method are promising. Nonetheless, the improvement found is rather marginal so I wondered if there could be an alternative approach to the filtering problem which yields better outputs. At this point, I found a possible alternative in matched filters. By construction, this kind of filters offer the best improvement on the S/N.

6.4 Matched filters

In the context of signal processing, a matched filter is the optimal linear filter for maximising the signal-to-noise ratio (S/N) in the presence of additive noise, obtained by convolving a conjugated time-reversed known template with an unknown signal to detect the presence of the template in the signal [83].

Given a known signal sequence $s(t)$ and another (a priori unknown) noise sequence

6.4. Matched filters

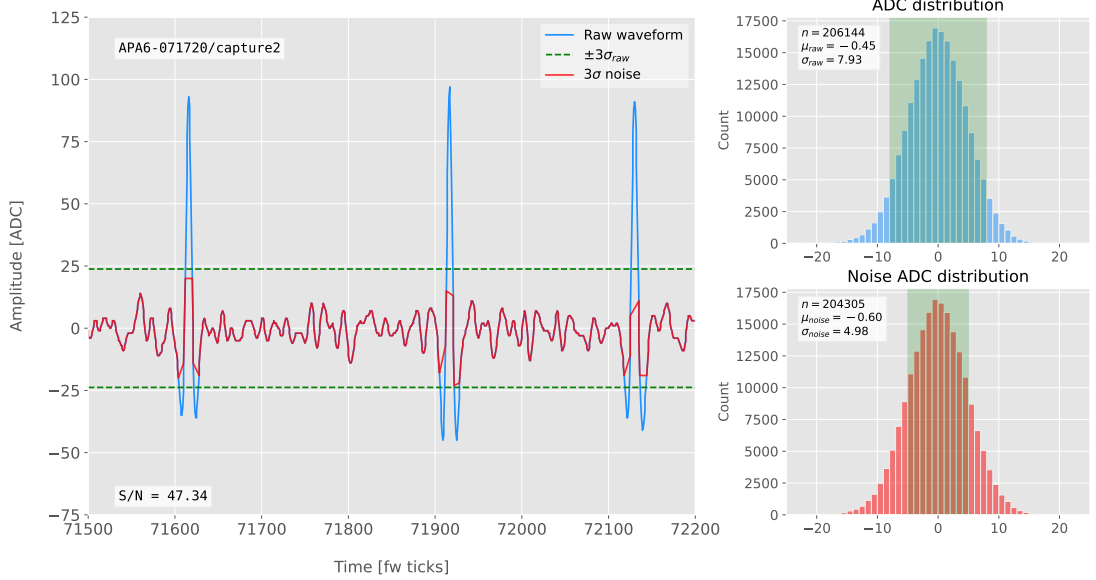


Figure 6.7: Left panel: Zoomed match filtered waveform corresponding to channel 7840 from the ProtoDUNE-SP raw data capture felix-2020-07-17-21:31:44 (blue line). The filter used was directly extracted from the data, being the 32 values around the first peak in the original waveform. The green dashed lines mark the region $\pm 3\sigma_{\text{raw}}$. The resulting noise waveform is also shown (red line). Top right panel: ADC distribution for channel 7840 after match filtering, where the green shaded region represents $\pm \sigma_{\text{raw}}$. Bottom right panel: noise ADC distribution for channel 7840 after match filtering, where the green shaded region represents $\pm \sigma_{\text{noise}}$

1564 $n(t)$, the input signal can be written as:

$$x(t) = s(t) + n(t). \quad (6.4)$$

1565 Now, considering a linear time-invariant filter, whose impulse-response function I
1566 will refer to as $h(t)$, one can write the output signal as:

$$\begin{aligned} y(t) &= x(t) * h(t) \\ &= (s(t) + n(t)) * h(t) \\ &= y_s(t) + y_n(t), \end{aligned} \quad (6.5)$$

1567 where $y_s(t)$ and $y_n(t)$ are simply the outputs of the filter due to the signal and the noise
1568 components respectively.

Chapter 6. Matched Filter approach to induction wire Trigger Primitives

1569 The goal of the matched filter is to detect the presence of the signal $s(t)$ in the input
 1570 sample $x(t)$ at a certain time t_0 , which effectively means we need to maximise the S/N.
 1571 This way, what one wants is to have a filter which gives a much bigger output when the
 1572 known signal is present than when it is not. Putting it in other words, the instantaneous
 1573 power of the signal output $y_s(t)$ should be much larger than the average power of the
 1574 noise output $y_n(t)$ at some time t_0 .

1575 For the case of the filtered signal, one can easily re-write it as an inverse Fourier
 1576 transform:

$$y_s(t) = \frac{1}{2\pi} \int_{-\infty}^{\infty} d\omega H(\omega)S(\omega)e^{i\omega t}, \quad (6.6)$$

1577 where $H(\omega)$ and $S(\omega)$ are the Fourier transforms of the impulse-response function (i.e.
 1578 the transfer function of the filter) and of the input signal, respectively.

1579 Now focusing on the noise, we can use the Wiener-Khinchin theorem [84] to write
 1580 the mean power of the noise after filtering as:

$$E|y_n(t)|^2 = \frac{1}{2\pi} \int_{-\infty}^{\infty} d\omega |H(\omega)|^2 S_n(\omega), \quad (6.7)$$

1581 where $S_n(\omega)$ is the power spectral density of the noise.

1582 Having these, one can write the instantaneous S/N at time t_0 as:

$$\begin{aligned} \left(\frac{S}{N} \right)_{t_0} &= \frac{|y_s|^2}{E|y_n(t)|^2} \\ &= \frac{1}{2\pi} \frac{\left| \int_{-\infty}^{\infty} d\omega H(\omega)S(\omega)e^{i\omega t_0} \right|^2}{\int_{-\infty}^{\infty} d\omega |H(\omega)|^2 S_n(\omega)}. \end{aligned} \quad (6.8)$$

1583 Once we have this expression, we need to find the upper limit of it to determine what
 1584 would be the optimal choice for the transfer function. One can use the Cauchy-Schwarz
 1585 inequality, which in the present case takes the form:

$$\left| \int_{-\infty}^{\infty} dx f(x)g(x) \right|^2 \leq \int_{-\infty}^{\infty} dx |f(x)|^2 + \int_{-\infty}^{\infty} dx |g(x)|^2, \quad (6.9)$$

6.4. Matched filters

for any two analytical functions $f(x)$ and $g(x)$. One can prove that making the choice:

$$\begin{aligned} f(x) &= H(\omega) \sqrt{S_n(\omega)} e^{i\omega t_0}, \\ g(x) &= \frac{S(\omega)}{\sqrt{S_n(\omega)}}, \end{aligned} \quad (6.10)$$

leads to the following upper bound for the S/N:

$$\left(\frac{S}{N} \right)_{t_0} \leq \frac{1}{2\pi} \int_{-\infty}^{\infty} d\omega \frac{|S(\omega)|^2}{S_n(\omega)}. \quad (6.11)$$

From Eqs. (6.8), (6.9) and (6.10) one can also derive the form of the transfer function such that the upper bound is exactly reached [85]:

$$H(\omega) \propto \frac{S^*(\omega) e^{-i\omega t_0}}{S_n(\omega)}. \quad (6.12)$$

From this last expression we can clearly see the way the matched filter acts. As the transfer function is proportional to the Fourier transform of the signal it will try to only pick the frequencies present in the signal [86].

The matched filter transfer function can be greatly simplified if the input noise is Gaussian. In that case, the power spectral density of the noise is a constant, so it can be re-absorbed in the overall normalisation of the transfer function. Moreover, considering that the input signal is a real function, one can simply set $S^*(\omega) = S(-\omega)$, which gives:

$$H(\omega) \propto S(-\omega) e^{-i\omega t_0}. \quad (6.13)$$

For a discrete signal, one can think of the input and impulse-response sequences as vectors of \mathbb{R}^N . Then, the matched filter tries to maximise the inner product of the signal and the filter while minimising the output due to the noise by choosing a filter vector orthogonal to the later. In the case of additive noise, that leads to the impulse-response vector:

$$h = \frac{1}{\sqrt{s^\dagger R_n^{-1} s}} R_n^{-1} s, \quad (6.14)$$

Chapter 6. Matched Filter approach to induction wire Trigger Primitives

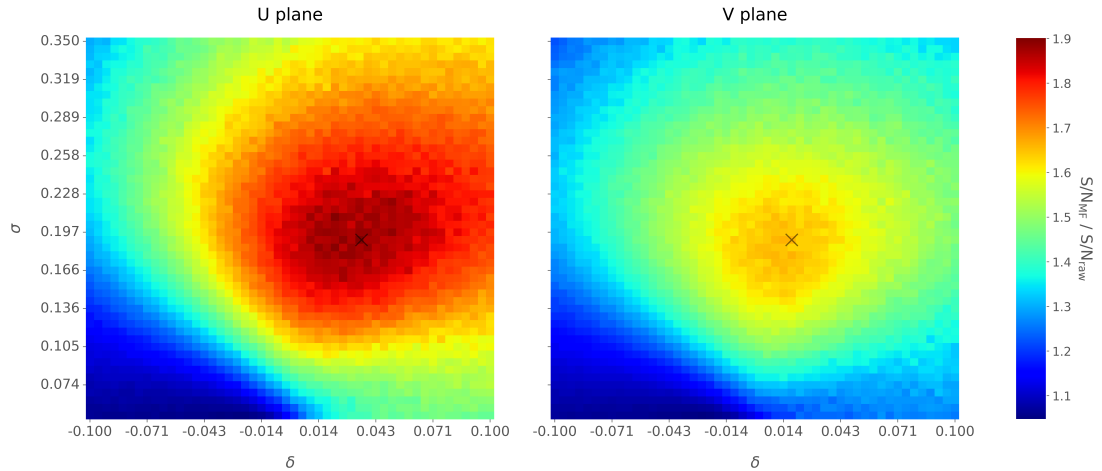


Figure 6.8: Relative improvement in the S/N for the raw data capture `felix-2020-07-17-21:31:44`, using the matched filter following the parametrisation in Eq. (6.17). The black crosses in both panels denote the location of the maximum ratio value.

1602 where s is a reversed signal template sequence of length N equal to the order of the filter
 1603 and R_n is the covariance matrix associated with the noise sequence n . For the Gaussian
 1604 noise case, the covariance matrix is simply the unit matrix, so the above expression
 1605 simplifies again to:

$$h = \frac{s}{|s|}. \quad (6.15)$$

1606 For this first stage of the study, I use a definition of the S/N per channel given by:

$$\text{S/N} = \frac{\max [ADC] - \mu_{noise}}{\sigma_{noise}}, \quad (6.16)$$

1607 where the subscript *noise* refers to a subset of the data obtained by only taking into
 1608 account waveform values within a $\pm 3\sigma$ range around the mean of the data and $\max [ADC]$
 1609 is the maximum of the original waveform. This definition is further discussed in App.
 1610 6.2, where I also show examples of its application to raw data and to a waveform filtered
 1611 with the current low-pass FIR filter.

1612 To test whether this choice of filter is appropriate one needs to choose a signal
 1613 template. As an example of how a matched filter would affect our signal, I simply took
 1614 the filter coefficients to be the 32 ADC values around a signal peak present in the data.

6.4. Matched filters

1615 In Fig. 6.7 (left panel) I plotted a zoomed region for channel 7840 in the raw data capture
1616 `felix-2020-07-17-21:31:44`, after applying the matched filter described before (blue
1617 line). When compared to the raw and FIR filtered case (see App. 6.2), after applying
1618 the match filter the standard deviation of the noise waveform (red line) decreases and at
1619 the same time the signal peaks are enhanced. This leads to an improvement of the S/N
1620 by a factor of 1.92 when compared to the raw waveform.

1621 In order to obtain the matched filter that is more suitable for our data, I explored
1622 different configurations of signal templates. In order to perform this exploration, I
1623 parametrised the signal using the bipolar function:

$$f(x) = -A(x + \delta) e^{-x^2/\sigma^2}, \quad (6.17)$$

1624 where the parameter δ controls the asymmetry between the positive and negative peaks
1625 and σ controls their width. The amplitude parameter A is set such that it keeps the
1626 height of the biggest peak to be less than 200 ADC in absolute value.

1627 As this parametrisation is only adequate for bipolar signals I will focus exclusively
1628 on the induction channels. Also, the optimal configurations I found for the U and V
1629 plane will be kept separate, i.e. I will have two sets of coefficients that will be applied to
1630 either the U and V planes of wires. I do so as I found this was the choice giving the
1631 best performance. Even so, as I will discuss, the differences are not very pronounced. In
1632 case it is not technically possible to separate channels in the firmware according to the
1633 wire plane they come from and use different sets of filter coefficients for them, we can
1634 just find a common unique set of coefficients. In such case, I do not expect our results
1635 to change dramatically.

1636 In Fig. 6.8 I present the results of our parameter scan, for channels in the induction
1637 planes U (left panel) and V (right panel). For each configuration of σ and δ the resulting
1638 matched filter was applied to all channels in the corresponding plane within the data
1639 capture `felix-2020-07-17-21:31:44`, the S/N improvement was computed with respect
1640 to the raw waveforms and then the S/N mean value was kept as a score for such filter.

Chapter 6. Matched Filter approach to induction wire Trigger Primitives

1641 One can see that the improvement obtained for the U plane is in general higher than the
1642 one for the V plane. In any case, I got substantially higher ratios than the ones obtained
1643 for the low-pass FIR filters. For the optimal configurations I attained improvements up
1644 to a factor of 1.85 for the U plane and 1.65 for the V plane.

1645 The sets of optimal matched filter coefficients were obtained for the parameters
1646 $\delta = 0.035$, $\sigma = 0.191$ for the U plane and $\delta = 0.018$, $\sigma = 0.191$ for the V plane. I
1647 show these two sets of coefficients in Fig. 6.9 (left panel). Also in Fig. 6.9 (right
1648 panel) I plot the distribution of the S/N improvement after the optimal match filters
1649 for the U and V were applied to the corresponding channels in the raw data capture
1650 `felix-2020-07-17-21:31:44`. As mentioned before, the mean improvement achieved
1651 for the U plane channels is slightly bigger than the one for the V channels. Note, however,
1652 that the spread of the distribution for the V plane is also smaller than the one for the U
1653 plane.

1654 I also performed a similar scan for the case of a low-pass FIR filter using the Parks-
1655 McClellan algorithm. In that case, the parameters to check were the cutoff frequency
1656 and the transition width of the filter. A summary of the results is given in App. 6.3.

1657 Overall, one can see that the improvements on the S/N are much more significant in
1658 the case of the matched filter than it is for the low-pass FIR filters. The analysis of this
1659 and other raw data captures from ProtoDUNE-SP suggest that matched filters increase
1660 the S/N of induction channels by a factor of 1.5 more than the optimal low-pass FIR
1661 filters.

1662 Although these results are by themselves great points in favour of the matched
1663 filter, more studies are needed to completely assess the robustness of this approach. I
1664 proceeded then to test the matched filter with simulated data samples.

1665 6.5 Using simulated samples

1666 In order to further test the matched filter, the next step was to generate and process
1667 data samples using *LArSoft* [87]. In this way, one can control the particle content of

6.5. Using simulated samples

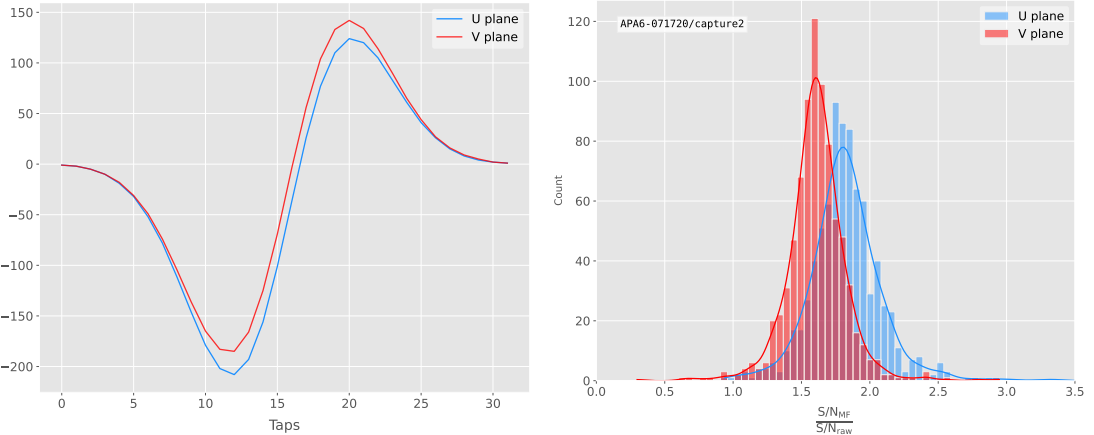


Figure 6.9: Left panel: Optimal matched filter coefficients for the U (blue line) and V (red line) planes. The filters were computed with our parametrisation in Eq. (6.17) for the parameter values $\delta = 0.035$, $\sigma = 0.191$ and $\delta = 0.018$, $\sigma = 0.191$ respectively. Right panel: Distribution of the relative change of the S/N on the two induction wire planes from the ProtoDUNE-SP raw data capture *felix-2020-07-17-21:31:44* after their respective optimal matched filters were applied.

1668 the samples, the orientation of the tracks and their energy, and therefore see how the
1669 matched filter behaves in various situations.

1670 To begin with, I prepared different monoenergetic and isotropic samples containing
1671 a single particle per event. Each sample contains a different particle species, namely
1672 electrons, muons, protons and neutral pions all with a kinetic energy of $E_k = 100$ MeV.
1673 I chose these because of the fairly different topologies they generate in the liquid argon,
1674 ranging from shower-like to track-like. The procedure I followed to generate the samples
1675 and process them is discussed in detail in App. ??.

1676 These were generated with the single particle gun and the Geant4 stage of the
1677 *LArSoft* simulation [87] was performed with the standard configuration for the DUNE
1678 FD 10kt module.

1679 For simplicity, I restricted the particles to start drifting in a single TPC volume
1680 (in this case TPC 0), so I can focus exclusively on the signals coming from one APA.
1681 The chosen kinetic energy for all the particles in my first trial is $E_k = 100$ MeV, so a
1682 necessary check is to see if all our tracks will be typically contained in one TPC volume.
1683 Fig. 6.10 (left panel) shows the distributions of the track lengths in the liquid argon

Chapter 6. Matched Filter approach to induction wire Trigger Primitives

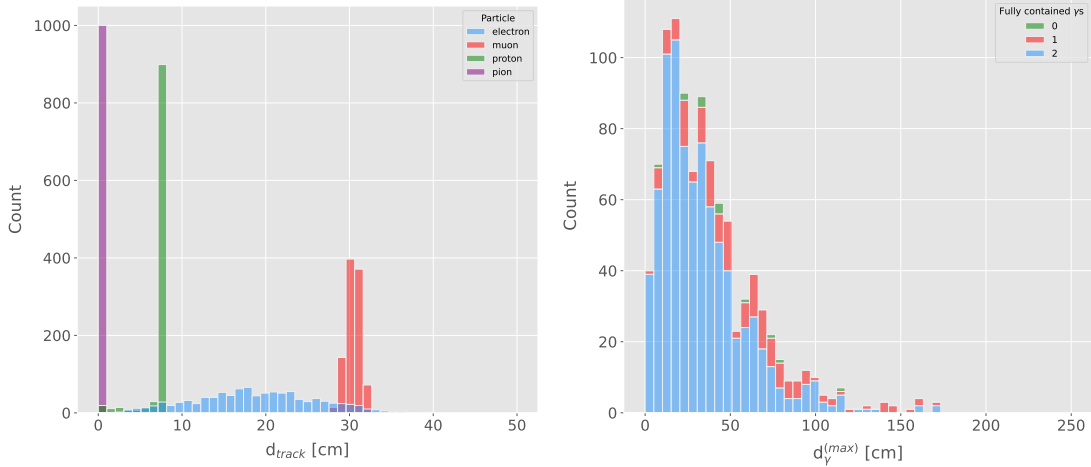


Figure 6.10: Left panel: distributions of the particles track length in the liquid argon for the generated $E_k = 100$ MeV monoenergetic samples, electrons (blue), muons (red), protons (green) and neutral pions (purple). Right panel: distribution of the length of the longest photon in the neutral pion sample after the decay process $\pi^0 \rightarrow \gamma\gamma$.

of all generated particles with $E_k = 100$ MeV. One can see that, in the case of the track-like particles (i.e. muons and protons), their length distributions are quite sharp and centered at relatively low distances (30 and 8 cm, respectively). For electrons, the distribution is quite broad but it does not extend past ~ 30 cm. The case of neutral pions can be misleading, as they decay promptly the track length associated with the true Monte Carlo particle is always < 1 cm. In Fig. 6.10 (right panel) I show the effective length distribution of the longest photon after the pion decays as $\pi^0 \rightarrow \gamma\gamma$, highlighting the number of fully contained photons in the TPC volume per event (either zero, one or both). One can see that the vast majority of events has both photons contained and that just a negligible number of them has none of them contained in the TPC volume. In any case, for the sake of caution, I will only keep the pion events with both photons contained.

Once I have prepared a sample at the Geant4 level, I need to process it through the detector simulation. In order to make adequate estimations of the noise levels and run the filtering and hit finder as I did with the ProtoDUNE data, one needs to turn off the default zero-suppression of the waveforms produced by the simulation. At this first stage I am only concerned with the waveforms with the noise added, so I keep the noise

6.5. Using simulated samples

addition option as true in the configuration. However, for studies related to the hit finder performance one will also need to store the noiseless waveforms in order to retrieve the truth information of the hits. I will discuss this approach next.

After the detector simulation stage, one needs to extract the no zero-suppressed noisy waveforms, along with their offline channel numbers, and store them in a certain format to be analysed later. To reduce the amount of data that will go for processing, I used the information from the Geant4 step of the simulation to select only the active channels, i.e. the channels where some ionisation electrons arrive. Moreover, as said previously, I only extract the waveforms from APA 0 and exclusively the ones coming from induction channels. The resulting ROOT file contains a tree with two branches, one containing the waveforms for each event and channel and the other with the corresponding offline channel numbers.

Finally, to extract the truth values for the orientation of the tracks and the energies of the particles I used a modified analysis module. This gives a ROOT file with a single tree, containing several branches with different information such as the components of the initial momentum of the particles, initial and final xyz location, track length, etc.

For the analysis of the resulting waveforms and truth values I used a custom set of Python libraries (available at [??]). Among other functionalities, these enable the user to read the ROOT files, export the raw data as pandas objects, apply the filters and compute the S/N of both the raw and filtered signals. So far, the default configuration for the filtering uses the set of optimal matched filter coefficients that I found using the ProtoDUNE data samples.

Additionally, for the analysis of the samples it was necessary to use two different reference frames, to study separately the signals coming from the U and V induction wire planes. As I am focussing on a single APA, the U and V wires have a different orientation in the yz plane. In the case of U wires, these are tilted 35.7° clockwise from the vertical (y direction), whereas the V wires are at the same angle but in the counter clockwise direction. Because of this, the best option is to deal with two new coordinate systems rotated by $\pm 35.7^\circ$ along the x axis, so the new y' and y'' directions are aligned with the

Chapter 6. Matched Filter approach to induction wire Trigger Primitives

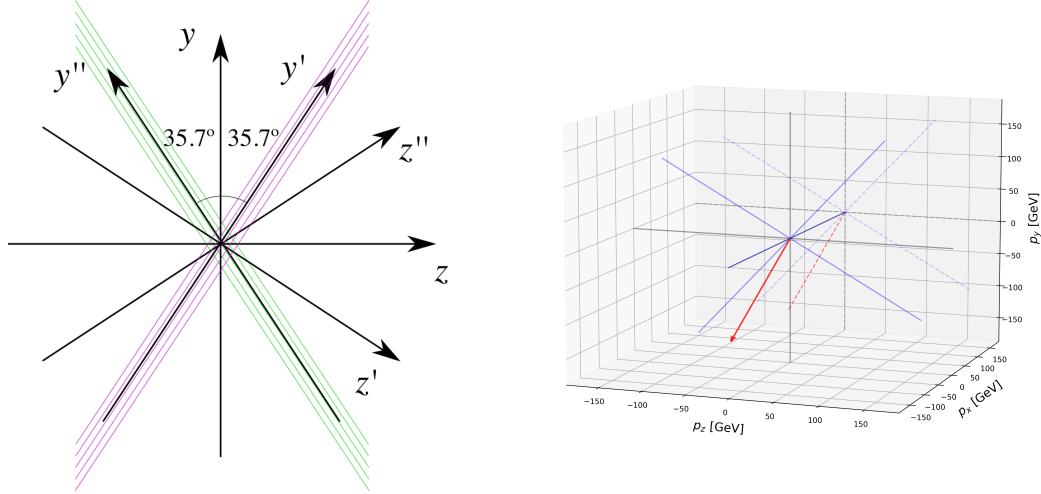


Figure 6.11: Left panel: schematic representation of the two new rotated reference frames used in this analysis (denoted as prime and double prime), viewed from the yz plane. The magenta stack of lines represent the wires in the U plane, whereas the green lines correspond to the wires in the V plane. Right panel: 3D representation of the momentum of one of the generated monoenergetic muons (red arrow) in the original reference frame (black lines), along with the new reference frame used for the U plane waveforms (blue lines). In the yz plane I added the projection of these three.

1730 U and V induction wires. Fig. 6.11 (left panel) shows a schematic representation of
 1731 the original reference frame together with the two rotated ones (denoted by primed and
 1732 double primed). This way, one can easily understand how parallel was a track to the
 1733 wires in the two induction planes. Fig. 6.11 (right panel) shows a 3D representation of
 1734 the momentum of a track (red arrow) in the original reference frame (black lines), along
 1735 with the new reference frame for U wires (blue lines). I added the projection in the yz
 1736 plane of this three, to show the usefulness of the new reference frame to tell whether a
 1737 track is parallel or normal to the wires in the induction plane.

1738 Fig. 6.12 shows the distribution of the average S/N improvement per event when one
 1739 applies the optimal matched filters. I produced separate distributions for the channels
 1740 in the U (red) and V (blue) induction wire planes. Notice that the S/N distributions
 1741 for the track-like particles, i.e. muons (top left panel) and protons (bottom left panel),
 1742 have significantly larger mean values than the distributions of the shower like particles,
 1743 i.e. electrons (top right panel) and neutral pions (bottom right panel). An important

6.5. Using simulated samples

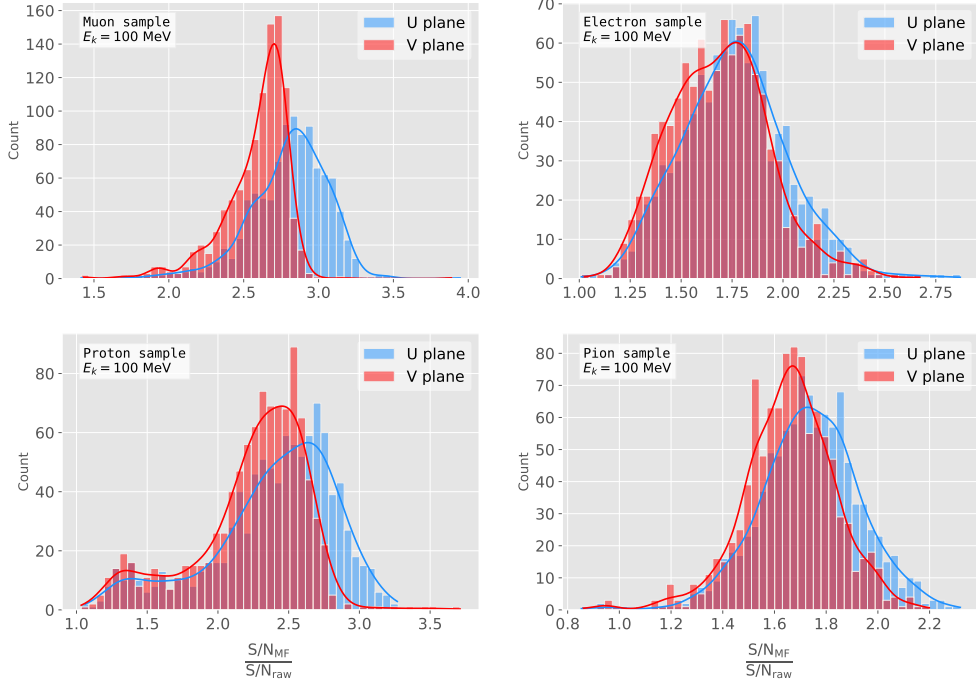


Figure 6.12: Distributions of the mean S/N improvement per event for the corresponding sample after applying the matched filters. Here I separated the change in the U plane (blue) and the V plane (red) channels. From top left to the right: muon, electron, proton and neutral pion. All the events have a fixed kinetic energy of $E_k = 100 \text{ MeV}$.

1744 difference between these results and the ones seen before for ProtoDUNE data is that,
 1745 overall, the improvements that I get for simulated data are bigger. This could be due
 1746 either to the default noise model used in the *LArSoft* simulation or to the simulated hits
 1747 having higher energy than the ones in the recorded data. Nonetheless, the concluding
 1748 message is that the previously optimised matched filters give an overall significant
 1749 improvement of the S/N for the different samples.

1750 About the convention I followed for the plots and results, in the case of the raw and
 1751 filtered S/N of each event in the sample I simply took the average of the quantities over
 1752 all the active channels in the event. That is, if a certain event has N_{chan} active channels
 1753 these two quantities are computed as:

$$(S/N_{fir})_{event} = \frac{\sum_{i=0}^{N_{chan}} (S/N_{fir})_i}{N_{chan}}, \quad (6.18)$$

$$(S/N_{raw})_{event} = \frac{\sum_{i=0}^{N_{chan}} (S/N_{raw})_i}{N_{chan}}.$$

Chapter 6. Matched Filter approach to induction wire Trigger Primitives

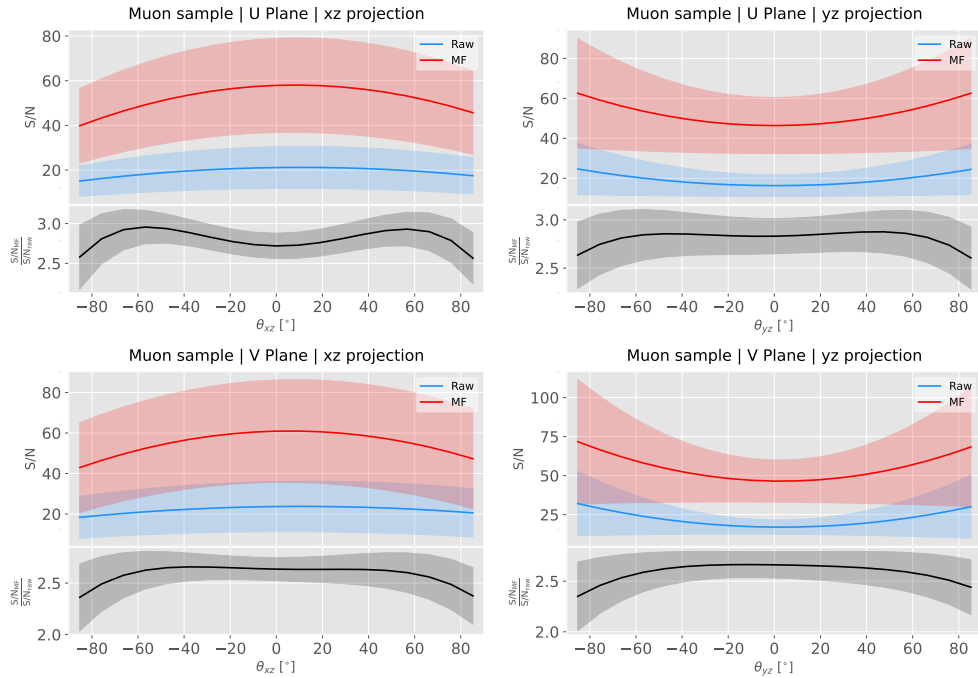


Figure 6.13: Angular dependence of the mean S/N and the S/N improvement, for the different monoenergetic samples considered (from top to bottom: electrons, muons, protons and neutral pions). The two columns on the left represent the values for the U plane waveforms. The top subplots show the mean S/N for raw (green) and filtered (red) waveforms whereas the bottom subplots depict the averaged S/N improvement (black).

1754 However, for the ratio of the raw and filtered S/N (what I called the S/N improvement)
 1755 per event I am not just taking the ratio of the previous two quantities but computing
 1756 the average of the individual ratios per channel in the event:

$$\left(\frac{S/N_{fir}}{S/N_{raw}} \right)_{event} = \frac{\sum_{i=0}^{N_{chan}} \left(\frac{S/N_{fir}}{S/N_{raw}} \right)_i}{N_{chan}}, \quad (6.19)$$

1757 and so:

$$\left(\frac{S/N_{fir}}{S/N_{raw}} \right)_{event} \neq \frac{(S/N_{fir})_{event}}{(S/N_{raw})_{event}}. \quad (6.20)$$

1758 6.5.1 Angular dependence

1759 Having these monoenergetic samples, one can also study the angular dependence of the
 1760 performance of the matched filter. This is an important point, as it is a well established
 1761 fact that for certain configurations (an extreme case configuration being signals normal

6.5. Using simulated samples

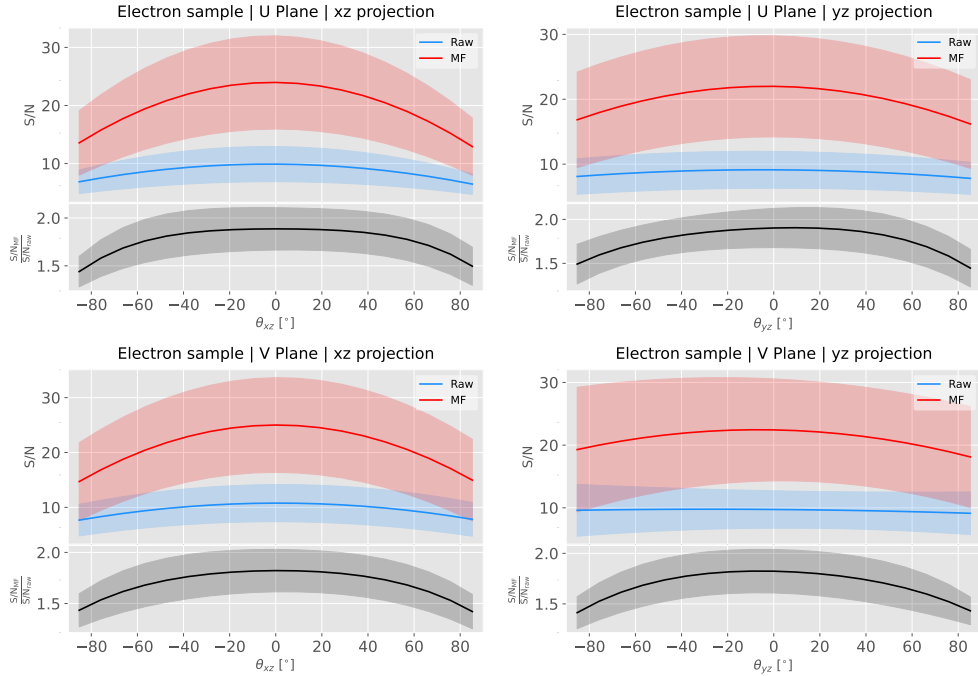


Figure 6.14: Angular dependence of the mean S/N and the S/N improvement, for the different monoenergetic samples considered (from top to bottom: electrons, muons, protons and neutral pions). The two columns on the left represent the values for the U plane waveforms. The top subplots show the mean S/N for raw (green) and filtered (red) waveforms whereas the bottom subplots depict the averaged S/N improvement (black).

1762 to the wire plane and perpendicular to the induction wires at the same time) the S/N is
 1763 much lower than average as the corresponding waveforms are severely distorted. In this
 1764 sense, I am interested to see how the matched filter behaves for these cases and how the
 1765 S/N improvement on those compare to the average.

1766 Fig. 6.13 shows the angular dependence of the S/N for the monoenergetic $E_k =$
 1767 100 MeV isotropic muons, for the different induction wire planes and projections. The
 1768 angles for each event are given by the components of the initial value of the momentum
 1769 of the particles, taking the angles of the projections on the xz and yz planes with respect
 1770 to the z axis (more accurately, one needs to compute these angles twice for each event, a
 1771 pair for the $xy'z'$ coordinate system and the other for the $xy''z''$). The top row shows the
 1772 dependence on the angles corresponding to the U plane, i.e. $\theta_{xz'}$ and $\theta_{y'z'}$, whereas the
 1773 bottom row shows the angular dependence viewed from the V plane, $\theta_{xz''}$ and $\theta_{y''z''}$. In
 1774 each plot, the top subplot represents the mean values of the S/N for the raw (blue) and

Chapter 6. Matched Filter approach to induction wire Trigger Primitives

1775 matched filtered (red) signals, and the bottom subplot the averaged S/N improvement
1776 (black). The solid lines represent the mean value obtained for the corresponding angular
1777 value, whereas the semitransparent bands represent one standard deviation around the
1778 mean at each point.

1779 As expected, the S/N is in general higher when tracks are parallel to the APA (i.e.
1780 $\theta_{xz} \sim 0$) and lower when it is normal to the plane ($\theta_{xz} \sim \pm 90^\circ$). In the same way, tracks
1781 parallel to the wires ($\theta_{yz} \sim \pm 90^\circ$) tend to have higher S/N than those perpendicular to
1782 these ($\theta_{yz} \sim \pm 0$).

1783 Fig. 6.14 shows the corresponding angular dependence information for the $E_k =$
1784 100 MeV electrons sample. Notice that, in this case, the S/N behaviour discussed above
1785 does not hold. A possible explanation can be that, because most hits in these events
1786 are produced by the secondary particles generated in the EM shower, the signal peaks
1787 whose S/N ratios were computed do not correspond to the directional information of
1788 the primary electron.

1789 6.5.2 Distortion and peak asymmetry

1790 As a little case of study, I selected two of the simulated $E_k = 100$ MeV monoenergetic
1791 muon events. With respect to the U induction plane, one is parallel to the APA (low
1792 $\theta_{xz'}$) and to the wires (high $\theta_{y'z'}$) and the other is normal to the APA plane (high $\theta_{xz'}$)
1793 and perpendicular to the wires (low $\theta_{y'z'}$). As expected from the results on the angular
1794 dependence discussed above, the former has a higher S/N (before and after the filtering)
1795 when compared to the latter. An interesting thing to notice about these two samples
1796 is that, even though one has a much bigger S/N than the other, it is the one with the
1797 smallest S/N the one that got the biggest averaged S/N improvement. In Table 6.1
1798 I included all the relevant parameters of these two $E_k = 100$ MeV muon events I am
1799 considering, namely, the angles with respect to the $xy'z'$ reference frame, the values of
1800 the S/N, the S/N improvement and also the so-called peak asymmetry Δ_{peak} that I will
1801 discuss next.

1802 One can try to understand better what is going on with these two events by looking

6.5. Using simulated samples

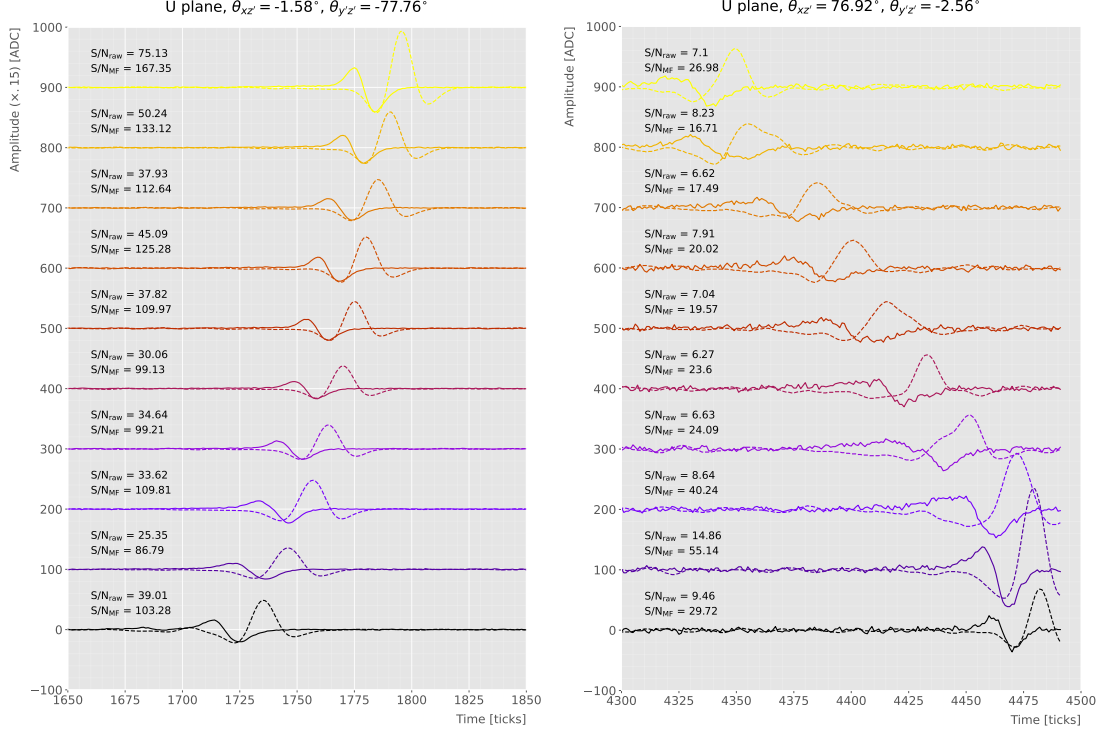


Figure 6.15: Selected consecutive waveforms corresponding to two monoenergetic $E_k = 100$ MeV muon events, one is parallel to the APA and to the wires in the U plane (left panel) and the other is normal to the APA plane and perpendicular to the U plane wires (right panel). The solid lines represent the raw waveforms whereas the dashed lines correspond to the waveforms after the matched filter was applied. The waveforms on the left panel have been scaled by a factor of 0.15 to have similar amplitude to the ones on the right panel.

Table 6.1: Characteristic parameters of the two monoenergetic muon events selected, relative to the U plane: projected angles in the xz' and yz' planes, S/N values for the raw and filtered waveforms, mean improvement of the S/N and peak asymmetry.

	$\theta_{xz'} (\circ)$	$\theta_{yz'} (\circ)$	S/N_{raw}	S/N_{MF}	$\frac{S/N_{\text{MF}}}{S/N_{\text{raw}}}$	$\Delta_{\text{peak}} (\text{ADC})$
High ("parallel")	-1.58	-77.76	41.65	112.44	2.83	-35.73
Low ("normal")	76.92	-2.56	8.07	25.46	3.12	-10.38

at the raw and filtered data from some of their active channels. Fig. 6.15 shows a selection of consecutive raw and filtered U plane waveforms from the event with high S/N (left panel) and the one with low S/N (right panel). Notice that to show both collections of waveforms at a similar scale I had to apply a factor of 0.15 to the waveforms with high S/N. Additionally, next to each waveform I included the values of the raw and matched filtered S/N for the corresponding channel. The first thing to notice in this plot

Chapter 6. Matched Filter approach to induction wire Trigger Primitives

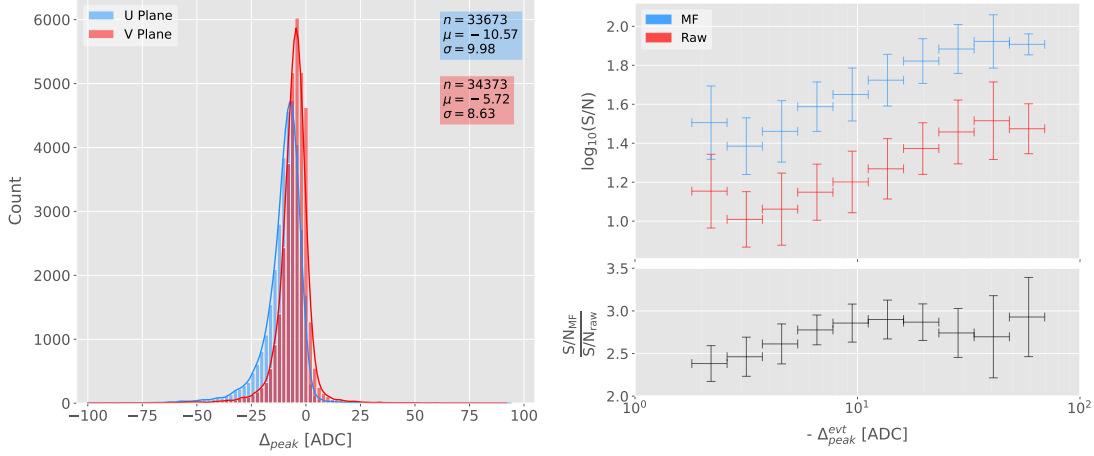


Figure 6.16: Left panel: peak asymmetry distribution for the case of the monoenergetic $E_k = 100$ MeV muon sample. Each value corresponds to a single bipolar signal peak from a channel in any event. The blue distribution represents the peaks on U plane channels, whereas the red corresponds to signal peaks in V wires. Right panel: relation between the mean peak asymmetry per event with the S/N for U channel waveforms from the $E_k = 100$ MeV muon sample. The top subplot shows the decimal logarithm of the mean S/N for the raw (red) and the matched filtered (blue) waveforms. The bottom subplot contains the mean S/N improvement ratio after the matched filter was applied.

is that the amplitude of the signal peaks from the normal track have a much smaller
 amplitude, and also appear quite distorted when compared to the others. On the other
 hand, although the matched filtered S/N is still smaller, the relative improvement is
 bigger than in the parallel case.

A way I found to quantify the difference between the shapes within these two events
 is their different peak asymmetry. One can define the peak asymmetry as the (signed)
 difference between the positive and the negative peaks of the bipolar shape, i.e.:

$$\Delta_{peak} \equiv h_+ - h_-, \quad (6.21)$$

where both heights h_+ and h_- are positive defined. Fig. 6.16 (left panel) shows the distribution of this peak asymmetry for all the waveforms corresponding to channels in the U (blue) and V (red) planes for the monoenergetic muon sample. One can see that these distributions are clearly shifted to negative values (with mean values $\mu_\Delta^U = -10.57$ ADC and $\mu_\Delta^V = -5.72$ ADC respectively). It is interesting to notice

6.5. Using simulated samples

that the peak asymmetry value of the sample with high S/N sits at the left tail of the distribution whereas the corresponding value of the sample with low S/N lies around the mean.

Now, one can try to correlate the peak asymmetry with the S/N and the S/N change per event. Fig. 6.16 (right panel) shows the result of comparing (minus) the mean peak asymmetry per event to the averaged raw (red) and matched filtered (blue) S/N per event (top subplot). The horizontal lines sit at the mean value obtained in the fit and represent the width of the $-\Delta_{peak}$ bins used, while the vertical lines indicate one standard deviation around that mean value. Notice that, when taking decimal logarithm on both, there is an approximate linear relation between these quantities, except for peak asymmetry values bigger than -5 ADC where the S/N remains constant.

Also, in the bottom subplot of Fig. 6.16 (right panel) I show the relation between the peak asymmetry and the mean S/N improvement. In this case, one see that there is a maximum at $\Delta_{peak} \sim -10$ ADC. As mentioned previously, this is also the value of the mean of the peak asymmetry distribution. In fact, it is expected that our filter favours the signal peaks with the most common values of the peak asymmetry, as this was one of the features I target in our filter coefficient optimisation through the parameter δ .

These results suggest that events with poorer values of the mean S/N, usually associated to non-favourable track orientations, tend to have smaller values of the mean peak asymmetry (in absolute value). Nonetheless, because our matched filters have been optimised to account for these asymmetries, the improvement on the S/N for these events is sizeable if not better than the one for events which already had a high S/N.

6.5.3 Hit sensitivity

One of the advantages of the matched filter, directly related to increasing the S/N, is the capability of picking hits that before fell below the threshold. For instance, Fig. 6.17 shows the raw ADC data from an example event (electron, $E_k = 100$ MeV) with the produced true hits superimposed (black boxes), together with the hits produced by the standard hit finder chain (blue circles), i.e. using the current FIR filter, and the hits

Chapter 6. Matched Filter approach to induction wire Trigger Primitives

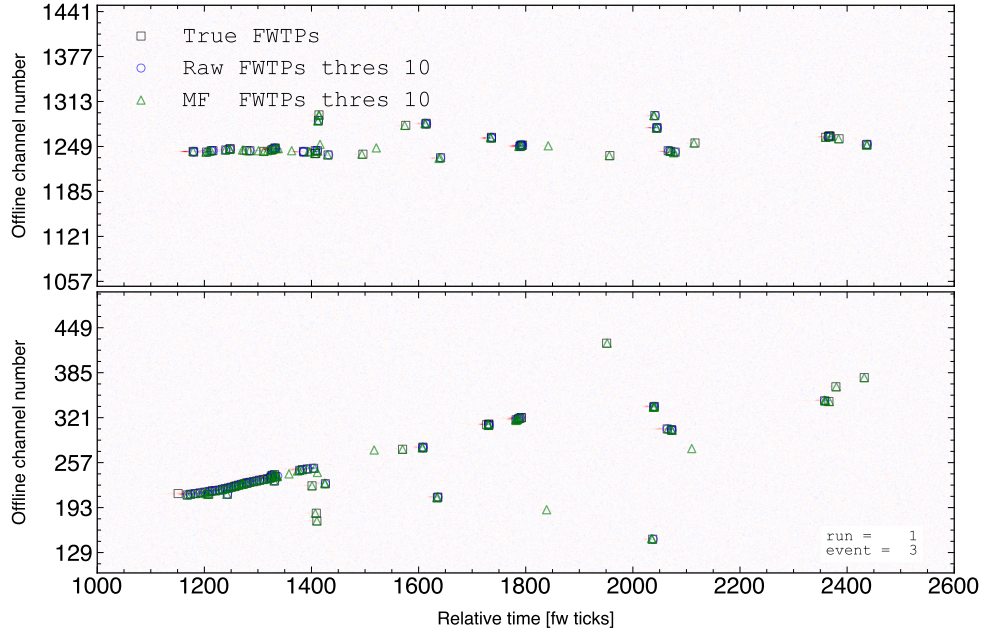


Figure 6.17: Raw data display in the plane time (in firmware ticks) vs. offline channel number for an $E_k = 100$ MeV electron event. The produced true hits are superimposed (black boxes) as well as the hits coming from the standard hit finder chain (blue circles) and the hit finder using the matched filter (green triangles).

1849 obtained using the matched filters (green triangles). Both the standard and the matched
 1850 filter hit finders were run with a threshold of 10 ADC. Notice that the standard hits
 1851 match well the true ones at the initial part of the event (where we have a track-like
 1852 object), but they miss most of the hits produced by the EM shower at later times. On
 1853 the other hand, the hits produced with the matched filter have a better agreement with
 1854 the true hits even for the more diffuse shower activity.

1855 Notwithstanding that now I get more hits with this combination of matched filter
 1856 and low threshold as a results of the enhancement of the signal peaks relative to the
 1857 noise level, it is also true that I pick some spurious hits not related to any real activity
 1858 if one lowers the thresholds too much. Therefore, some optimisation of the threshold is
 1859 needed. Basically one will need to make a trade-off between precision and sensitivity.

1860 Having this in mind, I tried to compare the produced hits one gets from the standard
 1861 hit finder and the ones resulting from applying the matched filter with the true hits.
 1862 By running the hit finders on our samples with different values of the threshold one

6.5. Using simulated samples

1863 can understand, for instance, how low one can set the threshold without getting mostly
1864 spurious hits and then evaluate the gains obtained from this.

1865 Because now I am also interested in seeing how the hit sensitivity changes with the
1866 energy, I prepared new isotropic samples with the same types of particles as before
1867 (muons, electrons, protons and neutral pions) but with a flat kinetic energy distribution
1868 ranging from 5 to 100 MeV.

1869 In order to estimate the hit sensitivity, given a certain sample, one needs to recover
1870 the set of true hits to be able to compare these with the ones produced. To do so,
1871 a modification in the procedure I was using to extract the raw waveforms is needed.
1872 For this kind of study I run the detector simulation in two steps, first I produce the
1873 waveforms without noise and extract them in the same format I used for the raw data,
1874 then the noise is added and the noisy waveforms are then written to a file as well.

1875 To have a better comparison between the true hits and the ones produced from
1876 the raw waveforms after applying the two filters, I applied also the FIR filter and the
1877 matched filters to the noiseless waveforms and then I run the hit finder with a minimal
1878 threshold (in this case I used 1 ADC) on these noiseless filtered waveforms. In this way
1879 I generated two sets of true hits, I will refer to them as standard true hits (with the
1880 current/default FIR filter) and matched filter true hits respectively. This allows a more
1881 precise matching between the different groups of hits produced, as it will account for
1882 any delays and distortions introduced by the FIR and the matched filters.

1883 In the case of the raw waveforms (with noise), I run the hit finder on them, with
1884 different values of the threshold, after applying either the FIR or the matched filters. I
1885 will name them simply standard hits and matched filter hits respectively. Then, I match
1886 the generated hits to the true hits (the standard hits with the standard true hits and
1887 the matched filter hits with the matched filter true hits). The matching is performed by
1888 comparing the channel number and the timestamp of the hits. To count as a match,
1889 I require that all hits with the same channel number and timestamp have overlapping
1890 hit windows, i.e. the time windows between their hit end and hit start times need to
1891 overlap. If more than one hit in one of the groups have hit overlap with the same hit in

Chapter 6. Matched Filter approach to induction wire Trigger Primitives

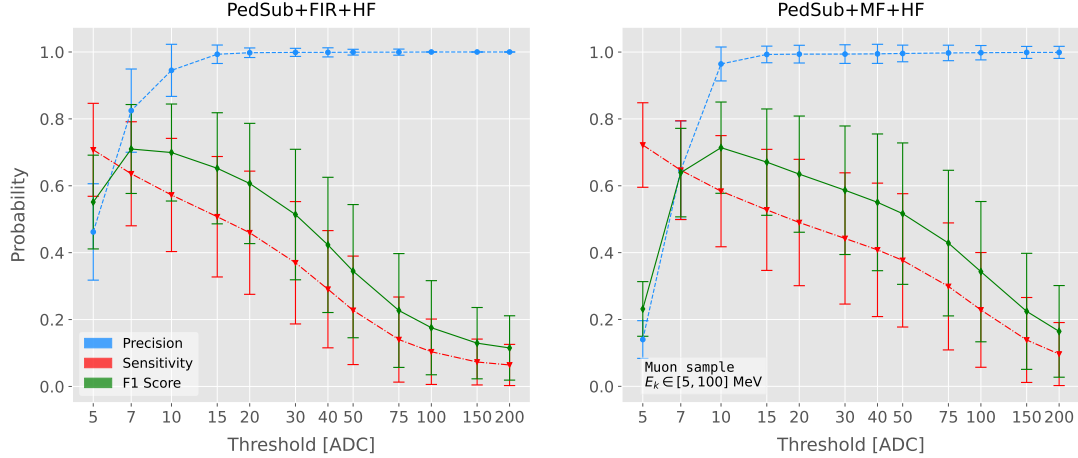


Figure 6.18: Dependence of the precision (blue), sensitivity (red) and F_1 (green) scores on the threshold values used in the hit finder, for the FIR (left panel) and matched filter (right panel) cases. The results were obtained after matching the hits to the true hits in the case of the isotropic muon sample with kinetic energy in the range 5 to 100 MeV, taking only into account the induction plane channels. The points represent the mean value while the error bars indicate one standard deviation around that mean value.

1892 the other group I only count the hit with closer hit peak time value.

1893 The generation of the samples, the procedure to produce the standard hits (with the
1894 default FIR filter) and matched filter hits and the matching of these with the true hits
1895 is described in detail in App. ??.

1896 To quantify the performance of the two hit finder approaches, I use a classical method
1897 from statistical classification known as confusion matrix [88]. This is basically a way of
1898 sorting the outputs of a binary classifier, considering the true values of the classification
1899 and the predicted values. It divides the outputs in four categories: true positive (TP,
1900 both true and predicted values are 1), false negative (FN, true value is 1 but predicted
1901 is 0), false positive (FP, true value is 0 but predicted is 1) and true negative (TN, both
1902 true and predicted values are 0)).

1903 The contents of the confusion matrix allow us to compute other derived scores to
1904 judge the performance of our classifiers. In this study, I will make use of three of these
1905 metrics, namely the precision or positive predictive value:

$$\text{PPV} = \frac{\text{TP}}{\text{TP} + \text{FP}}, \quad (6.22)$$

6.5. Using simulated samples

1906 the sensitivity or true positive rate:

$$\text{TPR} = \frac{\text{TP}}{\text{TP} + \text{FN}}, \quad (6.23)$$

1907 and the F_1 score [89]:

$$F_1 = \frac{2\text{TP}}{2\text{TP} + \text{FP} + \text{FN}}, \quad (6.24)$$

1908 which is the harmonic mean of the precision and the sensitivity.

1909 In our specific case I am not going to make use of the true negative value, as its
 1910 definition in this context can be ambiguous because one does not have clear instances in
 1911 the classification process. This way, I will only count the number of true positives as the
 1912 total amount of hits I can match between true and raw populations, the number of false
 1913 negatives will be the number of missing true hits and the false positive the number of
 1914 hits which do not match any true hit.

1915 In Fig. 6.18 I show the precision (blue), sensitivity (red) and F_1 (green) scores I
 1916 obtained for different values of the threshold used in the hit finder for the case of the
 1917 muon sample. Because the matched filters are only applied to induction channels, I only
 1918 consider here hits coming from the U and V planes. The panel on the left corresponds
 1919 to the scores I got when I ran the hit finder on the FIR filtered waveforms, whereas the
 1920 right panel contains the scores for the matched filter case. The points are centered at
 1921 the threshold value used and represent the mean value obtained for each score using all
 1922 the generated events, while the error bars indicate one standard deviation around the
 1923 mean value.

1924 One can see that the precision for the matched filter case is lower when the thresholds
 1925 are very low, as the noise baseline is slightly amplified, but then rises to high values
 1926 quicker than for the FIR case. The other difference one can spot is that the sensitivity
 1927 in the FIR case starts dropping faster at around the same threshold values where the
 1928 precision stabilizes around 1, while in contrast for the matched filter this rapid decrease
 1929 starts at higher threshold values. A similar scan for the same thresholds was performed
 1930 for the electron sample in the same energy range, yielding similar results.

Chapter 6. Matched Filter approach to induction wire Trigger Primitives

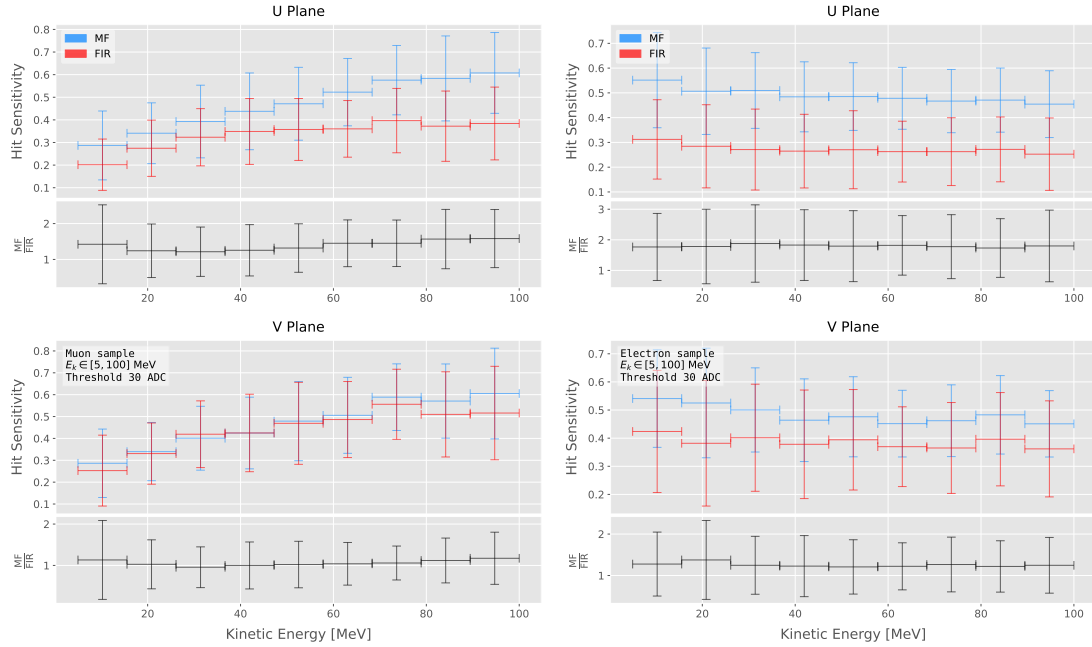


Figure 6.19: Dependence of the averaged hit sensitivity on the kinetic energy of the events for the matched filter (blue) and standard (red) hits, for the case of the muon (left panel) and electron (right panel) samples, separated between U (top plots) and V (bottom plots) induction wire planes. The top subplots contain the hit sensitivities for the two hit finder alternatives, while the bottom subplots show the ratio between the two. The horizontal lines sit at the mean value and represent the size of the energy bins, while the vertical error bars indicate one standard deviation around that mean value.

1931 In Fig. 6.19 I show the averaged hit sensitivity versus the kinetic energy of the
 1932 events, both for the matched filter hits (blue) and the standard hits (red). The left
 1933 panel corresponds to the muon sample, whereas the one on the right corresponds to the
 1934 electron sample, both with kinetic energies between 5 and 100 MeV. In each panel the
 1935 top plot corresponds to hits in the U plane, while the bottom plot contains the same
 1936 information for the V plane. Each plot contains two subplots, the one on the top shows
 1937 the hit sensitivity values for the matched filter and standard hits separate, while the
 1938 bottom subplot depicts the ratio between the matched filter and standard sensitivities.
 1939 The horizontal lines are placed at the mean value obtained in the fit and represent the
 1940 width of the E_k bins used, while the vertical error bars indicate one standard deviation
 1941 around that mean value. In both cases the threshold used was 30 ADC, as I required
 1942 the precision to be higher than 0.99 for both matched filter and standard cases.

6.5. Using simulated samples

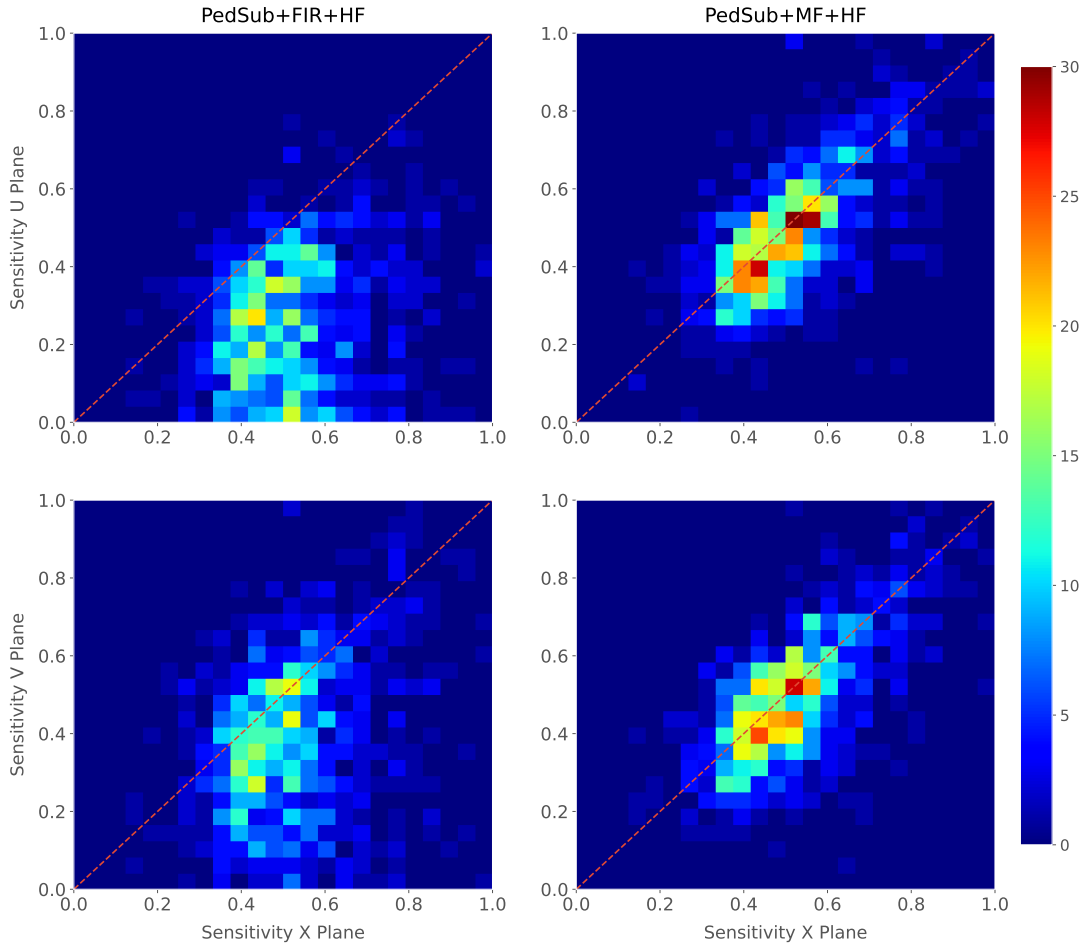


Figure 6.20: Distributions of the hit sensitivity in the U (top panels) and V (bottom panels) planes versus the hit sensitivity in the X plane, both for the standard hits (left panels) and the matched filter hits (right panels), in the case of the electron sample and a threshold of 30 ADC.

1943 One can see that, in general, the improvements are better for the U than for the V
 1944 plane. While for the U channels I achieved a mean improvement of 50% and 80% for
 1945 muons and electrons respectively, the improvement in the V plane is stalled at 10% and
 1946 25%. Nevertheless, if I look at the sensitivities for the matched filter hits in both planes
 1947 one can see these have similar mean values for each energy bin, while on the contrary
 1948 for the standard hits the sensitivity remains relatively high for the V plane. This way, it
 1949 looks there was a less significant gain because the hit sensitivity was already high.

1950 Another interesting observation is the different behaviors for muons and electrons.
 1951 While hit sensitivity for muons grows significantly with energy, in the case of electrons

Chapter 6. Matched Filter approach to induction wire Trigger Primitives

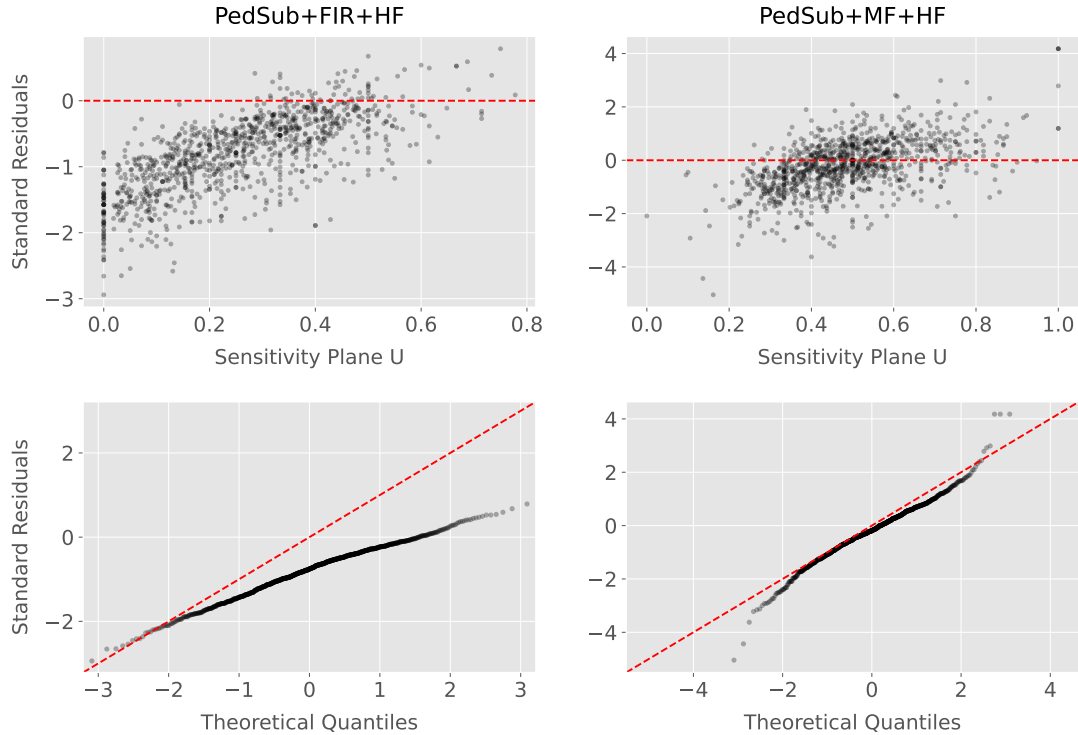


Figure 6.21: Top panels: standard residual plots of the hit sensitivities between the X and U planes. Bottom panels: quantile-quantile plots of the hit sensitivity standard residuals between the X and U planes. In all cases, the left panel corresponds to the standard hits while the right panel represents the matched filter case, all from the electron sample with a 30 ADC threshold.

1952 this slightly decreases the higher the kinetic energy of the event is. In any case, when it
 1953 comes to the improvement on the sensitivities, this remains almost constant in all cases.

1954 Furthermore, we can look at how the concurrence of hits between the different wire
 1955 planes has changed. For any given event, I expect to have a similar number of hits in the
 1956 three planes. As the ionisation electrons need to cross the U and V planes prior to reach
 1957 the collection plane X they will induce current in those wire planes. A way to check the
 1958 concurrence of hits across planes is looking at the relation between the hit sensitivities
 1959 for each individual event. One cannot expect the sensitivities to be exactly equal across
 1960 planes, but ideally they should be normally distributed around the diagonal.

1961 Fig. 6.20 shows the hit sensitivity in the U (top panels) and V (bottom panels)
 1962 planes versus the hit sensitivity in the X plane, for the case of the standard hits (left
 1963 panels) and the matched filter hits (right panels). All plots were generated for the

6.5. Using simulated samples

1964 electron sample and a threshold of 30 ADC. From these one can see a clear trend,
1965 when I use the standard hit finder chain the sensitivities in the induction planes are
1966 systematically lower than the hit sensitivity in the X plane, i.e. most of the points sit
1967 below the diagonal (red dashed line). In contrast, when the matched filters are applied,
1968 the majority of the events are distributed around the diagonal. This points out that the
1969 concurrence of hits across planes has improved.

1970 To exemplify the improvement I obtained, one can consider the residuals of the hit
1971 sensitivities for the X and U planes. Assuming the diagonal hypothesis, i.e. given a
1972 dataset of the form (x, y) for any x I take the predicted y value to be equal to the value
1973 of x , I can compute the standard residuals for the hit sensitivities in U given the ones for
1974 X. In Fig. 6.21 (top panels) I show these standard residuals against the corresponding
1975 values of the hit sensitivity in the U plane, for our electron sample with kinetic energy
1976 between 5 and 100 MeV. If I compare the scatter points in the case of the standard
1977 hits (left panel) and the matched filter hits (right panel), I see that the residuals of the
1978 standard hit finder case follow a certain pattern and their mean deviates from 0.

1979 To see clearly if the residuals are normally distributed, in Fig. 6.21 (bottom panels)
1980 I plot the corresponding quantile-quantile plot for both the standard (left panel) and
1981 matched filter (right panel) standard residuals. One can clearly see that the points for
1982 the standard case follow a strongly non-linear pattern, suggesting that the residuals
1983 do not follow a normal distribution. In contrast, for the matched filter hits the points
1984 conform to a roughly linear path, implying that in this case the normality condition is
1985 fulfilled.

1986 All these results hint at the fact that the concurrence of hits across the wire planes
1987 can be strengthened by applying the matched filters.

1988 **Chapter 7**

1989 **DM searches with neutrinos from
1990 the Sun**

1991 **7.1 Motivation**

1992 The idea of detecting neutrino signals coming from the Sun’s core to probe DM is not new.
1993 The main focus of these searches has usually been high-energy neutrinos originated from
1994 DM annihilations into heavy particles [90–93], although recent studies have proposed to
1995 look at the low-energy neutrino flux arising from the decay of light mesons at rest in the
1996 Sun [94–97] previously thought undetectable.

1997 In this chapter I try to demonstrate the capability of DUNE to constrain different
1998 DM scenarios. I used the neutrino fluxes arising from DM annihilations in the core
1999 of the Sun to compute the projected limits that DUNE would be able to set on the
2000 annihilation rates in the Sun and the DM scattering cross sections.

2001 **7.2 Gravitational capture of DM by the Sun**

2002 The Sun and the centre of the Earth are possible sources of DM annihilations, specially
2003 interesting because of their proximity. Their gravitational attraction ensured the capture
2004 of DM from the local halo through repeated scatterings of DM particles crossing them.

Chapter 7. DM searches with neutrinos from the Sun

2005 Only neutrinos produced from DM annihilations can escape the dense interior of these
2006 objects. Therefore, neutrino telescopes are the most useful experimental layouts to
2007 pursue DM searches from their cores.

2008 The neutrino flux from DM annihilations inside the Sun depends on the DM capture
2009 rate, which is proportional to the DM scattering cross section, and the annihilation rate,
2010 which is proportional to the velocity-averaged DM annihilation cross-section. The total
2011 number of DM particles inside the Sun follows the Boltzmann equation [94]:

$$\frac{dN_{DM}}{dt} = C_{\odot} - A_{\odot} N_{DM}^2, \quad (7.1)$$

2012 where C_{\odot} and A_{\odot} are the total Sun DM capture and annihilation rates respectively.
2013 In this expression I neglected the evaporation term, proportional to N_{DM} , which only
2014 contribute for $m_{DM} \lesssim 4$ GeV [98]. As the current threshold of neutrino telescopes is
2015 a few GeV, this region falls below the probed range but can be important in future
2016 low-energy projects.

2017 This equation has an equilibrium solution:

$$N_{DM}^{eq} = \sqrt{\frac{C_{\odot}}{A_{\odot}}}, \quad (7.2)$$

2018 which represents the amount of DM inside the Sun if the capture and annihilation have
2019 reached equilibrium. As the Sun is approximately 4.6 Gyr old, it is usually assumed that
2020 equilibrium has been achieved. Therefore, the anomalous neutrino flux from the Sun
2021 would only depend on the DM scattering cross section, enabling us to set limits on this
2022 quantity. If one does not assume equilibrium, some assumptions on the DM annihilation
2023 cross section are necessary to extract predictions from neutrino signals.

2024 Here, I am going to consider three possible scenarios for the DM interactions: DM
2025 scattering off electrons, spin-dependent (SD) and spin-independent interactions off nuclei.
2026 For the case of these last two, the cross sections will be given in terms of the SD and
2027 SI elastic scattering DM cross section off protons (assuming that DM interactions off

7.2. Gravitational capture of DM by the Sun

2028 protons and neutrons are identical), σ_p^{SD} and σ_p^{SI} , as [4, 94]:

$$\sigma_i^{\text{SD}} = \left(\frac{\tilde{\mu}_{A_i}}{\tilde{\mu}_p} \right)^2 \frac{4(J_i + 1)}{3J_i} |\langle S_{p,i} \rangle + \langle S_{n,i} \rangle|^2 \sigma_p^{\text{SD}}, \quad (7.3)$$

$$\sigma_i^{\text{SI}} = \left(\frac{\tilde{\mu}_{A_i}}{\tilde{\mu}_p} \right)^2 A_i^2 \sigma_p^{\text{SI}}, \quad (7.4)$$

2029 where $\tilde{\mu}_{A_i}$ is the reduced mass of the DM-nucleus i system, $\tilde{\mu}_p$ is the reduced mass of
 2030 the DM-proton system, A_i and J_i the mass number and total angular momentum of
 2031 nucleus i and $\langle S_{p,i} \rangle$ and $\langle S_{n,i} \rangle$ the expectation value of the spins of protons and neutrons
 2032 averaged over all nucleons, respectively (see Ref. [99] for a review on spin expectation
 2033 values).

2034 Since the Sun is mainly composed of Hydrogen, the capture of DM from the halo
 2035 is expected to occur mainly through spin-dependent scattering. However, since the
 2036 spin-independent cross section is proportional to the square of the atomic mass, heavy
 2037 elements can contribute to the capture rate (even though they constitute less than 2%
 2038 of the mass of the Sun). Heavy elements can also contribute to the spin-dependent cross
 2039 section if the DM has also momentum-dependent interactions.

2040 DM particles can get captured by the Sun if after repeated scatterings off solar
 2041 targets their final velocity is lower than the escape velocity of the Sun. In the limit of
 2042 weak cross sections, this capture rate can be approximately written as [4]:

$$C_{\odot}^{\text{weak}} = \sum_i \int_0^{R_{\odot}} dr 4\pi r^2 \int_0^{\infty} du_{\chi} \frac{\rho_{\chi}}{m_{\chi}} \frac{f_{v_{\odot}}(u_{\chi})}{u_{\chi}} \omega(r) \int_0^{v_e(r)} dv R_i^-(\omega \rightarrow v) |F_i(q)|^2, \quad (7.5)$$

2043 where the summation extends over all possible nuclear targets. In this expression, R_{\odot}
 2044 is the radius of the Sun, ρ_{χ} is the local DM density, m_{χ} the mass of the DM particle,
 2045 $f_{v_{\odot}}(u_{\chi})$ the DM velocity distribution seen from the Sun's reference frame, $R_i^-(\omega \rightarrow v)$
 2046 is the differential rate at which a DM particle with velocity v scatters a solar target of
 2047 mass m_i to end up with a velocity ω and $|F_i(q)|$ is the nuclear form factor of target i .

2048 The differential scattering rate takes a rather simple form when considering velocity-

Chapter 7. DM searches with neutrinos from the Sun

2049 independent and isotropic cross sections. In that case, this quantity is given by [4, 100]:

$$R_i^-(\omega \rightarrow v) = \frac{2}{\sqrt{\pi}} \frac{\mu_{i,+}^2}{\mu_i} \frac{v}{\omega} n_i(r) \sigma_i \left[\chi(-\alpha_-, \alpha_+) + \chi(-\beta_-, \beta_+) e^{\mu_i(\omega^2 - v^2)/u_i^2(r)} \right], \quad (7.6)$$

2050 where μ_i is the ratio between the DM mass and the mass of target i , $\mu_{i,\pm}$ is defined as:

$$\mu_{i,\pm} \equiv \frac{\mu_i \pm 1}{2}, \quad (7.7)$$

2051 $n_i(r)$ is the density profile of target i in the solar medium, $u_i(r)$ is the most probable

2052 velocity of target i given by:

$$u_i(r) = \sqrt{\frac{2T_\odot(r)}{m_i}}, \quad (7.8)$$

2053 where $T_\odot(r)$ is the temperature of the Sun, the quantities α_\pm and β_\pm are defined as:

$$\alpha_\pm \equiv \frac{\mu_{i,+}v \pm \mu_{i,-}\omega}{u_i(r)}, \quad (7.9)$$

$$\beta_\pm \equiv \frac{\mu_{i,-}v \pm \mu_{i,+}\omega}{u_i(r)}, \quad (7.10)$$

2054 and the function $\chi(a, b)$ is a Gaussian integral of the form:

$$\chi(a, b) \equiv \int_a^b dx e^{-x^2}. \quad (7.11)$$

2055 Finally, if one assumes the DM halo velocity distribution in the galactic rest frame

2056 to be a Maxwell-Boltzmann distribution, one can write the halo velocity distribution for

2057 an observer moving at the speed of the Sun with respect to the DM rest frame as:

$$f_{v_\odot}(u_\chi) = \sqrt{\frac{3}{2\pi}} \frac{u_\chi}{v_\odot v_d} \left(e^{-\frac{3(u_\chi - v_\odot)^2}{2v_d^2}} - e^{-\frac{3(u_\chi + v_\odot)^2}{2v_d^2}} \right), \quad (7.12)$$

2058 where:

$$\omega^2 = u_\chi + v_e(r)^2, \quad (7.13)$$

2059 is the DM velocity squared, v_\odot the relative velocity of the Sun from the DM rest frame

7.2. Gravitational capture of DM by the Sun

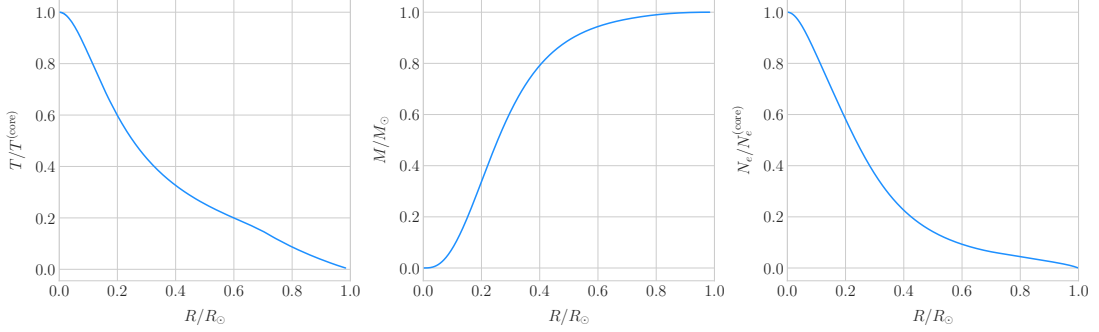


Figure 7.1: Input solar parameters used in our capture rate computation as functions of the Sun's radius, from left to right: temperature (with respect to the temperature at the core), mass (in solar masses) and electron number density (with respect to the electron density at the core). All quantities shown correspond to the standard solar model BS2005-OP [3].

and $v_d \simeq \sqrt{3/2}v_\odot$ the velocity dispersion.

For the case of strong scattering cross section, Eq. (7.5) ceases to be valid, as it escalates indefinitely with the cross section. In that limit, the capture rate saturates to the case where the probability of interaction is equal to one, which can be written as:

$$C_\odot^{\text{geom}} = \pi R_\odot^2 \left(\frac{\rho_\chi}{m_\chi} \right) \langle v \rangle \left(1 + \frac{3}{2} \frac{v_e^2(R_\odot)}{v_d^2} \right) \xi(v_\odot, v_d), \quad (7.14)$$

where $v_d = \sqrt{8/3\pi}v_\odot$ is the mean velocity in the DM rest frame and the factor $\xi(v_\odot, v_d)$ accounts for the suppression due to the motion of the Sun:

$$\xi(v_\odot, v_d) = \frac{v_d^2 e^{-\frac{3v_\odot^2}{2v_d^2}} + \sqrt{\frac{\pi}{6}} \frac{v_d}{v_\odot} (v_d^2 + 3v_e^2(R_\odot) + 3v_\odot^2) \text{Erf} \left(\sqrt{\frac{3}{2}} \frac{v_\odot}{v_d} \right)}{2v_d^2 + 3v_e^2(R_\odot)}. \quad (7.15)$$

Having these into account, one can write the total capture rate as a combination of both contributions, allowing a smooth transition between the two, as:

$$C_\odot = C_\odot^{\text{weak}} \left(1 - e^{C_\odot^{\text{geom}}/C_\odot^{\text{weak}}} \right). \quad (7.16)$$

I computed the capture rate from Eq. (7.16) in the case of interactions with electrons. To do so, I used the standard solar model BS2005-OP [3]. Fig. 7.1 shows the

Chapter 7. DM searches with neutrinos from the Sun

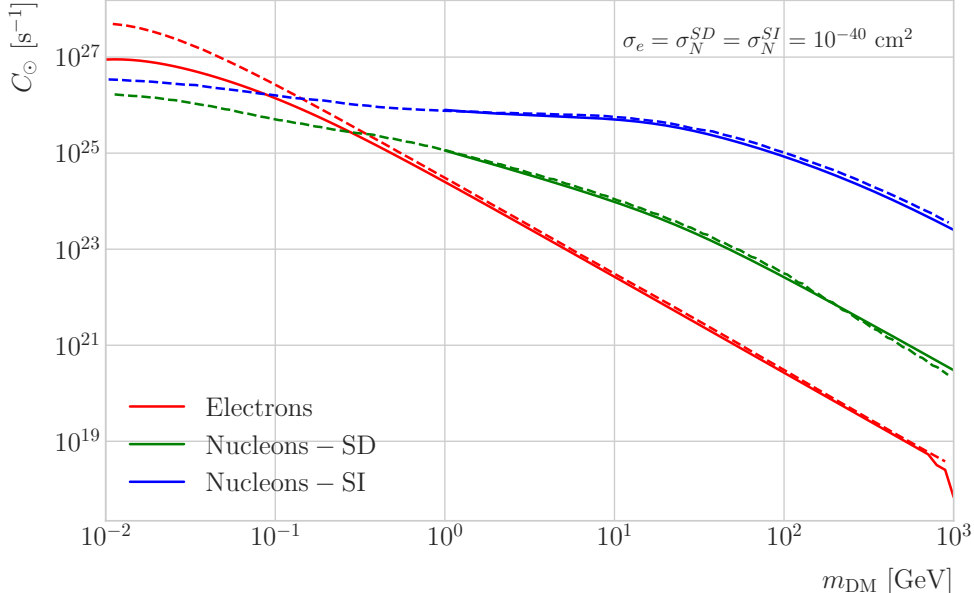


Figure 7.2: Capture rates as a function of the DM mass for the DM-electron interactions (red lines), SD DM-nucleons interactions (green lines) and SI DM-nucleons interactions (blue lines). Solid lines represent the values computed in this work while the dashed lines are the one given in Ref. [4]. All the rates are shown for a choice of scattering cross section of $\sigma_i = 10^{-40} \text{ cm}^2$.

2070 three parameters from the solar model that are needed for the computation, the solar
 2071 temperature (left panel), mass (central panel) and electron density (right panel) profiles.

2072 For the case of the interactions off nuclei, the computations are more convoluted
 2073 as one needs to add up the contributions of the different most abundant nuclei in
 2074 the Sun. Also, in contrast to the electron scenario where the form factor is trivially
 2075 $|F_e(q)|^2 = 1$, for any nucleus i one would need to consider some appropriate nuclear
 2076 density distribution (either a Gaussian approximation, a Woods-Saxon distribution, etc)
 2077 which would complicate the calculations even further.

2078 That is the reason why, at this stage of our study, I decided to take an alternative
 2079 approach to the computation of the DM-nucleus capture rates. I used the **DarkSUSY**
 2080 software, that allows us to compute these quantities performing a full numerical
 2081 integration over the momentum transfer of the form factors. The default standard
 2082 solar model used by **DarkSUSY** is BP2000¹ [101].

¹This is what they say in their manual, but I fear it is somewhat outdated. It appears to me this

7.2. Gravitational capture of DM by the Sun

2083 In Fig. 7.2 I show the results I obtained for the capture rates, for the case of
 2084 interactions off electrons (red solid line), SD (green solid line) and SI (blue solid line)
 2085 interactions of nucleons. In all cases I used a value of the scattering cross sections of
 2086 $\sigma_i = 10^{-40} \text{ cm}^2$. Note here one of the limitations of the **DarkSUSY** approach, one can
 2087 not extend the computation below $m_{\text{DM}} = 1 \text{ GeV}$. Nevertheless, this is not something
 2088 to worry about in this case, as I will discuss next. As a comparison, I added also the
 2089 values computed in Ref. [4] (same color scheme, dashed lines). One can see there is good
 2090 agreement between these and the **DarkSUSY** computation of the SD and SI interactions
 2091 for $m_{\text{DM}} \geq 1 \text{ GeV}$. In this regime their computations also matches quite well our
 2092 result for the electron capture rate. However, these start to differ significantly below
 2093 $m_{\text{DM}} = 1 \text{ GeV}$, being their estimate up to a factor of 5 bigger than ours for low masses.

2094 Let us comment briefly about the assumption I made before about not including
 2095 an evaporation term in the Boltzmann equation. If I include this term in the equation
 2096 (which will be proportional to the number of DM particles) the equilibrium solution
 2097 takes the form:

$$N_{\text{DM}}^{eq} = \sqrt{\frac{C_{\odot}}{A_{\odot}}} \frac{1}{\kappa + \frac{1}{2} E_{\odot} \tau_{eq}}, \quad (7.17)$$

2098 where E_{\odot} is the total evaporation rate, τ_{eq} is the equilibrium time in the absence of
 2099 evaporation:

$$\tau_{eq} = \frac{1}{\sqrt{C_{\odot} A_{\odot}}}, \quad (7.18)$$

2100 and κ is defined as:

$$\kappa \equiv \sqrt{1 + \left(\frac{E_{\odot} \tau_{eq}}{2} \right)^2}. \quad (7.19)$$

2101 Now, it is easy to proof that in case evaporation dominates $\kappa \gg 1$ and therefore:

$$N_{\text{DM}}^{eq} \simeq \frac{C_{\odot}}{E_{\odot}}. \quad (7.20)$$

2102 In contrast, if evaporation is irrelevant $\kappa \simeq 1$ and one recovers Eq. (7.2).

model is relatively old and do not see why they are not using others like [3]. Maybe one can double-check in the code to make sure.

Chapter 7. DM searches with neutrinos from the Sun

2103 In this way, one can define the evaporation mass as the mass for which the number
2104 of DM particles in equilibrium approaches Eq. (7.20) at 10% level:

$$\left| N_{DM}^{eq}(m_{\text{evap}}) - \frac{C_{\odot}(m_{\text{evap}})}{E_{\odot}(m_{\text{evap}})} \right| = 0.1 N_{DM}^{eq}(m_{\text{evap}}). \quad (7.21)$$

2105 This can be regarded as the minimum testable mass one can reach using the annihilation
2106 products of the DM in the Sun.

2107 It was reported in Ref. [4] that, in the case of both SD and SI DM interactions
2108 off nuclei, this value ranges from 2 to 4 GeV depending on the specific scattering
2109 cross section value, compatible with the usual assumptions in the literature. What is
2110 interesting is the case of the electron capture. It was found that, when one applies a
2111 cutoff in the velocity distribution of the DM trapped in the Sun slightly below the escape
2112 velocity, the evaporation mass for the DM-electron interaction decreases remarkably. For
2113 a moderate choice of $v_c(r) = 0.9v_e(r)$ one gets an evaporation mass of around 200 to
2114 600 MeV. This possibility opens a region of the parameter space that could be tested
2115 with neutrino detectors.

2116 7.3 Neutrino flux from DM annihilations

2117 When WIMPs annihilate inside the Sun a flux of high-energy neutrinos is expected from
2118 heavy quarks, gauge bosons and $\tau^+\tau^-$ final states, which decay before losing energy
2119 in the dense solar medium, as they will produce a continuum spectra up to $E_{\nu} \sim m_{\chi}$
2120 (in the case of direct annihilation to neutrinos one would have a line at $E_{\nu} = m_{\chi}$) [95].
2121 This kind of signal has been extensively studied in the literature, allowing to put strong
2122 limits on the SD WIMP-proton cross section for large m_{χ} . However, the number of
2123 high-energy neutrinos per WIMP annihilation is small and the spectrum depends on the
2124 unknown final state. Moreover, background rejection is easier for large m_{χ} but neutrinos
2125 with $E_{\nu} \gtrsim 100$ GeV are significantly attenuated by interactions in the Sun.

2126 Nevertheless, most WIMP annihilation final states eventually produce a low-energy
2127 neutrino spectrum. In this case one does not just consider the more massive final

7.4. Computing limits from solar neutrino fluxes

states but also annihilations into e^+e^- , $\mu^+\mu^-$ and light quarks [94]. In particular, light mesons would be produced and stopped in the dense medium, thus decaying at rest and producing a monoenergetic neutrino signal. The decay-at-rest of kaons will produce a $E_\nu = 236$ MeV ν_μ while in the case of pions one would have a $E_\nu = 29.8$ MeV ν_μ . In practice only K^+ and π^+ contribute to these signals, as K^- and π^- are usually Coulomb-captured in an atomic orbit and get absorbed by the nucleus. There is also a low-energy neutrino signal coming from muon decays, which are produced in kaon or pion decays, leptonic decays of other hadrons and heavy leptons or even directly from WIMP annihilations, which can decay at rest and contribute to the previous low-energy neutrino flux with a well known spectrum below 52.8 MeV.

These monoenergetic MeV neutrinos were previously considered undetectable but, due to the large yield, the known spectra and the modern advances in the detector technology, these low-energy neutrino flux can be a good probe of the SD WIMP-proton cross-section in standard solar WIMP capture scenario, as it is sensitive to low WIMP masses and insensitive to the particular final state. A good place to look for these signals are next-generation neutrino experiments such as DUNE.

7.4 Computing limits from solar neutrino fluxes

In order to use the neutrino fluxes from DM annihilations in the Sun, the first thing I need to do is to determine the expected number of atmospheric background events, for a given exposure, after directionality selection has been applied. I can write this number as:

$$N_B = \eta_B \int d\Omega \int_{E_{min}}^{E_{max}} dE_\nu \frac{d^2\Phi_{atm}^\mu}{dE_\nu d\Omega} \times \left(A_{eff}^{(\mu)}(E_\nu) T \right), \quad (7.22)$$

where η_B is the background efficiency, E_{min} and E_{max} the minimum and maximum energies to integrate over, $d^2\Phi_{atm}^\mu/dE_\nu d\Omega$ the differential flux of atmospheric muon neutrinos, $A_{eff}^{(\mu)}$ is the effective area of DUNE to muon neutrinos and T is the exposure time. The effective area can be expressed as the product of the neutrino-nucleus scattering cross section and the number of nuclei in the fiducial volume of the detector. This way

Chapter 7. DM searches with neutrinos from the Sun

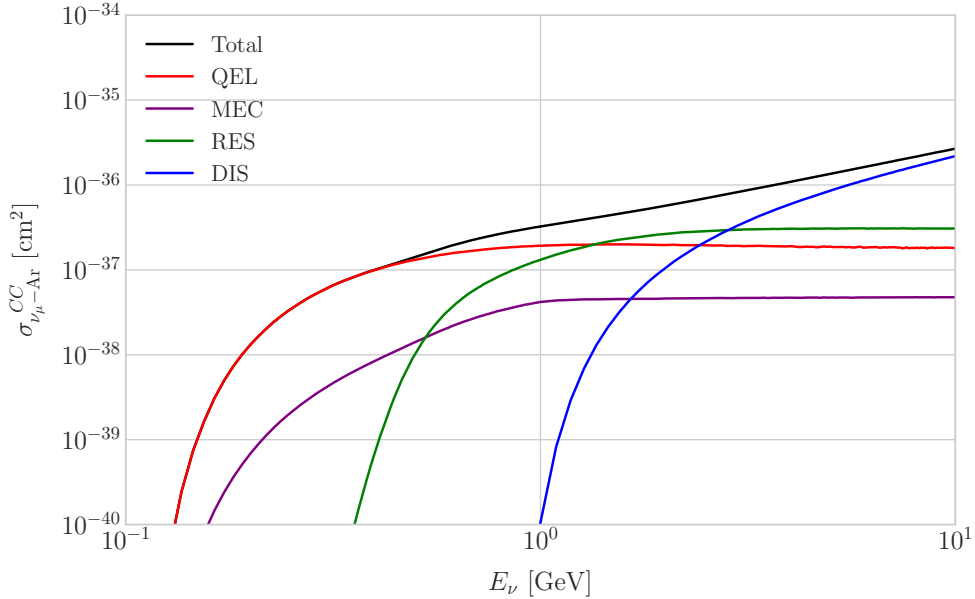


Figure 7.3: NuWro computed $\nu_\mu - {}^{40}\text{Ar}$ charged-current scattering cross section as a function of the neutrino energy E_μ . The black line shows to the total cross section, whereas the others correspond to the different contributions (in red quasi-elastic scattering, in green resonant pion exchange, in blue deep inelastic scattering and in purple meson exchange current).

2154 for DUNE I can write:

$$A_{eff}^{(\mu)}(E_\nu) = (6.0 \times 10^{-10} \text{ m}^2) \left(\frac{\sigma_{\nu - \text{Ar}}^{(\mu)}(E_\nu)}{10^{-38} \text{ cm}^2} \right) \left(\frac{M_{target}}{40 \text{ kT}} \right), \quad (7.23)$$

2155 where $\sigma_{\nu - \text{Ar}}^{(\mu)}$ is the $\nu_\mu - {}^{40}\text{Ar}$ charged-current scattering cross section. In Fig. 7.3 I
 2156 show the computed value of this cross section as a function of the neutrino energy E_ν ,
 2157 in the range of interest both for the atmospheric background and signal events. It was
 2158 computed using the NuWro Monte Carlo neutrino event generator [102], including the
 2159 charged-current contributions of the quasi-elastic scattering (red line), resonant pion
 2160 exchange (green line), deep inelastic scattering (blue line) and meson exchange current
 2161 (purple line).

2162 The background rejection will depend on the resolution of the detector and the
 2163 selection one applies on the events. A geometry argument can be used to estimate
 2164 the maximum background rejection one can achieve in this case, considering one can

7.4. Computing limits from solar neutrino fluxes

2165 efficiently discriminate all events coming from a direction different from that of the
 2166 Sun. In that case, the optimal background efficiency will simply be the relative angular
 2167 coverage of the Sun. Taking the angular diameter of the Sun as seen from the Earth to
 2168 be 0.5° , I have:

$$\eta_B^{(opt)} \approx \frac{\pi \left(\frac{0.5}{2}\right)^2}{360 \times 180} \simeq 3.03 \times 10^{-6}. \quad (7.24)$$

2169 This value will give a very optimistic estimate of the number of background events.
 2170 However, it can be regarded as an lower limit, as it represents the best case scenario.

2171 In Fig. 7.4 I show the fluxes of atmospheric neutrinos at the Homestake mine during
 2172 solar minimum, taken from Ref. [5]. The values are averaged over the two angular
 2173 directions. In blue I have the flux of muon neutrinos while in red I indicate the flux
 2174 of electron neutrinos. Additionally, the dashed lines correspond to both antineutrino
 2175 species.

2176 Using these values for the muon neutrino and the corresponding total CC cross
 2177 section, one can compute the number of expected background events by integrating over
 2178 the given energy range (as in this case the angular integral is trivial). As for the energy
 2179 range to integrate over, I choose the range for DUNE specified in [70], $E_{min} = 10^{-1}$ GeV
 2180 and $E_{max} = 10$ GeV. Taking all these into account, I found the number of background
 2181 events to be:

$$N_B \simeq \eta_B \times (3.827 \times 10^4) \times \left(\frac{\text{exposure}}{400 \text{ kT yr}} \right). \quad (7.25)$$

2182 In order to estimate the sensitivity of DUNE to this kind signal, one can consider a
 2183 hypothetical data set where the number of observed neutrinos is taken to be the expected
 2184 number of background events rounded to the nearest integer, $N_{obs} = \text{round}(N_B)$ [103].
 2185 Now, if I assume that the number of signal and background events seen by DUNE are
 2186 given by Poisson distributions with means equal to the expected number of signal and
 2187 background events, N_S and N_B , one can denote by N_S^{90} to the number of expected
 2188 signal events such that the probability of having an experimental run with a number of
 2189 events greater than N_{obs} is 90%. This number can be obtained as the numerical solution

Chapter 7. DM searches with neutrinos from the Sun

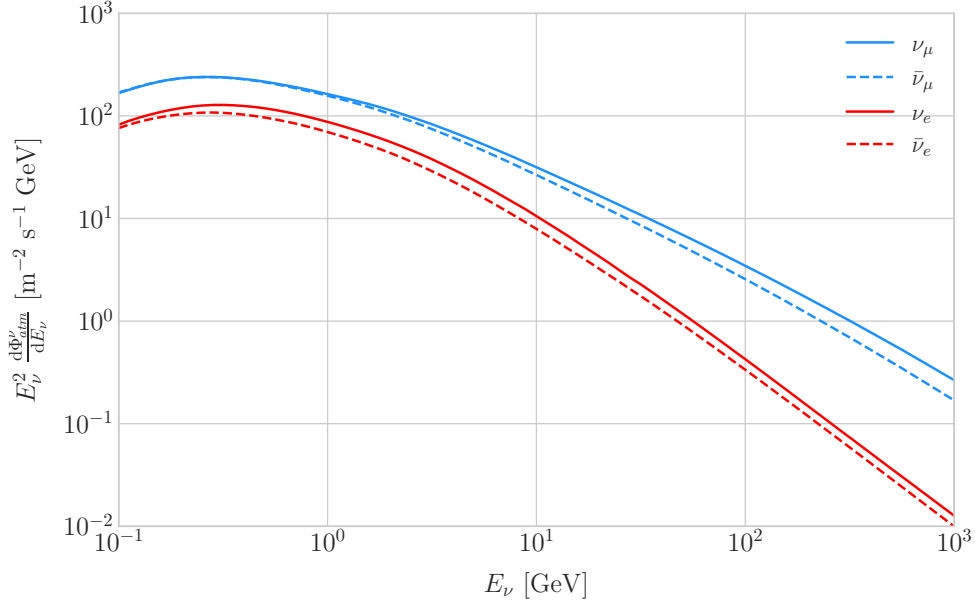


Figure 7.4: Expected atmospheric neutrino flux as a function of the neutrino energy E_ν at Homestake at solar minimum, taken from Ref. [5]. The blue solid (dashed) line correspond to muon neutrinos (antineutrinos) and the red solid (dashed) line correspond to electron neutrinos (antineutrinos).

2190 to the equation:

$$1 - \frac{\Gamma(N_{obs} + 1, N_S^{90} + N_B)}{N_{obs}!} = 0.9, \quad (7.26)$$

2191 where $\Gamma(x, y)$ is the upper incomplete gamma function.

2192 The number of signal events is related to the neutrino flux from DM annihilations in
2193 a similar way as the background events to the atmospheric neutrino flux. In this case I
2194 have:

$$N_S = \eta_S \Gamma_A^{eq} \int_{z_{min}}^{z_{max}} dz \frac{dN_\nu}{dAdN_Adz} \times (A_{eff}^\mu(z)T), \quad (7.27)$$

2195 where η_S is the signal efficiency, Γ_A^{eq} is the total annihilation rate of DM particles at
2196 equilibrium, $\Gamma_A^{eq} = A_\odot (N_{DM}^{eq})^2$, z_{min} and z_{max} the minimum and maximum relative
2197 energies to integrate over (in such a way that $z_{min,max} \leq E_{min,max}/m_{DM}$ for each m_{DM})
2198 and $dN_\nu/dAdN_Adz$ the muon neutrino flux per DM annihilation in the Sun.

2199 Knowing N_S^{90} one can use the relation in Eq. (7.27) to obtain $\Gamma_A^{eq,90}$ for different
2200 values of the DM mass. From there I can directly translate those values into the

7.5. Example: Kaluza-Klein Dark Matter

2201 upper limits for DUNE on the DM scattering cross sections, for a given exposure. The
2202 relation between the annihilation rate and the DM-nucleon cross section comes from the
2203 equilibrium condition through the solar DM capture rate. The details of the evolution
2204 of the number of DM particles inside the Sun and the computation of the capture rates
2205 are discussed in App. 7.2.

2206 7.5 Example: Kaluza-Klein Dark Matter

2207 Even though there are plenty of BSM theories which provide viable dark matter
2208 candidates, Kaluza-Klein type of models [104, 105] within the universal extra dimensions
2209 (UED) paradigm naturally predict the existence of a massive, stable particle that can
2210 play the role of the dark matter. In the UED scenario all the SM fields can propagate
2211 in one or more compact extra dimensions [106], as opposed to the idea of brane worlds
2212 [107, 108], where just gravity can propagate in the bulk while SM particles live at fixed
2213 points.

2214 Furthermore, in UED there is no violation of the translational invariance along the
2215 extra dimensions, thus leading to degenerate KK modes masses and also the conservation
2216 of the KK number in the effective four dimensional theory. At loop level, radiative
2217 corrections and boundary terms shift the masses of the KK modes and break KK
2218 number conservation into a KK parity. As a result, this theory only contains interactions
2219 between an even number of odd KK modes and therefore the lightest among the first KK
2220 excitations will be stable. This particle is usually denoted as the lightest Kaluza-Klein
2221 particle (LKP) and its mass is proportional to $1/R$, being R the size of the extra
2222 dimension.

2223 A viable DM candidate needs to be electrically neutral and non-baryonic, therefore
2224 good candidates among the first Kaluza-Klein excitations would be the KK neutral
2225 gauge bosons and the KK neutrinos [109]. Another possible candidate is the first KK
2226 excitation of the graviton, which receives negligible radiate contributions and therefore
2227 has a mass almost equal to $1/R$, but it has been shown that the lightest eigenstate from

Chapter 7. DM searches with neutrinos from the Sun

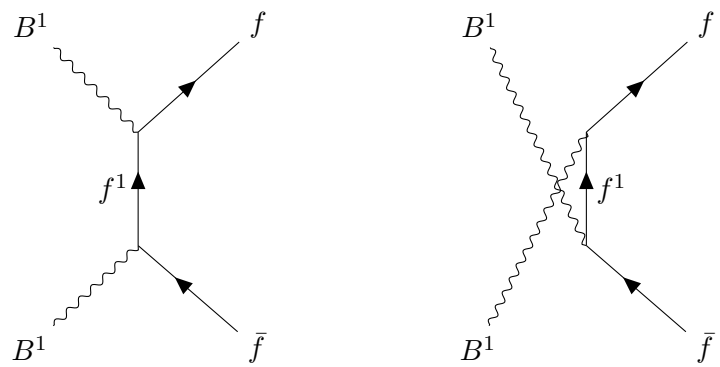


Figure 7.5: Feynman diagrams for B^1B^1 annihilation into SM fermions.

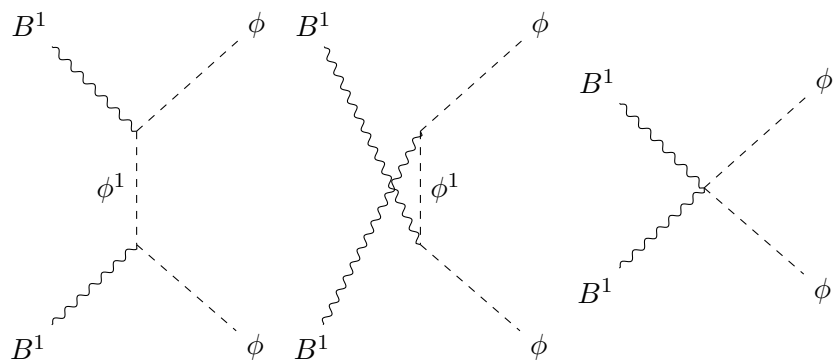


Figure 7.6: Feynman diagrams for B^1B^1 annihilation into a Higgs boson pair.

7.5. Example: Kaluza-Klein Dark Matter

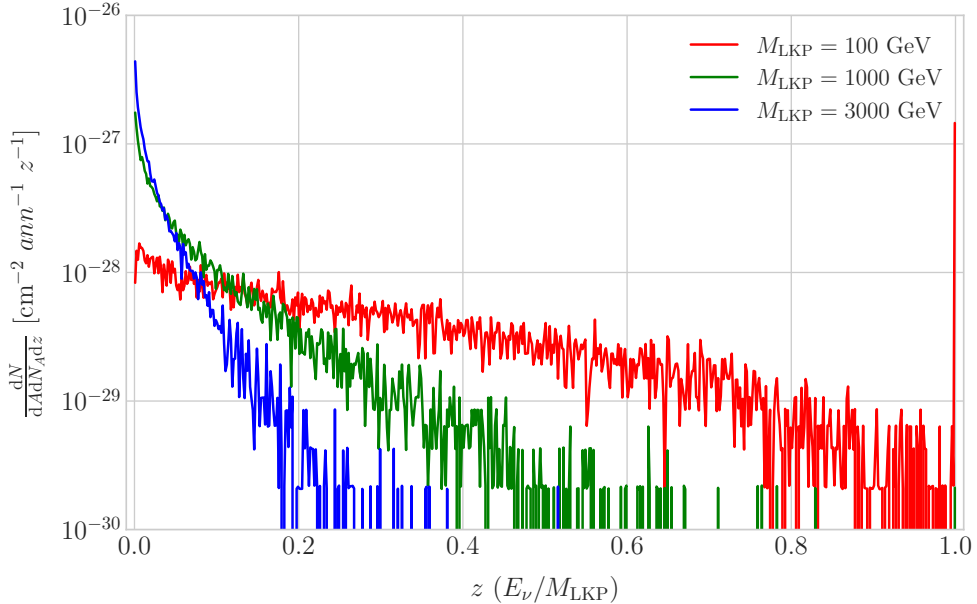


Figure 7.7: Computed spectra of muon neutrinos at the DUNE FD site from B^1 annihilations in the Sun for three different values of M_{LKP} , plotted in relative energy units for legibility.

the mixing of the gauge mass states (B^1, W_3^1) would be lighter, as B^1 and W_3^1 receive negative radiative corrections [110]. It is also understood that, when these corrections become sizeable, the eigenstates become approximately pure B^1 and W_3^1 states as the Weinberg mixing angle grows small with the KK number [110]. In that case, the LKP can be well-approximated as being entirely B^1 .

I need to compute the neutrino flux produced by the annihilations of the LKP in the core of the Sun, taking into account their propagation in the solar medium, as well as neutrino oscillations. To this end I used `WimpSim` [111, 112] to generate one million annihilation events in the Sun over a time span of four years and propagate them to the DUNE FD location ($44^\circ 20' \text{ N}, 103^\circ 45' \text{ W}$), for different values of M_{LKP} . In Fig. 7.7 I show the obtained muon neutrino spectra arriving to the detector from LKP annihilations in the Sun, per unit area and per annihilation, plotted in relative energy units for different values of the mass. As one could expect the spectra get steeper the higher is the mass, due to the absorption of high-energy neutrinos in the solar medium. Also, one can see the peak at $z = 1$ due to the direct annihilation into

Chapter 7. DM searches with neutrinos from the Sun

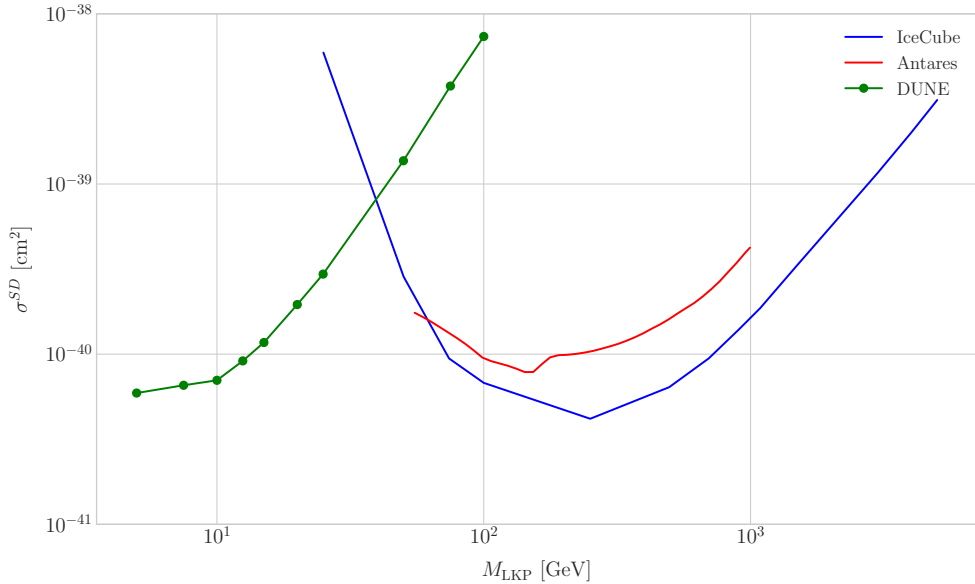


Figure 7.8: Projected 90% confidence level upper limit for DUNE (400 kT yr) on the spin-dependent B^1 -proton scattering cross section as a function of M_{LKP} (green dots). I also show the previous limits from IceCube [6] (blue line) and Antares [7] (red line) on the LKP cross section. The shaded area represents the disfavoured region (at 95% confidence level) on the mass of the LKP from LHC data [8].

2243 neutrinos $\chi\chi \rightarrow \nu\bar{\nu}$.

2244 Now, one can estimate the sensitivity of DUNE to this particular model by using
 2245 the methods I previously discussed. To begin with, I will use the optimistic estimation
 2246 of the background efficiency in Eq. (7.24) to get our upper bound. Using it, one can
 2247 directly compute the number of expected background events to be $N_B = 0.1101$ for an
 2248 exposure of 400 kT yr. Then, Eq. (7.26) give us a value of $N_S^{90} = 2.20$ for the 90%
 2249 exclusion number of expected signal events. By using the NuWro generated cross sections
 2250 and the computed neutrino fluxes from B^1 annihilations in the Sun I can estimate the
 2251 limits on the SD and SI DM-nucleus cross section using the relation in Eq. (7.2) and
 2252 the capture rates I computed with DarkSUSY.

2253 In Fig. 7.8 I show the projected sensitive for DUNE on the spin-dependent B^1 -proton
 2254 scattering cross section versus the mass of the DM particle, for a exposure of 400 kT yr
 2255 (green dots). I also include the previous results from IceCube [6] (blue line) and Antares
 2256 [7] (red line). The shaded area represents the disfavoured region from combined searches

7.6. High energy DM neutrino signals

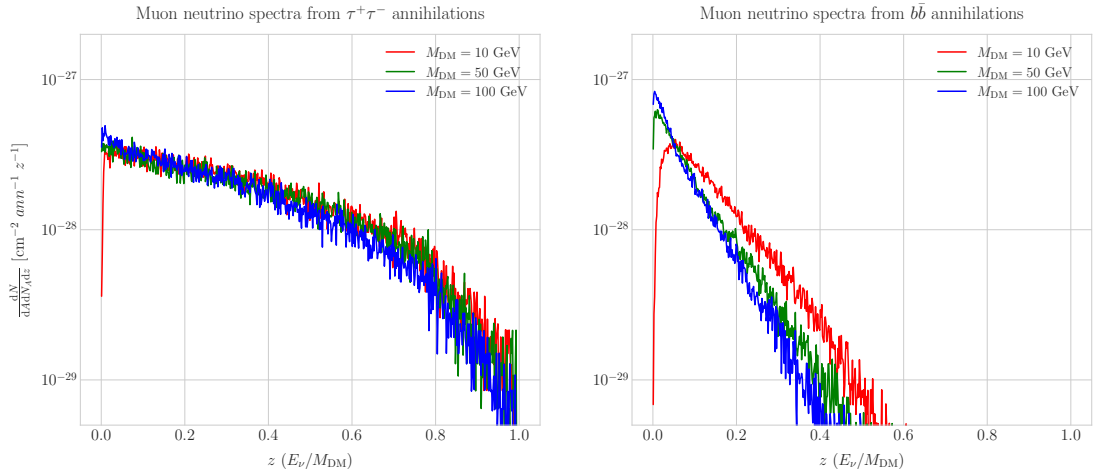


Figure 7.9: Computed spectra of muon neutrinos at the DUNE FD site from $\tau^+\tau^-$ (left panel) and $b\bar{b}$ (right panel) annihilations in the Sun for the DM masses $m_{\text{DM}} = 10 \text{ GeV}$ (red line), 50 GeV (green line) and 100 GeV (blue line), plotted in relative energy units.

2257 for UED by ATLAS and CMS [8].

2258 From the experimental point of view, this estimation lacked a detailed simulation of
 2259 the detector response and thus this must be consider as a mere optimistic sensitivity
 2260 computation. However, it shows the potential of DUNE to constrain this kind of exotic
 2261 scenarios, showing the region where it will be in a position to compete with other
 2262 neutrino telescopes. A more detailed analysis is needed if I am to make a realistic
 2263 estimation. Even though the region of the parameter space where DUNE would be
 2264 sensitive to this particular model is quite constrained by collider searches [8] and other
 2265 rare decay measurements [113, 114], it still constitutes an alternative indirect probe.

2266 7.6 High energy DM neutrino signals

2267 To have better estimates on the capability of the DUNE FD to constrain the parameter
 2268 space of DM using solar neutrino fluxes, I need to start accounting for the detector
 2269 resolution effects and the topologies of the different signatures. As a starting point, I
 2270 will focus on specific annihilation channels. For the case of DUNE, the relevant ones
 2271 are mainly the hard channels $\tau^+\tau^-$ and $\nu\bar{\nu}$ and the soft channel $b\bar{b}$. These are the open
 2272 annihilation channels for relatively low mass WIMPs that will actually give neutrino

Chapter 7. DM searches with neutrinos from the Sun

2273 fluxes. Other channels, like W^+W^- and ZZ , are open for more massive WIMPs, but
2274 those will produce usually a higher energy neutrino flux that will be out of reach for
2275 DUNE (usually the maximum neutrino energy is taken to be $E_{max} = 10$ GeV).

2276 In Fig. 7.9 I show the `WimpSim` [111,112] generated muon neutrino spectra at the
2277 DUNE FD location ($44^\circ 20' N, 103^\circ 45' W$) from $\tau^+\tau^-$ (left panel) and $b\bar{b}$ (right panel)
2278 annihilations in the core of the Sun, for different DM masses. Here, one can clearly see
2279 the meaning of the previous distinction between hard and soft channels. For the same
2280 DM mass value, the muon neutrino spectrum from the $\tau^+\tau^-$ channel is more flat and
2281 reaches higher energies than the one from the $b\bar{b}$ channel, which drops faster.

2282 In this case, I prepared two sets of files, one for $\tau^+\tau^-$ and the other for $b\bar{b}$, for DM
2283 masses in the range from 5 to 100 GeV (actually for $b\bar{b}$ the first mass point I took is
2284 7.5 GeV, as a WIMP with $m_{DM} = 5$ GeV can not kinematically self annihilate into $b\bar{b}$).
2285 Then, I prepared the `WimpSim` output fluxes in a specific way to use them as inputs to
2286 `NuWro`, which simulates the neutrino interaction with the argon.

2287 Because `WimpSim` outputs an event list together with the fluxes, I can use the former
2288 to generate the events. The direction of these is given in terms of the azimuth and
2289 altitude angles viewed from the specified location, so first I need to convert these into the
2290 DUNE FD coordinates. Once I have done it, each event can be processed with `NuWro`.
2291 To increase the number of samples and optimise the computation time, I generate 100
2292 interactions (i.e. `NuWro` events) for each `WimpSim` event². I restrict the event generation
2293 to charged current interactions, but I allow all the different contributions to the CC
2294 cross section, i.e. quasielastic scattering (QEL), meson exchange current process (MEC),
2295 resonant pion production (RES) and deep inelastic scattering (DIS). I just take into
2296 account the CC contribution because I am only interested in final states with charged
2297 leptons, as we have better chances of reconstructing the kinematics of CC events.

2298 For the atmospheric fluxes I follow a similar procedure, only that this time I do not
2299 have a set of events but the fluxes binned in azimuth and altitude angles. This way, I

²This also solves a problem related with the generation of the neutrino interactions in `NuWro`, as if you only produce one event each time you launch `NuWro` it will always produce an interaction of the dominant interaction type for that particular energy.

7.6. High energy DM neutrino signals

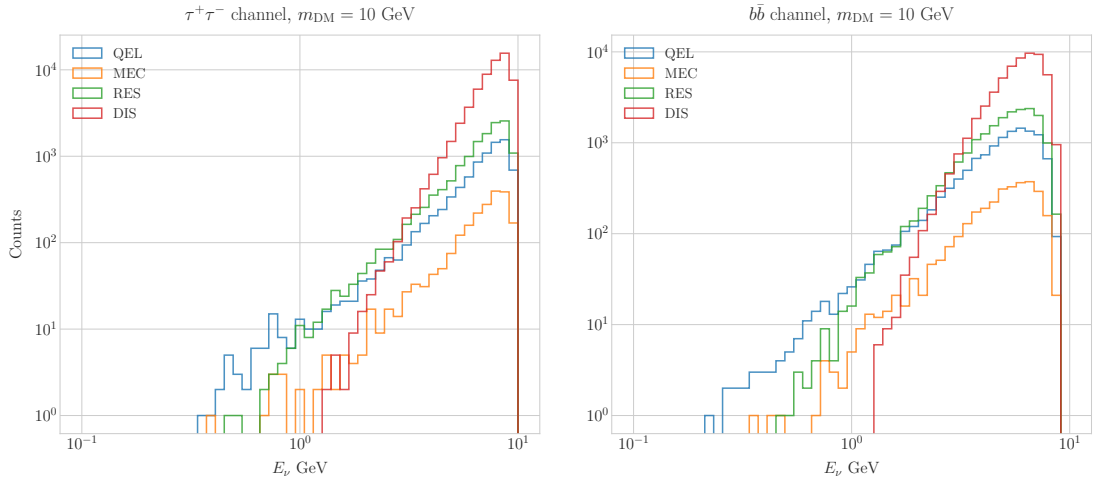


Figure 7.10: Distribution of the muon neutrino energies from the $\tau^+\tau^-$ (left panel) and $b\bar{b}$ (right panel) annihilation channels, for $m_{\text{DM}} = 10 \text{ GeV}$, separated by CC interaction type: QEL (blue), MEC (orange), RES (green) and DIS (red).

transform these to DUNE coordinates and process the fluxes for each bin separated with
 NuWro.

At this point, I have two sets of events with different energies and final states.
 In Fig. 7.10 one can see the distribution of the muon neutrino energies for the case
 $m_{\text{DM}} = 10 \text{ GeV}$, both for the $\tau^+\tau^-$ (left panel) and $b\bar{b}$ (right panel) channels, separated
 by interaction. One can clearly see that there are different energy regimes where the
 primary interaction type is different. This leads to a plurality of event topologies,
 therefore making it difficult to implement a general approach to the selection of events
 in detriment of the background. As a way to proceed, I decided to split our samples,
 based on the different interaction modes and contents of the final state, into a CC DIS
 sample and a single proton CC QEL sample.

7.6.1 DIS events

To begin with, I consider the high energy part of the spectrum. In this region DIS events
 dominate, i.e. interactions of the form $\nu_\mu + q_d(\bar{q}_u) \rightarrow \mu^- + q_u(\bar{q}_d)$. Therefore, our final
 estates will contain a muon and a hadronic jet from the fragmentation of the outgoing
 quark. As all these events have $E_\nu \gtrsim 1 \text{ GeV}$ the momentum transfer to the remnant

Chapter 7. DM searches with neutrinos from the Sun

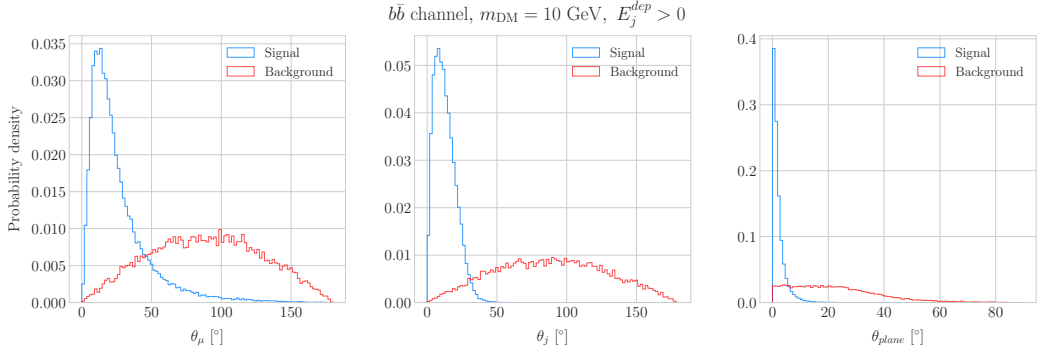


Figure 7.11: Distributions of θ_μ (left panel), θ_j (central panel) and θ_{plane} (right panel) for the $b\bar{b}$ sample with $m_{\text{DM}} = 10$ GeV (blue) and the atmospheric background (red).

2316 nucleus is negligible, for this reason the neutrino energy can be effectively reconstructed
 2317 just taking into account the momenta of the muon and the jet. This technique was
 2318 successfully used in Ref. [115] to select monoenergetic DM solar neutrino events from
 2319 $\nu\bar{\nu}$ annihilation channels.

2320 Using momentum conservation one sees that the plane generated by the momenta
 2321 of the muon and the jet needs to also contain the momentum of the neutrino. As we
 2322 are interested in neutrinos coming from the Sun, the momentum of the neutrino can be
 2323 regarded as known beforehand. This will allow us to define the angle of the outgoing
 2324 muon and jet with respect to the incoming neutrino. Moreover, one can also use that
 2325 information to reject poorly reconstructed jets, checking for deviations of these from the
 2326 momentum conservation plane.

2327 To account for the limited angular resolution of the detector, I smeared the momenta
 2328 of the muons and hadrons. In a liquid argon TPC muons are expected to be tracked with
 2329 high precision, therefore I take the associated angular resolution to be 1° . In the case of
 2330 jets, it is expected that for the hadrons dominating the cascade a detector like DUNE
 2331 has an angular resolution between 1° to 5° [70], so I take the latter, more conservative,
 2332 estimate.

2333 As a first selection step, I will just take into account particles with kinetic energies
 2334 above the detection threshold of DUNE. For muons and photons the specified threshold
 2335 energy is 30 MeV, for charged pions 100 MeV and for other hadrons 50 MeV [70]. This

7.6. High energy DM neutrino signals

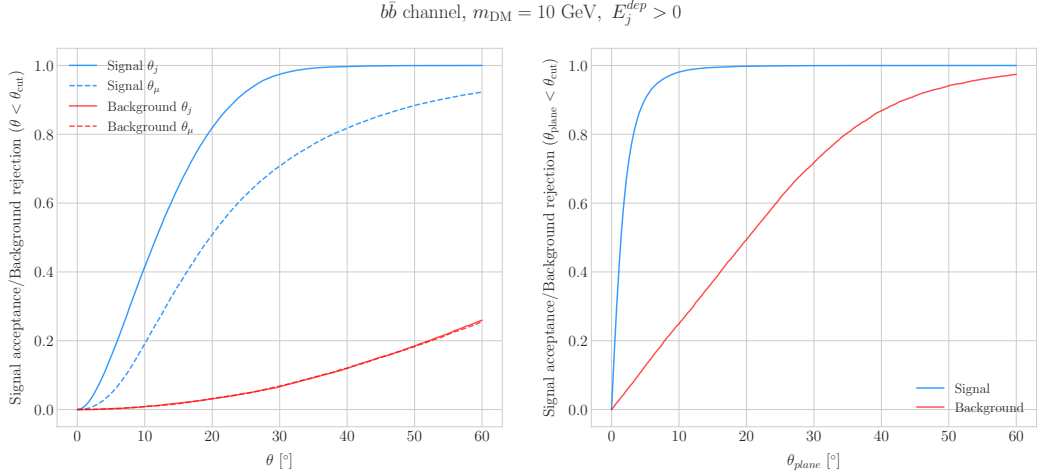


Figure 7.12: Left panel: signal efficiencies (blue lines) and background rejections (red lines) for events passing the cuts $\theta < \theta_{cut}$ for the jet (solid lines) and muon (dashed lines) angles. Right panel: signal efficiency (blue line) and background rejection (red line) for events passing the cut $\theta_{plane} < \theta_{cut}$ for the momentum conservation plane deviation.

way, if the outgoing muon in a certain event has an energy lower than the required threshold I will drop such event. For the case of hadrons and photons, I will only require to have at least one particle above the energy threshold, so then one can compute the jet momentum using the (smeared) momenta of the N particles above threshold as:

$$\vec{p}_j = \sum_{i=1}^N \vec{p}_i. \quad (7.28)$$

Additionally, I will also define an estimation of the deposited hadronic energy as:

$$E_j^{dep} = m_{^{39}\text{Ar}} - m_{^{40}\text{Ar}} + \sum_{i=1}^N \sqrt{|\vec{p}_i|^2 + m_i^2}. \quad (7.29)$$

This quantity is useful to select events with enough hadronic visible energy in the detector. For events where most of the hadronic energy is scattered across plenty of hadrons with individual energies below the detection threshold, this estimation will give $E_j^{dep} \leq 0$. In these cases it could be expected that the jet momentum is poorly reconstructed, and therefore I require events to pass the cut $E_j^{dep} > 0$.

For the events I can compute the angles for the muon and jet with respect to the

Chapter 7. DM searches with neutrinos from the Sun

2347 incoming neutrino as:

$$\cos \theta_\mu = \hat{p}_\nu \cdot \hat{p}_\mu, \quad (7.30)$$

$$\cos \theta_j = \hat{p}_\nu \cdot \hat{p}_j, \quad (7.31)$$

2348 and the deviation from the momentum conservation plane as:

$$\sin \theta_{plane} = \left| \frac{\hat{p}_\mu \times \hat{p}_\nu}{|\hat{p}_\mu \times \hat{p}_\nu|} \cdot \hat{p}_j \right|. \quad (7.32)$$

2349 In Fig. 7.11 I show some distributions of these quantities for the case of the $b\bar{b}$ sample
2350 with $m_{DM} = 10$ GeV (blue histograms) and for the atmospheric backgrounds (red).
2351 In order to select the atmospheric events I followed the same criteria as for the signal
2352 events. However, because in the signal case I used the true direction of the neutrino
2353 as input, as it should be that of the Sun at that time and therefore known, in the
2354 atmospheric case I used a set of solar positions as our ansatz for the neutrino direction.
2355 From the distributions, one can see that the muon and the jet for the signal events are
2356 predominantly forward and also that the deviations from the momentum conservation
2357 plane are peaked at zero, as one should expect.

2358 Now, I can start applying cuts to maximise our signal selection efficiency while at
2359 the same time I try to minimise the amount of atmospheric background events passing
2360 the selection. To this end, I will need to find some lower and upper cuts for θ_j and
2361 θ_μ and an upper bound for θ_{plane} . In Fig. 7.12 I show how upper bound cuts in the
2362 different angular variables affect the signal efficiency (blue lines) and the background
2363 rejection (red lines). Notice that the signal efficiency behaves in a quite different way
2364 when I apply cuts in the jet and the muon angles. On the contrary, the cuts on both
2365 variables have a similar effect on the background rejection.

2366 In order to obtain the optimal set of cuts, I perform a multidimensional scan. I
2367 do this separately for the $\tau^+\tau^-$ and the $b\bar{b}$ samples. For each case, I scan the possible
2368 cuts for each mass point and then I take the mean value of the signal efficiency for

7.6. High energy DM neutrino signals

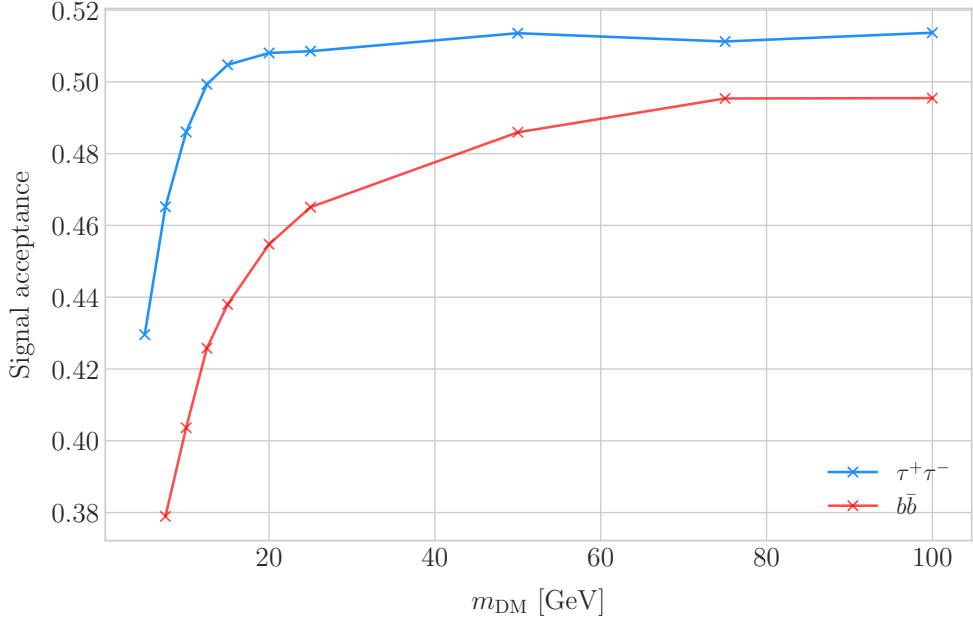


Figure 7.13: Signal efficiencies for the $\tau^+\tau^-$ (blue line) and $b\bar{b}$ (red line) DIS samples as functions of the DM mass, m_{DM} , obtained by applying the optimal angular cuts $\theta_\mu < 27^\circ$, $4^\circ < \theta_j < 26^\circ$ and $\theta_{\text{plane}} < 3.5^\circ$.

2369 each configuration, to get the mean efficiency for each set of cuts. I do a similar scan
 2370 for the atmospheric sample independently. Then, I take the sets of cuts such that
 2371 the background rejection achieved is greater than 99.8% and search for the one which
 2372 maximises the $\tau^+\tau^-$ and $b\bar{b}$ sample mean efficiencies. I found that with the cuts $\theta_\mu < 27^\circ$,
 2373 $4^\circ < \theta_j < 26^\circ$ and $\theta_{\text{plane}} < 3.5^\circ$ I get a background rejection of 99.80% while achieving
 2374 a 49.40% and 44.92% mean signal efficiencies for the $\tau^+\tau^-$ and $b\bar{b}$ signals respectively.

2375 In Fig. 7.13 I show the signal efficiencies as a function of the DM mass for the $\tau^+\tau^-$
 2376 (blue line) and the $b\bar{b}$ (red line) DIS events, after applying the cuts discussed above, as
 2377 well as the energy threshold and hadronic visible energy selections. One can see that
 2378 the efficiency grows with the mass, as annihilations of more massive DM particles will
 2379 produce a neutrino spectrum centered at higher energies, where DIS events dominate.
 2380 Notice also that the efficiency is higher for the $\tau^+\tau^-$ case at every mass point, as in
 2381 general this channel produces neutrinos at higher energies than the corresponding $b\bar{b}$
 2382 channel.

Chapter 7. DM searches with neutrinos from the Sun

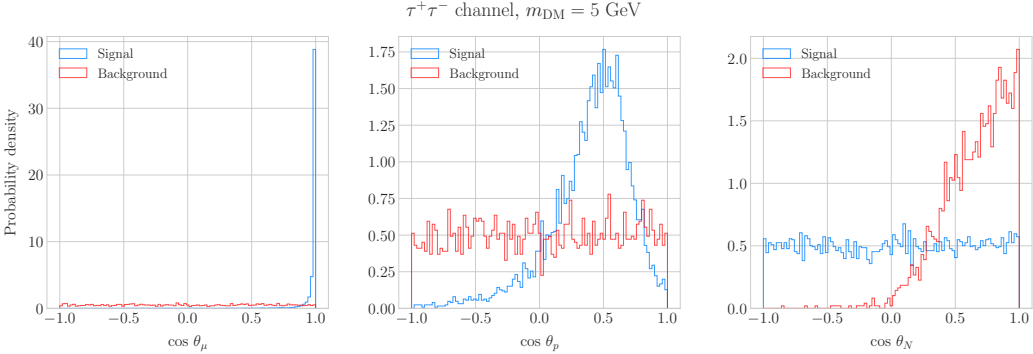


Figure 7.14: Distributions of $\cos \theta_\mu$ (left panel), $\cos \theta_p$ (central panel) and $\cos \theta_N$ (right panel) for the $\tau^+\tau^-$ QEL sample with $m_{\text{DM}} = 5$ GeV (blue) and the atmospheric background (red).

2383 7.6.2 Single proton QEL events

2384 Now, one can try to explore the low energy tail of the neutrino energy distributions. This
 2385 regime is dominated by the QEL interactions, i.e. events of the type $\nu_\mu + n \rightarrow \mu^- + p$.
 2386 In this case, as the typical energies are $E_\nu \lesssim 1$ GeV, the momentum transfer to the
 2387 remnant nucleus is sizeable. Therefore, I can not make the approximation I did before
 2388 and assume that the momentum of the muon and the proton will give an adequate
 2389 estimation of the reconstructed neutrino energy.

2390 In any case, as before, I can take the direction of the incoming neutrino as known.
 2391 That way, one can estimate the energy of the neutrino as:

$$E_\nu^{reco} = E_\mu + E_p + m_{^{39}\text{Ar}} - m_{^{40}\text{Ar}}, \quad (7.33)$$

2392 and using momentum conservation I can write the momentum of the remnant nucleus
 2393 as:

$$\vec{p}_N = \hat{p}_\nu (E_\mu + E_p + m_{^{39}\text{Ar}} - m_{^{40}\text{Ar}}) - \vec{p}_\mu - \vec{p}_p. \quad (7.34)$$

2394 As in the previous case, I need to drop the events where the muon or the proton fall
 2395 below the kinetic energy detection threshold [70]. Also, I again apply a smearing to the
 2396 momenta of the particles, a 1% for muons and 5% for protons.

2397 Having done that, one can compute the following angular variables for our selected

7.6. High energy DM neutrino signals

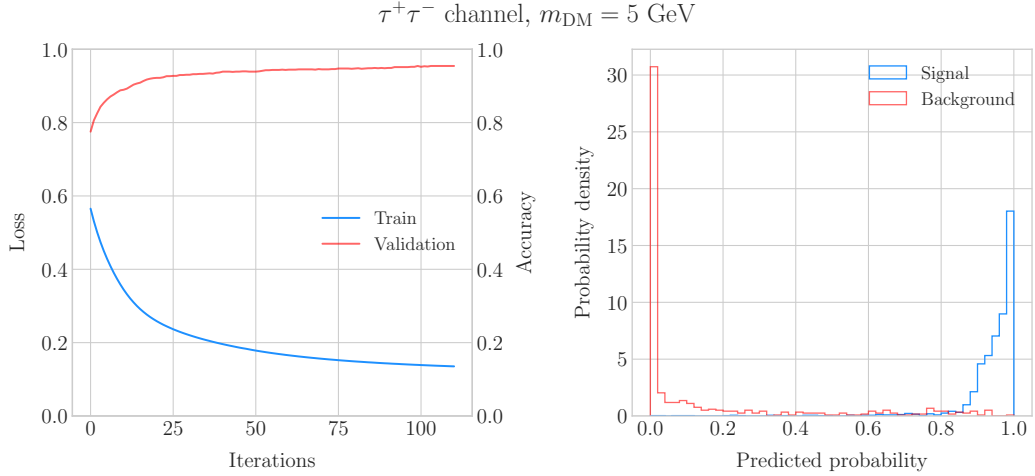


Figure 7.15: Left panel: value of the loss function for the training sample (blue line) and accuracy for the validation sample (red line) versus the number of iterations for the MLP classifier training. Right panel: distributions of the predicted probabilities assigned by the MLP classifier to the test sample for the $\tau^+\tau^-$ QEL signal with $m_{\text{DM}} = 5 \text{ GeV}$ (blue) and the atmospheric background (red).

2398 events:

$$\cos \theta_\mu = \hat{p}_\nu \cdot \hat{p}_\mu, \quad (7.35)$$

$$\cos \theta_p = \hat{p}_\nu \cdot \hat{p}_p, \quad (7.36)$$

$$\cos \theta_N = \hat{p}_\nu \cdot \hat{p}_N. \quad (7.37)$$

2399 Fig. 7.14 shows the distributions of these angular variables for the $\tau^+\tau^-$ QEL
 2400 sample with $m_{\text{DM}} = 5 \text{ GeV}$ (blue) and the atmospheric background (red). Again, for
 2401 the atmospheric events I used a random solar position as the ansatz for the incoming
 2402 neutrino direction. Notice that now, opposed to the DIS case where the signal had very
 2403 sharp distributions for the variables considered, the shapes of the angular distributions
 2404 for signal and background are not that much different.

2405 This effectively means that the usual approach of applying simple angular cuts would
 2406 not work as well as in the previous situation. Therefore, as a possible solution, I tried to
 2407 use a multilayer perceptron (MLP) classifier to separate between signal and background
 2408 events. Thus, the power of the hypothesis test will serve as an estimate of the signal

Chapter 7. DM searches with neutrinos from the Sun

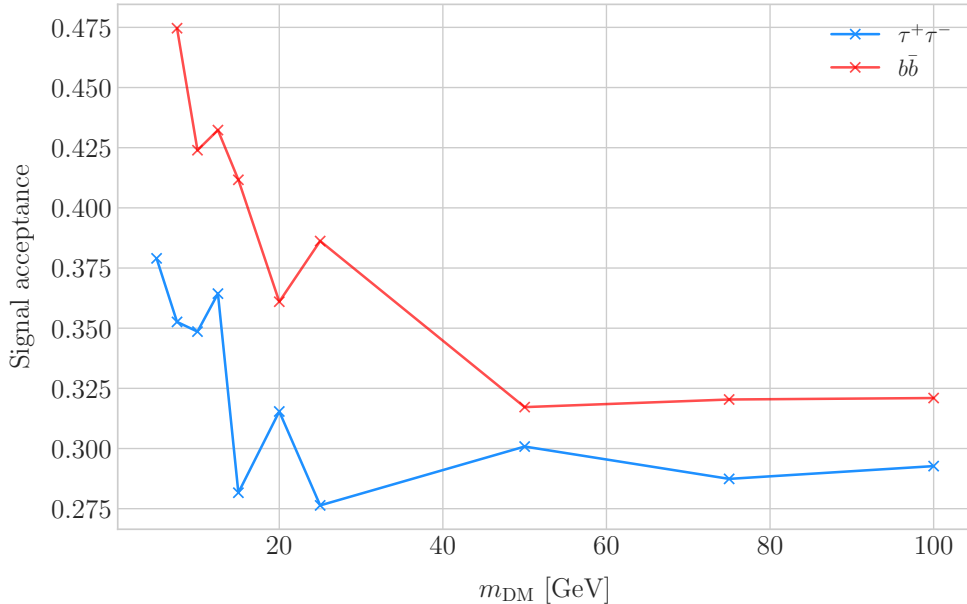


Figure 7.16: Signal efficiencies for the $\tau^+\tau^-$ (blue line) and $b\bar{b}$ (red line) single proton QEL samples as functions of the DM mass, m_{DM} , obtained by requiring a minimum predicted probability from the MLP classifier of 0.97 in order to achieve a background rejection greater than 99.8%.

efficiency, and in the same way one can take the size of the test to be our background rejection.

For each DM mass value and channel, as well as for the background sample, I divide our events into training, validation and test samples. The input variables for the classifier were the reconstructed neutrino energy from Eq. (7.33) and the angular variables defined in Eqs. (7.35 - 7.37). I used the MLP classifier implemented in `scikit-learn` [116], with a total of five hidden layers, the rectified linear unit activation function and adaptive learning rate. In order to account for fluctuations due to artifacts in the training process I repeated the training a thousand times for each sample, redefining each time the training, validation and test subsets, so one can take as our signal efficiency and background rejection the mean values of the powers and sizes of the tests.

The results of one of these training processes for the $\tau^+\tau^-$ QEL signal with $m_{\text{DM}} = 5$ GeV is shown in Fig. 7.15. On the left panel I show the loss function values (blue) and accuracy (red) at each iteration for the training and the validation samples respectively.

7.6. High energy DM neutrino signals

2423 The training stops either when the maximum number of iterations is reached (1000 in
2424 this case) or when the accuracy for the validation sample reaches a certain tolerance
2425 (I chose 10^{-4} as our tolerance). On the right panel I have the distributions for the
2426 predicted probability by the model, separated in true signal (blue) and background
2427 (red) events, for the test sample. One can see that both populations are well separated,
2428 obtaining a power of 44.97% and a size of 0.17% when I require a predicted probability
2429 greater than 0.97.

2430 Applying this criteria for each sample, I obtain the mean signal efficiencies shown in
2431 Fig. 7.16. Notice that the efficiencies for the channel $\tau^+\tau^-$ (blue line) are consistently
2432 lower than the ones for the $b\bar{b}$ channel (red line). This can be due to the fact that, for
2433 each DM mass point, the neutrino spectrum coming from the $b\bar{b}$ annihilation channel is
2434 centered at lower energies when compared to the $\tau^+\tau^-$ spectrum. This directly translates
2435 into more low energy neutrinos undergoing QEL interactions, which give signals that
2436 can be easily separated from the atmospheric background. This explanation also help us
2437 understand why in both cases the signal acceptance drops when the DM mass increases.
2438 In all cases, the background rejection took values between 99.8% to 99.9%. I will assume
2439 a 99.8% background rejection value in all cases to keep our estimation conservative.

2440 7.6.3 Results

2441 In order to estimate the DM-nucleon cross section sensitivities in the present case I need
2442 again to compute the expected number of background events. As I am now separating
2443 events by interaction type Eq. (7.25) does not hold anymore, as in that case I integrated
2444 over the total neutrino-argon cross section. In this instance, the expected background
2445 events for DIS events is approximately given by:

$$N_B^{DIS} \simeq \eta_B^{DIS} \times (4.655 \times 10^3) \times \left(\frac{\text{exposure}}{400 \text{ kT yr}} \right), \quad (7.38)$$

Chapter 7. DM searches with neutrinos from the Sun

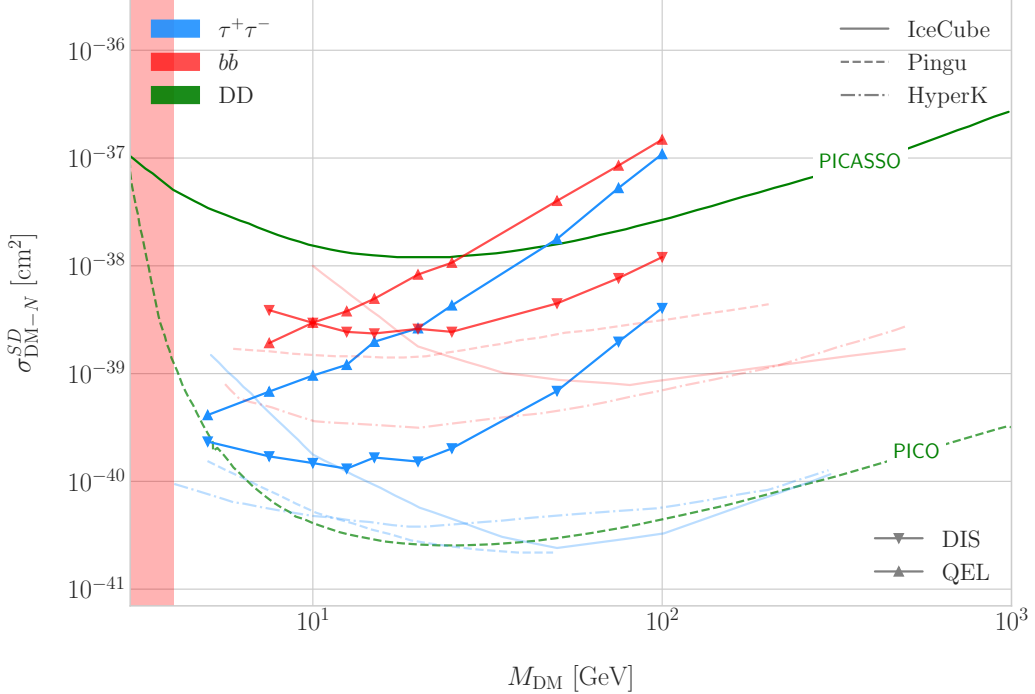


Figure 7.17: Projected 90% confidence level upper limit for DUNE (400 kT yr) on the spin-dependent DM-nucleon scattering cross section as a function of m_{DM} , for the annihilation channels $\tau^+\tau^-$ (blue) and $b\bar{b}$ (red) separated by interaction type (up triangles denote DIS interactions whereas down triangles represent QEL interactions). I also show the previous limits from IceCube [9] (solid lines) and the projected sensitivities for Pingu [10] (dashed lines) and Hyper-Kamiokande [11] (dash-dotted lines), as well as the direct detection limits from PICASSO [12] (solid green line) and PICO-60 C₃F₈ [13] (dashed green line).

2446 whereas for QEL events we have:

$$N_B^{QEL} \simeq \eta_B^{QEL} \times (2.248 \times 10^4) \times \left(\frac{\text{exposure}}{400 \text{ kT yr}} \right). \quad (7.39)$$

2447 Now, using these together with Eqs. (7.26) and (7.27) one can obtain the 90% C.L.
 2448 upper limit on the total annihilation rate at equilibrium for both kind of events. Then,
 2449 applying the computed DM-nucleons capture rates I can translate these into limits on
 2450 the DM-nucleon cross section by means of Eqs. (7.2), (7.5) and (7.6).

2451 Fig. 7.17 shows the obtained limits on the SD DM-nucleon cross section for DUNE,
 2452 using the DIS (up triangles) and QEL (down triangles) events both for the $\tau^+\tau^-$ (blue)
 2453 and the $b\bar{b}$ (red) samples, for an exposure of 400 kT yr. I also include the corresponding

7.7. Example: Leptophilic Dark Matter

2454 current limits from IceCube [9] (solid lines), as well as the projected sensitivities of Pingu
2455 [10] (dashed lines) and Hyper-Kamiokande [11] (dash-dotted lines). For comparison, I
2456 also show the reported direct detection limits from PICASSO [12] (solid green line) and
2457 PICO-60 C₃F₈ [13] (dashed green line).

2458 Notice that, for most of the mass range, the limits one can set by using the DIS
2459 events are stronger than those of the QEL interactions, except for the low mass part
2460 of both the $\tau^+\tau^-$ and the $b\bar{b}$ curves where the QEL events dominate. In general, the
2461 expected sensitivity of DUNE for DM masses $\lesssim 25$ GeV surpasses the stronger current
2462 indirect limits. However, experiments like Hyper-Kamiokande are foreseen to have an
2463 overall better sensitivity in this kind of searches, as they have a bigger active volume
2464 and accept a broader energy range.

2465 A pending question is what happens when we add the RES and MEC charged-current
2466 interaction contributions. In that case it would probably be more convenient to split
2467 the samples by final state interaction topologies. Also, another necessary improvement
2468 would be adding a full detector simulation and reconstructions. This will also require
2469 considering the effect of poorly reconstructed events or final states containing neutral
2470 particles such that they mimic the desired topology at the reconstruction level.

2471 7.7 Example: Leptophilic Dark Matter

2472 In general, the capture rate of DM particles by the Sun via interactions with electrons is
2473 several orders of magnitude smaller than the capture via DM-nucleus scattering. Thus,
2474 it would be sub-leading even when nucleon capture is loop suppressed. As I showed in
2475 Fig. 7.2, the capture rate via scattering off electrons only surpasses the capture rates
2476 via DM-nucleons interactions for DM masses $\lesssim 100 - 500$ MeV.

2477 However, if one considers a model where DM-nucleon interactions are forbidden even
2478 at loop level, then electron interactions will be the sole contributor to DM capture in
2479 the Sun. One can describe such scenario where the DM particles couple to leptons but
2480 not to the quark sector using effective operators.

Chapter 7. DM searches with neutrinos from the Sun

2481 In general, assuming that the DM particle is a Dirac fermion, the dimension six
 2482 operators describing the interaction between two DM particles and two leptons can be
 2483 written as:

$$\mathcal{L}_{eff} = G \sum_i (\bar{\chi} \Gamma_\chi^i \chi) (\bar{\ell} \Gamma_\ell^i \ell), \quad (7.40)$$

2484 where $G = 1/\Lambda^2$ is the effective coupling strength, Λ the cut-off of the effective field
 2485 theory and ℓ denotes any lepton. In principle, one should consider all the possible
 2486 Lorentz structures Γ_f^i in order to have a complete set of effective operators.

2487 However, some combinations will induce interactions with nucleons at loop level.
 2488 As we are specifically interested in interactions which forbid any communication with
 2489 the quark sector, I will not consider those [117]. In addition, some of the effective
 2490 operators give rise to velocity-suppressed scattering cross sections between DM particles
 2491 and leptons. I will also neglect those, as the suppression goes with the square of the DM
 2492 halo velocity which in units of the speed of light is $\sim 10^{-6}$.

2493 This way, the only Lorentz tensor structure that do not induce interactions with
 2494 quarks at loop level and gives a contribution to the scattering cross section that is not
 2495 velocity suppress is the axial-axial interaction. The effective Lagrangian is then given
 2496 by:

$$\mathcal{L}_{eff} = \frac{c_A^\chi c_A^\ell}{\Lambda^2} (\bar{\chi} \gamma^\mu \gamma^5 \chi) (\bar{\ell} \gamma_\mu \gamma^5 \ell), \quad (7.41)$$

2497 where c_A^χ and c_A^ℓ are the couplings for the different species. As the DM coupling appears
 2498 as a common factor for any lepton choice, I will redefine the corresponding coupling c_A^ℓ
 2499 to absorb c_A^χ . Also, for simplicity, I will assume that the couplings between the DM
 2500 particles and the leptons are flavour independent, i.e. I have just two couplings, c_A^e for
 2501 charged leptons and c_A^v for neutrinos.

2502 In the case of a scalar DM particle, the lowest order effective interaction with
 2503 leptons happens through a dimension five operator, generating scalar and pseudoscalar
 2504 interactions. However, the former induces interactions with quarks at two loop level
 2505 whereas the latter gives a velocity suppressed scattering cross section.

2506 From the effective Lagrangian in Eq. (7.41) it can be shown that the axial-axial

7.7. Example: Leptophilic Dark Matter

2507 contribution to the scattering cross section for the fermionic DM and a charged lepton
 2508 is given by:

$$\sigma_{\text{DM}-e}^{AA} = 3(c_A^e)^2 \frac{m_e^2}{\pi \Lambda^4}. \quad (7.42)$$

2509 If the DM interacts exclusively with fermions, then the only annihilation channels
 2510 that will give us a measurable neutrino flux coming out of the Sun are $\tau^+\tau^-$ and $\nu\bar{\nu}$. The
 2511 former channel, already explored previously in the more mainstream scenario of the DM
 2512 capture via scattering off nucleons, is open only for $m_{\text{DM}} > m_\tau \simeq 1776.86 \pm 0.12$ MeV
 2513 [118], a mass region where the solar DM capture by electrons is at least one order of
 2514 magnitude smaller than the capture via interactions with nucleons. On the contrary, the
 2515 latter allows us to explore a region where the capture rate via scattering off electrons
 2516 dominates over the rest.

2517 One downside of focusing in such low mass range is that it falls below the usual
 2518 limit of $m_{\text{evap}} \sim 4$ GeV usually explored in the literature. The pretext to explore this
 2519 region is the result discussed previously reported in Ref. [4], where DM evaporation in
 2520 the Sun for the case of capture via electron scattering could be negligible for masses
 2521 as low as $m_{\text{evap}} \sim 200$ MeV. This result is quite sensitive to the high velocity tail of
 2522 the DM velocity distribution in equilibrium inside the Sun, and therefore full numerical
 2523 simulations would be needed to assess the impact of this effect. However, this falls out of
 2524 the scope of our work.

2525 In this case, as I have a specific realisation of the interaction between the DM
 2526 and leptons, one can estimate the relic density of our DM for different values of the
 2527 couplings and the effective field theory scale Λ . The first step to do so is compute the
 2528 self-annihilation cross section. Because I consider cold relics, at the freeze-out time our
 2529 DM particles were non-relativistic and so one can expand the annihilation cross section
 2530 in terms of the relative velocity v between two annihilating DM particles as [119]:

$$\sigma_{\text{ann}}^{AA}|v| \approx \frac{1}{2\pi\Lambda^4} \sum_\ell \left(c_A^\ell\right)^2 m_\chi^2 \sqrt{1 - \frac{m_\ell^2}{m_\chi^2} \left[\frac{m_\ell^2}{m_\chi^2} + \frac{1}{12} \left(2 - \frac{m_\ell^2}{m_\chi^2}\right) v^2 \right]}, \quad (7.43)$$

Chapter 7. DM searches with neutrinos from the Sun

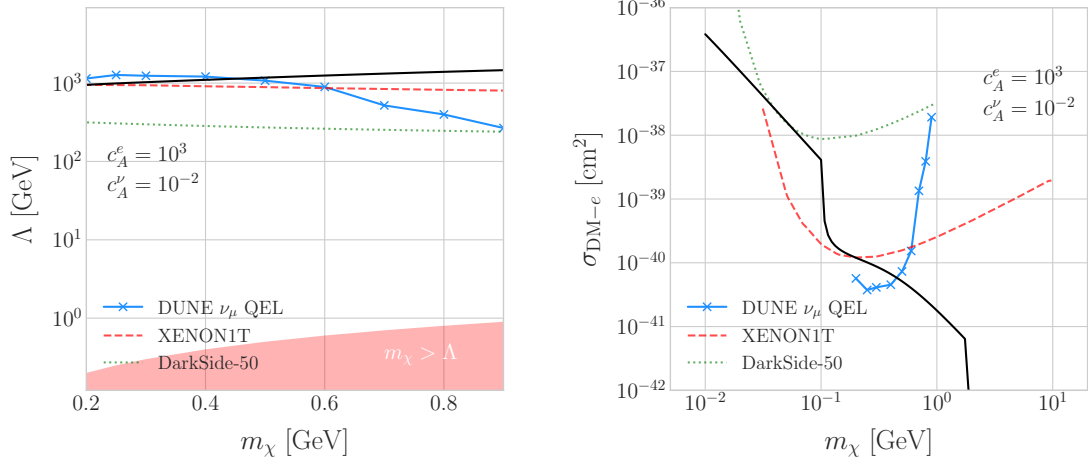


Figure 7.18: Left panel: Projected 90% confidence level sensitivity of DUNE (400 kT yr) to the scale Λ of an EFT containing only leptophilic DM axial-axial interactions (blue line). Right panel: . In both cases the corresponding limits from DarkSide-50 [14] (dotted green line) and XENON1T [15] (dashed red line) are also shown, together with the configurations for which the correct relic density is achieved (black line), all for the coupling values $c_A^e = 10^3$ and $c_A^\nu = 10^{-2}$.

2531 where the sum includes all the possible lepton final states with mass m_ℓ .
 2532 Solving the Boltzmann equation for the evolution of the DM density gives as a
 2533 solution a relic density of:

$$\Omega_\chi h^2 \approx \frac{(1.04 \times 10^9) x_F}{M_{Pl} \sqrt{g_*} (a + 3b/x_F)}, \quad (7.44)$$

2534 where $x_F = m_\chi/T_F$ being T_F the freeze-out temperature, g_* the number of relativistic
 2535 degrees of freedom at freeze-out and a and b the terms in the annihilation cross section
 2536 expansion $\sigma_{ann}|v| \approx a + bv^2 + \mathcal{O}(v^4)$. Using the current best fit for the relic DM density
 2537 $\Omega_\chi h^2 = 0.1198 \pm 0.0012$ [120] one can use these relations to compute the required
 2538 effective theory scale Λ at which the correct density is achieved for any combinations of
 2539 m_χ and c_A^ℓ .

2540 As discussed before, in the low DM mass region QEL interactions dominate. Moreover,
 2541 if I focus on direct annihilation to neutrinos, the energy of the muon neutrino flux is
 2542 known as it must be equal to the mass of the DM particle, $E_\nu = m_\chi$. That way, now
 2543 I do not need to use Eq. (7.33) in order to estimate the momentum transfer to the

7.7. Example: Leptophilic Dark Matter

2544 remnant nucleus, I can simply take:

$$\vec{p}_N = \hat{p}_\nu m_\chi - \vec{p}_\mu - \vec{p}_p. \quad (7.45)$$

2545 To estimate the signal efficiency and background rejection for this case I used again
2546 the MLP classifier from `scikit-learn`, using the same specifications as before. The
2547 only difference now is that I add also the reconstructed neutrino energy as one of the
2548 features to train the classifier with, because the characteristic monoenergetic flux for
2549 each m_χ value will help to distinguish between signal and background events.

2550 In this case, for masses below ~ 500 MeV I obtain a signal efficiency close to unity
2551 while keeping a background rejection of 99.9%. For bigger values of the mass, the signal
2552 efficiency drops significantly if I require to keep the background acceptance under 0.01%.
2553 However, because this kind of search is dominated by the background, sacrificing the
2554 signal acceptance to keep the background rejection to a minimum enhances the reach
2555 of the analysis. This way, for DM masses of the order of $m_\chi \sim 1$ GeV I end up with
2556 efficiencies as low as 1%.

2557 Now, estimating the number of background events using Eq. (7.39) one can go on
2558 and apply Eqs. (7.26) and (7.27) together with Eq. (7.42) to derive the sensitivity of
2559 DUNE to this kind of model. Fig. 7.18 (left panel) shows the potential reach of DUNE
2560 to constrain the EFT scale Λ this model containing only leptophilic DM axial-axial
2561 interactions (blue line), for a choice of couplings $c_A^e = 10^3$ and $c_A^\nu = 10^{-2}$. I also included
2562 the current limits on the DM-electron scattering cross section from DarkSide-50 [14]
2563 (dotted green line) and XENON1T [15] (dashed red line), reworked with Eq. (7.42) to
2564 show their implications for the EFT scale. The values of Λ for which the correct DM relic
2565 density value is achieved for each mass are also shown (black line). This tells us that,
2566 for that specific choice of couplings, DUNE would be sensitive to DM configurations
2567 allowed by the relic density constraint up to a mass of $m_\chi \sim 400$ MeV.

2568 In Fig. 7.18 (right panel) I show the same upper limits but for the DM-electron
2569 scattering cross section. From this view one can see that DUNE would be able to

Chapter 7. DM searches with neutrinos from the Sun

offer complementary information to the low energy DM-electron interaction searches performed by direct detection experiments, in a slightly higher mass range.

With the present example, although it focuses on a very specific realisation of the DM interactions, I show the potential of DUNE to constrain exotic DM scenarios. Thanks to its low backgrounds and superb angular resolution DUNE will be able to help with the systematic searches for dark sectors physics.

2576 Chapter 8

2577 Particle ID in GArSoft

2578 ND-GAr is a magnetised, high-pressure gaseous argon TPC (HPgTPC), surrounded by
2579 an electromagnetic calorimeter (ECal) and a muon detector (commonly refer to as μ ID).
2580 A detailed discussion on the requirements, design, performance and physics of ND-GAr
2581 can be found in the DUNE ND CDR [76] and the ND-GAr whitepaper (cite).

2582 In DUNE Phase II ND-GAr will fulfill the role of TMS, measuring the momentum
2583 and sign of the charged particles exiting ND-LAr. Additionally, it will be able to measure
2584 neutrino interactions inside the HPgTPC, achieving lower energy thresholds than those
2585 of the ND and FD LArTPCs. By doing so ND-GAr will allow to constrain the relevant
2586 systematic uncertainties for the LBL analysis even further.

2587 The goal of the present chapter is to review the requirements that the physics program
2588 of DUNE impose on ND-GAr, present the current status of its design and describe the
2589 GArSoft package, its simulation and reconstruction software.

2590 As decided during the DUNE Phase II workshop in June 2023 [reference], we want
2591 to build ND-GAr physics case by showing:

- 2592 • That ND-GAr can constrain systematic uncertainties that ND-LAr might miss.
- 2593 • The impact on the neutrino oscillation results if such systematic uncertainties are
2594 missed.
- 2595 • That ND-GAr is necessary to reach DUNE's main physics goals.

Chapter 8. Particle ID in GArSoft

2596 This way, the design of ND-GAr will be physics driven.

2597 In order to study the effects of final state interactions (FSI) in CC interactions,
2598 ND-GAr should be able to measure the spectrum of protons and charged pions at low
2599 energies. ND-GAr also needs to be able to measure the pion multiplicity, specially for
2600 energies above 100 MeV as at these energies the pions shower in the LAr, to inform the
2601 pion mass correction in the ND and FD LArTPCs.

2602 In order to correctly identify electrons, muons, pions, kaons and protons ND-GAr
2603 can use a combination of: dE/dx measurements in the HPgTPC, E_{ECAL}/p using the
2604 ECAL total energy and the momentum obtained from magnetic spectroscopy in the
2605 HPgTPC and penetration information through the ECAL and muon tagger.

2606 8.1 dE/dx measurement in the TPC

2607 Among the parameters extracted from the track fitting, ionisation is particularly useful
2608 for particle identification, as it is a function of the particle velocity. Although for the
2609 case of relativistic particles this dependence is not very strong, measuring the track on
2610 a large number of points may allow us to estimate the amount of ionisation accuratel.
2611 This, paired with a measurement of the momentum, may allow us to identify the particle
2612 type.

2613 The first calculation of the energy loss per unit length of relativistic particles using a
2614 quantum-mechanical treatment is due to Bethe [121]. Using this approach, the mean
2615 ionisation rate of a charged particle traveling through a material medium is (using
2616 natural units $G = \hbar = c = 1$):

$$\left\langle \frac{dE}{dx} \right\rangle = \frac{4\pi Ne^4}{m_e \beta^2} z^2 \left(\log \frac{2m_e \beta^2 \gamma^2}{I} - \beta^2 \right), \quad (8.1)$$

2617 where N is the number density of electrons in the medium, e the elementary charge, m_e
2618 is the electron mass, z the charge of the particle in units of e , β is the velocity of the
2619 particle, $\gamma = (1 - \beta^2)^{-1}$ and I denotes the effective ionisation potential averaged over
2620 all electrons. This relation is known as the Bethe-Bloch formula.

8.1. dE/dx measurement in the TPC

From Eq. (8.1) one can see that the ionisation loss does not depend explicitly on the mass of the charged particle, that for non-relativistic velocities it falls as β^{-2} , then goes through a minimum and increases as the logarithm of γ . This behaviour at high velocities is commonly known as the relativistic rise. The physical origin of this effect is partly due to the fact that the transverse electromagnetic field of the particle is proportional to γ , therefore as it increases so does the cross section.

It was later understood that the relativistic rise could not grow indefinitely with γ . A way to add this feature in the Bethe-Bloch formula is by introducing the so-called density effect term. It accounts for the polarisation effect of the atoms in the medium, which effectively shield the electromagnetic field of the charged particle halting any further increase of the energy loss [122]. Denoting the correction as $\delta(\beta)$, one can rewrite Eq. (8.1) as:

$$\left\langle \frac{dE}{dx} \right\rangle = \frac{4\pi Ne^4}{m_e \beta^2} z^2 \left(\log \frac{2m_e \beta^2 \gamma^2}{I} - \beta^2 - \frac{\delta(\beta)}{2} \right). \quad (8.2)$$

In general, the form of $\delta(\beta)$ depends on the medium and its state of aggregation, involving the usage of tabulated parameters and implicit relations [123].

Another standard method to compute the amount of ionisation a charged particle produces is the so-called photo-absorption ionisation (PAI) model proposed by Allison and Cobb [124]. Within their approach, the mean ionisation is evaluated using a semiclassical calculation in which one characterises the continuum material medium by means of a complex dielectric constant $\epsilon(k, \omega)$. However, in order to model the dielectric constant they rely on the quantum-mechanical picture of photon absorption and collision. Therefore, in the PAI model the computation of the ionisation loss involves a numerical integration of the measured photo-absorption cross-section for the relevant material.

In a particle physics experiment, the typical way of determining the energy loss per unit length as a function of the particle velocity is studying identified particles over a range of momenta. Once we have established this relation we can use it for other, unknown particles. In this sense, it makes sense to have a regular mathematical expression for this relation that one can use.

Chapter 8. Particle ID in GArSoft

2648 It happens that neither the Bethe-Bloch theory nor the PAI model from Allison and
2649 Cobb offer a close mathematical form for the ionisation curve. This is the reason why a
2650 full parametrisation of the ionisation curves can be useful. A parametrisation originally
2651 proposed for the ALEPH TPC [125] and later used by the ALICE TPC [126] group that
2652 manages to capture the features of the ionisation energy loss is:

$$f(\beta\gamma) = \frac{P_1}{\beta^{P_4}} \left(P_2 - \beta^{P_4} - \log \left[P_3 + \frac{1}{(\beta\gamma)^{P_5}} \right] \right), \quad (8.3)$$

2653 where P_i are five free parameters. Hereafter, we will refer to Eq. (8.3) as the ALEPH
2654 dE/dx parametrisation.

2655 8.1.1 Energy calibration

2656 In order to obtain the amount of energy loss by a charged particle due to ionisation
2657 in our TPC we need to determine the conversion between the charge deposited in our
2658 readout planes and the actual energy depositions. This procedure is known as energy
2659 calibration.

2660 In a general, the first step of the calibration involves a non-uniformity correction,
2661 to make sure that the detector response is uniform throughout the TPC. These are
2662 typically divided into three categories, non-uniformities in the transverse YZ plane,
2663 non-uniformities along the drift direction X and variations of the detector response
2664 over time (would not apply to us as the detector is not built yet). These would correct
2665 for effects such as electron diffusion and attenuation, space charge effects or channel
2666 misconfiguration. However, because at the moment I am only interested in making sure
2667 we recover a sensible result from our simulation, I will not apply uniformity corrections
2668 to our charge deposits.

2669 Other effects, like electron-ion recombination or ADC saturation, lead to a non-linear
2670 relation between the observed charge and the deposited energy in the detector, with the
2671 observed readout charge saturating at high ionisation energies. In this case, because we
2672 are dealing with gaseous argon and therefore recombination is not as important as in

8.1. dE/dx measurement in the TPC

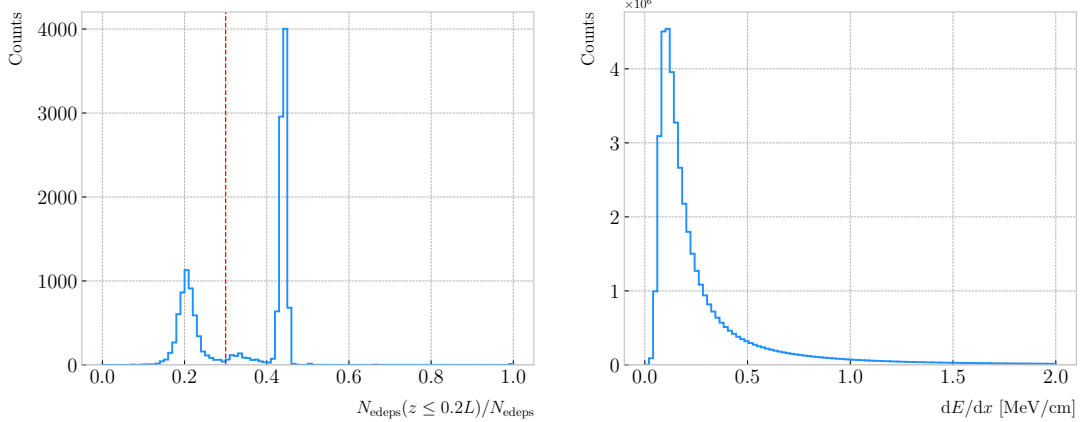


Figure 8.1: Left panel: distribution of the fraction of Geant4-level energy deposits per track with residual range less than 20% of the total track length, for the isotropic proton sample. Right panel: distribution of the ionisation per unit length of the energy deposits in the proton sample after removing the tracks with less than 30% of their energy deposits in the last 20% of the track.

liquid, we do not simulate recombination effects in the TPC. Even so, the simulation of the electronic response will still introduce charge saturation, and one needs to correct for it in order to obtain the exact amount of energy loss due to ionisation.

By default, the track fitting algorithm in GArSoft provides a `TrackIonization` object associated to each reconstructed track. It contains two collections of charge deposits, one for each fitting direction, consisting on pairs of charge values (dQ , in ADC) and step sizes (dx , in cm).

In order to estimate the ionisation loss in the ND-GAr TPC, I have used an MC sample consisting of single, isotropic protons propagating in the TPC. The starting points of the protons were sampled inside a $50 \times 50 \times 25$ cm box centered at $(100, -150, 1250)$, and their momenta are uniformly distributed in the range $0.25 - 1.75$ GeV. I ran the simulated sample through GArSoft's default detector simulation and reconstruction, and then a custom analyser module that extracts the ionisation data together with other reconstructed track information from the Kalman fit.

For studying the energy loss of the protons I select the reconstructed tracks that range out (i.e. slow down to rest) inside the TPC. A characteristic feature of the energy loss profile of any stopping ionising particle is the so-called Bragg peak, a pronounced

Chapter 8. Particle ID in GArSoft

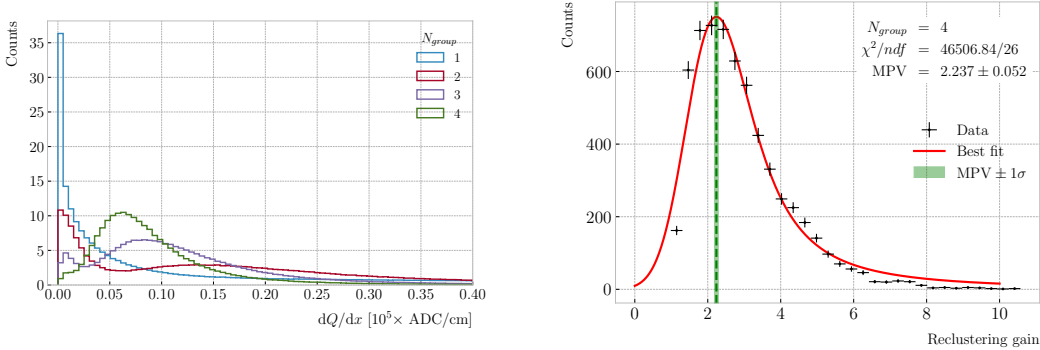


Figure 8.2: Left panel: distribution of the reconstructed ionisation charge per unit length for our MC stopping proton sample. The different colors indicate how many consecutive dQ/dx pairs were grouped together. Right panel: distribution of the median change in dQ/dx per track after $N_{group} = 4$ clusters were reclustered together.

peak that occurs immediately before the particle comes to rest. From Eq. (8.1) we can see that this behaviour is expected, as the energy loss for non-relativistic particles is inversely proportional to β^2 . In data, a way of identifying the Bragg peak, and thus select the stopping particles, is checking the number of energy deposits towards the end of the track. In this case, I count the fraction of the Geant4 simulated energy deposits with a residual range value (the distance from a given energy deposit to the last deposit in the track trajectory) less than a 20% of the corresponding track length¹. The distribution of this fraction of energy deposits for our proton sample is shown in Fig. 8.1 (left panel). We can clearly see two well separated peaks in this distribution, one centered at 0.2 and another, narrower, one centered at a higher value. The first one corresponds to non-stopping protons, as in that case the number of energy deposits towards the end of the track is uniformly distributed due to the absence of the Bragg peak. In that way, I apply a cut in this distribution, requiring that at least 30% of the simulated energy deposits sit in the last 20% of the tracks, to ensure that the Bragg peak is present.

Figure 8.1 (right panel) shows the distribution of the energy loss per unit length for the Geant4 simulated energy deposits of the selected stopping protons. We can see that

¹As we are applying this selection at the Geant4 level we could have simply selected the stopping protons using the `EndProcess` labels from the simulation. However, the Bragg peak identification method displayed here could serve as a starting point for a selection of stopping protons in real data.

8.1. dE/dx measurement in the TPC

it follows the expected shape of a Landau distribution, which describes the fluctuations of the ionisation energy losses [127]. This distribution has a characteristic asymmetric PDF, with a long right tail that translates into a high probability for high-energy ionisation losses. The origin of these fluctuations is mainly the possibility of transferring a high enough energy to an electron, so it becomes a ionising particle itself.

Now, from the point of view of the reconstruction, the objects that we have available to extract the ionisation information for the different reconstructed tracks are the collections of dQ and dx pairs, as stated before. The dQ values come from adding up the amplitude of all the reconstructed hits in a cluster, which is the input object to the Kalman fit.

Figure 8.2 (left panel) shows the distribution of the ionisation charge deposits per unit length for the track in the stopping proton sample (blue line). As one can notice, this distribution does not resemble the expected shape of the Landau PDF. This distribution peaks sharply at 0 and has a heavy tailed behaviour. Notice, however, how the distribution changes its shape as we group together N_{group} consecutive charge deposit pairs (red, purple and green lines). The distribution in the $N_{group} = 4$ case already has a shape which resembles that of the Geant4-level ionisation per unit length, so I will proceed using this amount of reclustering for the reconstruction-level depositions.

An extra factor I need to account for, when reclustering is applied, is how the overall dQ/dx per track changes. To do so, we can look at the ratio between the median dQ/dx after and before the reclustering. Figure 8.2 (right panel) shows the median enhancement in dQ/dx per track for the stopping proton sample in the case $N_{group} = 4$. Fitting a Landau distribution convolved with a Gaussian², I estimate the most probable value of this ratio to be $G_{group} = 2.24 \pm 0.05$.

At this point, I am left with determining the conversion between the charge deposits per unit length dQ/dx and the energy deposits per unit length dE/dx . To this end, we need a way of comparing the two. I can use the residual range z to get a prediction of

²In the literature, this distribution is often referred to as Landau+Gaussian or langau. In the following, I will use LanGauss to refer to such PDF.

Chapter 8. Particle ID in GArSoft

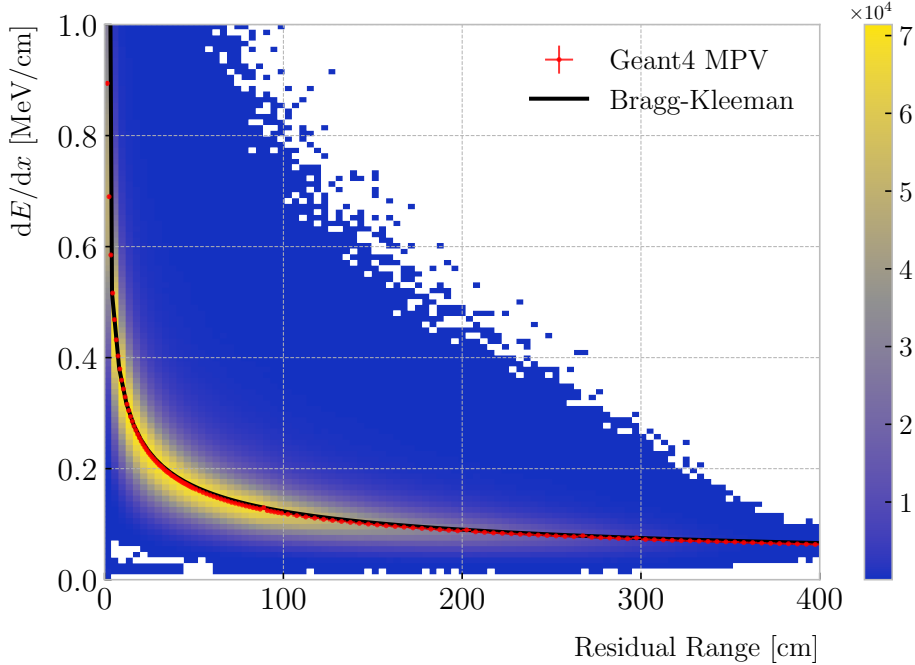


Figure 8.3: Distribution of the Geant4-simulated energy losses per unit length versus residual range for the stopping proton sample. The overlaid points represent the fitted most probable value of the dE/dx distribution in each residual range bin, whereas the curve is their best fit to the Bragg-Kleeman formula from Eq. (8.4).

2734 the most probable dE/dx by using the following empirical parametrisation [128]:

$$\frac{dE}{dx}(z) = \frac{z^{\frac{1}{p}-1}}{p\Lambda^{\frac{1}{p}}}, \quad (8.4)$$

2735 which is quoted in the literature as the Bragg-Kleeman formula. In order to obtain the
 2736 p and Λ parameters I perform a fit using the energy losses and the residual ranges given
 2737 by the Geant4 stage of our proton sample.

2738 Within our simulation, the residual range is sampled with a maximum size of
 2739 5 mm. Therefore, to perform the fit to the Bragg-Kleeman formula, we can use a
 2740 fine-grained residual range binning. For each of the residual range bins I extract the
 2741 dE/dx distribution and fit it to a LanGauss distribution, to obtain the value of the
 2742 most probable dE/dx in the bin together with a statistical uncertainty. I then fit Eq.
 2743 (8.4) to these most probable values and the centres of the residual range bins. This

8.1. dE/dx measurement in the TPC

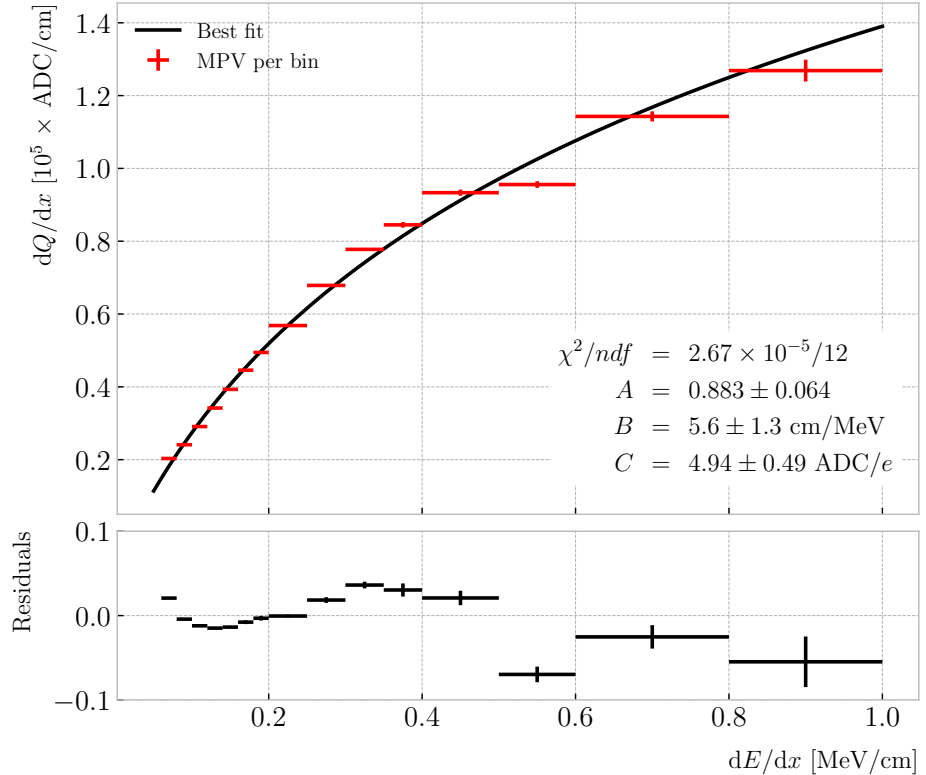


Figure 8.4: Fitted most probable dQ/dx values for each dE/dx bin (red points), obtained from the stopping proton sample. The overlaid curve (black line) represents the best fit to the logarithmic calibration function from Eq. (8.5).

procedure is depicted in Fig. 8.3, where I show the distribution of the energy loss per unit length versus the residual range, together with the most probable dE/dx values and their uncertainty in each bin (red points) and the curve with the best fit of the Bragg-Kleeman relation to those values (black line). The best fit is obtained for the parameter values $p = 1.8192 \pm 0.0005$ and $\Lambda = 0.3497 \pm 0.0008$ cm/MeV³.

Having an analytical expression that relates the residual range to dE/dx , I can take our reconstruction-level residual ranges from the stopping proton sample and compute the most probable energy loss associated.

In order to parametrise the charge saturation, we can use the following logarithmic

³These strange units for Λ come from dimensional analysis, just to keep the Bragg-Kleeman formula (8.4) consistent.

Chapter 8. Particle ID in GArSoft

2753 function inspired by the modified box model for recombination:

$$\frac{dE}{dx} = \frac{e^{\frac{dQ}{dx}B\frac{W_{ion}}{G_{group}C}} - A}{B}, \quad (8.5)$$

2754 where A and B are the calibration parameters we need to determine, W_{ion} is the average
 2755 energy to produce an electron-ion pair, G_{group} is the gain from the reclustering discussed
 2756 above and C is the calibration constant to convert number of electrons to ADC counts,
 2757 commonly refer to as gain (also to be obtained in the fit). In this case, I use a value
 2758 for the electron-ion production energy of $W_{ion} = 26.4$ eV [129]. This value, used in our
 2759 simulation as well, was measured for gaseous argon in normal conditions, and therefore
 2760 should be checked in the future to describe correctly the high-pressure argon-CH₄ mixture
 2761 of ND-GAr.

2762 For the calibration fit I follow a procedure similar to the previous one for Eq. (8.4).
 2763 Binning the dE/dx range, I fit a LanGauss distribution to the corresponding dQ/dx
 2764 distribution to obtain the most probable value. The resulting data points (red bars) are
 2765 shown in Fig. 8.4 (top panel), the horizontal error bars depict the width of the dE/dx
 2766 bin whereas the vertical bars represent the error associated to the most probable value
 2767 estimation. A fit to the logarithmic function in Eq. (8.5) is also shown (black line).
 2768 For this I weighted the data points using the inverse of their relative error, obtaining
 2769 a reduced chi-square value of $\chi^2/ndf = 2.22 \times 10^{-6}$. The best fit parameters I found
 2770 from this fit are $A = 0.883 \pm 0.064$, $B = 5.6 \pm 1.3$ cm/MeV and $C = 4.94 \pm 0.49$ ADC/e.
 2771 Figure 8.4 (bottom panel) shows the residuals between the data points and the fit.

2772 The value for the gain I obtained from the fit is in reasonable agreement with our
 2773 expectation. This value is set in GArSoft to 5 ADC/e by default.

2774 One interesting thing to check is what induces this non-linear relation between charge
 2775 and energy. The only effects that modify the amount of electrons reaching the readout
 2776 planes in the simulation are the transverse diffusion and the finite electron lifetime.
 2777 Once the electrons reach the readout chambers, the pad response functions are applied,
 2778 together with an electrons-to-ADC conversion and the ADC saturation limit.

8.1. dE/dx measurement in the TPC

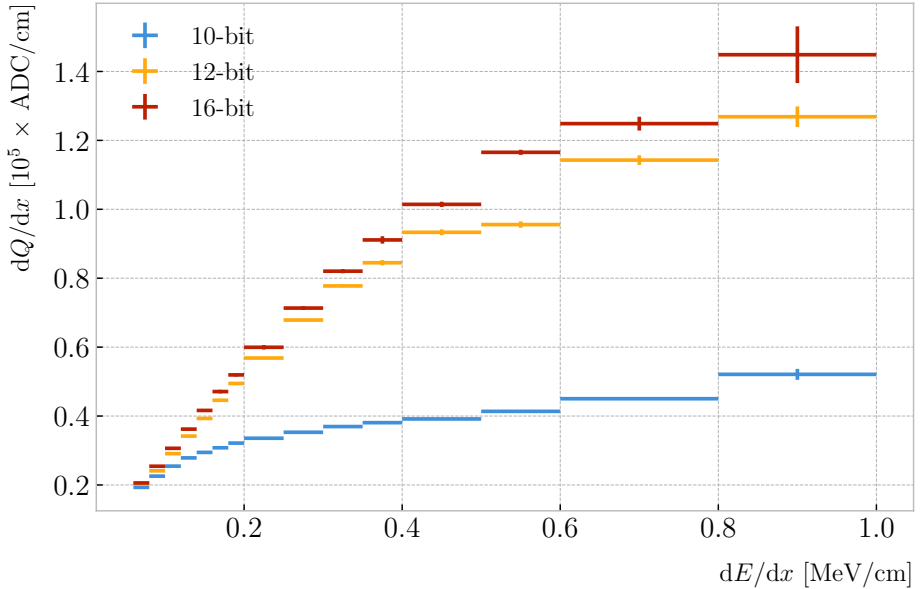


Figure 8.5: Fitted most probable dQ/dx values for each dE/dx bin for three different ADC bit limits, 10 (blue points), 12 (default, yellow points) and 16-bit (red points).

Table 8.1: Calibration parameters obtained from the fit of the ND-GAr simulated stopping proton sample to the calibration function from Eq. (8.5). The fits were performed for the 10, 12, and 16-bit ADC limits.

	χ^2/ndf	Best fit $\pm 1\sigma$		
		A	B (cm/MeV)	C (ADC/e)
10-bit	$1.83 \times 10^{-6}/12$	-9.3 ± 3.9	270 ± 69	27.1 ± 5.4
12-bit	$2.67 \times 10^{-5}/12$	0.883 ± 0.064	5.6 ± 1.3	4.94 ± 0.49
16-bit	$1.44 \times 10^{-5}/12$	0.949 ± 0.024	3.53 ± 0.58	4.52 ± 0.29

By default, GArSot applies a 12-bit ADC limit, which can be changed in the simulation configuration. However, it can only be increased up to 16-bit, as we represent the ADC collection as a `std::vector<short>`. This way, I tried to change the saturation parameter to see how it affects the relation between reconstructed charge and energy. Figure 8.5 shows a comparison between the most probable dQ/dx for 10, 12 and 16-bit ADC limits. As expected, the lower the limit is the sooner the charge saturates. For higher ADC limits the relation between energy and charge remains linear up to higher dE/dx values, but even for the 16-bit limit the saturation is noticeable for values $\gtrsim 0.5$ MeV/cm.

Chapter 8. Particle ID in GArSoft

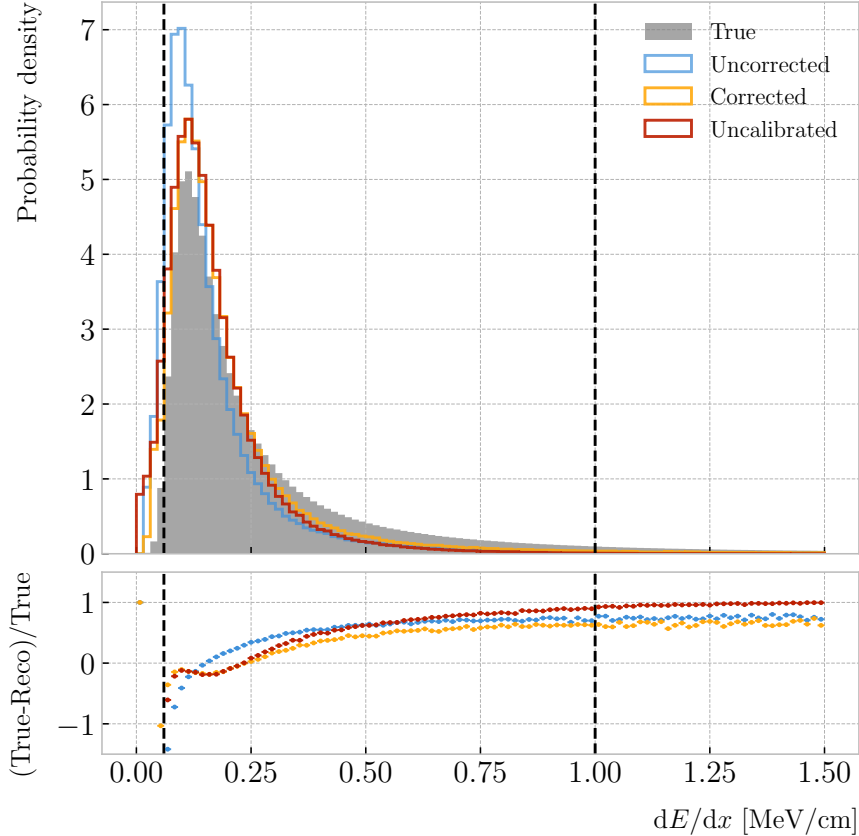


Figure 8.6: Top panel: area normalised dE/dx distributions for the true (solid grey) and the reconstructed energy deposits in the stopping proton sample, both after applying the calibration (blue) and the calibration and the normalisation correction (yellow). Also shown is the distribution obtained by applying a correction factor to the dQ/dx values but not the calibration (red). Bottom panel: fractional residuals for the uncorrected (blue), corrected (yellow) and uncalibrated (red) samples.

Table 8.1 shows the results of fitting the samples with 10 and 16-bits ADC limits to the calibration function from Eq. (8.5), using the weights based on their relative error as described previously. One interesting feature to notice is how different the best fit points look for the 10-bit ADC saturation when compared to the other two, which are consistent with each other.

At this point we can compare the dE/dx distribution one gets from Geant4, i.e. the true energy loss distribution, and the distribution I found by applying the calibration function to our collection of reconstructed dQ/dx values. Figure 8.6 (top panel) shows the true (solid grey) and reconstructed (blue, labeled as uncorrected) distributions

8.1. dE/dx measurement in the TPC

2797 together. The dashed vertical lines indicate the region of validity of the calibration fit, i.e.
2798 the left and right edges of the first and last dE/dx bin respectively. Notice that these
2799 histograms are area-normalised, as the total number of true energy deposits is much
2800 higher than the number of reconstructed charge deposits. This is due to a combination
2801 of effects, like the finite spatial resolution of the detector, the hit clustering used in the
2802 track fitting and the reclustering we have applied here.

2803 The two distributions are significantly different. That can be seen clearly when
2804 looking at the fractional residuals, shown in Fig. 8.6 (bottom panel). In particular,
2805 the position of the peak is off, which could bias the mean energy loss predictions. It
2806 seems like the difference between these may be due to an overall scaling factor. One
2807 possibility is to scale the most probable value of the reconstructed distribution to
2808 the most probable value predicted by Geant4. I do this by fitting both distributions
2809 using a LanGauss function, obtaining $dE/dx_{MPV, true} = 0.1145 \pm 0.0005$ MeV/cm and
2810 $dE/dx_{MPV, reco} = 0.0928 \pm 0.0005$ MeV/cm for the true and reconstructed most probable
2811 values respectively. These can be translated into an scaling factor $S = 0.579 \pm 0.006$.

2812 The result of applying the scaling correction can be seen in Fig. 8.6 (top panel).
2813 The corrected dE/dx distribution (yellow, labeled as corrected) peaks around the same
2814 value the true distribution does, as expected. Moreover, the high energy region is also
2815 slightly better described. For low ionisations, below the lower limit of the calibration
2816 fit, the differences between true and reconstructed are still significant. This low energy
2817 excess may be migration of some events from the peak region. The overall effect of the
2818 correction can be seen in the fractional residual plot in Fig. 8.6 (bottom panel).

2819 One can also check what happens if instead of applying the logarithmic calibration we
2820 simply scale the dQ/dx distribution (post reclustering) to have the same most probable
2821 value as the true dE/dx distribution. In this case, following an analogous procedure to the
2822 one described earlier, I found the scaling factor $S_{uncalibrated} = 0.414 \pm 0.002$ MeV/ADC⁴.
2823 The resulting distribution (red, labeled as uncalibrated) is also shown in in Fig. 8.6 (top
2824 panel). The behaviour of the new distribution is similar to the corrected case at low

⁴Notice that now the scaling factor is not dimensionless, as it acts more like a conversion factor here.

Chapter 8. Particle ID in GArSoft

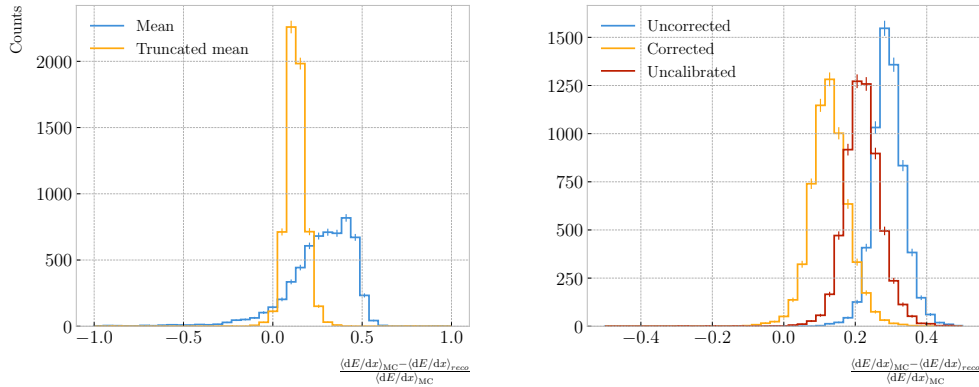


Figure 8.7: Left panel: fractional residuals between the true and the corrected dE/dx means (blue) and the 60% truncated means (yellow), for each event in the stopping proton sample. Right panel: fractional residuals between the true and the uncorrected (blue), corrected (yellow) and uncalibrated (red) dE/dx 60% truncated means, for each event in the stopping proton sample.

2825 energy losses, around the peak of the true distribution, but it is worse at describing the
 2826 high energy tail. This is expected, it is in the high ionisation regime where saturation
 2827 effects apply and therefore calibration is needed.

2828 8.1.2 Truncated dE/dx mean

2829 Once we have a collection of dE/dx values for each reconstructed track, we can compute
 2830 the corresponding most probable ionisation loss per unit length of the particle. This
 2831 is the value predicted by the Bethe-Bloch or the PAI models, and together with a
 2832 measurement of the momentum it allows for particle identification.

2833 However, estimating the most probable dE/dx value for each reconstructed track
 2834 is not a trivial task. As mentioned before, the dE/dx distributions follow Landau-like
 2835 distributions. Therefore, one should perform e.g. a LanGauss fit to correctly estimate
 2836 the most probable values. Automating this kind of fits is often problematic, as they
 2837 usually incur in convergence problems. Moreover, the reconstructed dE/dx distributions
 2838 we obtain tend to have relatively small statistics, which may also produce poor fits. In
 2839 practice, doing these unsupervised fits may degrade our performance, and a more robust
 2840 method is preferred.

8.1. dE/dx measurement in the TPC

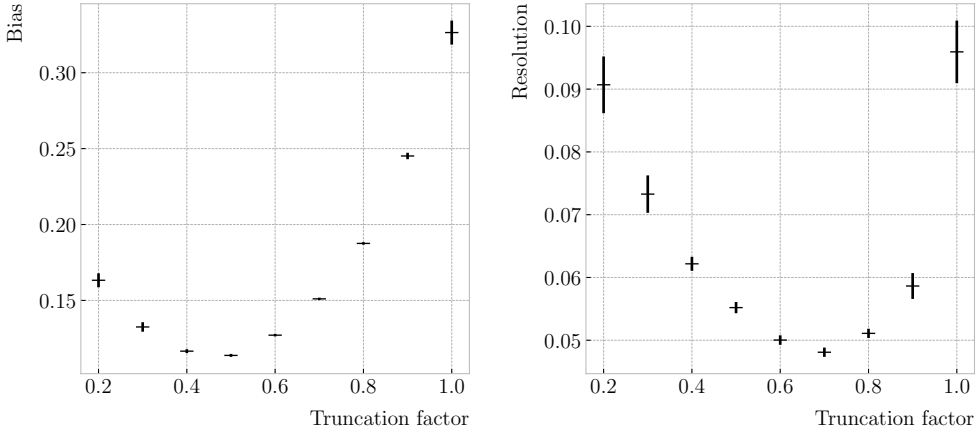


Figure 8.8: Estimated values of the mean dE/dx bias (left panel) and resolution (right panel) obtained using the corrected data from the stopping proton sample, for different values of the truncation factor.

2841 A possibility could be taking the mean of the reconstructed dE/dx distribution for
 2842 each particle. The problem with this approach is that the high energy Landau tail,
 2843 combined with our limited statistics, can induce large fluctuations in the computation
 2844 of the mean. Imagine you have two protons with the same kinetic energy, but due to
 2845 reconstruction problems in one case you did not get as many charge deposits reconstructed
 2846 in its high ionisation loss region. If you do not remove the tails the computed dE/dx
 2847 means will be significantly different.

2848 In order to avoid those fluctuations, one can compute the mean of a truncated dE/dx
 2849 distribution instead. By keeping only a given fraction of the lowest energy deposits
 2850 we obtain an estimate of the mean energy loss that is more resilient to reconstruction
 2851 inefficiencies and statistical effects. Figure 8.7 (left panel) shows a comparison between
 2852 the $\langle dE/dx \rangle$ computed by taking the mean of the full distribution (blue line) and the
 2853 60% lowest energy clusters (yellow line), for the stopping proton sample. The fractional
 2854 residuals are computed for each proton, taking the corresponding means using their
 2855 collections of true and reconstructed energy deposits. One can see that using the simple
 2856 mean translates into a high bias and uncertainty in the $\langle dE/dx \rangle$ estimation, whereas
 2857 applying the truncation reduces both significantly.

2858 Additionally, I performed a comparison between the 60% truncated mean dE/dx

Chapter 8. Particle ID in GArSoft

2859 obtained using the different calibration methods discussed earlier, namely the uncorrected
2860 (blue), corrected (yellow) and uncalibrated (red) distributions. The results are shown
2861 in Fig. 8.7 (right panel). While the widths of these distributions are similar, the bias
2862 obtained for the corrected sample, i.e. calibration function and correction factor applied,
2863 is a factor of ~ 2 lower than in the uncalibrated case and almost three times smaller
2864 than for the uncorrected sample.

2865 The next step is to optimise the level of truncation we are going to apply to our
2866 data. To do so, I used different truncation factors, i.e. the percentage of energy-ordered
2867 reconstructed energy deposits we keep to compute the mean, on the corrected dE/dx
2868 sample of the stopping protons. Then, following the same procedure of computing the
2869 fractional residuals as before, I fitted the resulting histograms using a double Gaussian
2870 function. This is simply the sum of two Gaussian functions of the type:

$$g(x; \mu, \sigma, A) = A e^{-\frac{(x-\mu)^2}{2\sigma^2}}. \quad (8.6)$$

2871 I do not add the classical normalisation factor of the Gaussian, $1/\sqrt{2\pi}\sigma$, therefore
2872 the amplitude A simply represents the maximum of the function. One of the two
2873 Gaussian functions describes the core part of the distribution, while the other captures
2874 the behaviour of the tails.

2875 For each truncation factor, I look at the bias and the resolution I obtain. I define
2876 these as the weighted means of the corresponding parameters in the fits:

$$\bar{x} = \frac{A_{core} x_{core} + A_{tail} x_{tail}}{A_{core} + A_{tail}}, \quad (8.7)$$

2877 where A_{core} and A_{tail} are the amplitudes of the core and tail distributions respectively
2878 and x is either the mean μ or the width σ of said distributions.

2879 Figure 8.8 shows the bias (left panel) and the resolution (right panel) I obtained
2880 for the stopping proton sample, using different values of the truncation. From these, it
2881 can be seen that a truncation factor of 50% minimises the bias in the estimation, while

8.1. dE/dx measurement in the TPC

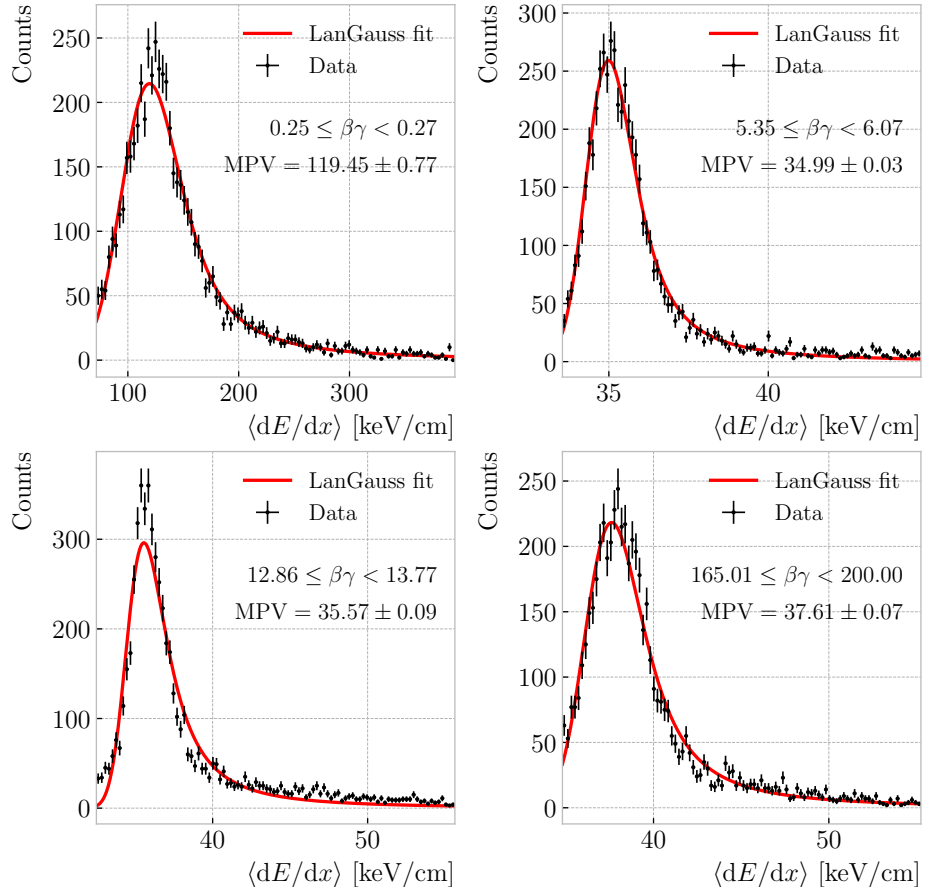


Figure 8.9: Examples of the truncated mean dE/dx LanGauss fits for various $\beta\gamma$ bins, from a simulated FHC neutrino sample.

2882 70% gives the best resolution. That way, I settled on the intermediate value of 60%
 2883 truncation, which yields a $\langle dE/dx \rangle$ resolution of 5.00 ± 0.08 % for stopping protons.

2884 8.1.3 Mean dE/dx parametrisation

2885 Now that we have a way to estimate the mean energy loss of a particle in the HPgTPC,
 2886 we can determine the value of the free parameters in the ALEPH formula, Eq. (8.3).
 2887 For this, I used a sample of 10^5 reconstructed FHC neutrino events inside ND-GAr. In
 2888 this case I cannot use the stopping proton sample, as we need to cover the full kinematic
 2889 range of interest for the neutrino interactions in our detector.

2890 The original data does not contain an estimation of the velocity of the tracks, instead
 2891 the tracks have a value for the reconstructed momentum and the associated PDG code

Chapter 8. Particle ID in GArSoft

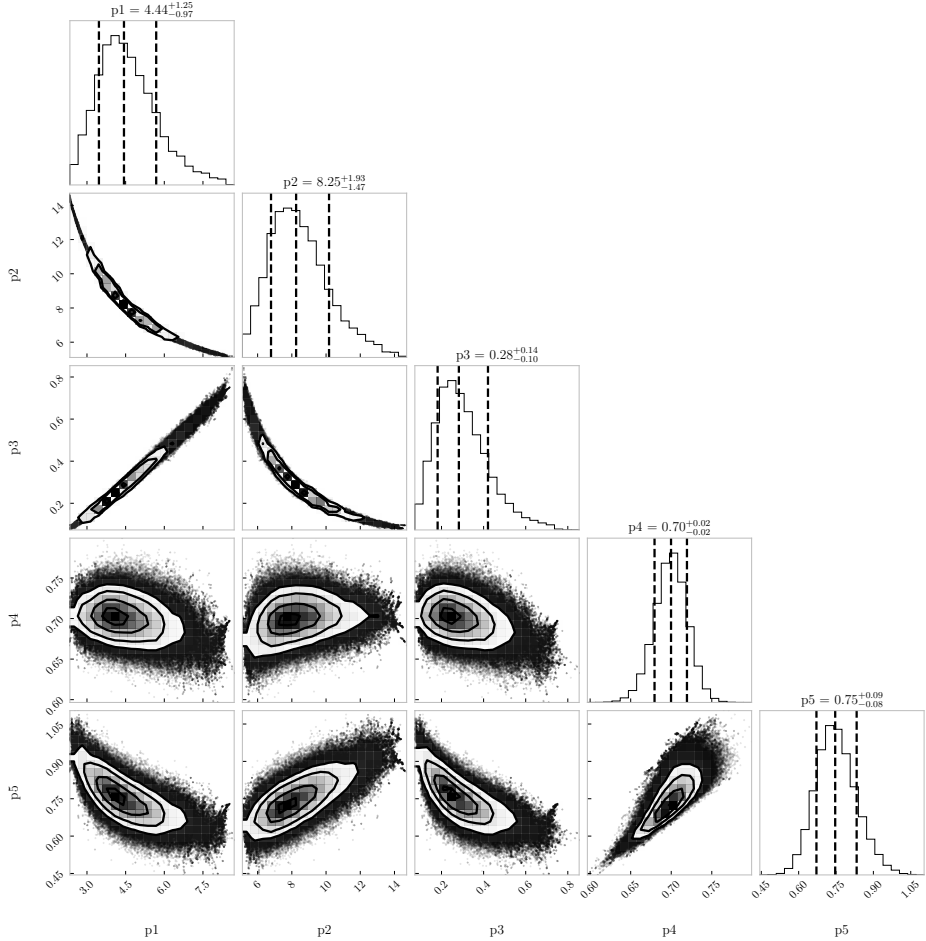


Figure 8.10: Resulting one and two dimensional projections of the posterior probability distributions of the ALEPH $\langle dE/dx \rangle$ parameters obtained by fitting the 60% truncated mean dE/dx values from a FHC neutrino sample in ND-GAr. The vertical dashed lines in the 1D distributions represent the 16th, 50th and 84th percentiles.

2892 of the Geant4-level particle that created the track. Therefore, one can select some of the
 2893 particles in the data, in this case I selected electrons, muons, pions and protons, and
 2894 compute β and γ using the reconstructed momentum and their mass. In terms of $\beta\gamma$
 2895 the mean dE/dx does not depend on the particle species, so one can consider all the
 2896 dataset as a whole. For this fit, I will express β in terms of the $\beta\gamma$ product as:

$$\beta = \frac{\beta\gamma}{\sqrt{1 + (\beta\gamma)^2}}, \quad (8.8)$$

2897 which can be easily proven from the definition of γ .

8.1. dE/dx measurement in the TPC

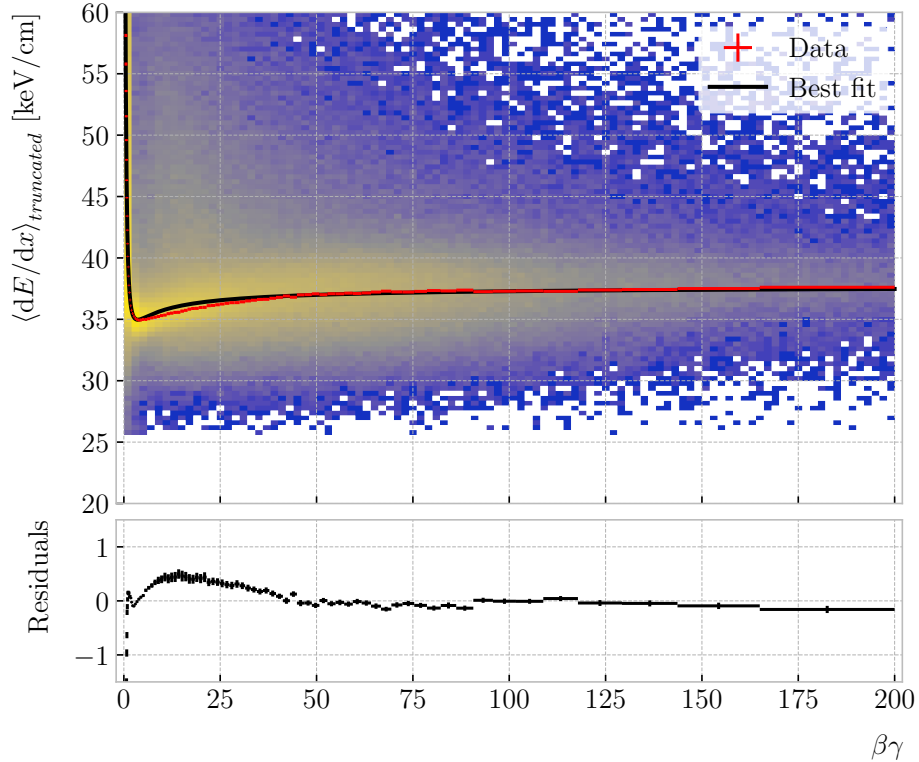


Figure 8.11: Truncated mean dE/dx obtained for the FHC neutrino sample as a function of the $\beta\gamma$ product (upper panel). Also shown are the fitted most probable values for each $\beta\gamma$ bin (red points) and the best fit obtained using the ALEPH parametrisation (black line). The residuals resulting from the fit are shown in the lower panel.

2898 Next, I bin the data in $\beta\gamma$. I chose a fine binning so as to capture the different
 2899 features of the ionisation curve. Instead of fixing the bin width, I select them so each one
 2900 has approximately the same statistics. Then, for each $\beta\gamma$ slice, I compute the median
 2901 and the interquartile range (IQR) of the $\langle dE/dx \rangle$ distribution. Using these, I make a
 2902 histogram in the range [median – IQR, median + 5 IQR], which I fit to a LanGauss
 2903 function in order to extract the MPV. Using this range accounts for the asymmetric
 2904 nature of the distributions, while also helps avoiding a second, lower maximum present
 2905 at low $\beta\gamma$, probably a result of reconstruction failures.

2906 A few examples of these fits are shown in Fig. 8.9. The chosen values of $\beta\gamma$ sit in
 2907 very distinct points along the $\langle dE/dx \rangle$ curve, going from the high ionisation region at
 2908 low velocities (top left panel), to the minimum point (top right panel), the beginning of

Chapter 8. Particle ID in GArSoft

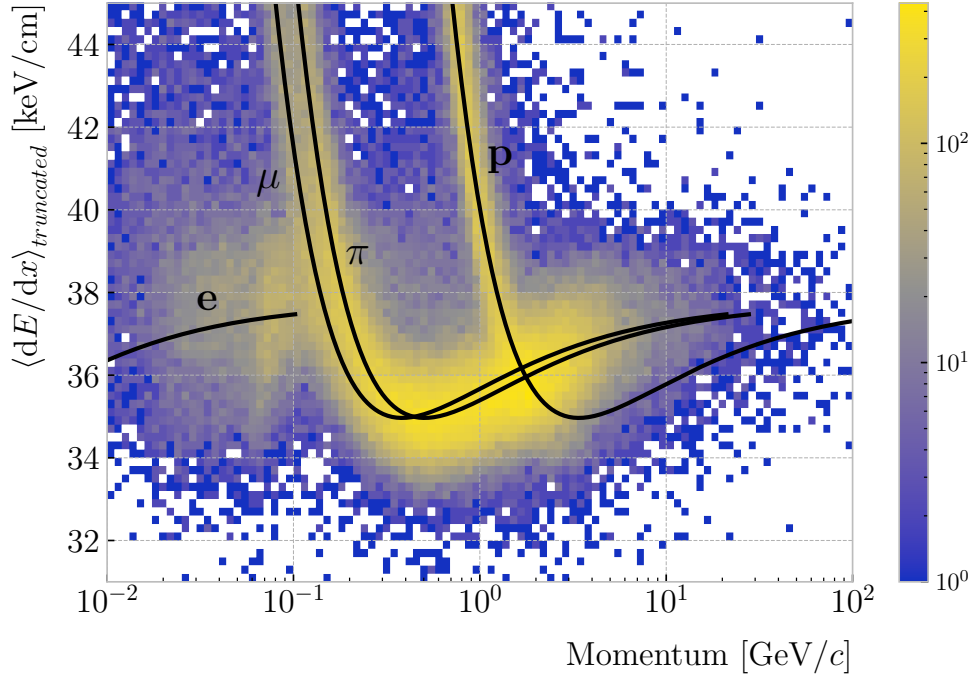


Figure 8.12: Distribution of the 60% truncated mean $\langle dE/dx \rangle$ versus reconstructed momentum for the FHC neutrino sample. The black lines indicate the predictions of the ALEPH parametrisation for electrons, muons, charged pions and protons.

2909 the relativistic rise (bottom left panel), and the plateau produced by the density effect
 2910 (bottom right panel).

2911 I used the resulting most probable $\langle dE/dx \rangle$ values and the centres of the $\beta\gamma$ bins as
 2912 the points to fit to the ALEPH formula. For this particular fit I used the least-squares
 2913 method to get a first estimation of the ALEPH parameters. Applying some uniform
 2914 priors, I then used these values as the starting point of a 100000 steps MCMC. Figure 8.10
 2915 shows the posterior probability distributions I obtain for each parameter. The reported
 2916 best fit points are based on the 16th, 50th, and 84th percentiles in the marginalised
 2917 distributions.

2918 The resulting fit (black line), compared to the data points (red points) and the
 2919 underlying distribution is shown in Fig. 8.11 (top panel). The overall fit is good, with a
 2920 reduced chi-squared of $\chi^2/ndf = 1.02$. However, there are some regions where the fit
 2921 does not describe the data correctly, like the very low $\beta\gamma$ regime, where the fit severely
 2922 underestimates for energy losses $\gtrsim 50$ keV/cm, and the start of the relativistic raise,

8.2. Muon and pion separation in the ECal and MuID

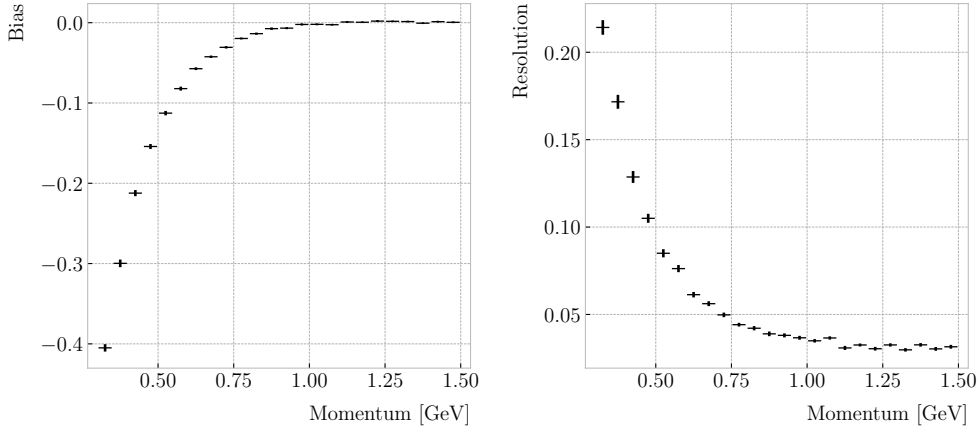


Figure 8.13: Estimated values of the mean dE/dx bias (left panel) and resolution (right panel) obtained for the true protons in a FHC neutrino sample.

where we have a slight overestimation. This is a result of those points having a larger uncertainty when compared to the ones around the dip or the plateau areas. These differences can be better seen in the residual plot, Fig. 8.11 (bottom panel).

8.1.4 Particle identification

8.2 Muon and pion separation in the ECal and MuID

As it could be seen from Fig. 8.12, it is not possible to separate muons and charged pions in the HPgTPC using dE/dx for momenta $\gtrsim 300 \text{ MeV}/c$. In ND-GAr, approximately 70% of the interactions in FHC mode will be ν_μ CC (compared to the 47% of $\bar{\nu}_\mu$ CC interactions when operating in RHC mode), while 24% are neutral currents. Out of these, around 53% and 47% of them will produce at least one charged pion in the final state, respectively. Figure 8.14 shows a comparison between the spectra of the primary muons and the charged pions for ν_μ CC interactions in ND-GAr producing one or more charged pions. From this, one can see that (i) the majority of muons and charged pions are not going to be distinguishable with a $\langle dE/dx \rangle$ measurement, and that (ii) particle identification is necessary both to classify correctly the ν_μ CC events and identify the primary muon within them.

ND-GAr features two other subdetectors which can provide additional information

Chapter 8. Particle ID in GArSoft

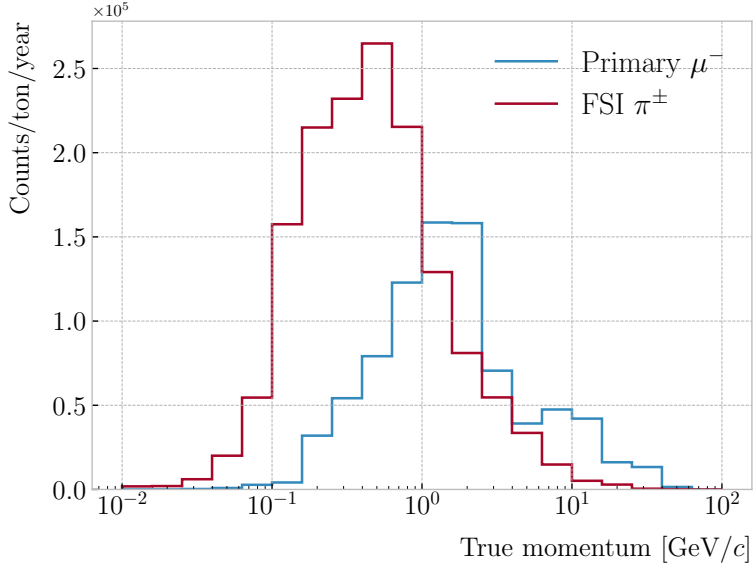


Figure 8.14: True momentum distribution for the primary muon in ν_μ CC $N\pi^\pm$ interactions inside the fiducial volume of ND-GAr (blue line), compared to the post FSI charged pion spectrum (red line).

for this task, namely the ECal and MuID. The current ECal design, described in (ref section), consists of 42 layers, made of 5 mm of Pb, 7 mm of plastic scintillator and a 1 mm PCB board. The total thickness of this calorimeter is 1.66 nuclear interaction lengths or 1.39 pion interaction lengths. The MuID design is in a more conceptual stage, however it is envisioned to feature layers with 10 cm of Fe and 2 cm of plastic scintillator⁵. With its three layers, it will have a thickness of 1.87 or 1.53 nuclear or pion interaction lengths, respectively.

Because pion showers are dominated by inelastic nuclear interactions, the signatures of these particles in the calorimeter will look significantly different from those of muons. Although our ECal is not thick enough to fully contain the hadronic showers of the charged pions at their typical energies in FHC neutrino interactions, they can still be used to understand whether the original particle was more hadron-like or MIP-like. In Fig. 8.15 I show two examples of energy distributions created by a muon (left panel) and a charged pion (right panel) of similar momenta interacting in the ECal. These

⁵It is not mentioned anywhere, but I assume that there should also be another layer of PCB board of 1 mm. However, in this case its contribution to the total thickness of the sampling calorimeter would be negligible.

8.2. Muon and pion separation in the ECal and MuID

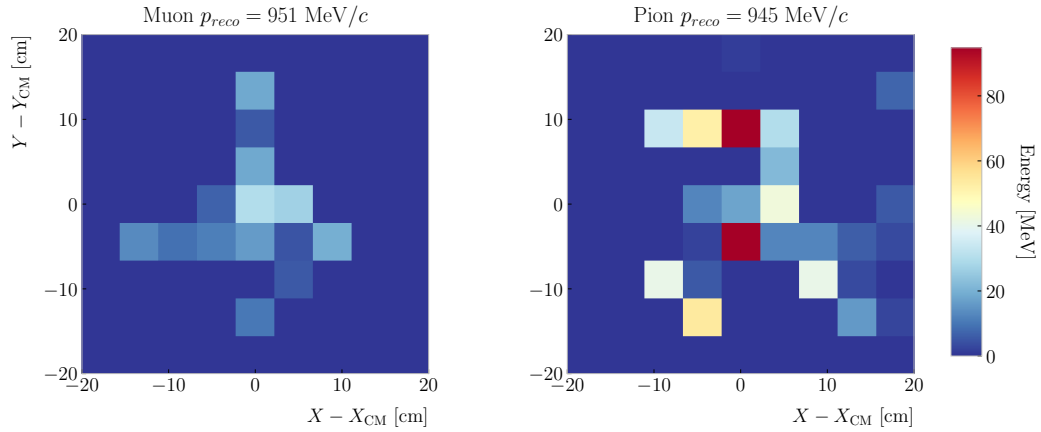


Figure 8.15: Distributions of energy deposits in the ECal for a muon (left panel) and a charged pion (right panel) with similar momenta. The energy is projected onto the plane perpendicular to the principal component of the hits, and the positions are relative to the center of the interaction.

2954 figures represent the transverse development of the interactions. For each of them, I
 2955 computed the principal component and centre of mass of the interaction, projecting
 2956 the position of the hits onto the plane perpendicular to that direction, and taking the
 2957 distances relative to the centre. It can be seen that the muon follows an almost MIP-like
 2958 behaviour, being the central bin in the histogram the one with the highest deposited
 2959 energy. On the other hand, the pion not only deposits more energy overall, but also this
 2960 energy is more spread-out among the different hits. It is this kind of information that
 2961 would allow us to tell apart muons from pions.

2962 This way, I identify three main action points that need to be addressed if one wants
 2963 to use these detectors to distinguish between muons and charged pions. These are:

- 2964 1. the way we make the associations between tracks in the HPgTPC to the activities
 2965 (what in GArSoft we call clusters) in the ECal and the MuID,
- 2966 2. what variables or features one can extract from the calorimeters that encapsulate
 2967 the information we are interested about,
- 2968 3. and how to carry out the classification problem.

Chapter 8. Particle ID in GArSoft

2969 8.2.1 Track-ECal matching

2970 One of the main players in the muon and pion separation is the way we associate clusters
2971 in the ECal to reconstructed tracks in the TPC. Missing some associations or making
2972 wrong ones can bias the ECal quantities that we can use for classifying particles. The
2973 current algorithm in GArSoft provides precise associations, i.e. most of the associations
2974 that it produces are correct, but it appears to miss an important number of associations
2975 (at least when using the default configuration).

2976 The current TPC track-ECal cluster association algorithm is divided in four parts.
2977 It first checks whether the track end point fulfils certain conditions to be extrapolated.
2978 There are two cut values in this step, one for the drift direction and other radial.

2979 If the point can be extrapolated, the code computes the coordinates of the centre
2980 of curvature using the Kalman fit estimates at the track end ($y, z, 1/R, \phi, \tan\lambda$). It
2981 then compares the distance between this and the cluster in the (z, y) plane with R . This
2982 introduces another cut in the perpendicular direction.

2983 The next step is different for clusters in the barrel or in one of the end caps. If it
2984 is a barrel cluster the algorithm extrapolates the track up to the radial distance of the
2985 cluster. There are three possible outcomes, the extrapolated helix can cut the cylinder
2986 of radius r_{clus} two, one or zero times. I get the cut point that is closer to the cluster and
2987 check that it is either in the barrel or the end caps. Computing the difference between
2988 the x coordinates of the cluster and the extrapolated point, the module checks that this
2989 is not greater than a certain cut. If the cluster is in an end cap, I propagate the track
2990 up to the x position of the cluster. Then, the algorithm computes the angle in the (z, y)
2991 plane between the centre of curvature and the cluster, α , and the centre of curvature
2992 and the propagated point, α' . A cut is applied to the quantity $(\alpha - \alpha')R$.

2993 If the cluster contains more than a certain number N of hits, I apply an extra cut to
2994 the dot product of the direction of the track at the propagated x value and the cluster
2995 direction.

2996 The code makes sure to only associate one end of the track (if any) to a cluster.

8.2. Muon and pion separation in the ECal and MuID

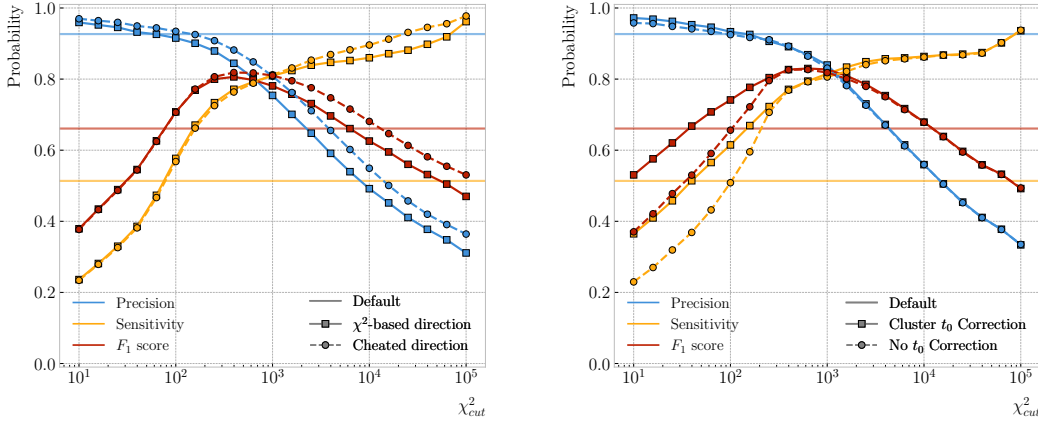


Figure 8.16: Left panel: comparison between the precision (blue), sensitivity (yellow) and F_1 score (red) obtained for the default (horizontal lines) and new algorithms, both with the χ^2 -based direction estimator (squares) and cheating the directions (circles), for different values of the χ^2 cut. Right panel: comparison of the performance of the new algorithm when applying the cluster t_0 correction (squares) and when (circles).

2997 However, it can associate more than one track to the same cluster. This makes sense,
2998 as different particles can contribute to the same cluster in the ECal, but it makes it
2999 difficult to quantify the relative contributions of the tracks to a certain cluster.

3000 As a way of comparing the performance of this algorithm, a new, simpler association
3001 module was written. The goal was to have a simple and robust algorithm, which depends
3002 on as few parameters as possible and that can produce a one-to-one matching between
3003 tracks and ECal clusters.

3004 For each reconstructed track, the new algorithms applies the same procedure to the
3005 forward and the backward fits irrespective of their end point positions. It first gets the
3006 Kalman fit parameters at the corresponding end point together with the X position, x_0 ,
3007 (y_0 , z_0 , $1/R$, ϕ_0 , $\tan\lambda$).

3008 For each ECal cluster, I compute the radial distance to the centre of the TPC and
3009 find the ϕ value in the range $[\phi_0, \phi_0 + \text{sign}(R)\phi_{max}]$ that makes the propagated helix
3010 intersect with the circle defined with such radius. The (x, y, z) position of the helix for
3011 the ϕ value found (if any) is then computed. In case there are two intersections, I keep
3012 the one that minimises the distance between (y, z) and (y_c, z_c) .

3013 I then calculate χ^2 value based on the Euclidean distance between the propagated

Chapter 8. Particle ID in GArSoft

3014 point and the cluster:

$$\chi^2/ndf = \frac{\sum_{n=0}^2 (x^{(n)} - x_c^{(n)})^2}{3}. \quad (8.9)$$

3015 If there was no intersection I store a -1 instead. In the end, for each reconstructed track
3016 in the event one ends up with two collections of χ^2 values, one for each ECal cluster
3017 and fit directions.

3018 The current code only supports having ECal clusters associated to one end of each
3019 track. We have two options to decide what track end to keep. The first one tries to
3020 cheat the selection, looking at the distance between the two track ends and the true
3021 start position of the associated MC particle. The second one keeps the track end with
3022 more χ^2 entries below the cut.

3023 This feature of only considering one track end limits the algorithm, making it not
3024 suitable for reconstructing events with particles originating outside the TPC. However,
3025 as for the moment the main concern of the group is the study of neutrino interactions
3026 off the gaseous argon, this is an acceptable assumption.

3027 In order to associate a cluster to a track, I take all clusters with a χ^2 value in the
3028 range $[0, \chi_{cut}^2]$. If a cluster has been assigned to more than one track we leave it with
3029 the one with the lowest χ^2 .

3030 This default behaviour of the algorithm can be modified to associate more than one
3031 track to each cluster. Not only that, but the χ^2 values can be used to assign relative
3032 weights to the different contributions.

3033 To evaluate the performance of the association method, I use a binary classification
3034 approach. In this case, I check the leading MC Track IDs associated to the reconstructed
3035 tracks and ECal clusters. I count an association as true positive (TP) if both Track
3036 IDs coincide. An association is considered false positive (FP) when the Track IDs are
3037 different. If a cluster has not been associated to any track but it shares the Track ID
3038 with a reconstructed track it is counted as a false negative (FN).

3039 For the testing, I used a sample of 10000 FHC neutrino events inside the HPgTPC.
3040 Figure 8.16 (left panel) shows the precision (blue line), sensitivity (yellow line), and F_1

8.2. Muon and pion separation in the ECal and MuID

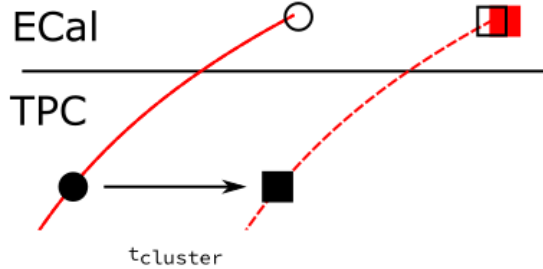


Figure 8.17: Schematics of a possible option to deal with track-ECal associations in non-zero t_0 neutrino interaction events, trying to correct for the drift direction uncertainty in a cluster-by-cluster basis using the cluster time, $t_{cluster}$.

3041 score (red line) I obtained for different values of χ^2_{cut} . For comparison, the same metrics
 3042 computed for the default algorithm with the current configuration are also shown (dashed
 3043 lines). In the case of the new algorithm, I used both the χ^2 -based method to estimate
 3044 the track direction described earlier (square markers) and the cheated direction from the
 3045 Geant-level information (circle markers). For either of these we achieve similar values of
 3046 the precision compared to the old code, while having a considerably higher sensitivity.
 3047 It can be seen that cheating the direction of the tracks only makes a difference at high
 3048 χ^2_{cut} , past the optimal value of the cut around the F_1 score maximum. Therefore, I set
 3049 the χ^2 method as the default.

3050 One of the possible weak points of this approach is that it relies on the position along
 3051 the drift direction to make the decisions. Within the current ND-GAr design implemented
 3052 in GArSoft, the timing information is provided by the ECal. That effectively means
 3053 that prior to make the track-ECal associations the reconstructed x positions of the track
 3054 trajectories differ from the simulated ones by an amount:

$$x_{reco}^{(n)} - x_{sim}^{(n)} = v_{drift} t_0, \quad (8.10)$$

3055 where v_{drift} is the mean drift velocity in our medium and the initial time is in the range
 3056 $t_0 \in [0, t_{spill}]$ where t_{spill} is the spill length. For a 10 μs spill this translates into a
 3057 maximum 30 cm uncertainty on the drift direction position.

3058 The current default in GArSoft sets $t_0 = 0$, but the functionality to randomly sample

Chapter 8. Particle ID in GArSoft

3059 this within the spill time is in place. Therefore, we need to understand what is the impact
3060 of a non-zero t_0 on the associations algorithm and foresee possible ways of minimising a
3061 loss in performance.

3062 Figure 8.17 represents a possible option to tackle the association problem when
3063 having events with a non-zero initial time t_0 . The black and white circles represent the
3064 original points, whereas the squares indicate the corrected positions. The end points of
3065 the track and the propagated points up to the cluster radius are indicated using filled
3066 and unfilled markers respectively. The red square represents the position of the cluster.

3067 Here I try to correct for the drift coordinate position using the time associated to the
3068 cluster. Assuming that the drift time is much larger than the propagation time, $t_{cluster}$
3069 could be used as a good estimation of the t_0 . An alternative can be using the earliest
3070 time associated to a hit in said cluster. Doing this for each cluster before computing
3071 the χ^2 value could be used as an alternative to knowing the specific value of the t_0 , as
3072 when the association is correct this will provide the right correction but its impact is
3073 small enough to not change the position significantly in the case the cluster does not
3074 correspond to a given track.

3075 I tested the effect of this correction again using a sample of 10000 FHC neutrino
3076 events. Figure 8.16 (right panel) shows the precision (blue line), sensitivity (yellow line),
3077 and F_1 score (red line) for the case the cluster t_0 correction is applied (square markers)
3078 and for the no correction case (circle markers), as a function of χ^2_{cut} . In this case, the
3079 differences are particularly notorious at low values of the cut. It makes sense, as the t_0
3080 effect becomes subdominant when the distance we consider grows large. Overall, the
3081 correction increases the sensitivity while keeping the precision almost unchanged. As a
3082 result, I apply the t_0 correction to the generated samples as the default.

3083 8.2.2 Classification strategy

3084 The problem of the muon and charged pion separation has to be viewed in the broader
3085 context of the particle identification in our detector. Focusing on the beam neutrino
3086 interactions, it is clear that we are going to have muons and pions spanning a broad

8.2. Muon and pion separation in the ECal and MuID

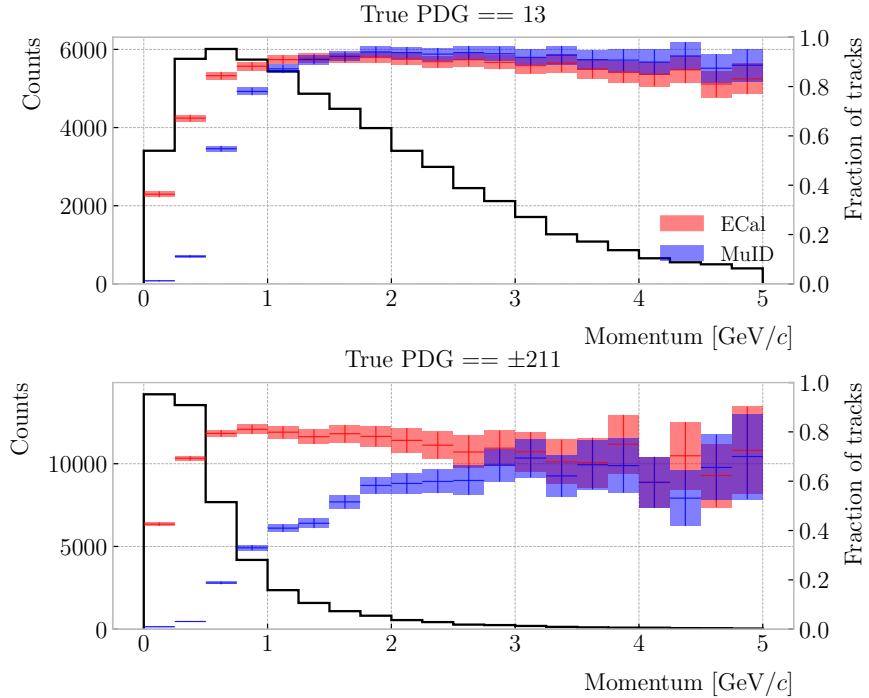


Figure 8.18: Momentum distribution for the reconstructed muons (top panel) and charged pions (bottom panel) in a FHC neutrino sample, together with the fraction of them reaching the ECal (red) and MuID (blue). Each entry corresponds to a reconstructed track, backtracked to a true muon or pion which has not produced any other reconstructed track.

3087 momentum range. Not only that, but we will also have other particles with similar
 3088 characteristics that will make the classification even more challenging. Therefore, we are
 3089 presented with a task that will depend heavily on the kinematic range we are looking at
 3090 each time, as both the available information and the possible impurities of other particle
 3091 species vary.

3092 For instance, distinguishing muons from pions could be difficult at low momenta, as
 3093 a great number of them do not reach the ECal. Therefore, we could think of tailoring a
 3094 version of the classification for that particular case, which could be complemented with
 3095 a dE/dx measurement. Likewise, for momenta $\gtrsim 1$ GeV muons and pions reach the
 3096 calorimeters efficiently, but so do protons. Because of this, one can try to train another
 3097 classifier for this energy range, and rely on other methods to remove as many of the
 3098 protons as possible.

Chapter 8. Particle ID in GArSoft

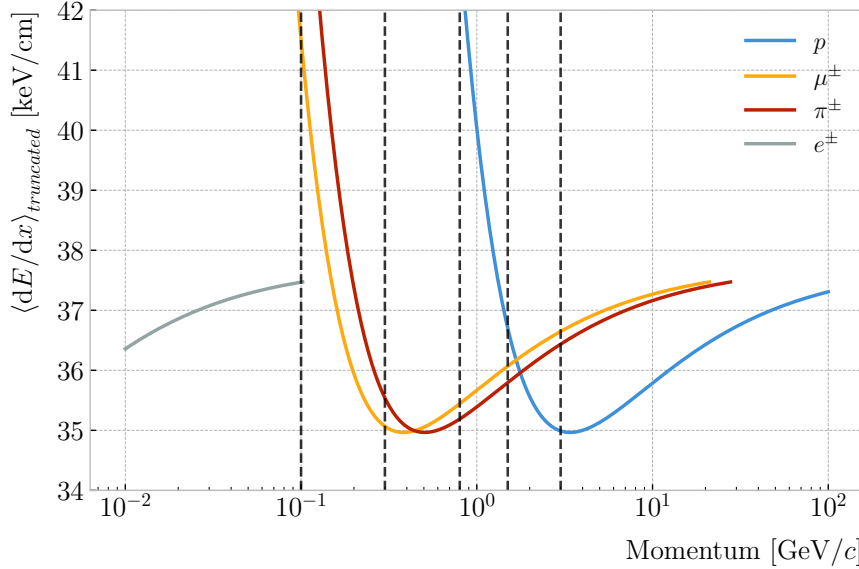


Figure 8.19: Predicted truncated mean dE/dx versus momentum, for electrons, muons, charged pions and protons, obtained using the ALEPH parametrisation. The vertical dashed lines represent the boundaries of the six regions used for the muon and pion classification training.

3099 Figure 8.18 shows the momentum distribution of the reconstructed muons (top) and
 3100 pions (bottom) in a FHC sample. It also contains the fraction of particles reaching the
 3101 ECal (red) and MuID (blue), for the different momentum bins. In Fig. 8.19 I show the
 3102 mean dE/dx of different particles as a function of the momentum, computed using the
 3103 ALEPH parametrisation with the best fit parameters found in Subsec. 8.1.2.

3104 Using these two figures as references, I decided to approach the classification by
 3105 dividing the problem into six different momentum regions. A summary of these can be
 3106 found in Tab. 8.2. The basic idea is to exploit all the information that is available in
 3107 each region and . For the problem at hand, I prepared separated samples of isotropic
 3108 single muons and pions, with momenta uniformly distributed along the corresponding
 3109 momentum range. Each sample contains 50000 events of the corresponding particle
 3110 species. I did not generate samples for the first region, as it is assumed that the separation
 3111 can be achieved using dE/dx only. For the last region, I generated particles up to a
 3112 momentum of 10 GeV/c, as that is well above the typical energies of muons and pions
 3113 from FHC neutrino interactions in ND-GAr.

8.2. Muon and pion separation in the ECal and MuID

Table 8.2: Momentum ranges and description of the PID approach assumed for the muon and pion classification task.

Momentum range	Description
$< 0.1 \text{ GeV}/c$	All tracks can be separated with dE/dx
$[0.1, 0.3) \text{ GeV}/c$	Use ECal for reaching muons and pions, dE/dx for the rest
$[0.3, 0.8) \text{ GeV}/c$	Use ECal for muons and pions, dE/dx for protons
$[0.8, 1.5) \text{ GeV}/c$	Use ECal and MuID for muons and pions, dE/dx for protons
$[1.5, 3.0) \text{ GeV}/c$	Use ECal and MuID for muons and pions, ToF for protons
$\geq 3.0 \text{ GeV}/c$	Use ECal and MuID for muons and pions, dE/dx and ToF for protons

3114 Additionally, I prepared another sample of 100000 FHC neutrino events. For each
 3115 interaction, I select the reconstructed particles which were backtracked to true muons or
 3116 charged pions. I use this dataset to perform validation checks, to see how the models
 3117 trained with the single particle data generalise to a more realistic scenario.

3118 To tackle this classification problem, I make use of Boosted Decision Trees (BDT). A
 3119 decision tree uses a flowchart-like structure to make decisions based on some input data.
 3120 It starts from a root node, which represents the complete dataset, and then it splits
 3121 this based on the variable or feature which gives the best separation between classes,
 3122 creating two new nodes. The process repeats for each node until it reaches a certain
 3123 limit, like a maximum number of splits or some tolerance criteria. The last set of nodes
 3124 are often called leave nodes, and represent the final prediction of the classifier.

3125 Boosting refers to a family of methods to combine the predictions from multiple
 3126 classifiers, following a sequential approach where each new model learns from the errors
 3127 of the previous one. The process starts with a simple decision tree, which is used to
 3128 make predictions on the training data. Then, the data points misclassified by the first
 3129 model are assigned higher weights, and another decision tree is trained on the data with
 3130 adjusted weights. The predictions of the two trees are then combined, and the cycle
 3131 repeats for a predefined number of iterations. Gradient boosting uses the direction of
 3132 the steepest error descent to guide the learning process and improve the accuracy with
 3133 each iteration.

Chapter 8. Particle ID in GArSoft

3134 8.2.3 Feature selection and importance

3135 Using the reconstructed tracks as a starting point, I compute a number of ECal and
3136 MuID variables for each of them. As there can be more than one cluster associated to a
3137 track, what I do is collect all associated clusters and compute these variables from the
3138 complete collection of associated hits. For the MuID, because it only features three layers
3139 and typically there will be less hits, I also allow single hits to be associated with tracks⁶.
3140 I can roughly divide the variables in three types: energy-related, geometry-related and
3141 statistical. In the following, I briefly describe the variables related exclusively to the
3142 ECal:

3143 • Energy-related ECal

- 3144 – ECal total energy (ClusterTotalEnergy): sum of the energy of all the ECal
3145 hits.
- 3146 – Mean ECal hit energy (HitMeanEnergy): mean of the hit energy distribution.
- 3147 – Standard deviation ECal hit energy (HitStdEnergy): standard deviation of
3148 the hit energy distribution.
- 3149 – Maximum ECal hit energy (HitMaxEnergy): maximum of the hit energy
3150 distribution.

3151 • Geometry-related ECal

- 3152 – Mean distance hit-to-cluster (DistHitClusterMean): mean of the distance
3153 distribution between the hits and the corresponding cluster's main axis.
- 3154 – RMS distance hit-to-cluster (DistHitClusterRMS): root mean square of the
3155 distance distribution between the hits and the corresponding cluster's main
3156 axis.
- 3157 – Maximum distance hit-to-centre (DistHitCenterMax): maximum of the
3158 distance distribution between the hits and the centre of the TPC.

⁶At the reconstruction level what happens is that non-clustered hits are put into single hit clusters, instead of being thrown away. This is necessary to keep the consistency of the track-cluster association code.

8.2. Muon and pion separation in the ECal and MuID

- 3159 – Time-of-Flight velocity (TOFVelocity): slope obtained when fitting a straight
3160 line to the hit time versus hit distance to the centre (i.e. $d = v \times t$).

3161 • Energy and geometry ECal

- 3162 – Radius 90% energy (Radius90E): distance in the hit-to-cluster distribution
3163 for which 90% of the total energy is contained in the hits that are closer to
3164 the axis (i.e. radius that contains 90% of the energy).

3165 • Statistical ECal

- 3166 – Number of hits (NHits): total number of hits associated to the track.
3167 – Number of layers with hits (NLayers): not really a count of all layers with
3168 hits but the difference between the last and the first layer with hits.

3169 Figure 8.20 shows the distributions of three different ECal variables, separating true
3170 muons (blue) and charged pions (red), for the five momentum ranges considered. I chose
3171 to show one feature from each category, namely the mean energy per hit (left column),
3172 the mean distance between the hits and the centre of the cluster (middle column), and
3173 the number of ECal layers with hits (right column). These give an idea of the separating
3174 power of the different features, and how it changes considerably with the energy. In
3175 the number of layers with hits distributions, the peak at 6 is due to the fact that the
3176 first six ECal layers sit inside the pressure vessel⁷. Therefore, some of the particles get
3177 stopped crossing it, never making it to the seventh layer.

3178 In the case of the MuID, because at low momenta a significant fraction of the particles
3179 do not make it past the ECal, I only consider the information coming from this detector
3180 for momenta ≥ 0.8 GeV/ c , i.e. for the last three momentum regions. The variables I
3181 extract from it are the following:

3182 • Energy-related MuID

⁷Note to self: check this. I thought the ECal barrel had 8 layers of tiles, and that all of them were inside the pressure vessel.

Chapter 8. Particle ID in GArSoft

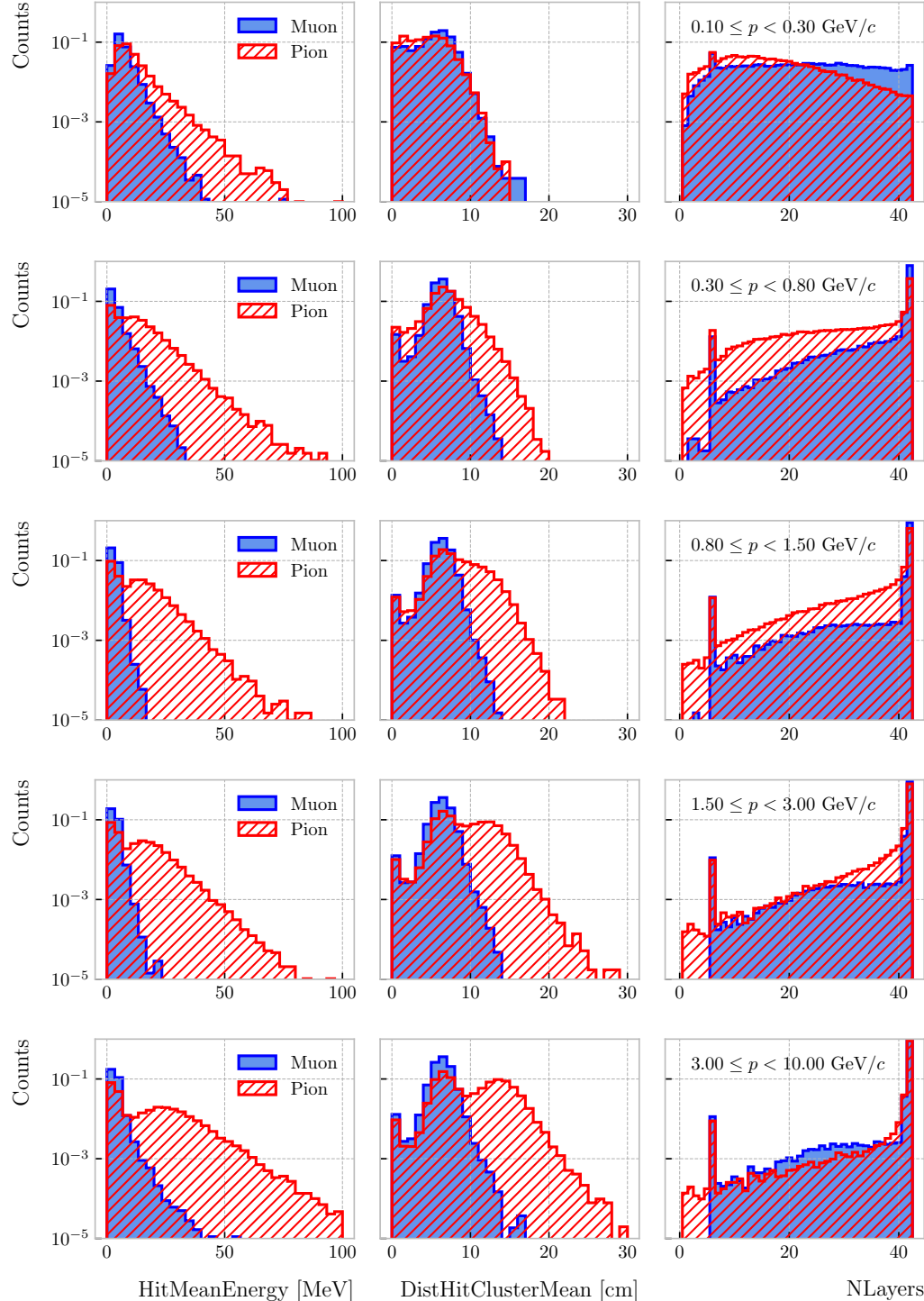


Figure 8.20: Example ECal feature distributions for muons (blue) and charged pions (red) in the five different momentum ranges considered (from top to bottom, in ascending momentum order). From left to right: mean hit energy, mean distance hit-to-cluster, and number of layers with hits.

8.2. Muon and pion separation in the ECal and MuID

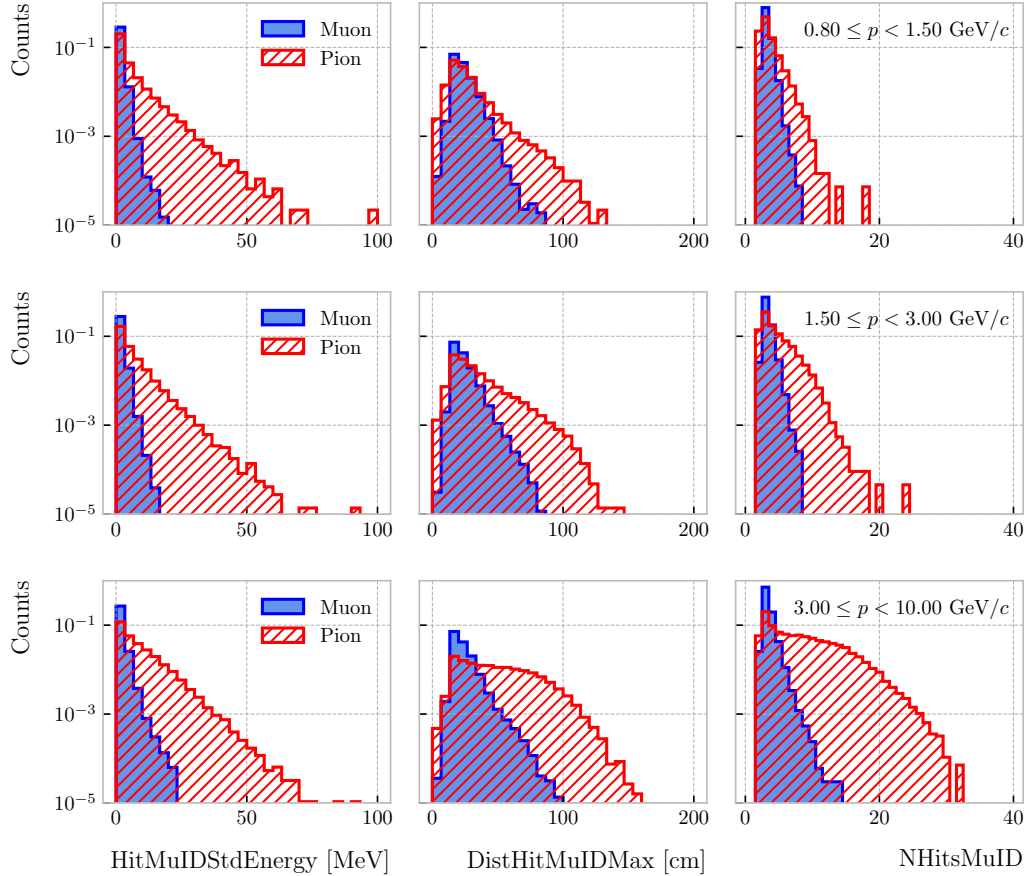


Figure 8.21: Example MuID feature distributions for muons (blue) and charged pions (red) in the three different momentum ranges considered (from top to bottom, in ascending momentum order). From left to right: standard deviation hit energy, maximum distance hit-to-hit, and number of hits.

- 3183 – MuID total energy (ClusterMuIDTotalEnergy): sum of the energy of all the
- 3184 MuID hits.
- 3185 – Mean MuID hit energy (HitMuIDMeanEnergy): mean of the MuID hit energy
- 3186 distribution.
- 3187 – Standard deviation MuID hit energy (HitMuIDStdEnergy): standard deviation
- 3188 of the MuID hit energy distribution.
- 3189 – Maximum MuID hit energy (HitMuIDMaxEnergy): maximum of the MuID
- 3190 hit energy distribution.

- 3191 • **Geometry-related MuID**

Chapter 8. Particle ID in GArSoft

- 3192 – Maximum distance MuID hit-to-hit (DistHitMuIDMax): maximum distance
- 3193 between pairs of MuID hits (not sure this is a good variable, distribution
- 3194 looks nuts).
- 3195 – Maximum distance MuID hit-to-centre (DistHitCenterMuIDMax): maximum
- 3196 of the distance distribution between the MuID hits and the centre of the
- 3197 TPC.

3198 • Statistical MuID

- 3199 – Number of hits (NHitsMuID): total number of MuID hits associated to the
- 3200 track.
- 3201 – Number of layers with hits (NLayersMuID): not really a count of all layers
- 3202 with MuID hits but the difference between the last and the first layer with
- 3203 MuIDhits.

3204 Figure 8.21 shows the distributions of three different MuID variables, separating true
3205 muons (blue) and charged pions (red), for the three momentum ranges which use the
3206 muon tagger information. In this case I decided to standard deviation of the MuID hit
3207 energy distribution (left column), the maximum distance between the MuID hit pairs
3208 (middle column), and the number of MuID hits (right column). These variables are used
3209 together with the ECal features at high momenta, providing additional disambiguation
3210 power.

3211 Once our features have been defined, one can do some exploratory analysis to
3212 understand how well the variables describe the target class, and avoid the black-box
3213 approach by what features are most relevant for the learning process. This way, I
3214 performed a feature analysis for each of the momentum ranges I divided this classification
3215 problem into. It follows three steps: first a principal component analysis (PCA), followed
3216 by a feature importance study using Gini and Shapley values, and finally a feature
3217 permutation importance analysis.

3218 The PCA is useful to understand the variance of the feature space. It is an
3219 unsupervised machine learning technique that allows the user to perform a dimensionality

8.2. Muon and pion separation in the ECal and MuID

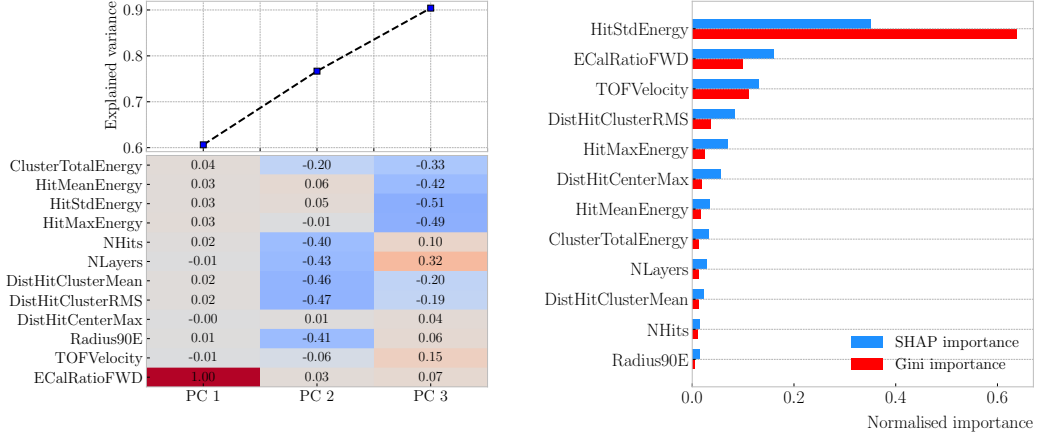


Figure 8.22: Left panel: cumulative explained variance for the first three principal components (top panel) and contribution of the different features to the principal axes in feature space (bottom panel). Right panel: Shapley (blue) and Gini (red) feature importances for the different input features. Both figures correspond to the samples in the momentum range $0.3 \leq p < 0.8$ GeV/c.

reduction. It uses a singular value decomposition of the input features to project them into a lower dimensional space. The idea is to find the matrix \mathbf{C}_m , whose columns are the first m orthonormal eigenvectors of the input covariance matrix. Consider the $n \times p$ real matrix of input data \mathbf{X} , where n is the number of samples and p the number of features. If \mathbf{X} is centred, i.e. the means of its columns are equal to zero, we can write the covariance matrix of \mathbf{X} as $\mathbf{C} = \mathbf{X}^\top \mathbf{X} / (n - 1)$. This matrix can be diagonalised, yielding:

$$\mathbf{C} = \mathbf{V} \mathbf{L} \mathbf{V}^\top, \quad (8.11)$$

where \mathbf{V} is a matrix of eigenvectors and \mathbf{L} a diagonal matrix with eigenvalues λ_i . Then, performing SVD on \mathbf{X} gives us:

$$\mathbf{X} = \mathbf{U} \mathbf{S} \mathbf{W}^\top, \quad (8.12)$$

where \mathbf{U} is a unitary matrix, whose columns are called left singular vectors, \mathbf{S} is a diagonal matrix of single values s_i , and \mathbf{W} is another unitary matrix, its columns known as right singular vectors. This way, we can write:

$$\mathbf{C} = \mathbf{W} \mathbf{S} \mathbf{U}^\top \mathbf{U} \mathbf{S} \mathbf{W}^\top / (n - 1) = \mathbf{W} \frac{\mathbf{S}^2}{n - 1} \mathbf{W}^\top. \quad (8.13)$$

Chapter 8. Particle ID in GArSoft

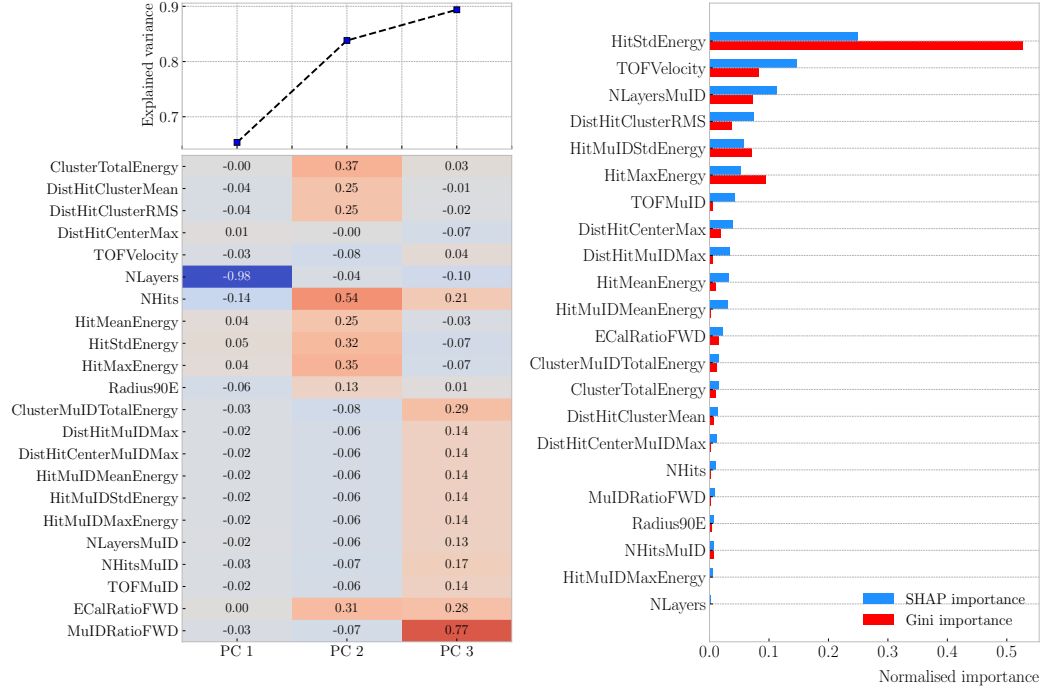


Figure 8.23: Left panel: cumulative explained variance for the first three principal components (top panel) and contribution of the different features to the principal axes in feature space (bottom panel). Right panel: Shapley (blue) and Gini (red) feature importances for the different input features. Both figures correspond to the samples in the momentum range $0.8 \leq p < 1.5 \text{ GeV}/c$.

meaning that the right singular vectors are also the eigenvectors of the covariance matrix.

The SVD can be computed numerically following an iterative approach.

This way, taking an input data vector $X \in \mathbb{R}^n$, the resulting feature vector $Y \in \mathbb{R}^m$

is given by:

$$Y = \mathbf{C}_m^\top X. \quad (8.14)$$

The new features capture most of the variance of the original sample, while being lower dimensional, as $m < n$.

Before applying the PCA reduction one needs to centre and scale the input data.

Centring is necessary when using SVD to obtain the eigenvectors of the covariance matrix, as only in that case we can do the identification with the right singular vectors from the input data. Scaling is needed when variables are on different scales, as some can then dominate the PCA procedure.

8.2. Muon and pion separation in the ECal and MuID

3242 I used the PCA module of `scikit-learn`, together with the `RobustScaler`, which
 3243 centres the data and scales it based on the interquartile range. In Fig. 8.22 (left panel)
 3244 and Fig. 8.23 (left panel) I show the results I obtained from the PCA for the momentum
 3245 ranges $0.3 \leq p < 0.8 \text{ GeV}/c$ and $0.8 \leq p < 1.5 \text{ GeV}/c$, respectively. Notice that in
 3246 the second case the number of features increases considerably, as this is the first region
 3247 which uses the MuID variables. I found that, in all the cases, adding a fourth PC does
 3248 not add additional information. As it can be seen in the top panels of the figures, the
 3249 cumulative explained variance is already over 80% with three PCs.

3250 The bottom panels show the contribution of the variables to the principal axes. For
 3251 the two first momentum regions, I observe a tendency of the energy-related and the
 3252 geometry-related ECal variables to be clustered together. For the other ranges, when
 3253 I include the MuID variables, there seems to be a division between ECal and MuID
 3254 variables. For these, it seems like the number of ECal layers with hits also plays an
 3255 important role.

3256 The next step in the analysis is to quantify the importance of the features based on
 3257 two additional metrics, namely the Gini and the Shapley values. The Gini importance,
 3258 often called mean decrease impurity, is based on how much a feature contributes to the
 3259 purity improvement at the splits in each decision tree. The purity is measured in terms
 3260 of the Gini impurity index, defined as:

$$I_G = 1 - \sum_i f_i, \quad (8.15)$$

3261 where f_i is the fractional abundance of the i -th class. Then, for each split one can
 3262 compute the weighted decrease in impurity as:

$$\Delta_G = \frac{N_t}{N} \left(I_G - \frac{N_t^R}{N_t} I_G^R - \frac{N_t^L}{N_t} I_G^L \right), \quad (8.16)$$

3263 where N represents the total number of samples, N_t the number of samples at the current
 3264 node, N_t^R and N_t^L the number of samples in the right and left children respectively,

Chapter 8. Particle ID in GArSoft

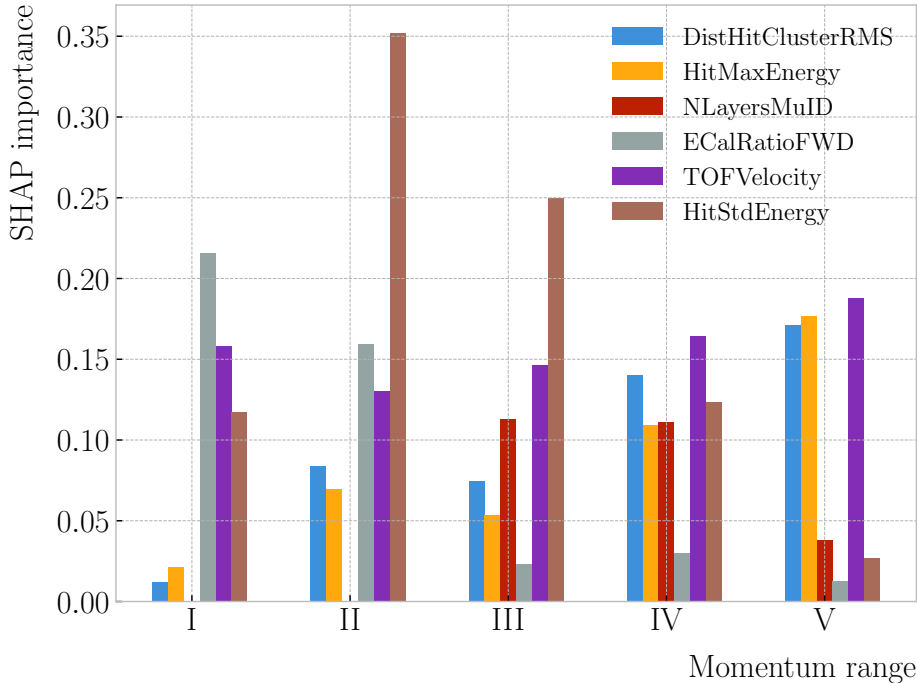


Figure 8.24: Evolution of the SHAP importance for the top six most important features across all five momentum ranges.

3265 I_G is the Gini impurity at the current node, and I_G^R and I_G^L the Gini impurities of the
3266 resulting right and left children.

3267 For each decision tree, one will have a normalised vector with the accumulated
3268 decrease in Gini impurity for each feature. In the case of a BDT, the feature importances
3269 are simply the mean for all the estimators in the ensemble⁸.

3270 The concept of Shapley values originated in the context of game theory, and it
3271 measures the marginal contribution of a feature in enhancing the accuracy of a classifier.
3272 Take F to be the set of all features in a problem, and $S \subseteq F$ the subset of features. To
3273 compute the Shapley value of the i -th feature, one has to train a model with that feature
3274 present, $f_{S \cup \{i\}}$, and another model trained without it, f_S . This has to be repeated for
3275 all possible combinations of subsets $S \subset F \setminus \{i\}$, and evaluating the models predictions

⁸Note to self: this appears not to be the case. If you get the `feature_importance` for each tree in the BDT and take the average, the result is not the same to be one reported in the `feature_importance` attribute of the BDT.

8.2. Muon and pion separation in the ECal and MuID

3276 on the appropriate sets of data x_S . This way, the Shapley value results:

$$\varphi_i = \sum_{S \subset F \setminus \{i\}} \frac{|S|! (|F| - |S| - 1)!}{|F|!} [f_{S \cup \{i\}}(x_{S \cup \{i\}}) - f_S(x_S)]. \quad (8.17)$$

3277 I trained the `GradientBoostingClassifier` from `scikit-learn` with the default
 3278 configuration in order to evaluate both the Gini and Shapley importances. The Gini
 3279 scores are automatically computed by `scikit-learn`, using the training data. For the
 3280 Shapley importance, I used the implementation from the `SHAP` package, computing
 3281 it using the test sample. The results can be seen in Fig. 8.22 (right panel) and
 3282 Fig. 8.23 (right panel), again for the momentum ranges $0.3 \leq p < 0.8 \text{ GeV}/c$ and
 3283 $0.8 \leq p < 1.5 \text{ GeV}/c$. The length of the bars denote either the SHAP (blue) or the Gini
 3284 (red) importance of the feature. One interesting thing to notice is that, when looking at
 3285 the Gini importance, there is always one feature that dominates over the rest. This is
 3286 not the case for the SHAP importance, where importances tend to be more balanced.

3287 Across all momentum ranges, I observe that the most important features are. For
 3288 the five momentum ranges considered, only six variables sit in the top five at least once.
 3289 Figure 8.24 shows the evolution of the SHAP importance of these six features. It is
 3290 interesting to see that the time-of-flight variable keeps its importance almost unchanged
 3291 for all momenta. Also, it looks like the ECal energy ratio gets less relevant the higher the
 3292 momentum is, but the RMS of the hit-to-cluster distance distribution and the maximum
 3293 ECal hit energy become more important in the last momentum ranges.

3294 The last step in the feature selection analysis is the feature permutation. This
 3295 technique measures the contribution of each feature to the performance of a model by
 3296 randomly shuffling its values and checking how some scores degrade. For the present
 3297 case, I am interested in the precision or purity, and the sensitivity or efficiency, as these
 3298 two are the most relevant metrics from a physics point of view. The `scikit-learn`
 3299 module provides the user with a method to perform the permutation scans.

3300 The results of these are shown in Fig. 8.25. For the different momentum ranges
 3301 I show the permutation importances for the ten most important features. For each

Chapter 8. Particle ID in GArSoft

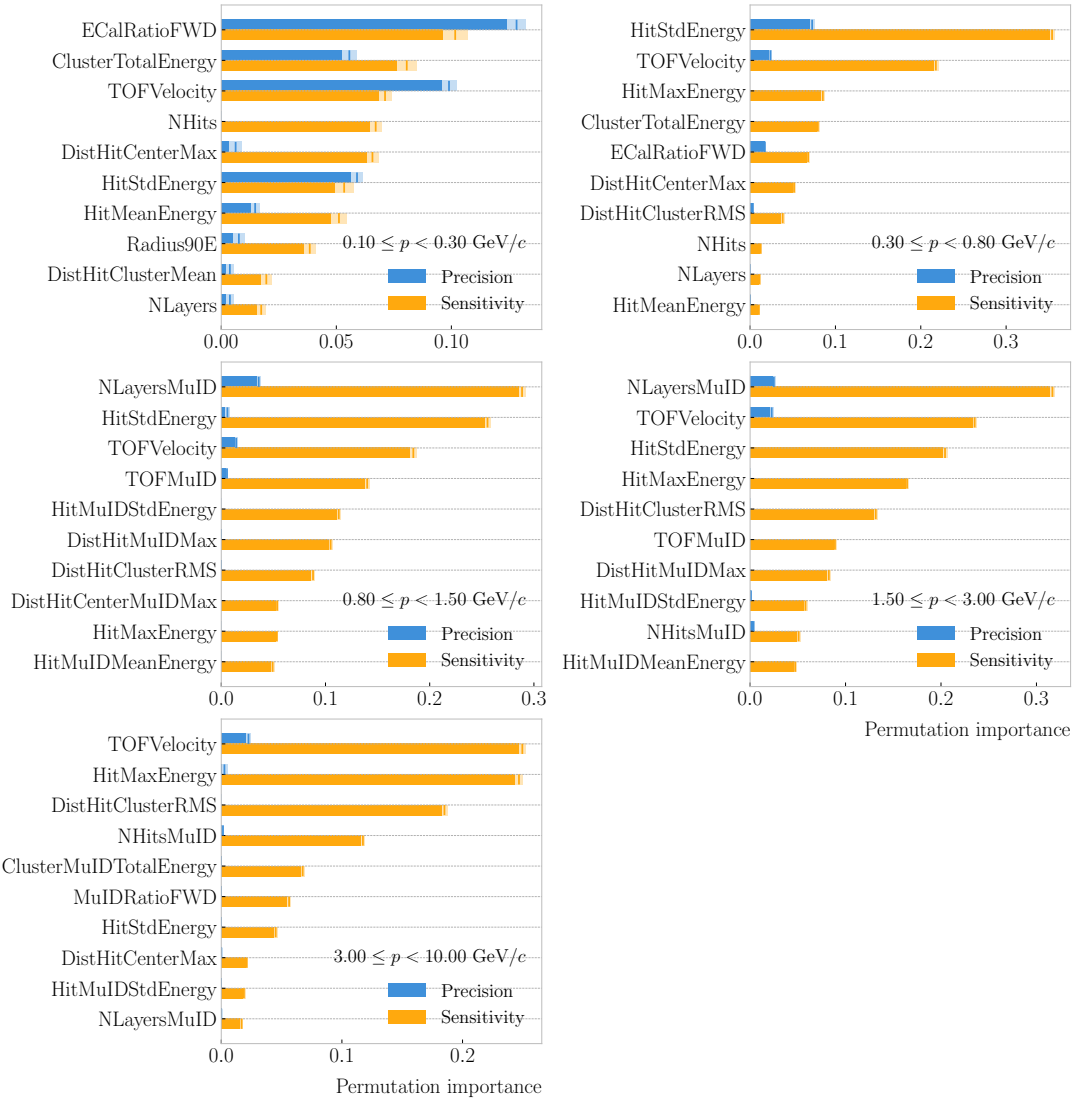


Figure 8.25: Permutation importances for the ten most important features in the different momentum ranges (from left to right, top to bottom, in increasing momentum order). The bars indicate the effect that permutations of each feature have on the purity (blue) and the sensitivity (yellow), the translucent regions representing one standard deviation around the central value.

8.2. Muon and pion separation in the ECal and MuID

3302 of the variables I report the effect the permutations have on the precision (blue) and
3303 sensitivity (yellow) of the models. The bars indicate the importance value, with the
3304 lighter part representing one standard deviation around the mean (hinted as an additional
3305 vertical line). Something to notice is that, in the first momentum region, the feature
3306 permutations have an effect on both the precision and the sensitivity. However, for the
3307 rest the precision is almost unaffected, while the sensitivity changes are considerably
3308 larger.

3309 It is also interesting to see that most of the variables identified as important here
3310 are the same I found when looking at the Shapley values. The behaviour of these across
3311 the momentum ranges is also similar, with the same patterns of some features being
3312 important at low momenta and then dropping in importance for the high momentum
3313 ranges.

3314 Wit this, I conclude the study of the features. I have prepared the training and
3315 testing datasets and understood what features are likely to have the largest impact on
3316 the performance of the classifiers.

3317 8.2.4 Hyperparameter optimisation

3318 Any BDT requires the user to specify a number of parameters that will dictate its
3319 behaviour. They can be divided into two categories: (i) tree-specific parameters, which
3320 affect each individual tree in the model, and (ii) boosting parameters, which control the
3321 boosting operation in the model. The value of these so-called hyperparameters affect the
3322 performance and predictive power of the models. Therefore, one needs to carefully select
3323 their optimal values in order to extract as much information as possible from the data.

3324 From all the parameters used to define a tree in the `scikit-learn` implementation
3325 of the BDT classifier, I only consider a subset of them. This is due to the fact that some
3326 are mutually exclusive, but also because I noticed that others have little effect on the
3327 problem at hand. Therefore, the parameters I investigate are the following:

- 3328 • `min_samples_split`: defines the minimum number of samples required in a node
3329 to be considered for splitting. Higher values prevent a model from learning relations

Chapter 8. Particle ID in GArSoft

3330 which might be highly specific to the particular sample, but may lead to under-fitting
3331 if the value is too low.

3332 • `min_samples_leaf`: defines the minimum samples required in a leaf node. For
3333 imbalanced problems it should take a low value, as there will not be many cases
3334 where the minority class dominates.

3335 • `max_depth`: maximum depth of a tree. Useful to prevent over-fitting, as higher
3336 depth will allow a model to learn relations specific to the training sample.

3337 In the case of the boosting parameters, the ones I look at are:

3338 • `learning_rate`: determines the impact of each tree on the final outcome. Low
3339 values make the model robust to the specific characteristics of a tree, and thus
3340 allow it to generalise well. However, that usually requires a large number of trees
3341 to model the data properly.

3342 • `n_estimators`: number of sequential trees to be trained. In general, BDTs are
3343 fairly robust at higher number of trees but it can still overfit at a point.

3344 • `subsample`: fraction of observations to be selected for each tree. Values slightly
3345 less than 1 make the model robust by reducing the variance.

3346 In general, hyperparameters depend on each other. Thus, it is not possible to
3347 optimise them independently. In the literature, we find two main strategies to explore
3348 the hyperparameter space. We could use a grid search, in which one discretises a
3349 portion of the space of hyperparameters and evaluates the model at each point. Another
3350 approach is the randomised search, where a certain number of random configurations of
3351 hyperparameters are explored.

3352 In this case, I used the random search to scan the hyperparameter space. Also,
3353 because it is not guaranteed that a set of hyperparameters can be efficiently applied
3354 across different datasets, I perform the optimisation for each of the momentum ranges
3355 considered. Table 8.3 shows the list of hyperparameters considered, and the range within

8.2. Muon and pion separation in the ECal and MuID

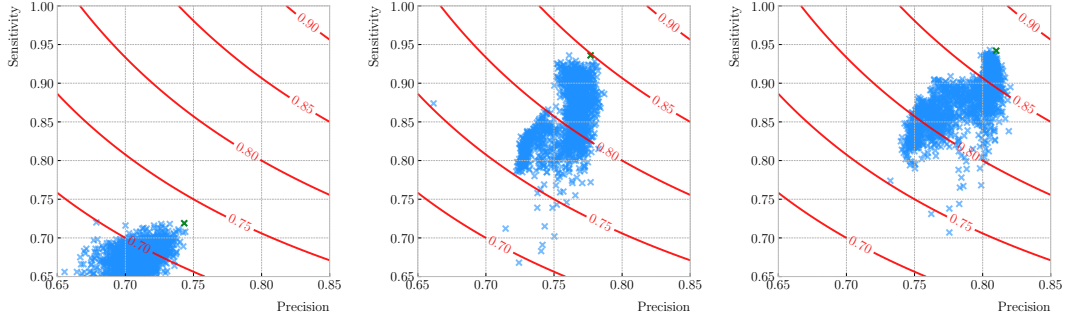


Figure 8.26: Values of the precision and sensitivity obtained for 10000 BDT hyperparameter configurations, for the momentum regions I, III and V. The red contours indicate the curves of equal F_1 -score, while the green crosses are the selected configurations.

3356 which I let them vary. I decided to fix the number of estimators to 400 in all cases, as
 3357 its value is correlated with that of the learning rate.

3358 I evaluate 10000 different hyperparameter configurations for each momentum range.
 3359 For the hyperparameter tuning, I used subsamples containing 10% of the full datasets,
 3360 keeping the original proportions between classes, in order to reduce the computational
 3361 load. The performance of the models was assessed using a stratified 3-fold cross-validation
 3362 with replacement. Cross-validation involves dividing the data in a number of subsets,
 3363 training the model using some of them, and testing it with the rest. In our case, I
 3364 divide the data in 3 equal-sized subsets, maintaining the class proportions of the original
 3365 dataset. Then, for 3 consecutive iterations, I train the models using 2 of the subsets
 3366 while I compute the precision and sensitivity scores with the other. This approach
 3367 provides a more robust estimate of the performance on unseen data.

3368 Figure 8.26 shows the results in the precision versus sensitivity plane, for the
 3369 momentum regions I, III and V (from left to right). The contours represent the curves
 3370 of equal F_1 -score, i.e. the harmonic mean of the precision and the sensitivity. In order
 3371 to select the optimal configurations (indicated in the plots with a green cross), I chose
 3372 the point with the highest F_1 -score.

3373 The results for the different momentum ranges are summarised in Tab. 8.3. One
 3374 can see some consistency in hyperparameter choices, with models generally preferring

Chapter 8. Particle ID in GArSoft

Table 8.3: Optimal values of the hyperparameters used by the BDT, for each momentum range.

Hyperparameter	Range	Best value				
		I	II	III	IV	V
<code>min_samples_split</code>	[0.001, 1]	0.10	0.06	0.05	0.27	0.06
<code>min_samples_leaf</code>	[0.001, 1]	0.02	0.03	0.01	0.02	0.07
<code>max_depth</code>	{2, 3, ..., 8}	8	2	4	2	7
<code>learning_rate</code>	[0.05, 1]	0.10	0.23	0.07	0.13	0.09
<code>subsample</code>	[0.01, 1]	0.75	0.65	0.79	0.86	0.95

Table 8.4: Performance metrics of the BDTs with optimal hyperparameters, for the different momentum ranges.

Metric	Value $\pm 1\sigma$				
	I	II	III	IV	V
Accuracy	0.779 ± 0.003	0.812 ± 0.003	0.846 ± 0.002	0.861 ± 0.003	0.874 ± 0.002
Precision	0.769 ± 0.003	0.752 ± 0.005	0.788 ± 0.002	0.805 ± 0.003	0.815 ± 0.003
Sensitivity	0.745 ± 0.009	0.921 ± 0.006	0.965 ± 0.002	0.967 ± 0.002	0.976 ± 0.001
F_1 -score	0.757 ± 0.004	0.828 ± 0.003	0.867 ± 0.002	0.879 ± 0.002	0.889 ± 0.002
ROC AUC	0.868 ± 0.003	0.865 ± 0.003	0.899 ± 0.002	0.902 ± 0.002	0.911 ± 0.001

3375 small values for the tree-specific parameters, small learning rate, and relatively large

3376 subsample sizes.

3377 Now that I have obtained the optimal values of the hyperparameters, I can train
3378 the different BDTs. In this case I use the complete datasets, keeping 20% of the data
3379 for testing. Table 8.4 shows the values of the different performance metrics obtained
3380 using the selected hyperparameters and 5-fold cross-validation. The last row indicates
3381 the value of the area under the receiver operating characteristic (ROC) curve. This
3382 represents the sensitivity of a model as a function of the false positive rate. I have
3383 included it here as it is a classic model metric used in the machine learning community.
3384 Overall, there is a clear trend of models performing better at higher momentum.

8.2. Muon and pion separation in the ECal and MuID

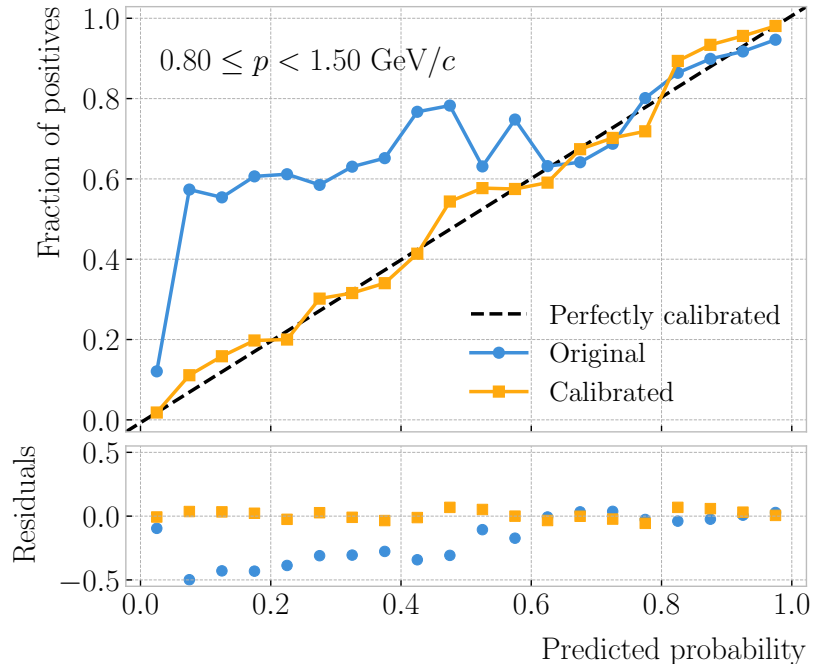


Figure 8.27: Reliability diagrams for the BDT classifier used in the momentum range $0.3 \leq p < 0.8$ GeV/ c , both for the original (blue circles) and calibrated (yellow squares) responses. For reference, the response of a perfectly calibrated classifier is also shown (black dashed line).

8.2.5 Probability calibration

So far, the trained BDTs are able to provide predictions of the class labels. Ideally, one would like the output of a classifier to give a confidence level about the prediction. However, it is not straightforward to interpret the outputs of our BDTs in terms of probabilities.

A way to visualise how well the predictions of a classifier are calibrated is using reliability diagrams [130]. They represent the probability of the positive label versus the probability predicted by the classifier. These can be obtained by binning the predicted probabilities, and then compute the conditional probability $P(y_{true} = 1 | y_i \leq y_{pred} < y_{i+1})$ by checking the fraction of true positive instances in each bin. The reliability diagram of a perfectly calibrated classifier would be a diagonal line.

In this case, I try to correct the raw response of the classifiers by applying a sigmoid

Chapter 8. Particle ID in GArSoft

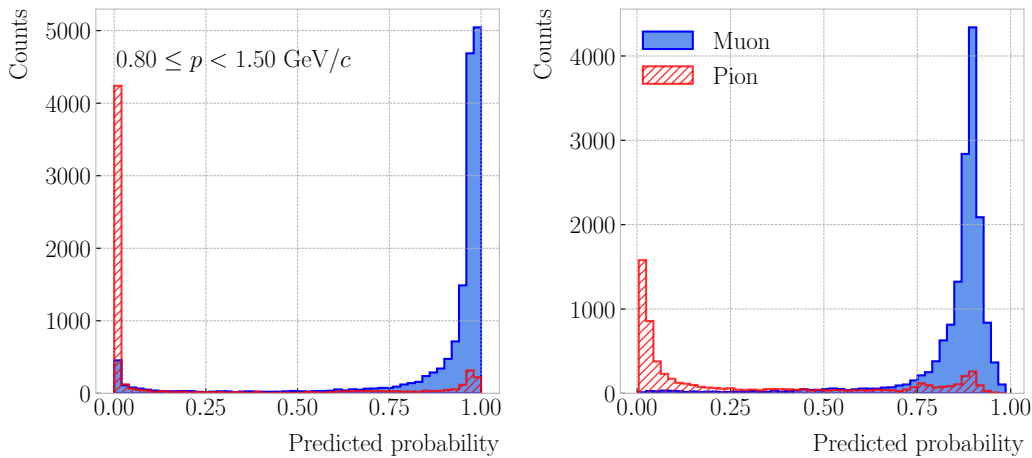


Figure 8.28: Uncalibrated (left panel) and calibrated (right panel) predicted probabilities assigned by the BDT classifiers for true muons (blue) and charged pions (red) in the momentum range $0.3 \leq p < 0.8 \text{ GeV}/c$.

3397 function:

$$\sigma(x; A, B) = \frac{1}{1 + e^{Ax+B}}, \quad (8.18)$$

3398 where the parameters A and B are real numbers determined using the method of least
3399 squares.

3400 For each classifier, I perform a grid search to obtain the optimal values of A and B .

3401 For any pair, I compute the predicted probabilities as $y_{pred} = \sigma(y_{raw}; A, B)$, where y_{raw}
3402 are the raw predictions of the classifier⁹. Then, I calculate the corresponding reliability
3403 curve, and take the sum of the squared residuals between it and the response of the
3404 perfectly calibrated classifier.

3405 Figure 8.27 shows the reliability diagrams for the original (blue) and calibrated
3406 (yellow) probability predictions of the classifier for the III momentum range, $0.3 \leq p <$
3407 $0.8 \text{ GeV}/c$. The original response of the classifier is given by $y_{pred} = \sigma(y_{raw}; -2, 0)$,
3408 which is the transformation applied by `scikit-learn` to produce the probability estimate.
3409 Notice how the calibrated prediction matches the ideal response much better than the
3410 original, across all the probability range.

3411 One can also compare the responses of the uncalibrated and calibrated classifiers

⁹In `scikit-learn` these correspond to the outputs of the `decision_function` method.

8.3. ECal time-of-flight

3412 broken down by true particle type, as shown in Fig. 8.28. It can be seen that the
3413 distributions for both muons (blue) and charged pions (red) smoothen after calibration,
3414 but still the separating power of the classifier remains unchanged.

3415 At this point, having the trained classifiers and the probability calibration parameters,
3416 I am able to assess the performance of the classification strategy in a physics-relevant
3417 case.

3418 8.2.6 Performance

3419 8.3 ECal time-of-flight

3420 Looking at Fig. 8.19, it is clear that for momentum values in the range $1.0 - 3.0 \text{ GeV}/c$
3421 it is not possible to separate pions and protons using a $\langle dE/dx \rangle$ measurement in the
3422 HPgTPC. However, in the previous section I assumed that protons at those energies
3423 could be identified by other means, and therefore were not an issue for the muon and
3424 pion discrimination.

3425 Some detectors, like ALICE [131] or the ILD concept [132], complement the PID
3426 capabilities of their gaseous trackers with time-of-flight measurements. The use of
3427 fast timing silicon sensors, with hit time resolutions under 100 ps, would allow for the
3428 identification of charged hadrons via a ToF measurement up to $5.0 \text{ GeV}/c$. In the case
3429 of ND-GAr, one could think of using the inner layers of the ECal, the ones consisting of
3430 high-granularity tiles, to obtain a ToF-based PID, with some inputs from the TPC.

3431 Measuring the momentum and the velocity of a charged particle allows for a
3432 determination of the mass through the relativistic momentum formula:

$$m = \frac{p}{\beta} \sqrt{1 - \beta^2}. \quad (8.19)$$

3433 In our case, the momentum is measured in the TPC, using the curvature and the dip
3434 angle of the helix inside the magnetic field. The velocity of the particle can be written

Chapter 8. Particle ID in GArSoft

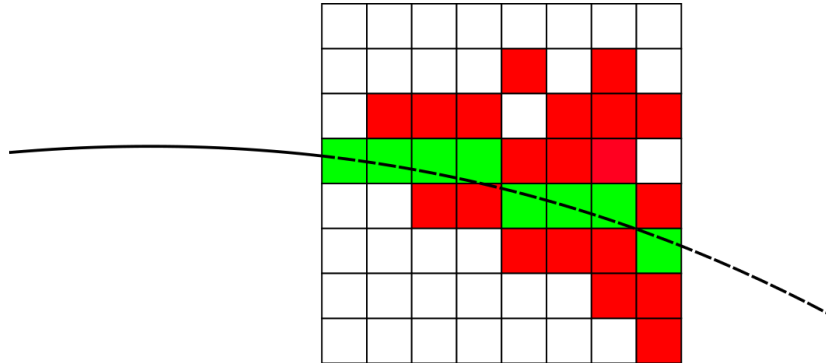


Figure 8.29: Schematic of the hit selection used for the ToF measurement. The grid represents the layers of the inner ECal, with coloured squares indicating the tiles with hits. Green squares indicate the selected hits.

3435 as:

$$\beta = \frac{\ell_{track}}{c\tau}, \quad (8.20)$$

3436 where ℓ_{track} is the length of the track, and τ the arrival time to the ECal.

3437 In GArSoft, the track length is computed at the Kalman filter stage. It is simply the
 3438 sum of the line segments along the track, either in the forward or backward fit. In this
 3439 case, because we are only interested in the particles that make it to the ECal, I choose
 3440 the fit direction based on the results of the track-cluster associations.

3441 Additionally, because the last 30 cm of the TPC radius are uninstrumented¹⁰, I need
 3442 to correct for the length of the tracks. Using the track fit parameters to propagate the
 3443 helix to its entry point in the ECal, one can write the total track length as:

$$\ell_{track} = \ell + \left| \frac{\phi_{EP} - \phi}{R^{-1}} \right| \sqrt{1 + \tan^2 \lambda}, \quad (8.21)$$

3444 where ϕ_{EP} is the angle of rotation at the entry point to the calorimeter, and ℓ , ϕ , R and
 3445 λ are the track length, angle of rotation, radius of curvature and dip angle at the last
 3446 point in the fit, respectively.

3447 To test the idea of performing a ToF measurement with the inner ECal, I generated
 3448 two data samples. Each consists of 10000 single particle events, either charged pions or

¹⁰Note to self: check this number.

8.3. ECal time-of-flight

3449 protons. Their momenta are uniformly distributed in the range $0.5 - 5.0 \text{ GeV}/c$, and
3450 their directions are isotropic. I process each sample using different values of the time
3451 resolution, from $\Delta\tau = 0$, the perfect time resolution case for comparison, to the current
3452 nominal value of $\Delta\tau = 0.7 \text{ ns}$, and the worse scenario of $\Delta\tau = 1.0 \text{ ns}$.

3453 8.3.1 Arrival time estimations

3454 In the simulation, the limited time resolution of the ECal is taken into account by
3455 applying a Gaussian smearing to the true hit times. Other effects, like the digitisation
3456 of the signals, are not taken into account and fall beyond the scope of this study. After
3457 the track-cluster, one ends up with a collection of ECal hits associated to each particle.
3458 From these, the arrival time of the particle to the ECal can be extracted.

3459 The simplest possibilities are to either take the time of the earliest hit or the hit
3460 closest to the entry point. Because these two coincide, in general, I focused only in
3461 the earliest hit time. However, this needs to be corrected, to account for the distance
3462 travelled from the entry point to the position of the hit:

$$\tau_{earliest} = \tau_{hit} - \frac{d_{EP-hit}}{c}, \quad (8.22)$$

3463 where τ_{hit} is the time of the earliest hit, and d_{EP-hit} is the distance between that hit
3464 and the entry point of the particle to the ECal. This is computed as the arc length
3465 between the entry point and the point of the extrapolated helix up to the layer of the
3466 hit. This way of correcting the time assumes c for the propagation of the particle, which
3467 may lead to biased estimates.

3468 I also tried to estimate the arrival times using information from the rest of the hits.
3469 In order to do this, as a simplifying assumption, I approximate the hadronic shower
3470 considering only its MIP component. For each layer, I keep only the hit in the tile closest
3471 to the point of the extrapolated track up to that layer. Figure 8.29 shows an example of
3472 how this hit selection works. The dashed line represents the extrapolated track, while
3473 the coloured squares are the tiles containing hits. Green indicates the tiles closer to the

Chapter 8. Particle ID in GArSoft

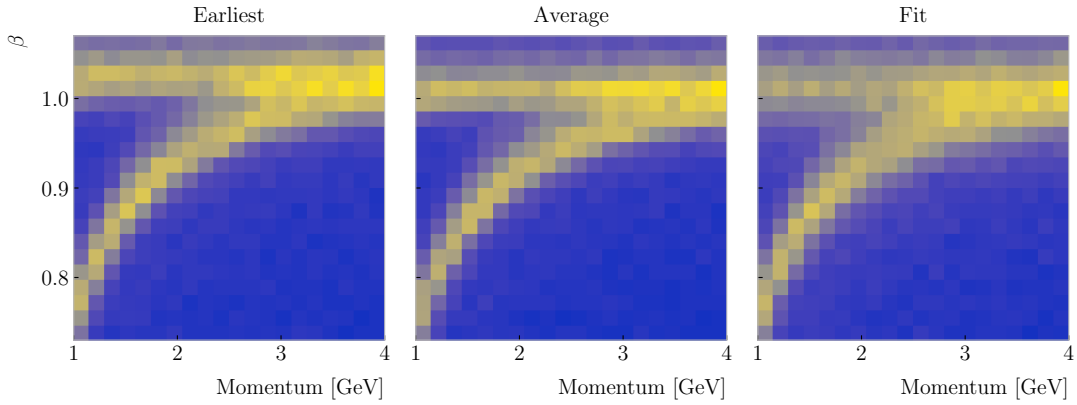


Figure 8.30: Particle velocity versus momentum measured with different ECal arrival time estimations. From left to right: earliest hit time, average hit time, and fitted hit time. In all cases the time resolution is $\Delta\tau = 0.1$ ns.

3474 track in each layer (in the sketch they correspond to the grid columns).

3475 Now, I can use these collections of hits to estimate the arrival times. A possibility
 3476 is to take the average of the times of the selected hits, denoted $\tau_{average}$. For that to
 3477 work, one needs to correct these times, in a similar way as in Eq. (8.22), before taking
 3478 the average. However, as before, this correction assumes that the particle travels at the
 3479 speed of light inside the ECal. Another option is to perform a linear fit to the hit times
 3480 and the distances to the entry point. In that case, the arrival time would be the fitted
 3481 value of the intercept, τ_{fit} . This method would not assume a speed of light propagation.

3482 Figure 8.30 shows the velocity estimations as a function of the particle momentum,
 3483 for the earliest hit time (left panel), average hit time (middle panel), and fitted hit time
 3484 (right panel). The two bands correspond to the π^\pm and the p particles. $\Delta\tau = 0.1$ ns.
 3485 Notice how, for the earliest hit time method, the velocities are significantly biased
 3486 towards larger values. For the multi-hit methods, the τ_{fit} estimate appears to produce a
 3487 larger variance than when using the $\tau_{average}$ method.

3488 8.3.2 Proton and pion separation

3489 Once we have the velocities of the particles, one can estimate their masses through
 3490 Eq. (8.19). The resulting mass spectra are shown in Fig. 8.31. I computed the masses

8.3. ECal time-of-flight

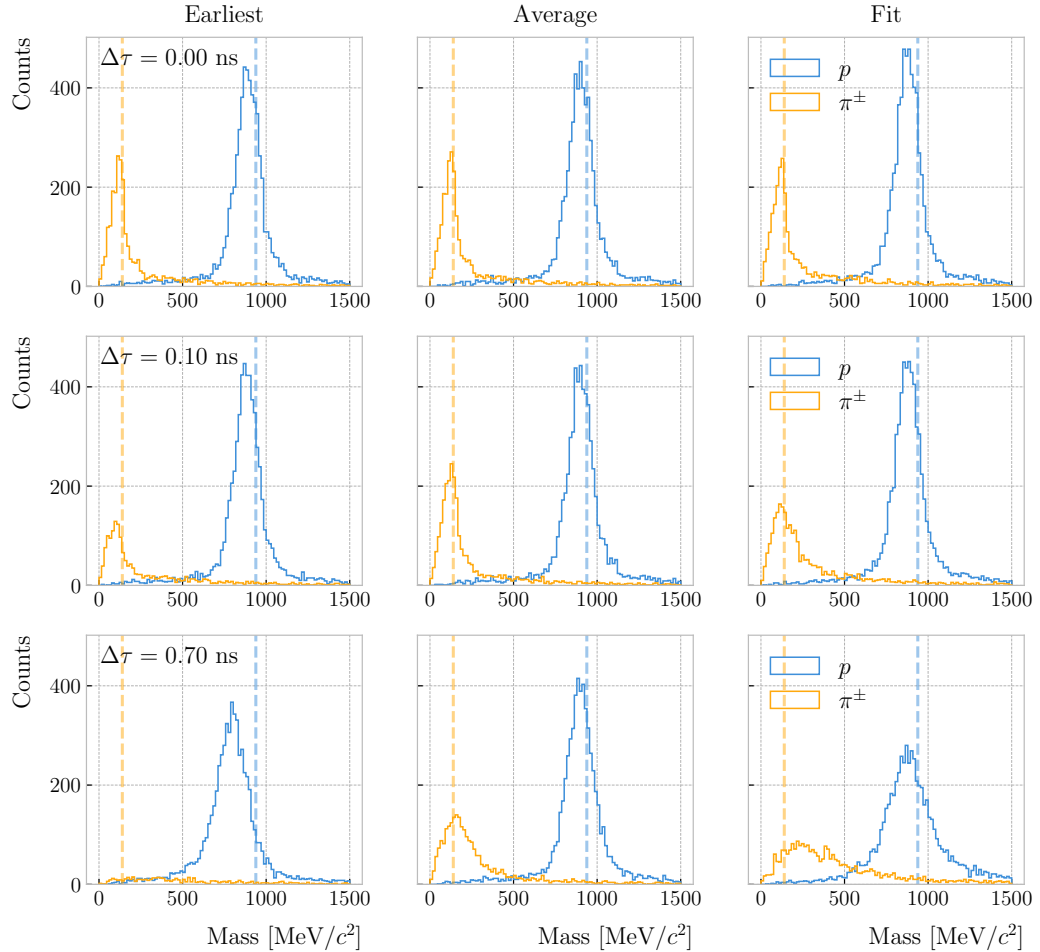


Figure 8.31: Mass spectra for p (blue) and π^\pm (yellow) particles, using different ECal time resolution values (from top to bottom, in ascending order), and arrival time estimates. From left to right: earliest hit time, average hit time, and fitted hit time. The dashed lines indicate the true masses of the particles.

for the three arrival time estimates discussed above, and three different values of the time resolution: $\Delta\tau = 0.00$ (perfect time resolution), $\Delta\tau = 0.10$ ns, and $\Delta\tau = 0.70$ ns. Although in all cases we have the same number of events, it appears as if the entries in the histograms decrease as the time resolution increases. Sometimes, the particles get unphysical values of $\beta > 1$, and in turn they do not contribute to the mass spectra. This is more likely to happen for higher values of $\Delta\tau$.

As noted before, the average hit time method produces the most robust estimates when increasing $\Delta\tau$. Intuitively this makes sense, as by taking the mean one averages

Chapter 8. Particle ID in GArSoft

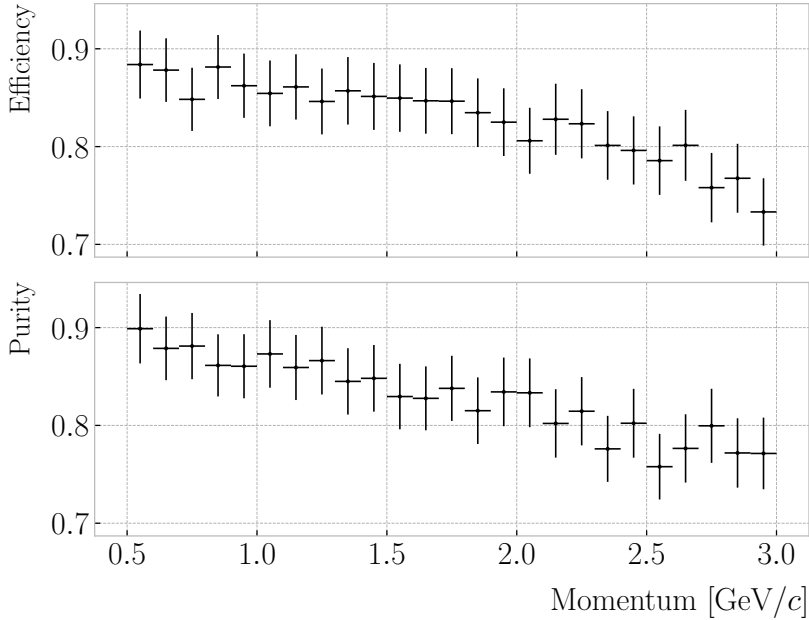


Figure 8.32: Efficiency (top panel) and purity (bottom panel) for the proton selection as a function of the momentum, for $\Delta\tau = 0.10$ ns.

3499 out the effect of the Gaussian smearing. Going forward, I will use this arrival time
 3500 estimator, as it appears to be the best performing one.

3501 It is possible to use the velocity estimations to select a sample of protons. In this
 3502 case, I do so by dividing the relevant momentum range in bins of 0.1 GeV/c . For each
 3503 momentum bin, I compute the expected velocity for the protons via the inverse of Eq.
 3504 (8.19), and then take the fractional residuals of the measured velocities. Using that
 3505 distribution, I choose the cut that maximises the F_1 -score of the proton selection.

3506 The results can be seen in Fig. 8.32, for the case $\Delta\tau = 0.10$ ns. As expected from
 3507 Fig. 8.30, the performance of the selection degrades rapidly with increasing momentum.
 3508 However, the purity is still around 75% at 3.0 GeV/c . This is likely to be sufficient, as
 3509 we do not expect protons or charged pions with higher energies from the beam neutrino
 3510 interactions.

3511 Figure 8.33

8.4. Charged pion decay in flight

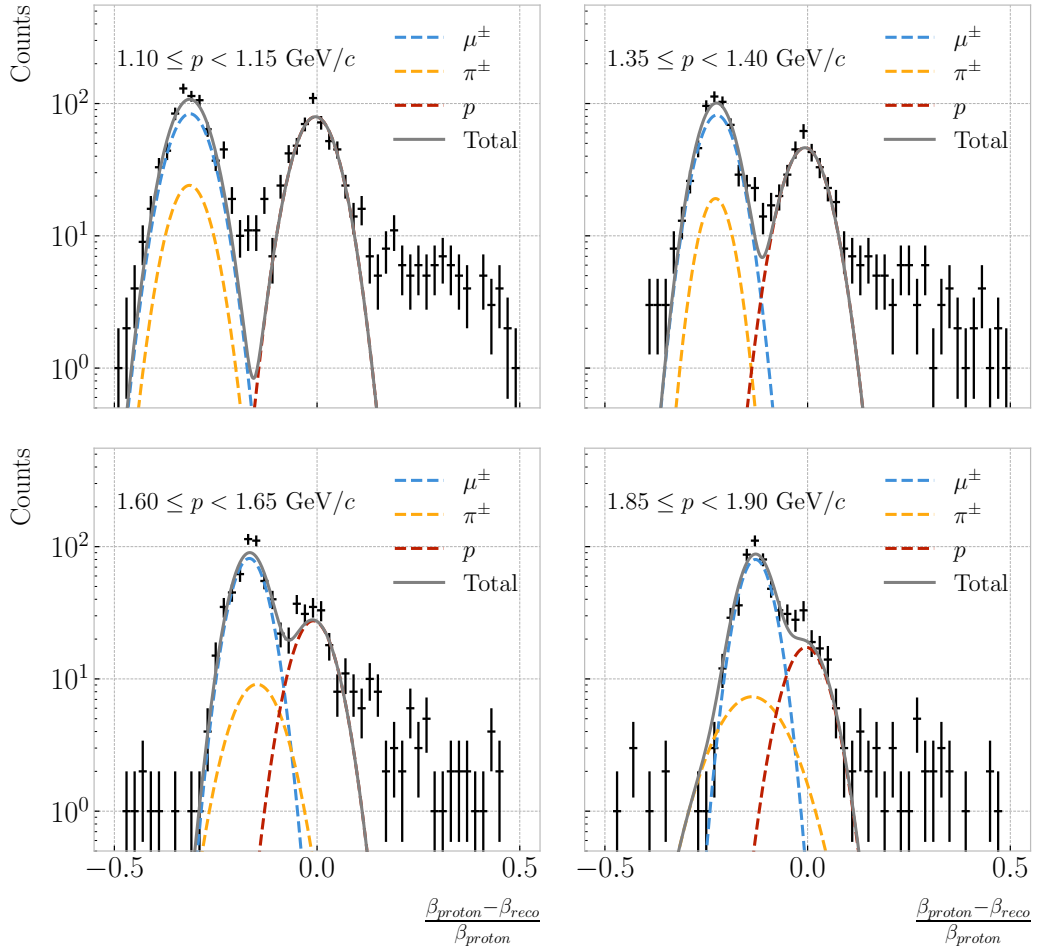


Figure 8.33: Distributions of the velocities measured by ToF with the inner ECal, for different momentum bins, in a FHC neutrino interaction sample. The Gaussian fits are performed around the maxima for each particle species.

3512 8.4 Charged pion decay in flight

3513 As discussed previously, in GArSoft the TPC tracks are formed after a pattern recognition
 3514 algorithm and a Kalman filter are applied to the TPC clusters. These two steps can
 3515 find discontinuities in the track candidates (e.g. due to a particle decay) when these
 3516 so-called breakpoints are large enough. However, for some, more subtle, cases they may
 3517 miss them and form a single reconstructed track. It has been noted in the literature
 3518 that Kalman filters offer, as a by-product, additional information to form test statistics
 3519 to identify these breakpoints [133, 134].

3520 Considering the mean life of the charged pion, $\tau = (2.6033 \pm 0.0005) \times 10^{-8} \text{ s}$, one

Chapter 8. Particle ID in GArSoft

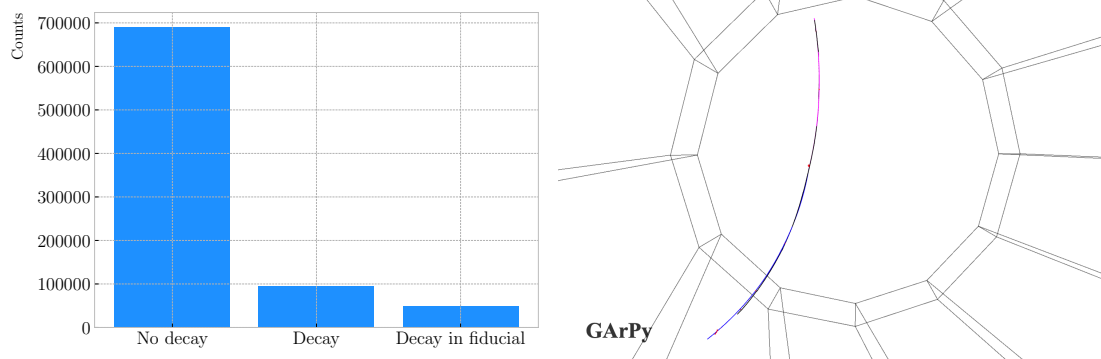


Figure 8.34: Left panel: number of non-decaying, decaying and decaying in the fiducial volume pions for a MC sample of 100000, $p = 500 \text{ MeV}/c$ isotropic positively charged pions inside the TPC. Right panel: event display for a positive pion decaying inside the fiducial volume, with a single reconstructed track for the pion and muon system.

3521 can estimate that about 12% of the pions with momentum $p \sim \mathcal{O}(500 \text{ MeV}/c)$ (roughly
 3522 the peak of the pion momentum distribution in ν_μ CC interactions off argon) decay
 3523 inside the TPC. Figure 8.34 (left panel) shows the amount of charged pions decaying in
 3524 the full TPC and fiducial volumes from an isotropic, monoenergetic sample of 100000
 3525 negatively charged pions with $p = 500 \text{ MeV}/c$. We see that about 10% of those decayed,
 3526 with more than half of them decaying inside the TPC fiducial volume.

3527 Figure 8.34 (right panel) shows an example event display of a charged pion (magenta
 3528 line) decays in flight inside the TPC, but because the angle of the muon (blue line) is
 3529 small both were reconstructed as one single track (black line). In this case, the composite
 3530 track reaches the ECal, where it undergoes a muon-like interaction, thus being classified
 3531 as a muon.

3532 A way to understand what decaying pion tracks were totally or partially reconstructed
 3533 together with the daughter muon is looking at the relative energy contributions to the
 3534 reconstructed track. In order to select a sample of such events, I require that a minimum
 3535 50% of the total energy comes from the pion and at least 20% from the muon.

3536 8.4.1 Track breakpoints

3537 To identify potential decays we can use the information we obtain from the Kalman
 3538 filter at each step of the fitted track. The simplest test we can think about is computing

8.4. Charged pion decay in flight

3539 the χ^2 of the mismatch between all the parameters in the forward and the backward fits:

$$\chi_k^{2 (FB)} = (\hat{x}_k^B - \hat{x}_k^F)^T [V^{(\hat{x}_k, B)} + V^{(\hat{x}_k, F)}]^{-1} (\hat{x}_k^B - \hat{x}_k^F), \quad (8.23)$$

3540 where \hat{x}_k^F , \hat{x}_k^B are the Kalman filter state vector estimates at step k in the forward and
3541 backward fits and $V^{(\hat{x}_k, F)}$, $V^{(\hat{x}_k, B)}$ the covariance matrices of \hat{x}_k^F and \hat{x}_k^B respectively.
3542 Using the values of the χ^2 at measurement k for the forward and backward fits we can
3543 compute another χ^2 value that characterises the overall track fit:

$$\chi_{track}^2 = \chi_k^{2 (F)} + \chi_k^{2 (B)} + \chi_k^{2 (FB)}, \quad (8.24)$$

3544 which remains approximately constant for all k .

3545 An alternative approach proposed in the context of the NOMAD experiment was
3546 using a fit with a more elaborate breakpoint hypothesis, so we can perform a comparison
3547 of the χ^2 with and without breakpoints. This can be achieved by using some alternative
3548 parametrisation with extra parameters, which allows some of the track parameters to
3549 be discontinuous at certain points. A decay changes the momentum magnitude and
3550 direction, so we can use the new state vector:

$$\alpha = (y, z, 1/R_F, 1/R_B, \phi_F, \phi_B, \tan\lambda_F, \tan\lambda_B)^T. \quad (8.25)$$

3551 As we already have the estimates from the standard Kalman filter and their
3552 covariance matrices at each point, we do not need to repeat the Kalman fit for the new
3553 parametrisation. Instead, I can compute the values of α at each point k that minimise
3554 the χ^2 resulting from comparing them to $\{\hat{x}_k^B, \hat{x}_k^F\}$. Introducing the two 5×8 matrices:

$$H^F = \begin{pmatrix} 1 & 0 & 0 & 0 & 0 & 0 & 0 & 0 \\ 0 & 1 & 0 & 0 & 0 & 0 & 0 & 0 \\ 0 & 0 & 1 & 0 & 0 & 0 & 0 & 0 \\ 0 & 0 & 0 & 0 & 1 & 0 & 0 & 0 \\ 0 & 0 & 0 & 0 & 0 & 0 & 1 & 0 \end{pmatrix}, \quad H^B = \begin{pmatrix} 1 & 0 & 0 & 0 & 0 & 0 & 0 & 0 \\ 0 & 1 & 0 & 0 & 0 & 0 & 0 & 0 \\ 0 & 0 & 0 & 1 & 0 & 0 & 0 & 0 \\ 0 & 0 & 0 & 0 & 0 & 0 & 1 & 0 \\ 0 & 0 & 0 & 0 & 0 & 0 & 0 & 1 \end{pmatrix}, \quad (8.26)$$

Chapter 8. Particle ID in GArSoft

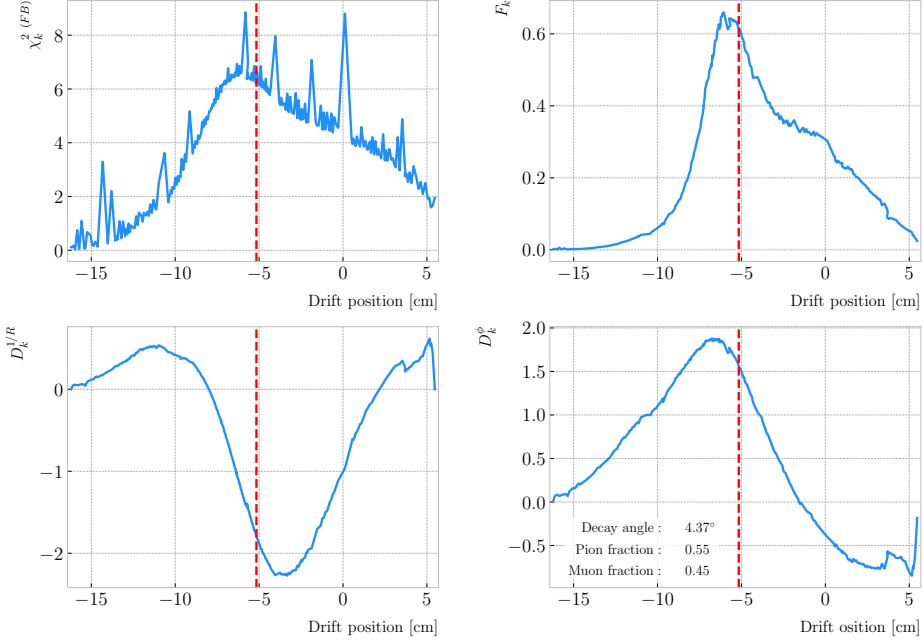


Figure 8.35: Values of $\chi_k^2(FB)$ (top left panel), F_k (top right panel), $D_k^{1/R}$ (bottom left panel) and D_k^ϕ (bottom right panel) versus position along the drift direction for a reconstructed track in a positive pion decay event. The vertical red dashed line indicates the true location of the decay point.

3555 we can write this as:

$$\begin{aligned}\chi_k^2(FB)(\alpha) &= (\hat{x}_k^F - H^F \alpha)^T \left[V^{(\hat{x}_k, F)} \right]^{-1} (\hat{x}_k^F - H^F \alpha) \\ &\quad + (\hat{x}_k^B - H^B \alpha)^T \left[V^{(\hat{x}_k, B)} \right]^{-1} (\hat{x}_k^B - H^B \alpha).\end{aligned}\tag{8.27}$$

3556 The minimum of $\chi_k^2(FB)(\alpha)$ is found when the measured new state vector takes the

3557 value:

$$\hat{\alpha}_k = V^{(\hat{\alpha}_k)} H^T (V^{(\hat{x}_k)})^{-1} \hat{X},\tag{8.28}$$

3558 where $\hat{X} = \{\hat{x}_k^B, \hat{x}_k^F\}$, $V^{(\hat{x}_k)}$ is the block diagonal matrix formed by $V^{(\hat{x}_k, F)}$ and $V^{(\hat{x}_k, B)}$

3559 and $V^{(\hat{\alpha}_k)}$ is the covariance matrix of $\hat{\alpha}_k$, given by:

$$V^{(\hat{\alpha}_k)} = \left(H^T (V^{(\hat{x}_k)})^{-1} H \right)^{-1}.\tag{8.29}$$

3560 From these new fit estimates we can compute the F statistic, which tells us whether

8.4. Charged pion decay in flight

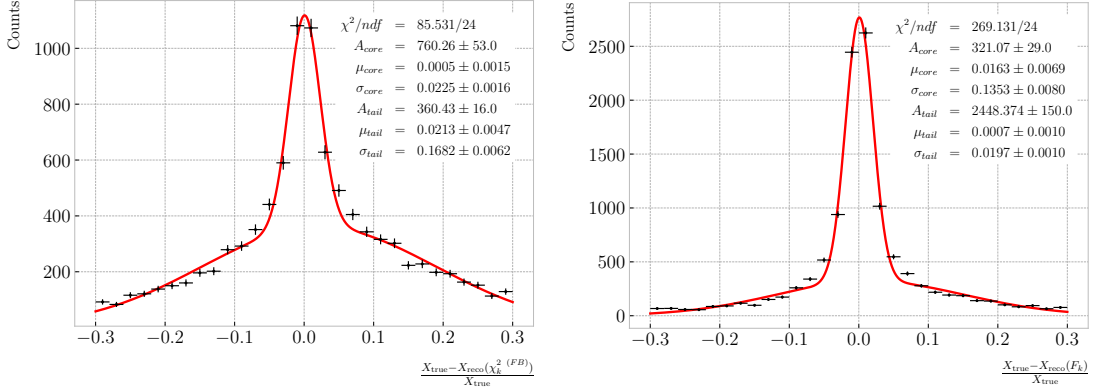


Figure 8.36: Fractional residual distributions of the true and reconstructed decay position along the drift coordinate, using the position of the maximum of $\chi_k^2(FB)$ (left panel) and F_k (right panel) as estimates of the decay position. Also shown are double Gaussian fits to these points (red lines).

3561 the model with breakpoint provides a statistically significant better fit:

$$F_k = \left(\frac{\chi_{\text{track},k}^2 - \chi_{\text{full},k}^2}{8 - 5} \right) / \left(\frac{\chi_{\text{full},k}^2}{N - 8} \right). \quad (8.30)$$

3562 One can also compute the signed difference of the duplicated variables divided by
3563 their standard deviation at each point. These represent how significant the discontinuity
3564 in each variable is. For any variable η we can write it as:

$$D_k^\eta = \frac{\hat{\eta}_k^B - \hat{\eta}_k^F}{\sqrt{\text{Var}[\hat{\eta}_k^F] + \text{Var}[\hat{\eta}_k^B] - 2\text{Cov}[\hat{\eta}_k^F, \hat{\eta}_k^B]}}. \quad (8.31)$$

3565 In our case, the relevant ones to look at are $D_k^{1/R}$ and D_k^ϕ .

3566 Figure 8.35 shows the values of $\chi_k^2(FB)$, F_k , $D_k^{1/R}$ and D_k^ϕ as functions of the position
3567 along the drift direction, for an example reconstructed track with 55.5% of the energy
3568 coming from the charged pion and 45.5% from the daughter muon. The true position of
3569 the decay is indicated (dashed red lines). Notice how $\chi_k^2(FB)$ and F_k , $D_k^{1/R}$ reach their
3570 maxima near the decay point. In the former case this indicates a large forward-backward
3571 difference in the track fit. In the later it represents that the extended state vector
3572 improves the fit particularly around that point.

Chapter 8. Particle ID in GArSoft

3573 I can estimate the decay position finding resolution by computing the difference
 3574 between the X position of the maxima of $\chi_k^2(FB)$ and F_k and the X position of the
 3575 true decay. Figure 8.36 represent the the fractional residual distributions for both
 3576 cases, from the sample of tracks containing pion decays. Fitting a double Gaussian to
 3577 the distributions (red lines) I find a resolution of $(3.31 \pm 0.15)\%$ and $(6.94 \pm 0.31)\%$
 3578 respectively.

3579 In principle, the F -statistic should follow a Fisher distribution with $(8 - 5)$ and
 3580 $(N - 8)$ degrees of freedom under the null hypothesis. In most of our cases $N \sim \mathcal{O}(100)$,
 3581 so the probability density functions will look very similar. In this case, it is safe to take
 3582 the limit $N \rightarrow \infty$ in the Fisher PDF:

$$\begin{aligned}\tilde{f}(x; a - b) &= \lim_{N \rightarrow \infty} f(x; a - b, N - a) \\ &= \frac{2^{-\frac{a-b}{2}}}{\Gamma(\frac{a-b}{2})} (a - b)^{\frac{a-b}{2}} x^{\frac{a-b}{2}-1} e^{-\frac{a-b}{2}x}.\end{aligned}\tag{8.32}$$

3583 In our case $a - b = 8 - 5 = 3$, so we would obtain a p-value of 0.05 at $x = 2.60$.

3584 Figure 8.37 contains the distributions of the maxima of $\chi_k^2(FB)$, F_k and D_k^ϕ and the
 3585 minima of $D_k^{1/R}$ for a sample of non-decaying pion tracks (blue) and another sample of
 3586 reconstructed tracks containing part of the pion and the daughter muon from a decay
 3587 inside the fiducial volume (red). Notice that, even though the values of $F_k^{(max)}$ for the
 3588 decay sample are typically larger than for the non-decaying one, just a small fraction of
 3589 the events go beyond the aforementioned value of $F = 2.60$. Therefore, from a practical
 3590 point of view, it is not the most efficient variable to use for selecting the decay events.

3591 However, looking at the $D_k^{1/R \ (min)}$ distribution we can see there is a big difference
 3592 between non-decaying and decaying events in this variable. One can use a combination
 3593 of these four variables to distinguish between the pion decay events (signal) and the
 3594 non-decaying pions (background).

3595 An approach to this classification could be using a boosted decision tree (BDT). One
 3596 of the advantages of BDTs is that they are easy to interpret and identify the relative
 3597 importance of the different input variables. Training a BDT with 400 estimators and a

8.4. Charged pion decay in flight

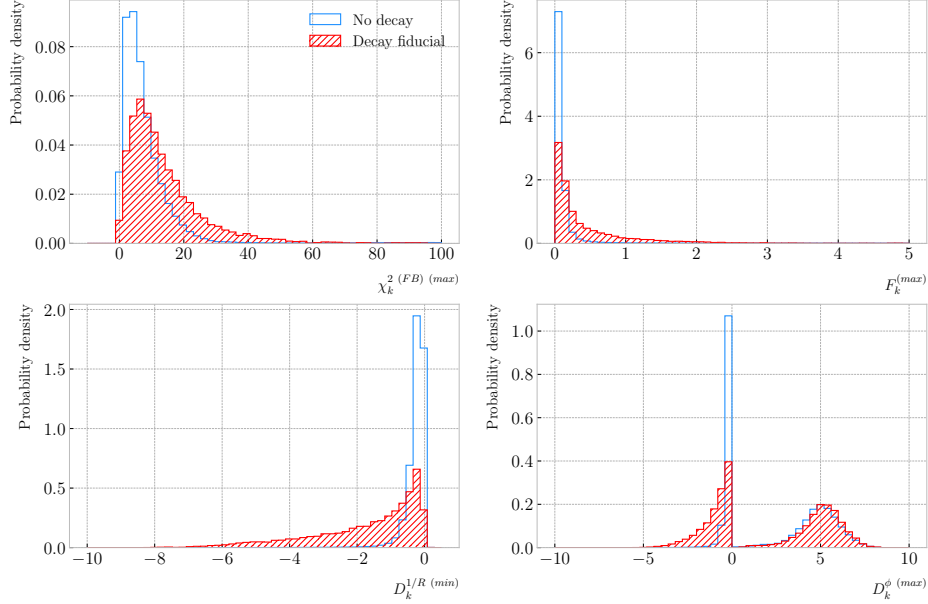


Figure 8.37: Distributions of the extreme values of $\chi_k^2(FB)$ (top left panel), F_k (top right panel), $D_k^{1/R}$ (bottom left panel) and D_k^ϕ (bottom right panel) for non-decaying reconstructed pion tracks (blue) and tracks which include the decay inside the fiducial volume (red).

maximum depth of 4 I can obtain an efficient classification without overtraining. Figure 8.38 (left panel) shows the distribution of probabilities predicted by the BDT for a test sample. The signal efficiency as a function of background acceptance, the so-called ROC curve, is shown in Fig. 8.38 (right panel). With a relative importance of 0.83, the most important variable turned out to be $D_k^{1/R}$ (min).

One thing we can check is how the resolution to the decay and the signal efficiency in the classification changes with the true decay angle. Using an equal-frequency binning for the decay angles, we can repeat the previous steps for each bin.

Figure 8.39 (left panel) shows the dependence on the decay angle of the decay finding resolution. We can see that for the $\chi_k^2(FB)$ maximum location method the resolution consistently lies between 12 to 16%. However, the $F_k^{(max)}$ approach gives a significantly better resolution for high angle values, reaching the 4 – 6% range for decay angles $\geq 4^\circ$.

For the classification dependence on the angle, I use the same classifier I trained before but evaluating the test sample for each individual angular bin. I compute the

Chapter 8. Particle ID in GArSoft

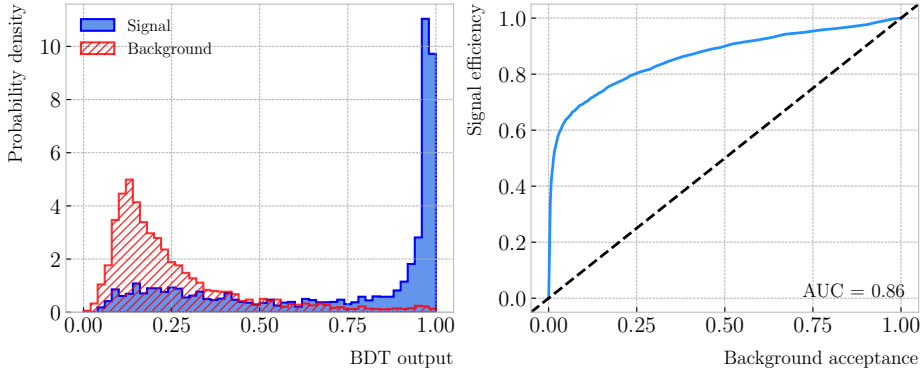


Figure 8.38: Left panel: distributions of the predicted probabilities assigned by the BDT classifier to a test sample of decaying pion+muon tracks (blue) and non-decaying pion tracks (red). Left: signal efficiency versus background acceptance (ROC curve) obtained from the BDT for the test sample.

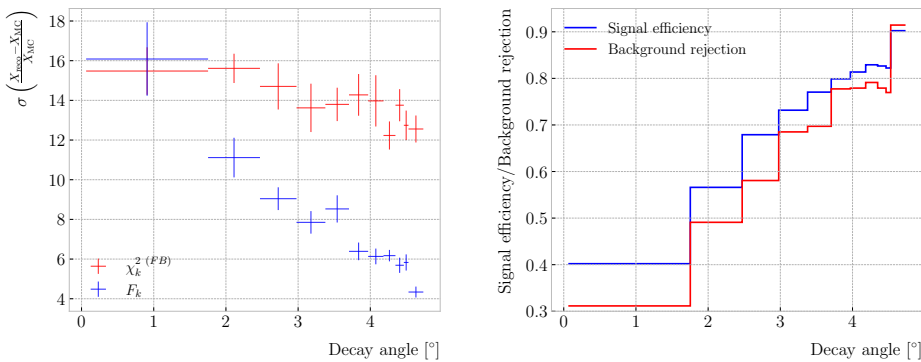


Figure 8.39: Left panel: dependence of the decay position finding resolution on the true value of the decay angle for the $\chi_k^2(FB)$ (red) and F_k (blue) methods. Right panel: signal efficiency (blue line) and background rejection (red line) from the BDT classifier versus true decay angle.

3612 signal efficiency in each bin for a fixed value of the background rejection, in this case
 3613 90%. Similarly, for the background rejection estimation I use a fixed signal efficiency
 3614 value of 90%. Figure 8.39 (right panel) represents the change in signal efficiency (blue)
 3615 and background rejection (red) with the value of the true decay angles.

8.5. Neutral particle identification

3616 8.5 Neutral particle identification

3617 8.5.1 ECal clustering

3618 Another important reconstruction item is the clustering algorithm of ECal hits in
3619 GArSoft. The default module features a NN algorithm that treats all hits in the same
3620 way, independently of the layer each hit comes from. However, the current ECal design
3621 of ND-GAr has two very different types of scintillator layers. The inner layers are made
3622 out of tiles, which provide excellent angular and timing resolutions. On the other hand,
3623 the outer layers are cross scintillator strips. That way, an algorithm that treats hits
3624 from both kinds of layers differently may be able to improve the current performance.

3625 Inspired by the reconstruction of T2K’s ND280 downstream ECal [135], the idea
3626 was to put together a clustering module that first builds clusters for the different ECal
3627 views (tiles, strips segmented in the X direction and strips segmented in Y direction),
3628 and then tries to match them together to form the final clusters.

3629 Working on a module-by-module basis, the algorithm first separates the hits depending
3630 on the layer type they come from. Then, it performs a NN clustering for the 3 sets of
3631 hits separately. For the tile hits it clusters together all the hits which are in nearest-
3632 neighbouring tiles and nearest-neighbouring layers, for strip hits it looks at nearest-
3633 neighbouring strips and next-to-nearest-neighbouring layers (as the layers with strips
3634 along the two directions are alternated). For strip clusters an additional cut in the
3635 direction along the strip length is needed.

3636 After this first clustering I then apply a recursive re-clustering for each collection
3637 of strip clusters based on a PCA method. In each case, we loop over the clusters with
3638 $N_{hits} \geq 2$, computing the centre of mass and three principal components. Propagating
3639 these axes up to the layers of the rest of the clusters, we check if the propagated point
3640 and the centre of mass of the second cluster are within next-to-nearest-neighbouring
3641 strips. An additional cut in the direction along the strip length is also needed. Moreover,
3642 I require that the two closest hits across the two clusters are at most in next-to-nearest-
3643 neighbouring strips. I merge the clusters if these three conditions are satisfied. The

Chapter 8. Particle ID in GArSoft

3644 re-clustering is repeated until no more cluster pairs pass the cuts.

3645 The clusters in each strip view are combined if their centres of mass are close enough
3646 and they point in the same direction. An alternative approach for the strip cluster
3647 merging could be to compute the overlap between the ellipsoids defined by the principal
3648 axes of the clusters, and then merge the pair if the overlap exceeds some threshold.
3649 Further study is needed to understand if this change would have an impact in the overall
3650 clustering performance.

3651 To merge the tile clusters to the combined strip clusters I propagate the principal
3652 axis of the strip cluster towards the inner layers, up to the centre of mass layer of the
3653 tile cluster. I merge the clusters if the distance between the propagated point and the
3654 centre of mass is below a certain cut.

3655 The last step is to check if clusters in neighbouring modules should be merged
3656 together, both across two barrel modules, across end cap modules and between barrel
3657 end cap modules. I check the distance between the two closest hits in the pair of clusters
3658 and merge them if it passes this and an additional direction cut.

3659 Figure ?? presents an example of the clustering steps relevant for strip layer hits, from
3660 the input hits (top left panel) to the NN clustering (top right panel) and re-clustering
3661 (bottom left panel) for each strip view and the final merging strip clusters (bottom
3662 right panel). It shows the hits from a single ECal barrel module in a ν_μ CC interaction
3663 event with a neutral pion and a proton in the final state. The two clusters on the left
3664 correspond to the photon pair from the π^0 decay and the one on the upper right corner
3665 is associated to the proton.

3666 This algorithm has a total number of eight free parameters that need to be optimised.
3667 I used a sample of 1000 ν_μ CC interactions in order to obtain the optimal configuration of
3668 clustering parameters. This sample was generated up to the default ECal hit clustering
3669 level, so then I could run the new clustering algorithm each time with a different
3670 configuration of parameters. As the number of parameters is relatively large, I only
3671 performed a coarse-grained scan of the parameter space. Sampling each of the eight
3672 parameters at three different points each I obtain 6561 different configurations. These

8.5. Neutral particle identification

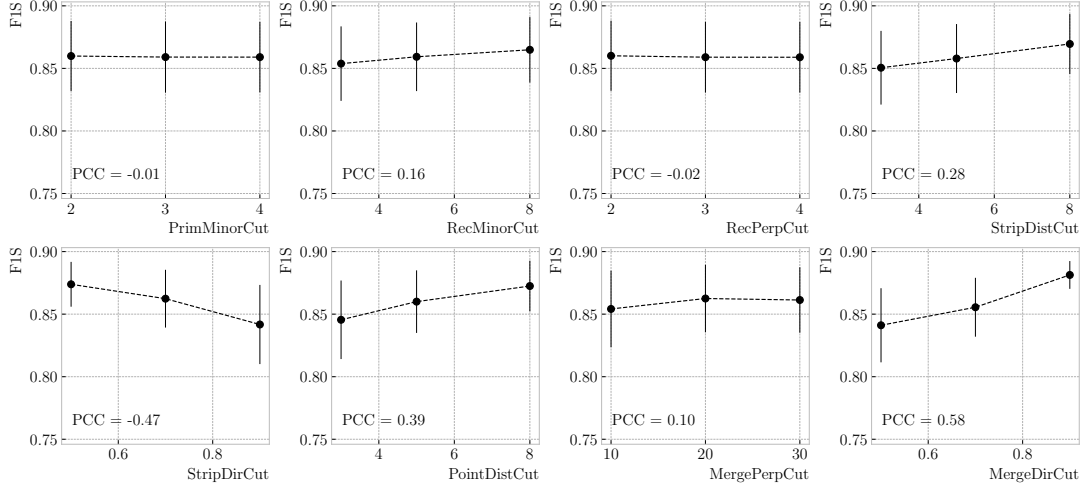


Figure 8.40: Mean values of the F_1 -score marginal distributions for the different free parameters of the new clustering algorithm, with the error bars representing one standard deviation around the mean. The F_1 -score values were computed for the 6561 possible parameter configurations using 1000 ν_μ CC interaction events.

Table 8.5: Summary of parameters and sampled values used in the optimisation of the clustering algorithm.

Name	Units	Sampled values	Description
PrimMinorCut	strips	2, 3, 4	Distance along strip length in NN clustering
RecMinorCut	strips	3, 5, 8	Distance between propagated point and CM along strip length in re-clustering
RecPerpCut	strips	2, 3, 4	Closest hit pair distance in re-clustering
StripDistCut	strips	3, 5, 8	Distance between CMs in strip cluster merging
StripDirCut	cos	0.5, 0.7, 0.9	Main axes direction cut in strip cluster merging
PointDistCut	tiles	3, 5, 8	Distance between propagated point and CM in strip-tile matching
MergePerpCut	cm	10, 20, 30	Closest hit pair distance in module merging
MergeDirCut	cos	0.5, 0.7, 0.9	Main axes direction cut in module merging

parameters, together with the used values, are summarised in Tab. 8.5.

In order to measure the performance of the clustering, I use a binary classification approach. For each formed cluster, I identify the Geant4 Track ID of the matching MC particle and the energy fraction of each hit. Then, I assign to each cluster the Track ID with the highest total energy fraction. For each of the different Track IDs associated to the clusters, I select the cluster with the highest energy (only from the hits with the same Track ID). I identify such a cluster as the main cluster for that Track ID. I count

Chapter 8. Particle ID in GArSoft

as true positives (TPs) the hits with the correct Track ID in each main cluster. False positives (FPs) are the hits with the incorrect Track ID for the cluster they are in, not only main clusters. The false negatives (FNs) are the hits with the correct Track ID in clusters other than the main.

Figure 8.40 shows the computed F_1 -score values for the different cuts. In each case, the central value represents the mean of the F_1 -score distribution for the specified value of the corresponding variable and the vertical error bar represents one standard deviation around the mean. Also shown are the Pearson correlation coefficients of these central values. We can see that five of the variables have a sizeable effect on the F_1 -score, with an absolute difference between the last and first values as big as 4%.

The working configuration is obtained as follows. I first select all configurations with purity $\geq 90\%$. Among those, I choose the combinations that yield the maximum F_1 -score. If more than one configuration remains I select the one with the highest sensitivity. Doing so, I end up with a parameter configuration with an efficiency of 88% and a 90% purity. Compared with the default algorithm, which gives an efficiency of 76% and a purity of 91% for the same sample, I have managed to improve the efficiency by a factor of 1.16.

8.5.2 π^0 reconstruction

One of the potential applications of the new ECal hit clustering is the reconstruction of neutral particles, in particular pions. Neutral pions decay promptly after being produced, through the $\pi^0 \rightarrow \gamma\gamma$ channel ($98.823 \pm 0.034\%$) of the time. The photon pair does not leave any traces in the HPgTPC (unless one or both of them converts into an electron-positron pair), but each of them will produce an electromagnetic shower in the ECal.

To test the potential impact of the new algorithm in π^0 reconstruction, I generated a MC sample of single, isotropic neutral pions inside the HPgTPC. All pions were generated with a momentum $p = 500$ MeV and their initial positions were uniformly sampled inside a $2 \times 2 \times 2$ m box aligned with the centre of the TPC. I ran both the

8.5. Neutral particle identification

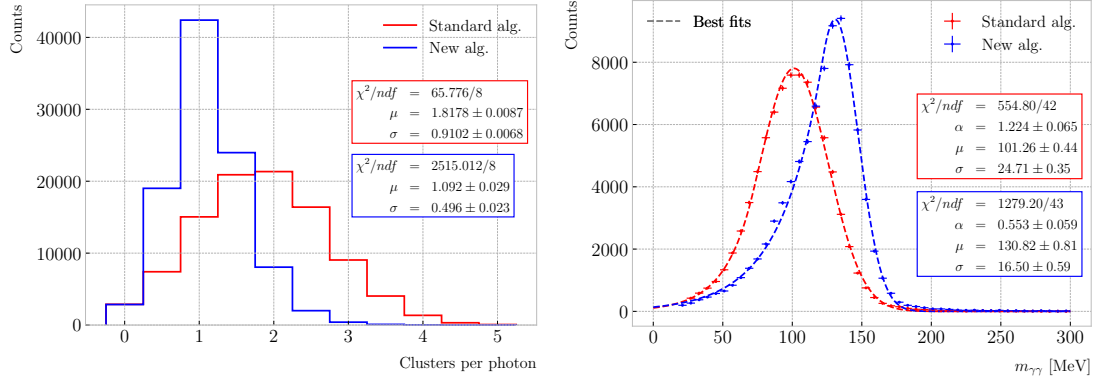


Figure 8.41: Left panel: distributions of the number of ECal clusters per photon from π^0 decays for the standard (red) and new (blue) clustering algorithms. Right panel: reconstructed invariant mass distributions for photon pairs from single π^0 events using the standard (red) and new (blue) ECal clustering algorithms.

3708 default and the new clustering algorithms, using for the latter the optimised configuration
3709 discussed above.

3710 The first thing to notice is that the number of clusters produced per photon has
3711 decreased. Figure 8.41 (left panel) shows these distributions for the default (red) and
3712 new (blue) algorithms. Using a simple Gaussian fit, we see that the mean number of
3713 ECal clusters per photon went from 1.82 ± 0.01 to 1.09 ± 0.03 . This effectively means that
3714 with the new algorithm the ECal activity of one true particle is typically reconstructed
3715 as a single object. From the reconstruction point of view this can be an advantage. As
3716 now most of the photon energy ends up in a single ECal cluster, I can simply use cluster
3717 pairs to identify the π^0 decay.

3718 In general, one calculates the invariant mass of the photon pair as:

$$m_{\gamma\gamma} = \sqrt{2E_1E_2(1 - \cos \theta)}, \quad (8.33)$$

3719 where E_i are the energies of the photons and θ the opening angle between them. In this
3720 case I can use the energies deposited in the ECal and their incident directions. This
3721 quantity is computed for all possible pairs of clusters, using their position together with
3722 the true decay point. In a more realistic scenario, e.g. ν_μ CC interaction, one could use
3723 the position of the reconstructed primary vertex instead. I also tried to use the principal

Chapter 8. Particle ID in GArSoft

3724 direction of the clusters, but that approach gave considerably worse results. For each
3725 event I only keep the pair with an invariant mass closer to the true π^0 mass value.

3726 Figure 8.41 (right panel) shows the invariant mass distributions for the photon pairs
3727 we get using the default (red) and the new (blue) ECal clustering algorithms. For the fit
3728 I used a modified version of the Crystal Ball function [136], obtained by taking the limit
3729 where the parameter controlling the power-law tail goes to infinity:

$$f(x; N, \mu, \sigma, \alpha) = N \cdot \begin{cases} e^{\frac{\alpha(2x-2\mu+\alpha\sigma)}{2\sigma}}; & x \leq \mu - \alpha\sigma, \\ e^{-\frac{(x-\mu)^2}{2\sigma^2}}; & x > \mu - \alpha\sigma. \end{cases} \quad (8.34)$$

3730 Comparing the fitted mean and standard deviation values for the Gaussian cores, we
3731 see that the distribution for the new algorithm is a 67% narrower and also peaks much
3732 closer to the true m_{π^0} value, going from 101.3 ± 0.4 MeV to 130.8 ± 0.6 MeV.

³⁷³³ Chapter 9

³⁷³⁴ Event selection in ND-GAr

³⁷³⁵ 9.1 CAFs and CAFAna

³⁷³⁶ 9.2 Event selection

³⁷³⁷ 9.2.1 ν_μ CC selection

³⁷³⁸ 9.2.2 Charged pion multiplicity

³⁷³⁹ Chapter 10

³⁷⁴⁰ Conclusions

³⁷⁴¹ Appendix A

³⁷⁴² An appendix

³⁷⁴³ Bibliography

- ³⁷⁴⁴ [1] DUNE collaboration, *Deep Underground Neutrino Experiment (DUNE), Far*
³⁷⁴⁵ *Detector Technical Design Report, Volume I Introduction to DUNE, JINST* **15**
³⁷⁴⁶ (2020) T08008 [2002.02967]. 15, 59, 60, 61, 64, 65, 66, 72, 73, 74, 81, 82
- ³⁷⁴⁷ [2] DUNE collaboration, *Deep Underground Neutrino Experiment (DUNE), Far*
³⁷⁴⁸ *Detector Technical Design Report, Volume IV: Far Detector Single-phase*
³⁷⁴⁹ *Technology, JINST* **15** (2020) T08010 [2002.03010]. 15, 69
- ³⁷⁵⁰ [3] J.N. Bahcall, A.M. Serenelli and S. Basu, *New solar opacities, abundances,*
³⁷⁵¹ *helioseismology, and neutrino fluxes, Astrophys. J. Lett.* **621** (2005) L85
³⁷⁵² [[astro-ph/0412440](#)]. 22, 42, 129, 131
- ³⁷⁵³ [4] R. Garani and S. Palomares-Ruiz, *Dark matter in the Sun: scattering off electrons*
³⁷⁵⁴ *vs nucleons, JCAP* **05** (2017) 007 [[1702.02768](#)]. 22, 127, 128, 130, 131, 132, 155
- ³⁷⁵⁵ [5] M. Honda, M. Sajjad Athar, T. Kajita, K. Kasahara and S. Midorikawa,
³⁷⁵⁶ *Atmospheric neutrino flux calculation using the NRLMSISE-00 atmospheric model,*
³⁷⁵⁷ *Phys. Rev. D* **92** (2015) 023004 [[1502.03916](#)]. 22, 135, 136
- ³⁷⁵⁸ [6] M. Colom i Bernadich and C. Pérez de los Heros, *Limits on Kaluza-Klein dark*
³⁷⁵⁹ *matter annihilation in the Sun from recent IceCube results, Eur. Phys. J. C,* **80** 2
³⁷⁶⁰ (2020) 129 **80** (2019) [[1912.04585](#)]. 23, 140
- ³⁷⁶¹ [7] ANTARES collaboration, *Search for Dark Matter in the Sun with the ANTARES*
³⁷⁶² *Neutrino Telescope in the CMSSM and mUED frameworks, Nucl. Instrum. Meth.*
³⁷⁶³ *A* **725** (2013) 76 [[1204.5290](#)]. 23, 140

BIBLIOGRAPHY

- 3764 [8] N. Deutschmann, T. Flacke and J.S. Kim, *Current LHC Constraints on Minimal*
3765 *Universal Extra Dimensions*, *Phys. Lett. B* **771** (2017) 515 [[1702.00410](#)]. 23, 140,
3766 141
- 3767 [9] ICECUBE collaboration, *Search for GeV-scale dark matter annihilation in the Sun*
3768 *with IceCube DeepCore*, *Phys. Rev. D* **105** (2022) 062004 [[2111.09970](#)]. 24, 152,
3769 153
- 3770 [10] C.-S. Chen, F.-F. Lee, G.-L. Lin and Y.-H. Lin, *Probing Dark Matter*
3771 *Self-Interaction in the Sun with IceCube-PINGU*, *JCAP* **10** (2014) 049
3772 [[1408.5471](#)]. 24, 152, 153
- 3773 [11] N.F. Bell, M.J. Dolan and S. Robles, *Searching for dark matter in the Sun using*
3774 *Hyper-Kamiokande*, *JCAP* **11** (2021) 004 [[2107.04216](#)]. 24, 152, 153
- 3775 [12] E. Behnke et al., *Final Results of the PICASSO Dark Matter Search Experiment*,
3776 *Astropart. Phys.* **90** (2017) 85 [[1611.01499](#)]. 24, 152, 153
- 3777 [13] PICO collaboration, *Dark Matter Search Results from the Complete Exposure of*
3778 *the PICO-60 C₃F₈ Bubble Chamber*, *Phys. Rev. D* **100** (2019) 022001
3779 [[1902.04031](#)]. 24, 152, 153
- 3780 [14] DARKSIDE collaboration, *Constraints on Sub-GeV Dark-Matter–Electron*
3781 *Scattering from the DarkSide-50 Experiment*, *Phys. Rev. Lett.* **121** (2018) 111303
3782 [[1802.06998](#)]. 24, 156, 157
- 3783 [15] XENON collaboration, *Light Dark Matter Search with Ionization Signals in*
3784 *XENON1T*, *Phys. Rev. Lett.* **123** (2019) 251801 [[1907.11485](#)]. 24, 156, 157
- 3785 [16] P.F. de Salas, D.V. Forero, S. Gariazzo, P. Martínez-Miravé, O. Mena,
3786 C.A. Ternes et al., *2020 global reassessment of the neutrino oscillation picture*,
3787 *JHEP* **02** (2021) 071 [[2006.11237](#)]. 31, 56, 61
- 3788 [17] W. Pauli, *Dear radioactive ladies and gentlemen*, *Phys. Today* **31N9** (1978) 27. 37

BIBLIOGRAPHY

- 3789 [18] F. Reines and C.L. Cowan, *Detection of the free neutrino*, *Phys. Rev.* **92** (1953)
3790 830. 37
- 3791 [19] S.L. Glashow, *Partial-symmetries of weak interactions*, *Nuclear Physics* **22** 579. 37
- 3792 [20] S. Weinberg, *A model of leptons*, *Physical Review Letters* **19** 1264. 37
- 3793 [21] A. Salam, *Weak and Electromagnetic Interactions*, *Conf. Proc. C* **680519** (1968)
3794 367. 37
- 3795 [22] A. Pich, *The Standard Model of Electroweak Interactions*, in *2010 European
3796 School of High Energy Physics*, pp. 1–50, 1, 2012 [[1201.0537](#)]. 38
- 3797 [23] ALEPH, DELPHI, L3, OPAL, SLD, LEP ELECTROWEAK WORKING GROUP,
3798 SLD ELECTROWEAK GROUP, SLD HEAVY FLAVOUR GROUP collaboration,
3799 *Precision electroweak measurements on the Z resonance*, *Phys. Rept.* **427** (2006)
3800 257 [[hep-ex/0509008](#)]. 41
- 3801 [24] R. Davis, D.S. Harmer and K.C. Hoffman, *Search for neutrinos from the sun*,
3802 *Physical Review Letters* **20** 1205. 42
- 3803 [25] J.N. Bahcall, N.A. Bahcall and G. Shaviv, *Present Status of the Theoretical
3804 Predictions for the ^{37}Cl Solar-Neutrino Experiment*, . 43
- 3805 [26] B.T. Cleveland, T. Daily, R. Davis, Jr., J.R. Distel, K. Lande, C.K. Lee et al.,
3806 *Measurement of the solar electron neutrino flux with the Homestake chlorine
3807 detector*, *Astrophys. J.* **496** (1998) 505. 43
- 3808 [27] SAGE collaboration, *Measurement of the solar neutrino capture rate with gallium
3809 metal. III: Results for the 2002–2007 data-taking period*, *Phys. Rev. C* **80** (2009)
3810 015807 [[0901.2200](#)]. 43, 55
- 3811 [28] F. Kaether, W. Hampel, G. Heusser, J. Kiko and T. Kirsten, *Reanalysis of the
3812 GALLEX solar neutrino flux and source experiments*, *Phys. Lett. B* **685** (2010) 47
3813 [[1001.2731](#)]. 43, 55

BIBLIOGRAPHY

- 3814 [29] Q.R. Ahmad, R.C. Allen, T.C. Andersen, J.D. Anglin, G. Bühler, J.C. Barton
3815 et al., *Measurement of the Rate of $\nu_e + d \rightarrow p + p + e^-$ Interactions Produced by*
3816 *8B Solar Neutrinos at the Sudbury Neutrino Observatory*, . 43
- 3817 [30] Q.R. Ahmad, R.C. Allen, T.C. Andersen, J. D. Anglin, J.C. Barton, E.W. Beier
3818 et al., *Direct Evidence for Neutrino Flavor Transformation from Neutral-Current*
3819 *Interactions in the Sudbury Neutrino Observatory*, . 43
- 3820 [31] T.K. Gaisser and M. Honda, *Flux of atmospheric neutrinos*, . 44
- 3821 [32] K. Hirata, T. Kajita, M. Koshiba, M. Nakahata, S. Ohara, Y. Oyama et al.,
3822 *Experimental study of the atmospheric neutrino flux*, . 44
- 3823 [33] D. Casper, R. Becker-Szendy, C.B. Bratton, D.R. Cady, R. Claus, S.T. Dye et al.,
3824 *Measurement of atmospheric neutrino composition with the imb-3 detector*, . 44
- 3825 [34] M. Ambrosio, R. Antolini, C. Aramo, G. Auriemma, A. Baldini, G. C. Barbarino
3826 et al., *Measurement of the atmospheric neutrino-induced upgoing muon flux using*
3827 *macro*, . 44
- 3828 [35] W. Allison, G. Alner, D. Ayres, W. Barrett, C. Bode, P. Border et al.,
3829 *Measurement of the atmospheric neutrino flavour composition in soudan 2*, . 44
- 3830 [36] SUPER-KAMIOKANDE collaboration, *Evidence for oscillation of atmospheric*
3831 *neutrinos*, *Phys. Rev. Lett.* **81** (1998) 1562 [[hep-ex/9807003](#)]. 44
- 3832 [37] P. Minkowski, $\mu \rightarrow e\gamma$ at a Rate of One Out of 10^9 Muon Decays?, *Phys. Lett. B*
3833 **67** (1977) 421. 47
- 3834 [38] M. Gell-Mann, P. Ramond and R. Slansky, *Complex Spinors and Unified Theories*,
3835 *Conf. Proc. C* **790927** (1979) 315 [[1306.4669](#)]. 47
- 3836 [39] T. Yanagida, *Horizontal gauge symmetry and masses of neutrinos*, *Conf. Proc. C*
3837 **7902131** (1979) 95. 47

BIBLIOGRAPHY

- 3838 [40] R.N. Mohapatra and G. Senjanovic, *Neutrino Mass and Spontaneous Parity
3839 Nonconservation*, *Phys. Rev. Lett.* **44** (1980) 912. 47
- 3840 [41] J. Schechter and J.W.F. Valle, *Neutrino Masses in SU(2) x U(1) Theories*, *Phys.
3841 Rev. D* **22** (1980) 2227. 47
- 3842 [42] B. Pontecorvo, *Mesonium and anti-mesonium*, *Sov. Phys. JETP* **6** (1957) 429. 48
- 3843 [43] M. Gell-Mann and A. Pais, *Behavior of neutral particles under charge conjugation,
3844 .* 48
- 3845 [44] B. Pontecorvo, *Neutrino Experiments and the Problem of Conservation of
3846 Leptonic Charge*, *Zh. Eksp. Teor. Fiz.* **53** (1967) 1717. 48
- 3847 [45] B. Pontecorvo, *Inverse beta processes and nonconservation of lepton charge*, *Zh.
3848 Eksp. Teor. Fiz.* **34** (1957) 247. 49
- 3849 [46] Z. Maki, M. Nakagawa and S. Sakata, *Remarks on the unified model of elementary
3850 particles*, *Prog. Theor. Phys.* **28** (1962) 870. 49
- 3851 [47] PARTICLE DATA GROUP collaboration, *Review of particle physics*, *Phys. Rev. D*
3852 **110** (2024) 030001. 52
- 3853 [48] L. Wolfenstein, *Neutrino Oscillations in Matter*, *Phys. Rev. D* **17** (1978) 2369. 52
- 3854 [49] B.T. Cleveland, T. Daily, R. Davis, Jr., J.R. Distel, K. Lande, C.K. Lee et al.,
3855 *Measurement of the solar electron neutrino flux with the Homestake chlorine
3856 detector*, *Astrophys. J.* **496** (1998) 505. 55
- 3857 [50] G. Bellini et al., *Precision measurement of the ^{7}Be solar neutrino interaction rate
3858 in Borexino*, *Phys. Rev. Lett.* **107** (2011) 141302 [[1104.1816](#)]. 55
- 3859 [51] SUPER-KAMIOKANDE collaboration, *Solar neutrino measurements in
3860 super-Kamiokande-I*, *Phys. Rev. D* **73** (2006) 112001 [[hep-ex/0508053](#)]. 55

BIBLIOGRAPHY

- 3861 [52] SNO collaboration, *Combined Analysis of all Three Phases of Solar Neutrino*
3862 *Data from the Sudbury Neutrino Observatory*, *Phys. Rev. C* **88** (2013) 025501
3863 [1109.0763]. 55
- 3864 [53] SUPER-KAMIOKANDE collaboration, *Atmospheric neutrino oscillation analysis*
3865 *with external constraints in Super-Kamiokande I-IV*, *Phys. Rev. D* **97** (2018)
3866 072001 [1710.09126]. 55
- 3867 [54] ICECUBE collaboration, *Measurement of Atmospheric Neutrino Oscillations at*
3868 *6–56 GeV with IceCube DeepCore*, *Phys. Rev. Lett.* **120** (2018) 071801
3869 [1707.07081]. 55
- 3870 [55] KAMLAND collaboration, *Reactor On-Off Antineutrino Measurement with*
3871 *KamLAND*, *Phys. Rev. D* **88** (2013) 033001 [1303.4667]. 55
- 3872 [56] RENO collaboration, *Measurement of Reactor Antineutrino Oscillation Amplitude*
3873 *and Frequency at RENO*, *Phys. Rev. Lett.* **121** (2018) 201801 [1806.00248]. 55
- 3874 [57] DAYA BAY collaboration, *Measurement of the Electron Antineutrino Oscillation*
3875 *with 1958 Days of Operation at Daya Bay*, *Phys. Rev. Lett.* **121** (2018) 241805
3876 [1809.02261]. 55
- 3877 [58] K.J. Kelly, P.A.N. Machado, S.J. Parke, Y.F. Perez-Gonzalez and R.Z. Funchal,
3878 *Neutrino mass ordering in light of recent data*, *Phys. Rev. D* **103** (2021) 013004.
3879 55
- 3880 [59] P. Dunne, “Latest Neutrino Oscillation Results from T2K.” Jul, 2020. 55
- 3881 [60] MINOS collaboration, *Combined analysis of ν_μ disappearance and $\nu_\mu \rightarrow \nu_e$*
3882 *appearance in MINOS using accelerator and atmospheric neutrinos*, *Phys. Rev.*
3883 *Lett.* **112** (2014) 191801 [1403.0867]. 55
- 3884 [61] OPERA collaboration, *Final Results of the OPERA Experiment on ν_τ*
3885 *Appearance in the CNGS Neutrino Beam*, *Phys. Rev. Lett.* **120** (2018) 211801
3886 [1804.04912]. 55

BIBLIOGRAPHY

- 3887 [62] K2K collaboration, *Measurement of Neutrino Oscillation by the K2K Experiment*,
3888 *Phys. Rev. D* **74** (2006) 072003 [[hep-ex/0606032](#)]. 55
- 3889 [63] DUNE collaboration, *Long-baseline neutrino oscillation physics potential of the*
3890 *DUNE experiment*, *Eur. Phys. J. C* **80** (2020) 978 [[2006.16043](#)]. 55
- 3891 [64] HYPER-KAMIOKANDE collaboration, *Physics potential of Hyper-Kamiokande for*
3892 *neutrino oscillation measurements*, *PoS NuFact2019* (2019) 040. 55
- 3893 [65] SUPERNEMO collaboration, *Probing New Physics Models of Neutrinoless Double*
3894 *Beta Decay with SuperNEMO*, *Eur. Phys. J. C* **70** (2010) 927 [[1005.1241](#)]. 57
- 3895 [66] SNO+ collaboration, *Current Status and Future Prospects of the SNO+*
3896 *Experiment*, *Adv. High Energy Phys.* **2016** (2016) 6194250 [[1508.05759](#)]. 57
- 3897 [67] NEXT collaboration, *Sensitivity of a tonne-scale NEXT detector for neutrinoless*
3898 *double beta decay searches*, *JHEP* **2021** (2021) 164 [[2005.06467](#)]. 57
- 3899 [68] L. Bathe-Peters, S. Gardiner and R. Guenette, *Comparing generator predictions*
3900 *of transverse kinematic imbalance in neutrino-argon scattering*, [2201.04664](#). 58
- 3901 [69] DUNE collaboration, *Snowmass Neutrino Frontier: DUNE Physics Summary*,
3902 [2203.06100](#). 61, 62
- 3903 [70] DUNE collaboration, *Deep Underground Neutrino Experiment (DUNE), Far*
3904 *Detector Technical Design Report, Volume II: DUNE Physics*, [2002.03005](#). 61, 63,
3905 77, 79, 135, 144, 148
- 3906 [71] SUPER-KAMIOKANDE collaboration, *Search for Proton Decay via $p \rightarrow e^+ \pi_0$ and*
3907 *$p \rightarrow \mu^+ \pi_0$ in a Large Water Cherenkov Detector*, *Phys. Rev. Lett.* **102** (2009)
3908 141801 [[0903.0676](#)]. 62
- 3909 [72] S. Raby, *Grand Unified Theories*, in *2nd World Summit: Physics Beyond the*
3910 *Standard Model*, 8, 2006 [[hep-ph/0608183](#)]. 62

BIBLIOGRAPHY

- 3911 [73] KAMIOKANDE-II collaboration, *Observation of a Neutrino Burst from the*
3912 *Supernova SN 1987a*, *Phys. Rev. Lett.* **58** (1987) 1490. 63
- 3913 [74] R.M. Bionta et al., *Observation of a Neutrino Burst in Coincidence with*
3914 *Supernova SN 1987a in the Large Magellanic Cloud*, *Phys. Rev. Lett.* **58** (1987)
3915 1494. 63
- 3916 [75] DUNE collaboration, *The DUNE Far Detector Vertical Drift Technology,*
3917 *Technical Design Report*, 2312.03130. 67, 68
- 3918 [76] DUNE collaboration, *Deep Underground Neutrino Experiment (DUNE) Near*
3919 *Detector Conceptual Design Report, Instruments* **5** (2021) 31 [2103.13910]. 71,
3920 72, 75, 79, 159
- 3921 [77] J. Strait, E. McCluskey, T. Lundin, J. Willhite, T. Hamernik, V. Papadimitriou
3922 et al., *Long-baseline neutrino facility (lbnf) and deep underground neutrino*
3923 *experiment (dune) conceptual design report volume 3: Long-baseline neutrino*
3924 *facility for dune june 24, 2015*, 1601.05823. 76
- 3925 [78] C. Green, J. Kowalkowski, M. Paterno, M. Fischler, L. Garren and Q. Lu, *The*
3926 *Art Framework*, *J. Phys. Conf. Ser.* **396** (2012) 022020. 83
- 3927 [79] DUNE DAQ, “dtp-firmware.”
3928 <https://gitlab.cern.ch/dune-daq/readout/dtp-firmware>, 2020. 91
- 3929 [80] DUNE DAQ, “dtp-simulation.”
3930 <https://gitlab.cern.ch/dune-daq/readout/dtp-simulation>, 2020. 94
- 3931 [81] DUNE DAQ, “dtpemulator.”
3932 https://github.com/DUNE-DAQ/dtpemulator/tree/fmlopez/filter_ana,
3933 2022. 94
- 3934 [82] J. McClellan and T. Parks, *A personal history of the Parks-McClellan algorithm*,
3935 *IEEE Signal Processing Magazine* **22** (2005) 82. 95

BIBLIOGRAPHY

- 3936 [83] G. Turin, *An introduction to matched filters*, *IEEE Transactions on Information*
3937 *Theory* **6** (1960) 311. 98
- 3938 [84] J.W. Goodman, *Statistical Optics*, Wiley (1985). 100
- 3939 [85] B. Dwork, *Detection of a pulse superimposed on fluctuation noise*, *Proceedings of*
3940 *the IRE* **38** (1950) 771. 101
- 3941 [86] L. Wainstein and V. Zubakov, *Extraction of Signals from Noise*, Prentice-Hall
3942 (1962). 101
- 3943 [87] E.D. Church, *Larsoft: A software package for liquid argon time projection drift*
3944 *chambers*, 1311.6774. 104, 105
- 3945 [88] S.V. Stehman, *Selecting and interpreting measures of thematic classification*
3946 *accuracy*, *Remote Sensing of Environment* **62** (1997) 77. 118
- 3947 [89] A.A. Taha and A. Hanbury, *Metrics for evaluating 3d medical image*
3948 *segmentation: analysis, selection, and tool*, *BMC Medical Imaging* **15** (2015) . 119
- 3949 [90] J. Silk, K.A. Olive and M. Srednicki, *The Photino, the Sun and High-Energy*
3950 *Neutrinos*, *Phys. Rev. Lett.* **55** (1985) 257. 125
- 3951 [91] M. Srednicki, K.A. Olive and J. Silk, *High-Energy Neutrinos from the Sun and*
3952 *Cold Dark Matter*, *Nucl. Phys. B* **279** (1987) 804. 125
- 3953 [92] J.S. Hagelin, K.W. Ng and K.A. Olive, *A High-energy Neutrino Signature From*
3954 *Supersymmetric Relics*, *Phys. Lett. B* **180** (1986) 375. 125
- 3955 [93] T.K. Gaisser, G. Steigman and S. Tilav, *Limits on Cold Dark Matter Candidates*
3956 *from Deep Underground Detectors*, *Phys. Rev. D* **34** (1986) 2206. 125
- 3957 [94] N. Bernal, J. Martín-Albo and S. Palomares-Ruiz, *A novel way of constraining*
3958 *WIMPs annihilations in the Sun: MeV neutrinos*, *JCAP* **08** (2013) 011
3959 [1208.0834]. 125, 126, 127, 133

BIBLIOGRAPHY

- 3960 [95] C. Rott, J. Siegal-Gaskins and J.F. Beacom, *New Sensitivity to Solar WIMP*
3961 *Annihilation using Low-Energy Neutrinos*, *Phys. Rev. D* **88** (2013) 055005
3962 [1208.0827]. 125, 132
- 3963 [96] C. Rott, S. In, J. Kumar and D. Yaylali, *Dark Matter Searches for Monoenergetic*
3964 *Neutrinos Arising from Stopped Meson Decay in the Sun*, *JCAP* **11** (2015) 039
3965 [1510.00170]. 125
- 3966 [97] DUNE collaboration, *Searching for solar KDAR with DUNE*, *JCAP* **10** (2021)
3967 065 [2107.09109]. 125
- 3968 [98] G. Busoni, A. De Simone and W.-C. Huang, *On the Minimum Dark Matter Mass*
3969 *Testable by Neutrinos from the Sun*, *JCAP* **07** (2013) 010 [1305.1817]. 126
- 3970 [99] V.A. Bednyakov and F. Simkovic, *Nuclear spin structure in dark matter search:*
3971 *The Zero momentum transfer limit*, *Phys. Part. Nucl.* **36** (2005) 131
3972 [hep-ph/0406218]. 127
- 3973 [100] A. Gould, *WIMP Distribution in and Evaporation From the Sun*, *Astrophys. J.*
3974 **321** (1987) 560. 128
- 3975 [101] J.N. Bahcall, M.H. Pinsonneault and S. Basu, *Solar models: Current epoch and*
3976 *time dependences, neutrinos, and helioseismological properties*, *Astrophys. J.* **555**
3977 (2001) 990 [astro-ph/0010346]. 130
- 3978 [102] T. Golan, J.T. Sobczyk and J. Zmuda, *NuWro: the Wroclaw Monte Carlo*
3979 *Generator of Neutrino Interactions*, *Nucl. Phys. B Proc. Suppl.* **229-232** (2012)
3980 499. 134
- 3981 [103] G. Cowan, K. Cranmer, E. Gross and O. Vitells, *Asymptotic formulae for*
3982 *likelihood-based tests of new physics*, *Eur. Phys. J. C* **71** (2011) 1554 [1007.1727].
3983 135
- 3984 [104] T. Kaluza, *Zum Unitätsproblem der Physik*, *Sitzungsber. Preuss. Akad. Wiss.*
3985 *Berlin (Math. Phys.)* **1921** (1921) 966 [1803.08616]. 137

BIBLIOGRAPHY

- 3986 [105] O. Klein, *Quantum Theory and Five-Dimensional Theory of Relativity. (In
3987 German and English)*, *Z. Phys.* **37** (1926) 895. 137
- 3988 [106] T. Appelquist, H.-C. Cheng and B.A. Dobrescu, *Bounds on universal extra
3989 dimensions*, *Phys. Rev. D* **64** (2001) 035002 [[hep-ph/0012100](#)]. 137
- 3990 [107] N. Arkani-Hamed, S. Dimopoulos and G.R. Dvali, *The Hierarchy problem and new
3991 dimensions at a millimeter*, *Phys. Lett. B* **429** (1998) 263 [[hep-ph/9803315](#)]. 137
- 3992 [108] L. Randall and R. Sundrum, *A Large mass hierarchy from a small extra
3993 dimension*, *Phys. Rev. Lett.* **83** (1999) 3370 [[hep-ph/9905221](#)]. 137
- 3994 [109] G. Servant and T.M.P. Tait, *Is the lightest Kaluza-Klein particle a viable dark
3995 matter candidate?*, *Nucl. Phys. B* **650** (2003) 391 [[hep-ph/0206071](#)]. 137
- 3996 [110] H.-C. Cheng, K.T. Matchev and M. Schmaltz, *Radiative corrections to
3997 Kaluza-Klein masses*, *Phys. Rev. D* **66** (2002) 036005 [[hep-ph/0204342](#)]. 139
- 3998 [111] M. Blennow, J. Edsjö and T. Ohlsson, *Neutrinos from WIMP annihilations using
3999 a full three-flavor Monte Carlo*, *JCAP* **01** (2008) 021 [[0709.3898](#)]. 139, 142
- 4000 [112] J. Edsjö, J. Elevant and C. Niblaeus, *WimpSim Neutrino Monte Carlo*. 139, 142
- 4001 [113] U. Haisch and A. Weiler, *Bound on minimal universal extra dimensions from
4002 anti-B → X(s)gamma*, *Phys. Rev. D* **76** (2007) 034014 [[hep-ph/0703064](#)]. 141
- 4003 [114] A. Freitas and U. Haisch, *Anti-B → X(s) gamma in two universal extra
4004 dimensions*, *Phys. Rev. D* **77** (2008) 093008 [[0801.4346](#)]. 141
- 4005 [115] C. Rott, D. Jeong, J. Kumar and D. Yaylali, *Neutrino Topology Reconstruction at
4006 DUNE and Applications to Searches for Dark Matter Annihilation in the Sun,
4007 JCAP* **07** (2019) 006 [[1903.04175](#)]. 144
- 4008 [116] F. Pedregosa, G. Varoquaux, A. Gramfort, V. Michel, B. Thirion, O. Grisel et al.,
4009 *Scikit-learn: Machine learning in Python*, *Journal of Machine Learning Research*
4010 **12** (2011) 2825. 150

BIBLIOGRAPHY

- 4011 [117] J. Kopp, V. Niro, T. Schwetz and J. Zupan, *DAMA/LIBRA and leptonically*
4012 *interacting Dark Matter*, *Phys. Rev. D* **80** (2009) 083502 [[0907.3159](#)]. 154
- 4013 [118] PARTICLE DATA GROUP collaboration, *Review of Particle Physics*, *PTEP* **2020**
4014 (2020) 083C01. 155
- 4015 [119] M. Beltran, D. Hooper, E.W. Kolb and Z.C. Krusberg, *Deducing the nature of*
4016 *dark matter from direct and indirect detection experiments in the absence of*
4017 *collider signatures of new physics*, *Phys. Rev. D* **80** (2009) 043509 [[0808.3384](#)].
4018 155
- 4019 [120] PLANCK collaboration, *Planck 2018 results. VI. Cosmological parameters*, *Astron.*
4020 *Astrophys.* **641** (2020) A6 [[1807.06209](#)]. 156
- 4021 [121] H. Bethe, *Zur theorie des durchgangs schneller korpuskularstrahlen durch materie*,
4022 *Annalen der Physik* **397** (1930) 325. 160
- 4023 [122] E. Fermi, *The ionization loss of energy in gases and in condensed materials*,
4024 *Physical Review* **57** (1940) 485. 161
- 4025 [123] R. Sternheimer, M. Berger and S. Seltzer, *Density effect for the ionization loss of*
4026 *charged particles in various substances*, *Atomic Data and Nuclear Data Tables* **30**
4027 (1984) 261. 161
- 4028 [124] W.W.M. Allison and J.H. Cobb, *Relativistic Charged Particle Identification by*
4029 *Energy Loss*, *Ann. Rev. Nucl. Part. Sci.* **30** (1980) 253. 161
- 4030 [125] W. Blum, L. Rolandi and W. Riegler, *Particle detection with drift chambers*,
4031 *Particle Acceleration and Detection* (2008), 10.1007/978-3-540-76684-1. 162
- 4032 [126] ALICE TPC collaboration, *Particle identification of the ALICE TPC via dE/dx*,
4033 *Nucl. Instrum. Meth. A* **706** (2013) 55. 162
- 4034 [127] L. Landau, *On the energy loss of fast particles by ionization*, *J. Phys. (USSR)* **8**
4035 (1944) 201. 165

BIBLIOGRAPHY

- 4036 [128] W. Ulmer and E. Matsinos, *Theoretical methods for the calculation of Bragg*
4037 *curves and 3D distributions of proton beams*, *The European Physical Journal*
4038 *Special Topics* **190** (2010) 1. 166
- 4039 [129] E. Aprile, A.E. Bolotnikov, A.L. Bolozdynya and T. Doke, *Noble Gas Detectors*,
4040 Wiley (Oct., 2008), 10.1002/9783527610020. 168
- 4041 [130] D.S. Wilks, *Statistical Methods in the Atmospheric Sciences*, Academic Press. 205
- 4042 [131] ALICE collaboration, *Production of pions, kaons and protons in pp collisions at*
4043 $\sqrt{s} = 900 \text{ gev with alice at the lhc}$, **1101.4110**. 207
- 4044 [132] U. Einhaus, *Charged hadron identification with de/dx and time-of-flight at future*
4045 *higgs factories*, **2110.15115**. 207
- 4046 [133] R. Frühwirth, *Application of filter methods to the reconstruction of tracks and*
4047 *vertices in events of experimental high energy physics*, Ph.D. thesis, Technischen
4048 Universität Wien, 1988. 213
- 4049 [134] P. Astier, A. Cardini, R.D. Cousins, A. Letessier-Selvon, B.A. Popov and
4050 T. Vinogradova, *Kalman filter track fits and track breakpoint analysis*, *Nuclear*
4051 *Instruments and Methods in Physics Research Section A: Accelerators,*
4052 *Spectrometers, Detectors and Associated Equipment* **450** (2000) 138. 213
- 4053 [135] T2K UK collaboration, *The Electromagnetic Calorimeter for the T2K Near*
4054 *Detector ND280*, *JINST* **8** (2013) P10019 [**1308.3445**]. 221
- 4055 [136] J.E. Gaiser, *Charmonium Spectroscopy From Radiative Decays of the J/ψ and ψ'*,
4056 Ph.D. thesis, Stanford University, 1982. 226